Interactions and diffractive magneto-optics in arrays of magnetic nanoelements

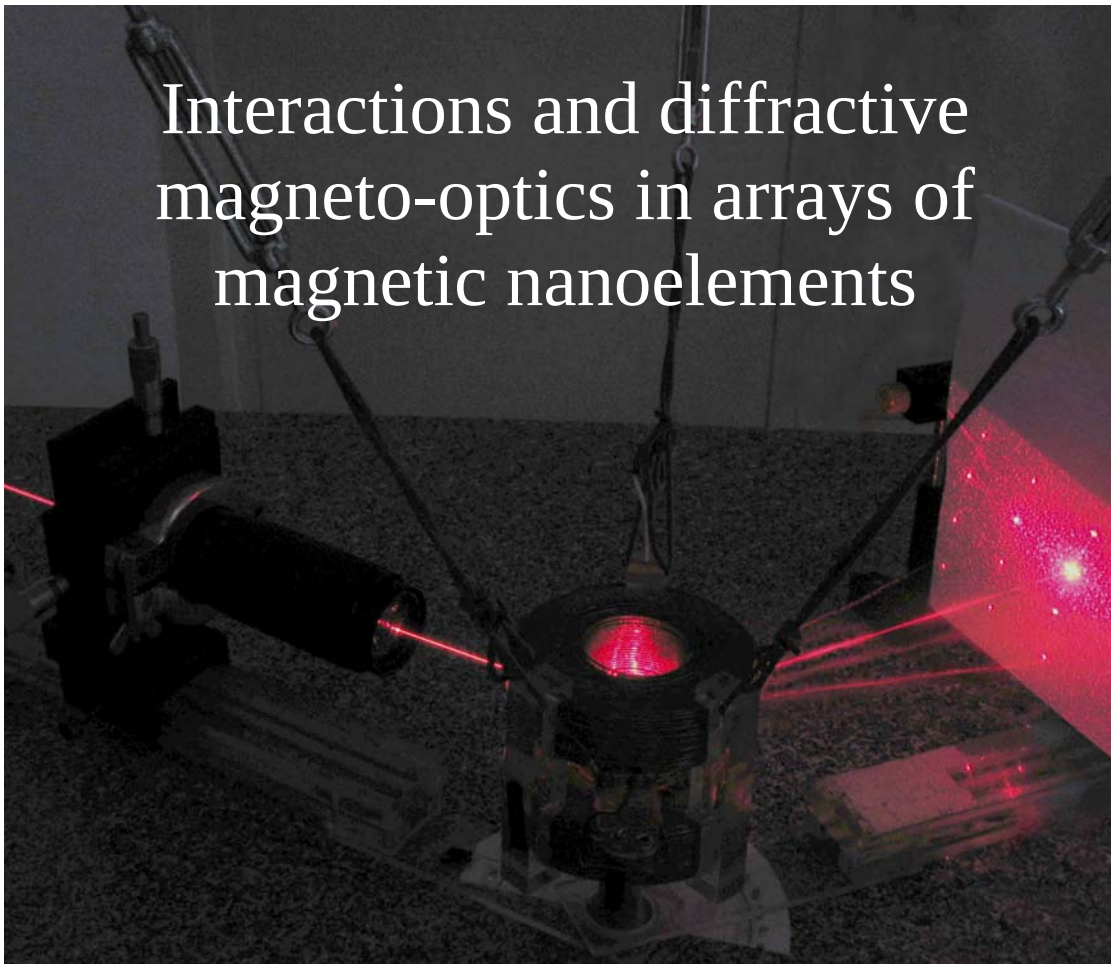

Rubén Álvarez Sánchez

Departamento de Física de la Materia Condensada

Universidad Autónoma de Madrid

2006

Universidad Autónoma de Madrid
Facultad de Ciencias
Departamento de Física de la Materia Condensada

Interacciones y magneto-óptica en el difractado en redes de nanoelementos magnéticos

Memoria para optar al grado de
Doctor en Ciencias Físicas
Presentada por

Rubén Álvarez Sánchez

Y supervisada por el doctor

José Luis Costa Krämer

Instituto de Microelectrónica de Madrid (IMM)
Centro Nacional de Microelectrónica (CNM)
Consejo Superior de Investigaciones Científicas (CSIC)

Tres Cantos, Noviembre 2006

Este trabajo ha sido financiado por la Consejería de Educación de la Comunidad de Madrid (CAM) a través de una beca predoctoral perteneciente al programa de Formación de Personal Investigador (FPI)

Trabajo realizado en:

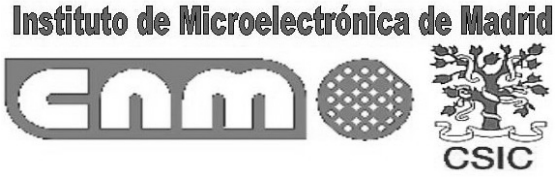

Instituto de Microelectrónica de Madrid (IMM-CNM-CSIC)

C/ Isaac Newton 8, PTM
28760 Tres Cantos (Madrid)

To my family

—He intentado describirte a mis amigos del grupo de terapia de grupo, trabajando en esta habitación, apartado del mundo. Esa extraña mente medieval en su claustro.
—Debió intrigarles mucho, sin duda —murmuró Ignatius […]—. Pronto podrán verme en carne y hueso

La conjura de los necios
(A Confederacy of dunces)
John Kennedy Toole

En resolución, él se enfrascó tanto en su lectura que se le pasaban las noches leyendo de claro en claro, y los días de turbio en turbio, y así, del poco dormir y del mucho leer, se le secó el cerebro, de manera que vino a perder el juicio.

El ingenioso hidalgo D. Quijote de la Mancha
Miguel de Cervantes

INDEX OF CONTENTS

OBJECTIVES AND MOTIVATION

The continuing need to increase the storage density in information technology devices combined with the commercial requirement of miniaturization for these devices, requires the understanding of the behavior of smaller and smaller magnetic entities and the appropriate quantification of interactions at smaller and smaller scales.

The magnetic recording industry has come a long way since the introduction of the first hard disk, the IBM RAMAC (Random Access Method of Accounting and Control), in 1956, a system with 5Mb of storage capacity on fifty 24–inch discs. Compared to present day hard disks, it represents a nearly 20 million times increase in areal density of information storage. This is just an illustrative example on how steep is the roadmap for development of hard disk systems. Indeed, the areal density growth rate increased from 25% per year in the early eighties up to 100% per year nowadays.

It is not certain however, that the incredible areal density growth rate of hard disks will continue in the next decade. With the aim of sustaining such an accelerated development and in order to overcome several limitations present in current hard disk systems the creation and exploration of new ideas and technologies is mandatory.

The most widely known limitation is due to the so–called superparamagnetic limit. This establishes a fundamental limit to the areal density that can be achieved. If the density is increased above this limit, the grains of the magnetic material happen to be so small that they become thermally unstable in a short time scale and the information stored is eventually lost. There are several approaches to push the limit to higher recording densities (smaller bit sizes), most of them being applied in recent years to commercial products: AntiFerromagnetically Coupled (AFC) media [1,2], perpendicular recording [3,4], heat assisted recording [5] or the use of patterned media [6, 7].

Due to their complex nanostructures, extremely small length scale, low dimensionality and interplay among constituents, nanostructured materials often exhibit new and enhanced properties over their bulk counterparts. Their novel

properties can also be tailored through extra degrees of freedom, such as structure, constituent materials, etc. Clearly, a challenge for the future is the understanding and control of the magnetic phenomena on the nanoscale.

This thesis is dedicated to understand the magnetic properties of 1D and 2D magnetic arrays, concentrating on interactions between the different elements of the array themselves and the array with a continuous ferromagnetic thin film. This is done by modeling and fabricating different types of structures, quantifying different effects both theoretically and experimentally. Among the properties studied, some magneto-optical effects are remarkable.

The completion of this primary objective is useful in many fields of knowledge and technology:

- The study of collective effects in reduced dimensionality is the basis for new technologies in the field of magnetic recording media and is also useful for magnetic logical devices.

- In the area of biomedical applications, a good understanding on the interactions of the magnetic elements embedded in a magnetic array is essential for the development and fabrication of an ophthalmic implantable orbital pressure transducer (main goal of one of the projects of the IMM). This device translates the pressure into the orbital cavity into variations of the magnetic susceptibility of an array of magnetic elements embedded in a grating of elastic material by means of the modification of the separation between the elements of the array.

- Other biomedical device currently under development at the IMM is based in the interactions between a continuous thin film and a pattern fabricated on top of it, which requires the modeling of stray fields and gradients.

The thesis is divided in seven chapters.

In the first chapter, some basics on fabrication of pattered magnetic media are explained.

Chapter II is centered in magneto-optics. The magneto-optical Kerr effect is phenomenologically described together with some magneto-optical based apparatus.

Chapter III is focused in diffractive magneto-optics, a novel technique capable of providing extra information about magnetization reversals that is hidden for conventional magneto-optics.

In chapter IV, the magneto-optic properties of 2D arrays are studied as a function of the interelement separation. Both conventional magneto-optics and diffractive magneto-optics are used to determine the onset of the interaction and the reversal mechanisms present in the patterns.

Chapter V is dedicated to the theoretical analysis of the magnetostatic energy and shape anisotropy of magnetic arrays as a function of both the element and the array shape

According to the results of that analytical model it seems that it is possible to tailor the shape anisotropy of a magnetic array. In chapter VI, this is experimentally studied.

Finally, in chapter VII, the knowledge acquired in the previous chapters is applied to an heterostructure consisting on a pattern over a continuous film in order to replicate the domain structure of the pattern into the continuous layer. A novel pure magneto-optic effect closely related to this pattern transfer is also presented.

OBJETIVOS Y MOTIVACIÓN

La continua necesidad de incrementar la capacidad de almacenamiento en dispositivos relacionados con las tecnologías de la información, combinado con el requisito comercial de miniaturización de dichos dispositivos, demanda una profunda comprensión del comportamiento de entidades magnéticas de cada vez menor tamaño así como una apropiada cuantificación de las interacciones en cada vez menores escalas.

La industria de dispositivos de grabación magnética ha recorrido un gran camino desde la aparición del primer disco duro, el RAMAC (Random Access Method of Accounting and Control) de IBM, en 1956; un sistema de 5Mb de capacidad de almacenamiento en 50 discos de 24 pulgadas. Comparado con los discos duros actuales, representa un incremento en la densidad de almacenamiento por unidad de área de cerca de 20 millones de veces mayor. Esto es solamente un ejemplo ilustrativo de la pronunciada tendencia seguida en el desarrollo de discos duros. De hecho, la tasa de incremento anual en la densidad de almacenamiento por unidad de área ha pasado del 25% a principios de los años 80 hasta el 100% actual.

Sin embargo, no es cierto que esta increíble tasa de incremento anual en la densidad de almacenamiento por unidad de área pueda mantenerse en la próxima década. Con el propósito de conservar un desarrollo tan acelerado y de cara a superar ciertas limitaciones presentes en los actuales sistemas de discos duros, es necesaria la creación y exploración de nuevas ideas y tecnologías.

La limitación más conocida se debe al llamado límite superparamagnético. Se establece así un límite fundamental a la densidad de almacenamiento por unidad de área. Si la densidad se incrementa por encima de ese límite, los granos que conforman el material magnético pueden llegar a ser tan pequeños que sean térmicamente inestables en una escala de tiempos pequeña, conllevando la pérdida de la información almacenada. Existen distintas aproximaciones que pueden trasladar este límite hasta mayores densidades de grabación (menores tamaños de bit), muchas de ellas aplicadas en los últimos años en dispositivos comerciales: Medios antiferromagnéticos acoplados (AFC) [1,2], grabación con imanación perpendicular [3,4], grabación asistida por calor [5] o el uso de redes de elementos [6,7].

Debido a sus complejas nanoestructuras, a lo extremadamente reducido de su escala, a su baja dimensionalidad y a las interacciones entre sus constituyentes, los materiales nanoestructurados suelen exhibir nuevas e intensificadas propiedades comparados con sus análogos de tamaño macroscópico. Sus novedosas propiedades también pueden ser diseñadas a través de una serie de grados de libertad adicionales, como la estructura, materiales constituyentes, etc. Claramente, la comprensión y control de los fenómenos magnéticos en la nanoescala es un desafío para el futuro.

Esta tesis está dedicada al estudio de las propiedades magnéticas de redes de elementos magnéticos de 1 y 2 dimensiones, prestando especial atención a las interacciones entre los distintos elementos que constituyen la red y a las existentes entre los elementos de la red y una lámina delgada continua de material ferromagnético. Esto se consigue modelando y fabricando distintos tipos de estructuras así como cuantificando distintos efectos tanto teórica como experimentalmente. De entre las propiedades estudiadas, destacan algunos efectos magneto-ópticos.

La consecución de este objetivo principal es útil para varios campos del conocimiento y la tecnología

- El estudio de efectos colectivos en dimensionalidad reducida es la base de nuevas tecnologías en el campo de la grabación magnética y de cara al desarrollo de dispositivos lógicos magnéticos.

- En el área de las aplicaciones biomédicas, una buena comprensión de las interacciones entre los elementos magnéticos de una red es esencial para el desarrollo y fabricación de un transductor implantable para medir la presión ocular (principal objetivo de uno de los proyectos del IMM). Este dispositivo traduce la presión dentro de la cavidad orbital en variaciones de la susceptibilidad magnética de una red de elementos magnéticos fabricada sobre un sustrato flexible, por medio de la modificación de la separación entre los elementos de dicha red.

- Otro dispositivo biomédico actualmente en desarrollo en el IMM está basado en interacciones entre una lámina delgada de material ferromagnético y una estructura fabricada sobre dicha lámina. Esto requiere el modelado de stray fields y gradientes de campo.

La tesis está dividida en 7 capítulos.

En el primer capítulo, se explican los fundamentos de fabricación de redes de elementos magneticos.

El capítulo II se centra en la magneto-óptica. El efecto Kerr magneto-óptico se describe desde el punto de vista fenomenológico, junto con una serie de aparatos de medida basados en la magneto-óptica.

El capítulo III presta especial atención a la magneto-óptica en el difractado, una técnica novedosa capaz de proporcionar información adicional sobre los mecanismos de inversión de la imanación, oculta para la magneto-óptica convencional.

En el capítulo IV, se estudian las propiedades magneto-ópticas de redes 2D en función de la separación entre elementos. Se usan tanto la magneto-óptica convencional como la magneto-óptica en el difractado para determinar el comienzo de la interacción y los mecanismos de inversión de la imanación presentes en los elementos de la red.

El capítulo V está dedicado al análisis teórico de la energía magnetostática y la anisotropía de forma de redes de elementos magnéticos en función tanto de la forma de los elementos como de la forma de las redes.

De acuerdo con los resultados de ese modelo teórico, se abre la posibilidad de diseñar la anisotropía de forma de una red de elementos magnéticos. En el capítulo VI se estudia esta posibilidad desde el punto de vista experimental.

Finalmente, en el capítulo VII, el conocimiento adquirido en los capítulos anteriores se aplica a una heteroestructura consistente en una red sobre una capa continua de material de cara a replicar la estructura de dominios de la red in la lámina continua. Se presenta en este capítulo un novedoso efecto puramente magneto-óptico estrechamente relacionado con esta transferencia de patrones.

References:

[1] V. Skumryev, S. Stoyanov, Y. Zhang, . Hadjipanayis, D. Givord, J. Nogués. Nature **423**, 850 (2003)

[2] E.E. Fullerton, D.T. Margulies, M.E. Schabes, M. Carey, B. Gurney, A. Moser, M. Best, G. Zeltzer, K. Rubin, M. Doerner, Appl. Phys. Lett. **77**, 3806 (2000)

[3] S. Iwasaki, Y. Nakamura, IEEE Trans. Magn. **MAG-13**, 1272 (1977)

[4] H. Takano, Y. Nishida, A. Kuroda, H. Sawaguchi, Y. Hosoe, T. Kawabe, H. Aoi, H. Muraoka, Y. Nakamura, K. Ouchi, J. Magn. Magn. Mat., **235**, 241 (2001)

[5] J.J.M. Ruigrok, R. Coehoorn, S.R. Cumpson, H.W. Kesteren, J. Appl. Phys. **87**, 5398 (2000)

[6] S.Y. Chou, P.R. Krauss, L. Kong, J. Appl. Phys. **79**, 6101 (1996)

[7] M.A.M. Haast, J.R. Schuurhuis, L. Abelmann, J.C. Lodder, Th.J. Popma, IEEE Trans. Magn. **34**, 1006 (1998)

CHAPTER I:

SOME BASICS ON PATTERN FABRICATION AND MAGNETIC MEASUREMENT: EXPERIMENTAL TECHNIQUES USED IN THIS THESIS

Index

SOME BASICS ON SAMPLES FABRICATION AND MAGNETIC MEASUREMENT: EXPERIMENTAL TECHNIQUES USED IN THIS THESIS

1.Introduction

The spectacular progress in miniaturization during the last decades is closely related to the improvement of micro and submicro fabrication techniques. In particular, thin film growth and patterning techniques represent the basis of the current industrial advances in information technologies. The dimensionality reduction required by miniaturization entails the appearance of novel properties that ought to be studied in order to sustain the development of new technologies.

Thus, at least a basic knowledge of the fabrication techniques is convenient in order to investigate the fundamental magnetic properties of the matter in reduced dimensionality.

The fabrication processes of thin film patterned media can be divided into two steps: patterning and material growth. The material used is responsible for the magnetic properties of the thin film and during the growth process some of these properties can be modified or even tailored.

Amongst the great variety of existing fabrication techniques, just a few of them used to fabricate the samples studied in this thesis are explained in what follows, paying special attention to sputtering and lithographic techniques.

In addition, two widely used apparatus for magnetic measurements and magnetic characterization (Vibrating Sample Magnetometer –VSM– and Magnetic Force Microscope –MFM–) are also described.

The magneto-optic (MO) measurements and domain imaging techniques, in which this thesis is focused, are detailed in chapters II & III.

2.Patterning techniques I: An overview

Two approaches, termed *bottom-up* and *top-down*, can be used to study the effect of a reduced dimensionality.

Magnetism, being a structure and size dependent property, is specially sensitive to size effects. For example, when reducing the size of the magnetic elements to the nanoscale, thermal fluctuations might overcome the ferromagnetic anisotropy of the material reaching the so-called superparamagnetic limit. At this superparamagnetic limit, the thermal energy given by k_BT (k_B is the Boltzmann constant and T is the temperature in Kelvin) is larger than the energy corresponding to the magnetocrystalline anisotropy, given by KV (where K is the magnetocrystalline anisotropy constant of the material, in J/m^3, and V is the volume of the considered magnetic element). This way, the hysteresis characteristic of the ferromagnetic materials is lost, causing the loss of information in the magnetic information storage media. The problem might be solved either increasing the anisotropy (K) or the volume (V). An increment in the anisotropy implies a change in the material to be used whereas the volume of the dots might be increased by performing the growth process in several stages with conditions detailed in references [I.1-I.4] thus fabricating nanopillars instead of dots.

2.1.Bottom-up techniques

Bottom-up techniques consists of fabricating low dimensionality systems from its basic components. Bottom-up techniques include MBE techniques, in particular, self-assembly and self-organization procedures. Self-assembly consists of a random deposition of adatoms all along the substrate surface subsequently followed by a growth on random nucleation sites. On the other hand, self-organization consists of a regular distribution of the adatoms all along the target surface.

Both self-assembly and self-organization have the advantage of being techniques capable of patterning large areas what make them useful and worthwhile for large scale fabrication. Nevertheless, from a technological point of view, the material size and long range order demands necessary for recording technology media has never been produced by these techniques. In addition, bottom up techniques does not allow nowadays to fully control the shape and separation of the magnetic elements.

2.2.Top-down techniques

Contrary to bottom-up techniques, top-down methods consists in reducing the dimensionality from bulk material by lithographic techniques. The term lithography refers to a three step method consisting on an uniform resist coating of the sample or substrate, followed by an exposure and ended with a development of the coating.

According to [I.5], lithographic techniques can be classified into three main categories: lift-off, electrodeposition and etching. The first two are post-deposition methods in which the pattern transfer is performed on the substrate subsequently followed by a thin film growth. The etching, on the other hand is performed directly on a previously grown thin film. In all these three cases a pattern must be done on an uniformly deposited –spinned– resist by performing an exposition on it, commonly to electrons (e-beam lithograpy), UV light (photolithography) and X-ray (X-ray photolithography). Depending on the exposition method, a mask might be needed. For example, e-beam lithography is a method with no physical mask, performed using a scanning electron microscope (SEM), whereas in photolithography the whole sample is exposed to the radiation of a UV light source and a mask is needed to selectively radiate certain areas of the sample.

During the exposition, the chemical properties of the resist are locally changed. This allows to selectively remove either the exposed or the non-exposed parts submerging the sample into a chemical agent known as developer. This step in which the pattern is transferred to the resist is known as development.

It is noteworthy that the resolution limit of the lithographic techniques is eventually determined by the radiation wavelength. While the e-beam lithography might reach a resolution of a few tens of nanometers, conventional photolithography resolution limit is around one micrometer.

The etching technique consist on the removal of material from a thin film using either chemical or physical processes. Thus, after growing a thin film on a substrate and uniformly coating it with resist, the pattern is transferred to the resist by exposition plus development. The next step of removing the material not covered by the resist can be done either chemically (known as wet etching), physically by ion bombardment (known as dry etching) or by a combination of both (reactive ion etching). Wet etching is an isotropic method that causes tilted patterns. On the contrary, dry etching yields sharp profiles and therefore is more

used for patterning ultrafine structures. After performing the etching, the residual resist must be removed either stripping it with an oxygen plasma (that can badly damage the magnetic properties of the pattern) or by chemical means (being aware that the etching process hardens the resist).

In the etching technique (see fig. I-1 a&b) either positive or negative resist might be used. If positive resist is used, the resist removed during development is the exposed one (fig I-1a). In contrast, when using negative resist, the non-exposed part is removed during development (fig I-1b). A complete description of the etching technique and a list of etching recipes for some common materials can be found in [I.6].

In both the lift-off technique (fig. I-1 c) and the electrodeposition (fig. I-1 d), the thin film is grown after performing the development of the resist. Thus, the first step of both processes is the spin coating of the substrate, followed by an exposition of the pattern in either positive or negative resist and by a subsequent development.

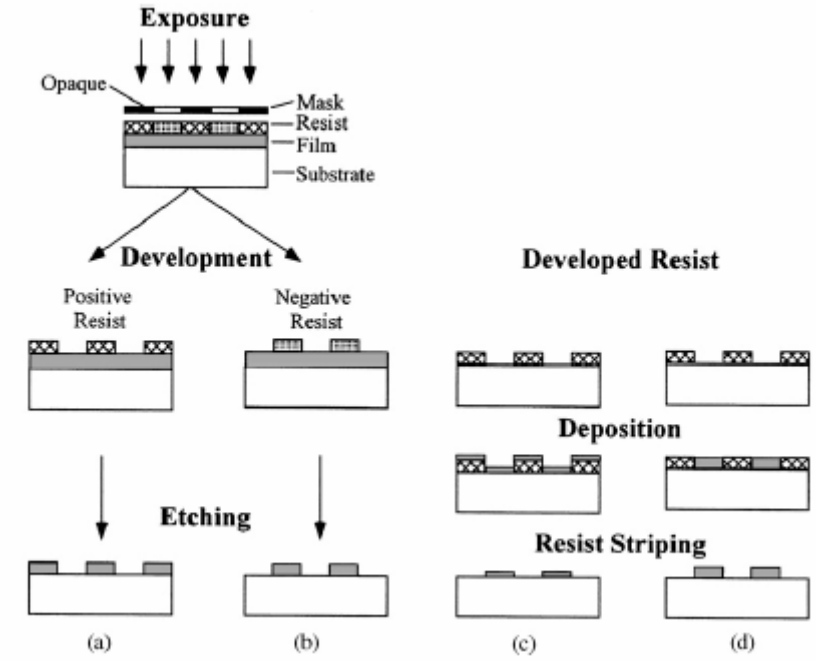

Fig. I-1: Sketch of lithographic processes from [I.5]. a) positive resist and etching, b) negative resist and etching, c) lift-off and d) electrodeposition.

The main difference between lift-off and electrodeposition is the way the material is grown on the patterned substrate.
In the case of the lift-off, the material is sputtered or evaporated in low pressure chambers, whereas in electrodeposition the material is deposited by current circulation through an electrolyte. Thus, electrodeposition is a technique suited to fabricate patterns with high aspect ratios. On the contrary, the lift-off method is more suited to fabricate planar patterns since both the resist coated and non-coated areas are covered by the grown material. Therefore, in order to properly remove the remanent resist after the pattern transfer, it is mandatory a large ratio resist vs. grown material. Both procedures are sketched in fig. I-1 c&d.

Both lift-off and etching have been used to fabricate the samples analyzed in this work. In each case either e-beam lithography or optical lithography has been used. E-beam lithography is performed using a Scanning Electron Microscope (SEM) and a electron-sensitive resist (Polymethylmethacrilate, PMMA). Elements of some tens of nanometers diameter and very different shapes may be obtained using this technique, but the lithography cannot be performed in large areas (less than 2x2 mm^2 and typically one order of magnitude lower). In addition, this method is quite slow and very expensive compared to optical techniques.

UV optical lithography might pattern very large areas using a mask but its resolution limit only allow elements size in the range of the microns. A special case of optical lithography that will be discussed in more detail in the following section is the Laser Interference Lithography (LIL), a technique capable of pattern large areas (in the order of cm^2) with a minimum element diameter in the order of some tens of nanometers.

3.Patterning techniques II: Laser Interference Lithography

Laser Interference Lithography (LIL) is an alternative maskless lithographic technique capable of generating patterned structures over large areas in short time expositions. In this technique, known since the late 60´s due to the invention of the laser, a photoresist is exposed to an interference pattern produced by two coherent laser beams. The way this interference pattern can be controlled and modified and, therefore, the limitations of the LIL is determined by the principle of interference.

3.1.Theoretical background

In order to explain the principle of interference, lets consider two planar waver $\mathbf{k}_1$ and $\mathbf{k}_2$ incident to a surface under an angle Θ with respect to the Z direction (perpendicular to the plane, see the inset of fig. I-2a). Thus, $\mathbf{k}_1 = k(\hat{\mathbf{x}}\sin\Theta + \hat{\mathbf{z}}\cos\Theta)$ and $\mathbf{k}_2 = k(-\hat{\mathbf{x}}\sin\Theta + \hat{\mathbf{z}}\cos\Theta)$, where k is the wave number, related to the radiation source wavelength by $k=2\pi/\lambda$.

Denoting by $\mathbf{r}$ the position vector ($\mathbf{r}=x\hat{\mathbf{x}}+z\hat{\mathbf{z}}$), the intensity of the resulting wave can be spatially resolved as follows:

$$I(\mathbf{r}) \propto \left| e^{i\mathbf{k}_1\cdot\mathbf{r}} + e^{i\mathbf{k}_2\cdot\mathbf{r}} \right|^2 = 4\cos^2\left(\frac{1}{2}(\mathbf{k}_1+\mathbf{k}_2)\cdot\mathbf{r}\right) \qquad \text{(I-1)}$$

Hence, an expression for the intensity resolved in the X direction is obtained:

$$I(x) \propto \cos^2(kx\sin\Theta) \qquad \text{(I-2)}$$

The minimal resolvable feature size Δx corresponds to the distance between an intensity maximum and its adjacent minimum. It can be calculated using the following fact:

$$k\Delta x \sin\Theta = \pi/2 \qquad \text{(I-3)}$$

Hence,

$$\Delta x = \frac{\lambda}{4\sin\Theta} \qquad \text{(I-4)}$$

The period P of the patterning is the distance between two adjacent maxima, i.e., twice Δx. Thus, the minimum period of the patterning is directly proportional to the used wavelength. Moreover, the minimum possible period is half the incident wavelength and is obtained when the incidence angle is close to $\pi/2$.

3.2.Experimental setup

LIL setups might be classified into dual beam interferometers and Lloyd's mirror interferometers. In dual beam interferometers, the incident light is directed into a beam splitter, dividing that way the original beam into two with half the original intensity. Each branch is directed towards the sample by a mirror in a way that they interfere just over the sample.

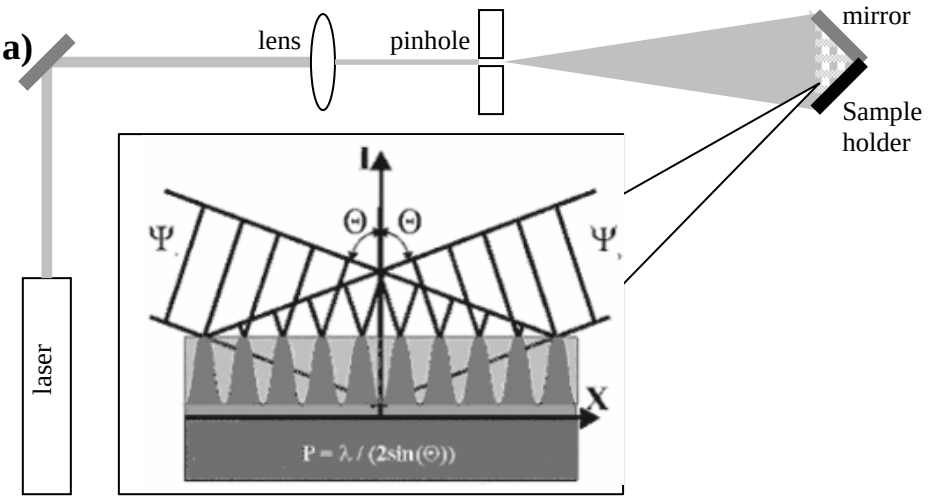

Fig. I-2: (a) Simplified sketch of the Lloyd's mirror interferometer setup. A laser beam is expanded and spatially filtered by a lens and a pinhole. The broad beam is then directed onto a mirror-sample system. (b) setup at the MESA$^+$ Institute.

In Lloyd's mirror interferometer (the setup used in the MESA$^+$ Institute for patterning the samples in this thesis, see fig. I-2), a laser beam is focused by a lens into a pinhole, thus expanding the incident beam. The broad beam is then directed onto a mirror-sample system. This mirror-sample system is known as Lloyd's mirror. As shown in fig. I-2, the mirror is placed at 90º of the sample and the whole system is placed in such a way that the light reflected by the mirror interferes with the light directly incident to the sample.

Each exposition in a LIL setup creates a pattern of lines. By just rotating the sample square, rectangular or circular shapes might be patterned embedded in square or triangular lattices.

In the MESA$^+$ setup, a stable 200mW Nd:YAG laser with λ=1064 nm, together with two consecutive frequency duplicators. Thus, the final wavelength of the incident beam is λ=1064 nm. Hence, the minimum expected periodicity is 266 nm.

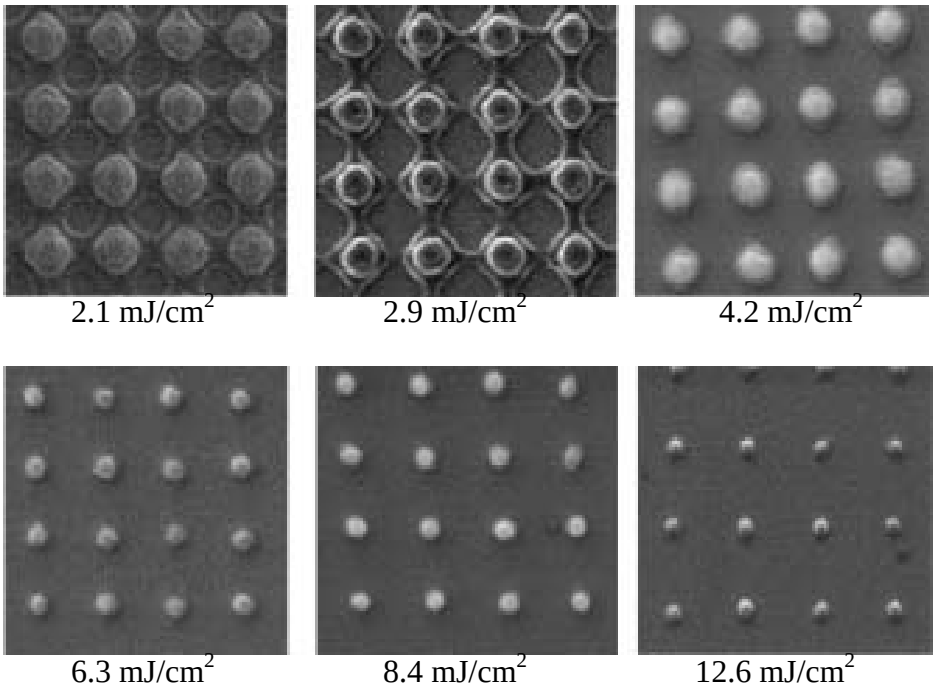

Fig. I-3: 600 nm periodicity patterns by LIL. The size of the elements are modulated modifying the areal dose of exposition. The larger the dose, the lower the element size (from [I.7]).

The size of the elements of the arrays generated by LIL is related to the periodicity of the array. In principle, the element size is 1/3 of the pattern periodicity. Nevertheless, this size might be modulated modifying the exposition time and, therefore, the areal dose (in mJ/cm^2) (see fig. I-3, from [I.7]). A detailed explanation of the patterning process can be found in reference [I.7] and a thorough description of the LIL setup in [I.8].

3.3.Comparison with other lithographic techniques

Interference lithography offers advantages over scanning electron-beam lithography due to its ability to define grid patterns over large areas in a single, fast, mask less exposure. In addition, since interference lithography defines periodic patterns with well-controlled periodicity, it provides an absolute reference that may facilitate read/write head position tracking [I.9].
In table I-1, the three methods used to fabricate the patterns for this thesis are compared.

Patterning method	Advantages	Disadvantages
E-beam	• Maskless • High control on the shape and size of the elements of the pattern • Capable of performing submicron patterns	• Slow • Expensive • Only small areas can be patterned in a reasonable time
UV Photolithography	• Capable of patterning large areas • Fast (just a few seconds per exposition) • Inexpensive	• Needs a mask • Cannot pattern elements below the micron range
Laser Interference Lithography	• Maskless • Capable of patterning large areas • Fast (few seconds per exposition) • Capable of performing submicron patterns • Inexpensive	• Only arrays of a few basic shapes can be patterned • The size of the element strongly depends on array periodicity • Very sensitive to mechanical vibrations

Table I-1: Advantages and disadvantages of LIL and the two most common patterning methods: UV photolithography and e-beam lithography.

In addition to the comparison in table I-1, table I-2 shows a direct comparison between e-beam lithography and laser interference lithography, focusing in two characteristics, the maximum patterned area and the minimum element size.

Patterning method	Maximum reported patterned area	Minimum reported element size	References
E-beam	10×10 mm^2	10 nm	[I.10], [I.11]
Laser Interference Lithography	50×50 cm^2	20 nm	[I.12-I.16]

Table I-2: Comparison of two submicron patterning methods, LIL and e-beam lithography.

A complete comparison of the different patterning techniques can be found in [I.5].

4.Thin film growth: Sputtering.

Thin film deposition techniques by sputtering have been known since the end of the nineteenth century, but have been industrially used only the last 30 years.

Sputtering is a physical process in which atoms in a solid target material are ejected into the gas phase due to bombardment of the material by energetic ions inside a vacuum chamber. This chamber is firstly set to a pressure below 10^{-7} mbar, and then filled till reaching a pressure between 10^{-2}-10^{-4} mbar with a gas to be ionized (typically Ar). Once reached the pressure working conditions, the cathode is fed with high voltage. Under this conditions, a plasma is created and the positive ions of the gas (Ar^+ ions) are accelerated towards the cathode (target) containing the material to deposit. The collision between the Ar^+ ions and the target yield small particles of the material on the cathode that are subsequently deposited in the substrate.

Nowadays, sputtering is the most common thin film deposition technique. This is due to several factors, in particular to the fact that the deposition is more adherent to the substrate than, for example, in thermal evaporation methods. In addition, it

is possible to deposit some materials that cannot be deposited by thermal evaporation (for instance, the composition of an alloy in thermal evaporation techniques is often altered).

The following facts about sputtering are noteworthy:

- The sputtering ratio and, consequently, the deposition speed vary for different metals, alloys and insulators
- It is possible to combine different materials in the deposition
- The thickness control is simple and easily reproducible
- The plasma might be optimized in order to obtain better thickness uniformity of the thin film.
- High energy electrons can be moved away from the sample avoiding the heating.
- The metallic film adhesion can be enhanced polarizing the substrate.

Most of this advantages of the sputtering are due to the low deposition speed characteristic of this method, which allows to fine tune the thin film characteristics.

4.1.Brief description of the thin film growth process

Regardless of the sputtering technique used, the thin film growth process can be described in the following way (see fig. I-3):
The particles from the bombarded cathode reach the substrate with energies between 10 and 40 eV. This particles transfer their energy to the substrate, becoming a loosely bonded type of particles known as adatoms. The adatoms diffuse over the substrate surface, exchanging energy with substrate atoms and other adsorbed particles until they are either adsorbed at low energy sites or desorbed by evaporation or resputtering. These low energy sites can be, for example, defects on the substrate surface or crystallographic variations.

The adatoms diffusivity mainly depends on the interaction between the same adatoms and the substrate atoms and on the temperature of the substrate.

As more sputtered atoms arrives at the substrate surface, the nuclei are formed and become large enough to form islands of growth material. As the growth process continues, these islands continue enlarging till they eventually enter in close contact to form a continuous film.

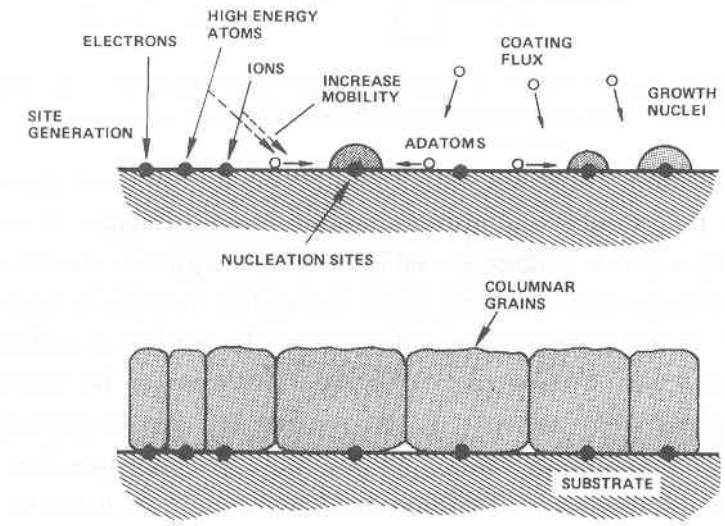

Fig. I-3: Schematic illustration of film nucleation and growth processes (from [I.18])

The resulting thin film strongly depends on the substrate temperature and on the Ar pressure during deposition. These dependencies are schematized in the phase diagram of fig. I-4.

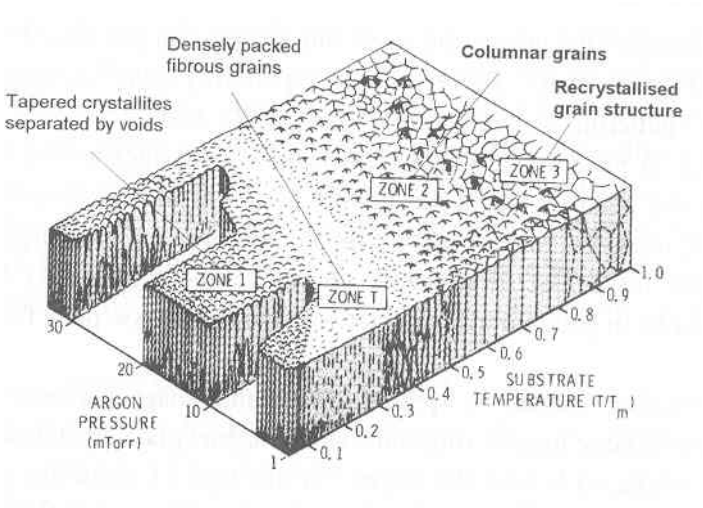

Fig. I-4: Thornton phase diagram for sputtered thin film structures. T_m represents the melting point of the sputtered material in Kelvin. (from [I.18])

Fig. I-5, show two Transmission Electron Microscope (TEM) images of two CoNi/Pt multilayers grown at RT but at different pressure. The higher the pressure, the more roughness of the resulting thin film.

The control of the roughness of the thin film is very important in the particular case of magnetic multilayers with out-of-plane (perpendicular) magnetization like Co/Pt, Co/Pd, Fe/Pt and Fe/Pd and other compounds with Fe and Co alloys. Since in these multilayers the perpendicular magnetization is due an interface effect, a rough thin film like the one in fig. I-9 b) will be magnetically different from a flat interface multilayer. The magnetic properties of these multilayers also depend on other factors like the number of bilayers, the relative thickness of the layers within a bilayer and, the total thickness of the thin film. A complete experimental analysis of these dependencies can be found in [I.22, I.23, I.24].

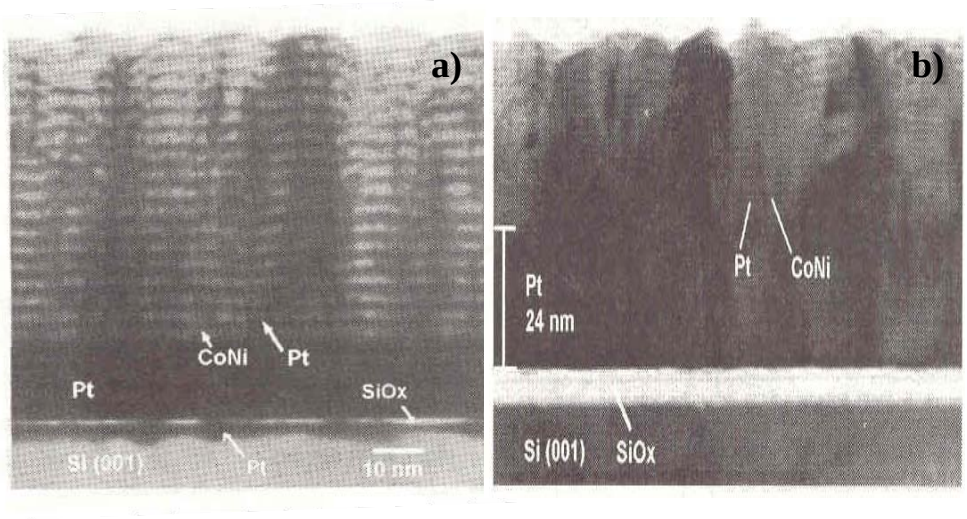

Fig. I-5: Transmission Electron Microscope (TEM) images Co/Pt multilayer at different Ar^+ pressures during sputtering deposition at Room Temperature (RT). a) P_{Ar}=16μbar, b) P_{Ar}=40μbar (both images from [I.22])

Depending on the number of electrodes used, the sputtering configurations might be classified in different categories:

4.2.Planar diode sputtering

In this configuration, the target is used as a cathode and the substrate as an anode. When a voltage close to 1000 V is applied to the cathode, an Ar^+ plasma can be created. Planar diode is the simplest configuration but in this case it is difficult to control the process and avoid the film contamination. Moreover, in order to preserve some reproducibility, the current density and substrate temperature must be carefully controlled. The advantages of the planar diode can be summarized in the following list.

- It is possible to grow thin film of refractory metals and insulators
- Guarantees an optimum adherence
- Allows low temperature epitaxy
- The deposited film is uniform even on large dimensions substrates

In contrast, the disadvantages of the planar diode are:

- It has a low deposition speed
- The substrate must be refrigerated

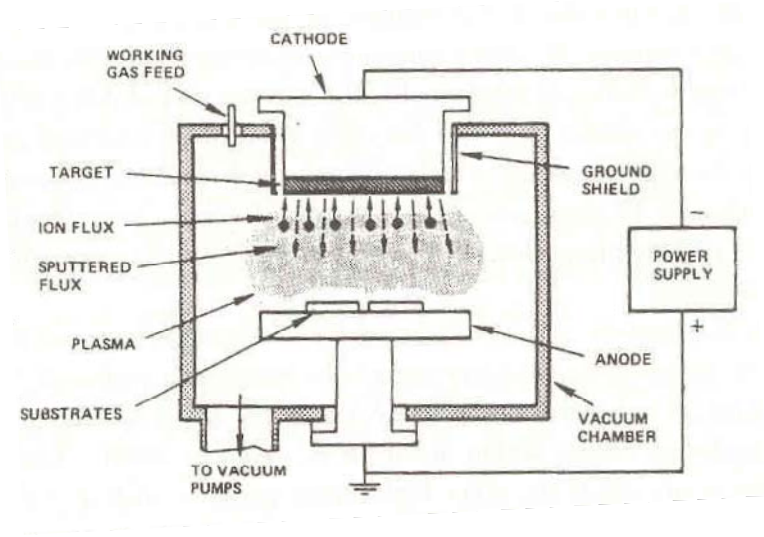

Fig. I-6: Sketch of a planar diode sputtering (from [I.18])

4.3.Triode sputtering

In the triode sputtering, three electrodes are used. In addition to the anode an the target cathode, a filament (as an electron source) is used. The electrons from the filament are accelerated to the anode ionizing the Ar gas. Thus, the objective of the hot filament is to increase the number of Ar^+ ions reaching the cathode and to maintain the value of the polarization. The final result is an increment of the deposition speed with respect to the planar diode system.

The low working pressure in this method provides some advantages:

- Higher deposition rate.
- Better purity and density of the film due to the minor gas amount.
- The direct and constant deposition from target to substrate allows the use of masks.
- The independent control of the plasma density allows the accurate control of the film deposition

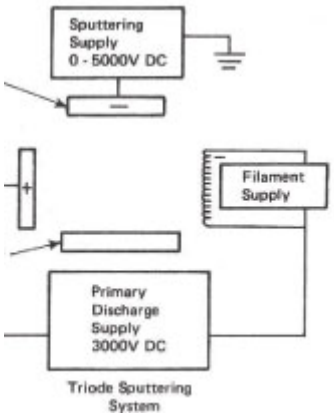

Fig. I-7: Sketch of a triode sputtering

On the other hand, the use of a hot filament present some disadvantages such as:

- Cannot be performed a reactive sputtering, a technique commonly used for nitride deposition.
- The filament itself contributes to the contamination of the film that can be even damaged.

4.4.RF-Sputtering

With the radiofrequency sputtering (RF-sputtering) it is possible to deposit dielectric materials with high resistivity. With the previous methods this is impossible because the charge of the insulator target (negative with respect to the applied voltage) cannot be effectively evacuated.

Using the radiofrequency the plasma can be created without employing the thermo-ionic emission. An efficient plasma needs a RF greater than 10 MHz.

The main advantages of the RF-sputtering with respect to the diode and triode sputtering are:

- Using pressures around $2 \cdot 10^{-4}$ mbar, the reproducibility is increased and the amount of impurities is reduced
- Since no filament is used, the impurities are even more reduced
- Using reactive sputtering (in which the gas of the chamber is such that the material of the target chemically reacts with it), oxides, nitrides, sulphurs, etc, might be deposited

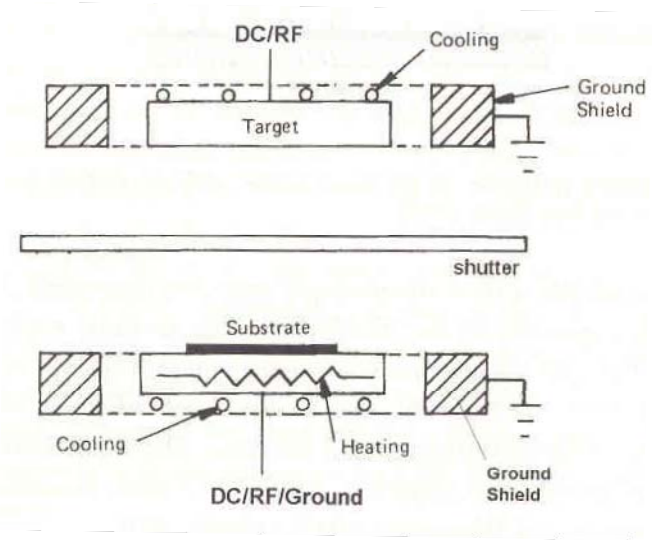

Fig. I-8: Sketch of a RF-sputtering (from [I.19])

4.5.Cathode magnetron

In order to increase the probability of ionizing the gas, cathodes containing permanent magnet (or electromagnets) are developed. These cathodes permit the confinement of the electrons in a restricted area, increasing that way the probability of a collision of the electrons with the gas.
The inconvenient of this method is that the magnetic confinement yields a preferential erosion area in the target, that diminishes its lifetime.

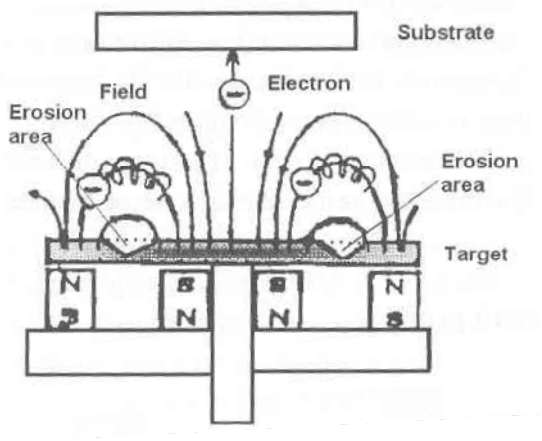

Fig. I-9: Sketch of a magnetron sputtering (from [I.20])

5.Magnetic measurement techniques I: VSM

If a sample of any material is placed in a uniform magnetic field, created between the poles of a electromagnet, a dipole moment will be induced. If that sample vibrates with sinusoidal motion a sinusoidal electrical signal can be induced in suitable placed pick-up coils. This signal has the same frequency of vibration than the vibration motion and its amplitude will be proportional to the magnetic moment, amplitude, and relative position with respect to the pick-up coils system. The Vibrating Sample Magnetometer (VSM) is a tool that takes advantage of this fact to magnetically characterize a sample.

The principle of this setup rests on a flux method which consists in measuring flux induces (Φ) in a coil by periodic displacement of the sample. More precisely, one makes vertically vibrate (Z axis) at a frequency (*f*) a sample placed at the center of a coil of measurement with a constant amplitude.

The induced voltage in the detection coils by a magnetic sample of moment (μ) is obtained starting from the theorem of reciprocity:

$$\Phi = (B/I)\mu \qquad \text{(I-5)}$$

where B is the magnetic field which would be produced by a fictitious current I circulating in the detection coils.

The induced voltage is given by the relation:

$$E = -\,d\Phi/dt = -\,\mu\,\frac{d\left(B/I\right)}{dz}\frac{dz}{dt} \qquad \text{(I-6)}$$

One of the interests of this method of measurement is its speed because the parasitic drifts are pseudo-continuous signals easily eliminated by synchronous detection.

In the VSM, the sample is fixed to a small sample holder located at the end of a sample rod mounted in a electromechanical transducer. The transducer is driven by a power amplifier which itself is driven by an oscillator at a frequency of 75Hz. Thus, the sample vibrates along the Z axis perpendicular to the magnetizing field. The latter induced a signal in the pick-up coil system that is fed to a differential amplifier. The output of the differential amplifier is subsequently fed into a tuned amplifier and an internal lock-in amplifier that receives a reference signal supplied by the oscillator. The output of this lock-in amplifier, or the output of the magnetometer itself, is a DC signal proportional to the magnetic moment of the sample being studied. The electromechanical transducer can move along X, Y and Z directions in order to find the saddle point (which Calibration of the vibrating sample magnetometer is done by measuring the signal of a pure Ni standard of known the saturation magnetic moment placed in the saddle point.

Fig. I-10 shows and sketch of a VSM (left) and a photo (right) the commercial VSM10, used for some measurements in this thesis.

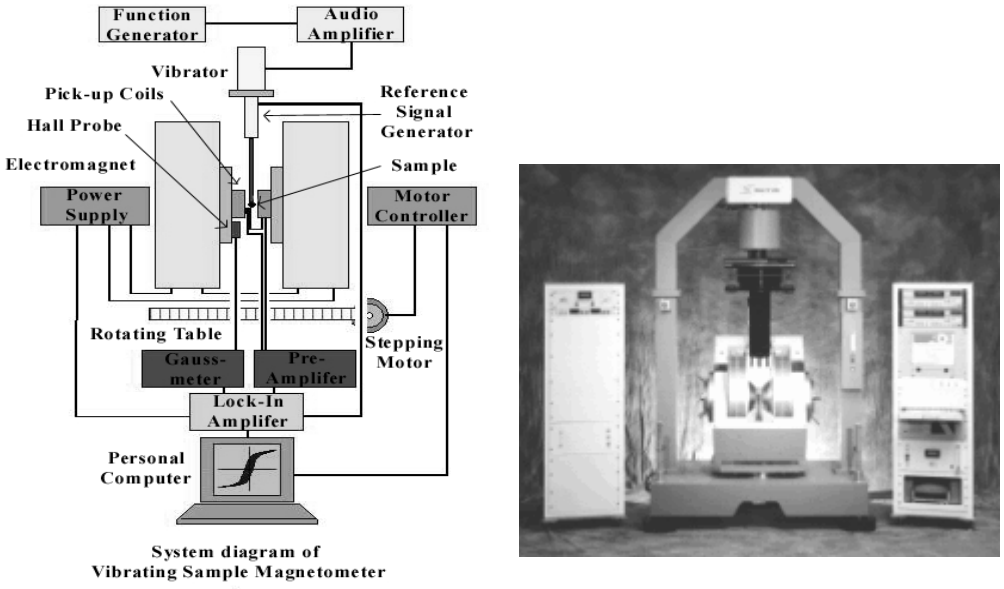

Fig. I-10: Sketch (a) and photo (b) of a commercial VSM (ADE VSM10). Images from ADE webpage (http://www.ade.com).

Using a vibrating sample magnetometer the DC magnetic moment can be measured as a function of temperature, magnetic field, angle and time. Therefore, it allows to perform susceptibility and magnetization studies.

6.Magnetic measurement techniques II: MFM

The Magnetic Force Microscopy (MFM) belongs to the Scanning Probe Microscopy (SPM) technique in which a fine tip is brought into atomically close contact with a sample surface without actually touching the surface. This is done by sensing the force (attractive or repulsive) between the probe tip and the surface. The forces are extremely small. The tip is then moved back and forth over the sample surface and can measure the topography with almost atomic resolution. MFM technique requires no sample preparation, and it can operate in the atmosphere [I.25, I.26].

The MFM is a variation of the Atomic Force Microscope (AFM), an instrument capable of imaging the surface of insulating samples with very high resolution,

presented in 1986 by Binnig, Quate and Gerber [I.25]. The difference between AFM and MFM resides in the magnetic coating of the probe tip in the latter.

In the MFM, the interaction between the stray field of the sample and that of the tip makes the tip either attracted or repelled by the sample (see fig. I-11). The resulting force on the tip can be detected by measuring the displacement of the end of the cantilever, usually by optical means focusing a laser beam at the end of the probe. Thus the domain structure can be determined.

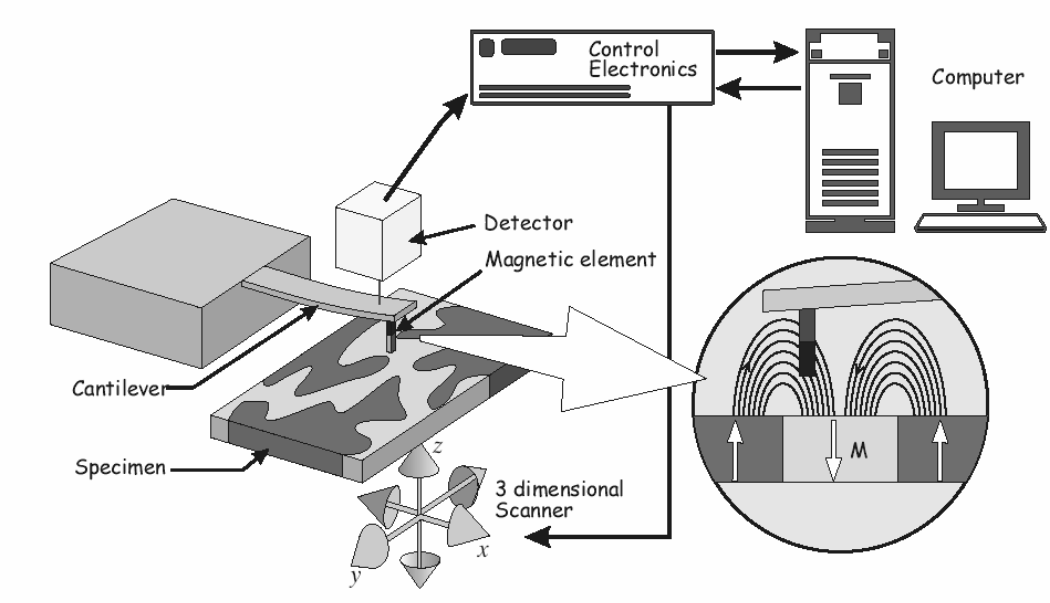

Fig. I-11: Sketch of an MFM (from [I.27])

In very rough surfaces the MFM image might be influenced by the topography, so care must be take in order to obtain a purely magnetic contrast image.

The cantilever is usually around 200µm in length, equipped with a 4µm long, 50nm diameter tip. The distance between the tip and the sample surface is around 30nm. The forces measured in typical MFM applications are in the order of 30pN, with typical cantilever deflections on the order of nanometers.

An image of the magnetic stray field of the sample is obtained by slowly scanning the cantilever over the sample surface, controlling the movement of the probe

with piezoelectrics. Typical scan areas are from 1 up to 200µm with imaging times in the order of 5 to 30 minutes.

Compared to other techniques that can be used to image magnetic stray fields with very high resolution, such as Lorentz microscopy [I.28] or spin-polarized STM [I.29], MFM has the advantage that it is a non–destructive technique that does not require exhaustive sample preparation or extremely clean surfaces.

References:

[I.1] F. Dumestre, B. Chaudret, C. Amiens, P. Renaud, P. Fejes, Science, **303**, 821 (2004)

[I.2] S. Sun, C.B. Murray, D. Weller, L. Folk, A. Moser, Science, **287**, 1989 (2000)

[I.3] O. Fruchart, M. Klaua, J. Barthel, J. Kirschner, Phys. Rev. Lett., **83**, 2769 (1999)

[I.4] Q. Xie, A. Madhukar, P. Chen, N.P. Kobayashi, Phys. Rev. Lett., **75**, 2542 (1995)

[I.5] J. I. Martin, J. Nogués, K. Liu, J.L. Vincent, I.K. Schuller. J. Magn. Magn. Mat., **256**, 449 (2003) and references therein

[I.6] J.L. Vossen, W. Kern (Eds.), *Thin film processes*, Academic Press, New York (1978)

[I.7] R. Murillo, Ph.D. thesis, chapter 3, Universiteit Twente, Enschede (2006)

[I.8] R.Murillo, H.A. van Wolferen, L. Abelmann, J.C. Lodder, Microelectronic Engineering, **78-79**, 260 (2005)

[I.9] M. Farhoud, J. Ferrera, A.J. Lochtefeld, T.E. Murphy, M.L. Schattenburg, J. Carter, C.A. Ross, H.I. Smith, J. Vac. Sci. Technol. B, **17**, 3182 (1999)

[I.10] M.A.M. Haast, Ph.D. thesis, chapter 3, Universiteit Twente, Enschede (1999)

[I.11] A. Maeda, M. Kume, T. Ogura, K. Kuroki, T. Yamada, M. Nishikawa, Y. Harada, J. Appl. Phys, **76**, 6667 (1994)

[I.12] R. O'Barr, S.Y. Yamamoto, S. Schultz, W. Xu, and A. Scherer, J. Appl. Phys. **81**, 4730 (1997).

[I.13] J.P. Spallas, R.D. Boyd, J.A. Britten, A. Fernandez, A.M. Hawryluk, M.D. Perry, D.R. Kania, J. Vac. Sci. Technol. B, **14**, 2005 (1996)

[I.14] T.A. Savas, M. Farhoud. H. I. Smith, M. Hwang, C.A. Ross, J. Appl. Phys., **85**, 6160 (1999)

[I.15] C.A. Ross, H. I. Smith, T.A. Savas, M. Hwang, R. Chantrell, IEEE Trans. Magn., **35**, 3781 (1999)

[I.16] C. Ross, H.I. Smith, Data Storage, **5**, 41 (1998)

[I.17] D. Streblechenko, M.R. Scheinfein, J. Vac. Sci. Technol. A, **16**, 1374 (1998)

[I.18] J.A, Thornton, *Semiconductor materials and process technology handbook*, G.E. McGuire, Noyes Pub. (1988)

[I.19] B. Chapman, *Glow discharge processes*, John Wiley & sons, Inc. (1980)

[I.20] M. Naoe, N. Matsushita, S. Nakagawa, J. Magn. Magn. Mat., **134**, 395 (1994)

[I.21] H. R. Kaufman, J. J. Cuomo, J. M. E. Harper, J. Vac. Sci. Techn. **21**, 725 (1982)

[I.22] Q. Meng, Ph. D. Thesis, chapter 2, Universiteit Twente Enschede (1996)

[I.23] P. de Haan, Q. Meng, T. Katayama, J.C. Lodder, J. Magn. Magn. Mat. **113**, 29 (1992)

[I.24] Q. Meng, W.P. van Drent, J.C. Lodder, U. Enz, Th.J.A. Popma, 14th ICMFS proceedings, Düsseldorf (Germany), digest p225 (1994)

[I.25] G. Binnig, C.F. Quateand, Ch. Gerber, Phys. Rev. Lett., **56**, 930 (1986).

[I.26] U. Hartman, T. Göddenhenrich, C. Heiden, J. Magn. Magn. Mat., **101**, 163 (1991)

[I.27] A.G. van den Bos, Ph.D. thesis, chapter 1, Universiteit Twente, Enschede (2003)

[I.28] J.C. Suits, R.H. Geiss, C.J. Lin, D. Rugar, A.E. Bell, Appl. Phys. Lett. **49**, 419 (1986)

[I.29] R. Wiesendanger, D. Bürgler, G. Tarrach, A. Wadas, D. Brodbeck, H.J. Güntherodt, G. Güntherodt, R.J.Gambino, R. Ruf, J. Vac. Sci. Technol. **B9**, 519 (1991)

[I.30] R. García and R. Pérez, Surf. Science Reports. **47**, 197 (2002)

CHAPTER II:

MAGNETO-OPTIC KERR EFFECT AND RELATED TECHNIQUES

Index

MAGNETO OPTIC KERR EFFECT AND RELATED TECHNIQUES

1.Introduction:

In 1845 Michael Faraday notice that when the electromagnetic radiation passes through a magnetized material its polarization characteristics and/or intensity are modified. Some years later, in 1876 John Kerr [II.1] observed that the direction of vibration of plane polarized light was altered when the polarized ray was reflected from a ferromagnetic mirror placed in a magnetic field. These modifications are known as magneto-optic (MO) phenomena. In particular they are known by the name of their discoverers: the MO Faraday and Kerr effects. Both are related to the rotation of the plane of polarization of an incident plane polarized beam when it reflects (Kerr effect) or passes through (Faraday effect) a magnetized sample.
From now on only the Kerr effect in magnetic thin films (patterned or not) will be taken into account since the thin film thicknesses corresponding to the magnetic patterns used in the following chapters are either grown over an opaque substrate or has enough thickness to be opaque to the light source.

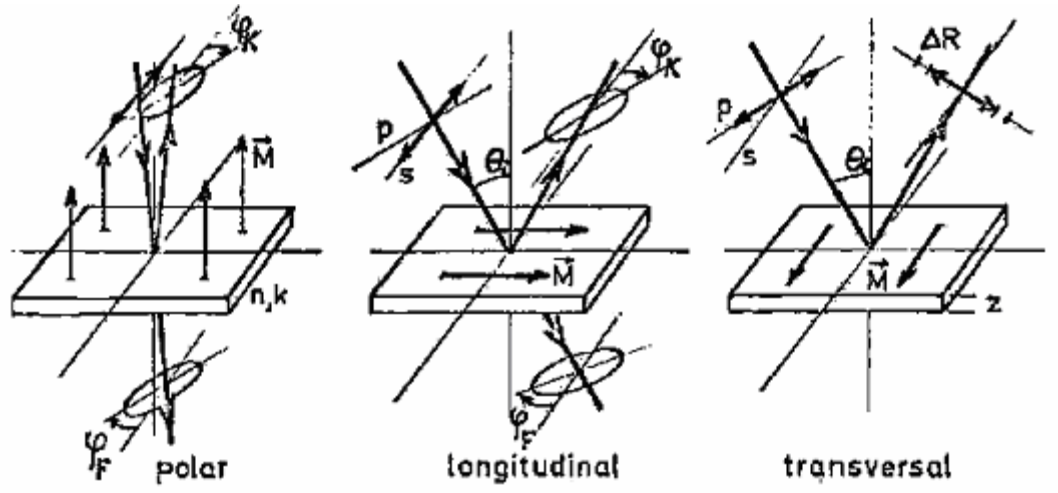

Fig. II-1: The three different types of MOKE (from [II.2]). Subscript K accounts for Kerr effect whereas subscript F account for Faraday effect.

The magneto-optic Kerr effect (MOKE) can be classified in three different configurations (fig. II-1) depending on the relative orientation of the magnetization of the sample **M** with respect to the sample surface (characterized by its normal vector **n**) and the plane incidence (characterized by the incident radiation **k**). In the transversal Kerr effect geometry, the magnetization is within the sample plane and perpendicular to the plane of incidence (mathematically, $\mathbf{M}\times(\mathbf{k}\times\mathbf{n})=0$). In the longitudinal Kerr effect configuration, the magnetization is also within the sample plane but parallel to the plane of incidence, i.e., $\mathbf{M}\cdot(\mathbf{k}\times\mathbf{n})=0$ and $\mathbf{M}\cdot\mathbf{n}=0$. The polar Kerr effect is characterized by a magnetization perpendicular to the sample but parallel to the plane of incidence, i.e., $\mathbf{M}\cdot(\mathbf{k}\times\mathbf{n})=0$ and $\mathbf{M}\times\mathbf{n}=0$.

One of the main features of the Kerr techniques is its high sensitivity. It has been reported in the literature MOKE measurements from magnetic samples a few monolayers thick [II.3, II.4] .

2.MOKE formalism:

An electromagnetic beam reflected in a magnetized surface yields two reflected beams. One of them is the standard reflection (DC intensity), purely optical, described by the Fresnel formulae and coefficients. The other one is a small component perpendicularly polarized to the standard reflection beam (Kerr intensity). This second component is the magneto-optic contribution which yields the change in rotation and ellipticity.

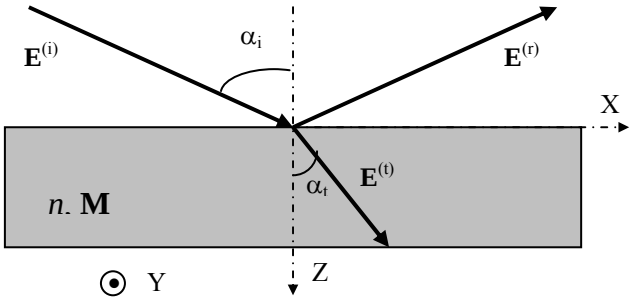

Fig. II-2: Coordinate system and variables involved in the description of the Kerr effect

The phenomenological theory of MOKE is just a direct utilization of Maxwell equations to a gyroelectric media characterized by a dielectric tensor like (II-1).

Thus, the MOKE formalism can be explained assuming a situation like the one depicted in Fig. II-2, where a linearly polarized beam incident at an angle α_i is reflected by a magnetic surface with refractive index *n* and magnetization **M** at an angle $\alpha_r=-\alpha_i$.

Under the latter assumptions, in the dielectric law, $\mathbf{D}=\varepsilon\mathbf{E}$, the permittivity (complex) tensor might be expressed in the form [II.5, II.6, II.7, II.8]:

$$\varepsilon = \varepsilon_{xx}\begin{pmatrix} 1 & -iQm_z & iQm_y \\ iQm_z & 1 & -iQm_x \\ -iQm_y & iQm_x & 1 \end{pmatrix} \tag{II-1}$$

where m_i are the direction cosines of the magnetization **M** ($m_j=\frac{M_j}{M_S}$) and $Q=i\frac{\varepsilon_{xy}}{\varepsilon_{xx}}$ is the magneto-optical constant. Note that the modulus of the complex magneto-optical constant Q is the gyroelectric constant ($|Q|<<1$). Moreover, the dependence of the diagonal elements of the dielectric tensor ε is second order, so it can be neglected [II.8] yielding (II-1).

If placing the magnetized material in the vicinity of an external applied field **H**, the permittivity tensor might be split into its real and imaginary part. Thus, ε might be also expressed as (see [II.9])

$$\varepsilon = \begin{pmatrix} \varepsilon'_{xx} & \varepsilon'_{xy}+ig_z & \varepsilon'_{xz}-ig_y \\ \varepsilon'_{xy}-ig_z & \varepsilon'_{yy} & \varepsilon'_{yz}+ig_x \\ \varepsilon'_{xz}+ig_y & \varepsilon'_{yx}-ig_x & \varepsilon'_{zz} \end{pmatrix} \tag{II-2}$$

Here $\mathbf{g}=(g_x, g_y, g_z)$, called the gyration vector, accounts for the magneto-optical component and whose values are generally small compared to the eigenvalues of the real tensor ε'.
Accordingly, the dielectric law might be written as follows:

$$\mathbf{D}=\varepsilon_0(\varepsilon'\mathbf{E}+i\mathbf{E}\times\mathbf{g}) \tag{II-3}$$

The direction of **g** is called axis of gyration of the material. To first order **g** is proportional to the external magnetic field. Thus, assuming for simplicity

$\varepsilon'_{xx}=\varepsilon'_{yy}=\varepsilon'_{zz}$, **g** might be expressed as $\mathbf{g}=\varepsilon_0\chi^{(m)}\mathbf{H}$, where the tensor $\chi^{(m)}$ is the magneto-optical susceptibility (scalar in isotropic media).

Using the dielectric tensor in eq. (II-1), Maxwell equations have to be solved, which leads to a reflection matrix (expressed in *s* and *p* components):

$$R=\begin{pmatrix} r_{pp} & r_{ps} \\ r_{sp} & r_{ss} \end{pmatrix} \qquad \text{(II-4)}$$

The reflection matrix in (II-3) relates the *p*- and *s*-polarized components of the reflected beam with respect to the *p* and *s* components of the incident beam. The coefficients of the reflection matrix are known as the Fresnel coefficients of reflectivity and r_{ij} is the ratio of the incident *j*-polarized electric field and the reflected *I*-polarized electric field.

References [II.5], [II.6] and [II.10] provide some expressions for the Fresnel coefficients.

The Kerr signal is given by the quotient of the Fresnel coefficients. Then, the complex Kerr angles are defined as follows:

$$\Theta_p = \frac{r_{sp}}{r_{pp}} = \theta_p + i\varepsilon_p$$

$$\Theta_s = \frac{r_{ps}}{r_{ss}} = \theta_s + i\varepsilon_s \qquad \text{(II-5)}$$

where θ_i and ε_i are respectively the Kerr rotation and ellipticity. Here the subscripts denote the polarization of the incoming light.

The incident angle α_i will determine the ratio between the Kerr signal and the DC intensity. Choosing the optimum incident angle is crucial to obtain a good signal-to-noise ratio (SNR). In fig. II-3 (from [II.11]) the rotation θ, ellipticity ε and modulus of the Kerr angle |Θ| for both polarizations (continuous line for *p*-polarization and dashed line for *s*-polarization) are analyzed as a function of the incident angle in polar and longitudinal configurations. Another similar plot for the polar geometry can be found in [II.12]. Fig. II-3 (last row) shows the dependence of the MO intensity as a function of the incidence angle in the transverse geometry. As shown in Fig. II-3, the optimum angle for the polar

configuration is 0 degrees while for both longitudinal and transverse Kerr effect, the optimum incidence angle is around 75 degrees.

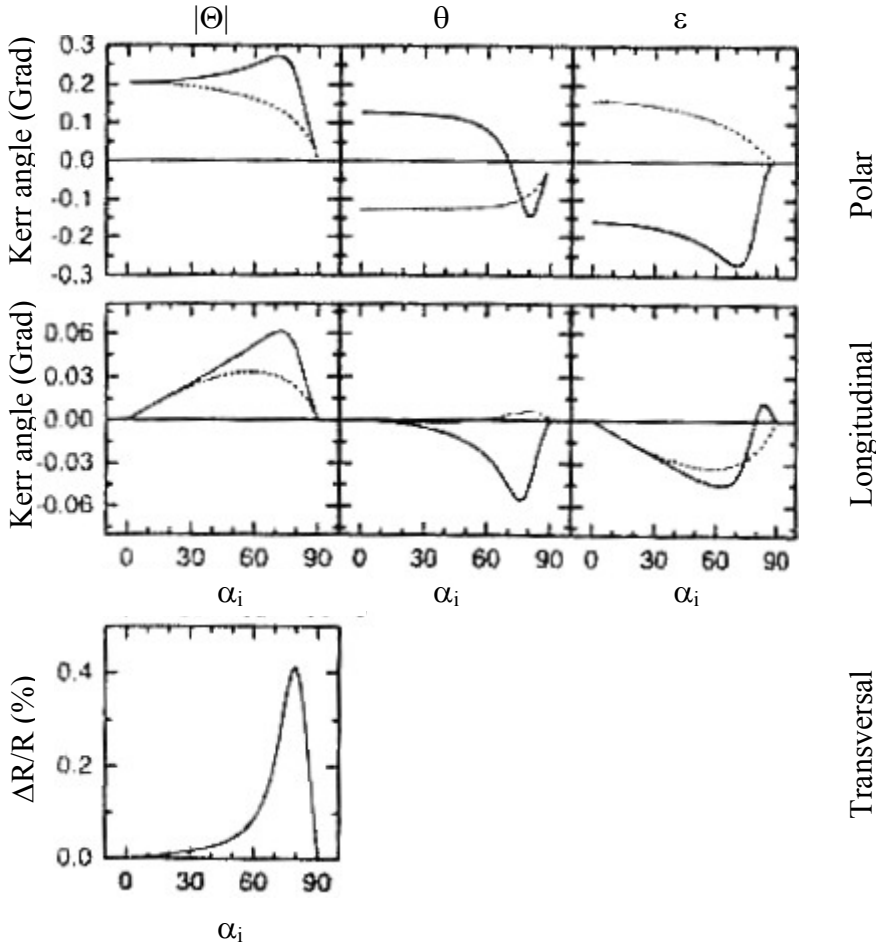

Fig. II-3: (From [II.11]) First two rows: Calculated modulus of the complex Kerr angle Θ (left), Kerr rotation θ (center) and ellipticity ε (right) as a function of incidence angle α_i (measured from the surface normal) at 670 nm wavelength for polar and longitudinal Kerr effects. Continuous line accounts for *p*-polarized light and dashed line for *s*-polarized light. Last row: Kerr intensity as a function of the incidence angle α_i (measured from the surface normal) at 670 nm wavelength for transverse Kerr effect.

It is important to note that the transverse case is slightly different from the rest of the configurations since it yields MO effects only in reflection (i.e. there is no transversal Faraday effect) and in *p*-polarization. Moreover, due to its geometry, the MO component of the reflected light is *p*-polarized. Therefore, the transverse MOKE causes an amplitude variation of the intensity of the light. This can be seen from fig. II-1 and eq. (II-3). Given that the magnetization is perpendicular to the plane of incidence, the cross product $\mathbf{E}\times\mathbf{g}$ (where $\mathbf{g}$ is directly proportional to the magnetization) is either zero (*s*-polarization) or points along the propagation direction (*p*-polarization). Since *p*-polarized light has a different direction in the reflected beam, transverse MOKE will be noticeable as a light amplitude modulation.

3.Polar Kerr setup:

The set-up for measuring polar Kerr optical rotation and ellipticity is depicted in figure II-4. It consists of a white light source whose light passes through a polarizer P_1 at a fixed angle $\pi/4$ rad,. This polarizer is followed by two birefringent elements, a elasto-optic modulator M and a Babinet-Soleil type compensator C. The modulator has temporally periodic birefringent phase shift, $\varphi=\varphi_0\sin(\omega_M t)$, with frequency $\omega_M=2\pi\cdot 50\text{kHz}$ and amplitude $\varphi_0=2.41$. This value is a compromise for detecting the Fourier components I_1 and I_2 of the light intensity at ω_M and $2\omega_M$ by use of the lock-in amplifiers A_1 and A_2 (fig. II-4) simultaneously at near optimum SNRs [II.13, II.14, II.15]. The compensator exhibits an arbitrary adjustable birefringent phase shift γ. Furthermore, the neutral lines of these two birefingent elements are parallel to the *s* and *p* directions defined by the plane of incidence and the sample surface.

After passing through the compensator, the light is focused with a quartz lens L_1 onto the sample S (optically represented by its reflection matrix R) at an incidence angle α_i. The reflected beam is then focused again by a second quartz lens L_2. Strain-free lenses have to be selected in order to avoid interference of their birefringence with the MO effects of the sample. The resulting beam passes through a polarizer P_2 at an adjustable angle β. The final beam is received in a detector D simultaneously connected to three lock-in amplifiers A_0, A_1 and A_2. As previously said, the latter two detect, respectively, the first and second Fourier components of the incoming intensity whereas the first one detects the DC component of the intensity, which is independent of both β and γ. The DC intensity I_0 is used to normalize the Fourier components I_1 and I_2.

Using a mathematical subterfuge, detailed in reference [II.22] and also in appendix II.A for the sake of completeness, the quotients I_1/I_0 and I_2/I_0 provide the polar Kerr ellipticity and rotation respectively.

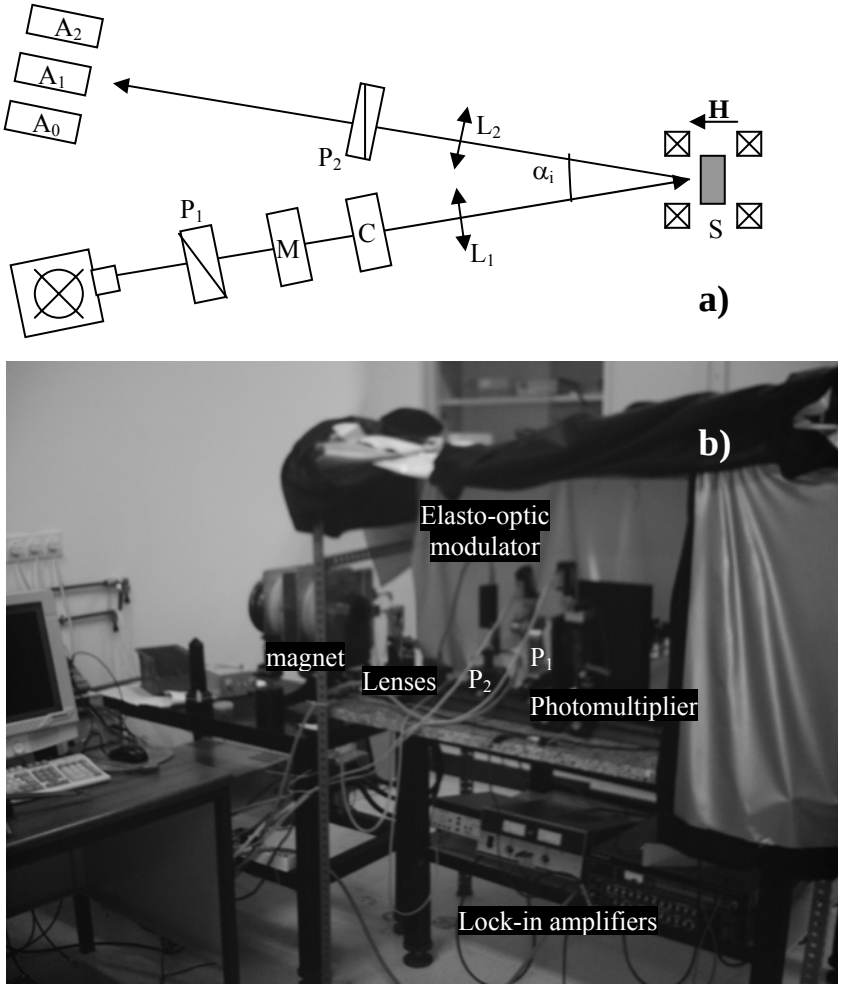

Fig. II-4: Polar Kerr sketch (a) and IMM setup (b). The incident beam, at an angle α_i crosses a polarizer P_1 (angle $\pi/4$), then a elasto-optic modulator M and a Babinet-Soleil compensator C. The resulting beam is focused by a lens L_1. The reflected beam is focused by a lens L_2 and then crosses a polarizer P_2 before being analyzed by a detector which consists of three lock-in amplifiers (A_0, A_1, A_2) that detect the DC component of the light (A_0) and its first (A_1) and second (A_2) Fourier components.

4.Kerr microscope:

The Kerr microscope is a tool that makes use of the MOKE technique to provide real-time images of the magnetic domains in a sample. The contrast in the images is due to the Kerr-rotation of polarized light reflected at the sample surface. In the visible range of light, the Kerr angle is rather small, of the order of $\theta \sim 0.1^{\circ}$, so is usual to make use of digital image processing and contrast enhancement.
A major virtue of the Kerr microscope is the fact that it can be easily operated in relatively high magnetic fields and is thus very well suited to study field-induced dynamical processes. In addition, it is possible to obtain an image of the domain pattern of large samples.
The lateral resolution that can be achieved is limited by optical diffraction effects and may reach values of about 300 nm (few microns in the IMM homemade longitudinal Kerr microscope) in the optimum case (in the polar geometry. See [II.16, II.17]).

The Kerr microscope might be configured according to the three geometries of the Kerr effect, i.e., polar, longitudinal and transversal. The polar configuration is the one capable of provide contrast between out-of-plane domains. On the other hand, both transversal and longitudinal MOKE configurations provide images of in-plane domains.

Since transverse MOKE consists of a small amplitude modulation of the light intensity (a reflectivity ratio around 0.5% between the DC component of the light and the Kerr signal for Co) only in the *p*-polarized component, it yields very little contrast. Therefore, the longitudinal configuration is most suited in order to enhance the image contrast in the case of in-plane domains.

A complete mathematical description of the contrast optimization in Kerr microscopies can be found in [II.18].

The IMM setup, sketched in fig. II-5, is rather simple. It consists of a white light source (typically a Xe lamp), followed by a lens, a diaphragm and a polarizer. The sample is situated between the Helmholz coils. The reflected light is polarized, focused by a lens and finally recorded in a video camera.
The contrast between the different domains is achieved placing the angle of the polarizers in a close-to-extinction position.
Obviously, a good alignment of the system is mandatory in order to optimize the contrast.

The undesirable diffraction noise that might appear in the system can be reduced eliminating the non-focused lateral light by placing a diaphragm just between the lens L_1 and the polarizer P_1.

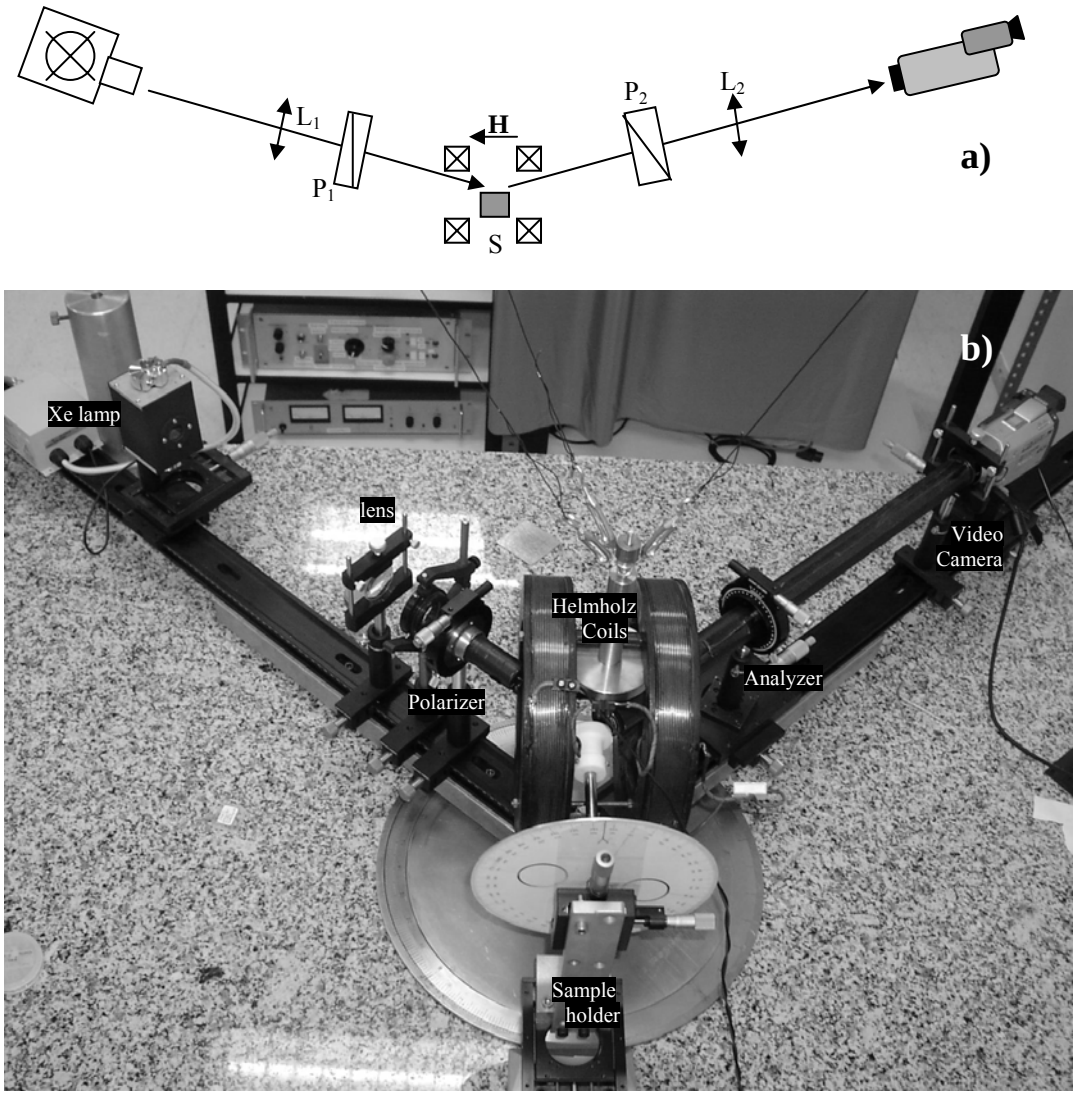

Fig. II-5: Kerr microscope sketch (a) and IMM setup (b) in longitudinal geometry. The light from the Xe lamp, focused by a lens L_1, is then polarized by P_1. After being reflected by the sample S is again polarized by P_2. Finally the images are recorded by a digital video camera connected to a computer. The contrast in the Kerr microscope is achieved by setting relative polarizations close to optical extinction.

5.Transversal Kerr setup:

As previously seen, the transversal Kerr effect is rather special since the effect that yields consists of a modulation of the intensity amplitude of the light. The transversal MOKE setup uses this property to obtain hysteresis loops of magnetic samples with in-plane magnetization. This is a very flexible technique capable of measuring hysteresis loops from either small areas (a few microns) or larger areas (several millimeters) by properly adjusting the focus of the lenses.

The setup consists of a light source, in this case a He-Ne laser (λ=630 nm, 1.5 mW) that emits linearly polarized light. The emitted light is focused by a lens and then hit the sample, that is placed into the Helmholtz coils. The reflected light is polarized and the intensity of the resulting beam is measured by a photodiode. Depending on the width of the reflected beam, a second lens might be used to focus the reflected light into the photodiode. According to what was previously explained, both polarizers should be in *p* position in order to maximize the ratio between the Kerr signal and the DC-signal.

In the IMM setup an adjustable attenuator is also used to fine-tune the intensity of the reflected beam within the optimal range of the photodiode.

The Helmholtz coils provide the external uniaxial field perpendicular to the plane of incidence. The coil is fed with a sinusoidal current and provides 70 Oe per ampere circulating through the windings. This sinusoidal current is controlled by a wave generator set at 5 Hz. This frequency is in the range of low speed magnetization dynamics but provides a good quantity of loops per second. This is very important since the simple setup itself is quite noisy due to laser light instability, ambient light and mechanical vibrations of the setup. Thus, provided an oscilloscope capable of averaging the signal received by the photodiode, low-noise hysteresis loops might be easily obtained with no bandwidth loss.

As mentioned above, the light intensity measured in the photodiode consists of two contributions. One of them is the reflected intensity (or DC-intensity) and the other one is the Kerr contribution. The latter represent a few fraction of the whole intensity so previously to the intensity enhancement in the oscilloscope, the DC-component must be removed using a compensator.

The hysteresis loop if finally obtained setting the intensity supplied to the coils as the X axis (which is proportional to the external applied field) and the Kerr

component of the reflected intensity as the Y axis (which is proportional to the magnetization in the sample).

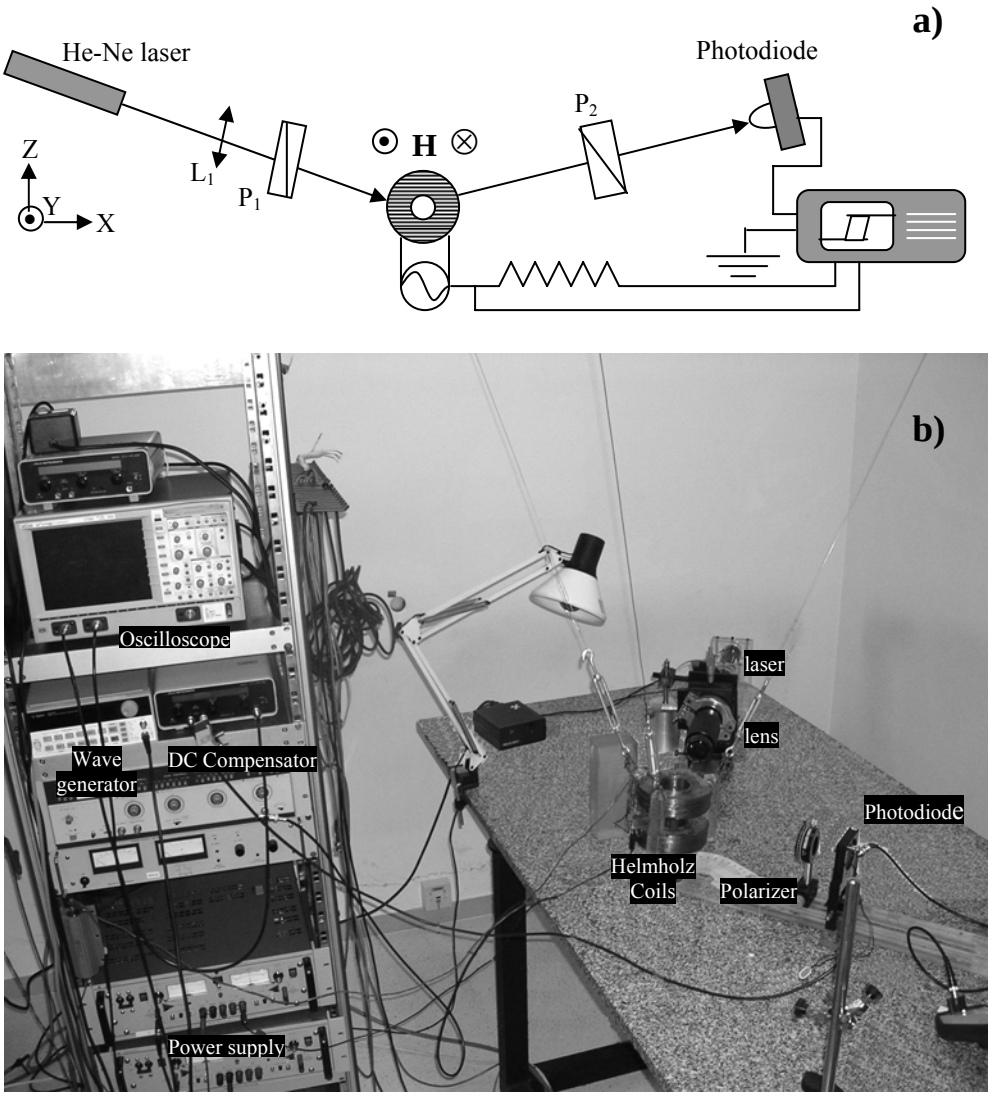

Fig. II-6: Transversal Kerr sketch (a) and IMM setup (b). The light from the He-Ne laser, focused by a lens L_1, is then *p*-polarized by P_1. After being reflected by the sample S, the beam is then *p*-polarized by P_2. The resulting signal is then collected in a photodiode and sent to an oscilloscope (Y axis) together with the current supplied to the coils (X axis). This signal many time averaged yields a noise-reduced hysteresis loop.

6.Summary:

An extended overview of the Kerr effect discovered by Michael Faraday and John Kerr in the XIX century has been presented. Firstly, the basics of Magneto-Optical Kerr Effect (MOKE) are mathematically shown from the phenomenological point of view. In addition, related magneto-optical (MO) techniques for magnetic measurement and imaging used in this thesis are briefly presented. The main advantage of these techniques lay in their sensitivity, being capable of measuring samples a few monolayers thick.

The different apparatus sketched and described take advantage of the different MOKE geometries to measure either the in-plane (transversal Kerr setup) or the out-of-plane magnetization (polar Kerr setup). The transversal Kerr setup measures small light intensity variations with reflectivity ratios of a few tenths percent. On the other hand, the polar Kerr setup analyzes Kerr rotations variations of a few hundredths of degree.

A Kerr microscope in the longitudinal configuration has been also described. This apparatus is capable of spatially resolve the magnetization in a sample, providing real time images of its magnetization state at selected external field values.

The above mentioned setups are the basic tools used henceforward in this thesis to characterize the different magnetic patterns fabricated.

7.References:

[II.1] J. Kerr, Phil. Magn. **5**, 161 (1878)

[II.2] F. Briones, Ph.D. Thesis, chapter 1, Universidad Complutense de Madrid. (1972)

[II.3] C. Liu, M.R. Moog, S.D. Bader, Phys. Rev. Lett. **60**, 2422 (1988)

[II.4] J.A.C. Bland, M.J. Padgett, K.D. Mackay, D.A. Johnson, J. Phys. Cond. Mat. **1**, 4407 (1989)

[II.5] C.Y. You, S.C. Shin. J.Appl.Phys., **84**, 541 (1998)

[II.6] R.P. Hunt, J. Appl. Phys. **38**, 1652 (1967)

[II.7] L.D. Landau, E.M. Lifshitz, *Electrodynamics of continuous media*, 82, Pergamon Press (1960)

[II.8] A.V. Sokolov, *Optical properties of metals*, Blackie & Son Ltd. (1967)

[II.9] F. Jonsson, C. Flytzanis. Phys. Rev. Lett. **82**, 1426 (1999)

[II.10] H.F. Ding, S. Pütter, H. P. Oepen, J. Kirschner, J. Mang. Magn. Mat. **212**, L5 (2000)

[II.11] F.U. Hillebrecht. Chapter B4. 36th IFF Spring School: Magnetism goes nano (2005)

[II.12] A. J. Collins, M. Husni, R. M. Jones. J. Phys. E: Sci. Instrum. **11**, 547 (1978)

[II.13] S.N. Jasperson, S.E Schnatterly, Rev. Sci. Instrum. **40** 761 (1969)

[II.14] K. Sato, Japan J. Appl. Phys. **20** 2403 (1981)

[II.15] P.O.J. Nederpel, J.W.D. Martens, Rev. Sci. Instum. **56** 687 (1985)

[II.16] A. Hubert, Phys. Statu Solidi **22**, 709 (1967)

[II.17] F. Schmidt, A. Hubert, J. Magn. Magn. Mat. **61**, 307 (1986)

[II.18] A. Hubert, R. Schäfer. Magnetic Domains, chapter 2. Springer-Verlag Berlin Heidelberg (1998)

[II.19] F. Jonsson, C. Flytzanis, Opt. Lett. **24**, 1514-1516 (1999)

[II.20] R. Atkinson, P. H. Lissberger. Appl. Op.,**31**, 6076 (1992)

[II.21] L.Wenzel, A.Hubert, V.Kamberski. J.Magn.Magn.Mat., **175**, 205 (1997)

[II.22] W.S. Kim, M. Aderholz, W. Kleemann. Meas. Sci. Technol. **4** 1275 (1993)

[II.23] T. Schmitte, Ph.D. thesis, chapter 3, Rürh-Universitat Bochum (2002)

[II.24] S.-shen Yan, R. Schreiber, P. Grünberg, R. Schäfer. J. Magn. Magn. Mat., **210**, 309 (2000)

[II.25] J. Zak, E.R. Moog, C. Liu, S.D. Bader, Phys.Rev.B, **43**, 6423 (1991).

[II.26] I. Reichl, Ph.D. thesis, chapter 2, Technischen Universität Wien (2005)

CHAPTER III:

DIFFRACTIVE MAGNETO-OPTIC KERR EFFECT AND RELATED TECHNIQUES

Index

DIFFRACTIVE MAGNETO OPTIC KERR EFFECT AND RELATED TECHNIQUES

1.Introduction:

The Diffractive Magneto-Optic Kerr effect (DMOKE) is alternative MOKE measurement method for patterned samples. It basically consists on measuring magneto-optical variations in the diffraction spot created by a magnetic array. The light intensity in these diffraction spots yielded by an array of magnetic elements mainly consists of a DC contribution, that can be described with conventional diffraction theory, and a small magneto-optical modulation of that contribution (around 1% for Co arrays), the DMOKE signal.

In order to study the magneto-optical component, the DC contribution ought to be compensated and the resulting DMOKE signal is amplified. This Kerr component contains information about the magnetization in the sample, but the corresponding signal is different than that from the reflection spot [III.1 to III.16]. Indeed, as it is shown here for 1D and 2D arrays of very different element shapes, different diffraction orders yield different DMOKE signals. This experimentally corroborated fact hold not only in arrays of magnetic elements [III.1] but also on arrays of holes fabricated in a continuous thin film [III.16]. Therefore experimental measurements point out that there exists an important dependence of the DMOKE signal with the shape of the array. This dependence has been recently theoretically studied from a phenomenological point of view by different research groups ([III.2], [III.4]).

This chapter is then focused in the theoretical description of transversal and polar DMOKE from a phenomenological point of view. A brief description of the setup used for performing the measurements is also presented.

2.Transverse DMOKE formalism and setup:

As previously stated, transverse DMOKE can be measured in a conventional transversal MOKE setup (fig. II-6) just placing the photodiode in the desired diffracted spot. Considering the transversal geometry with the notation in fig. III-1, the light intensity in the different diffraction spots *n*X and *m*Y might be measured.

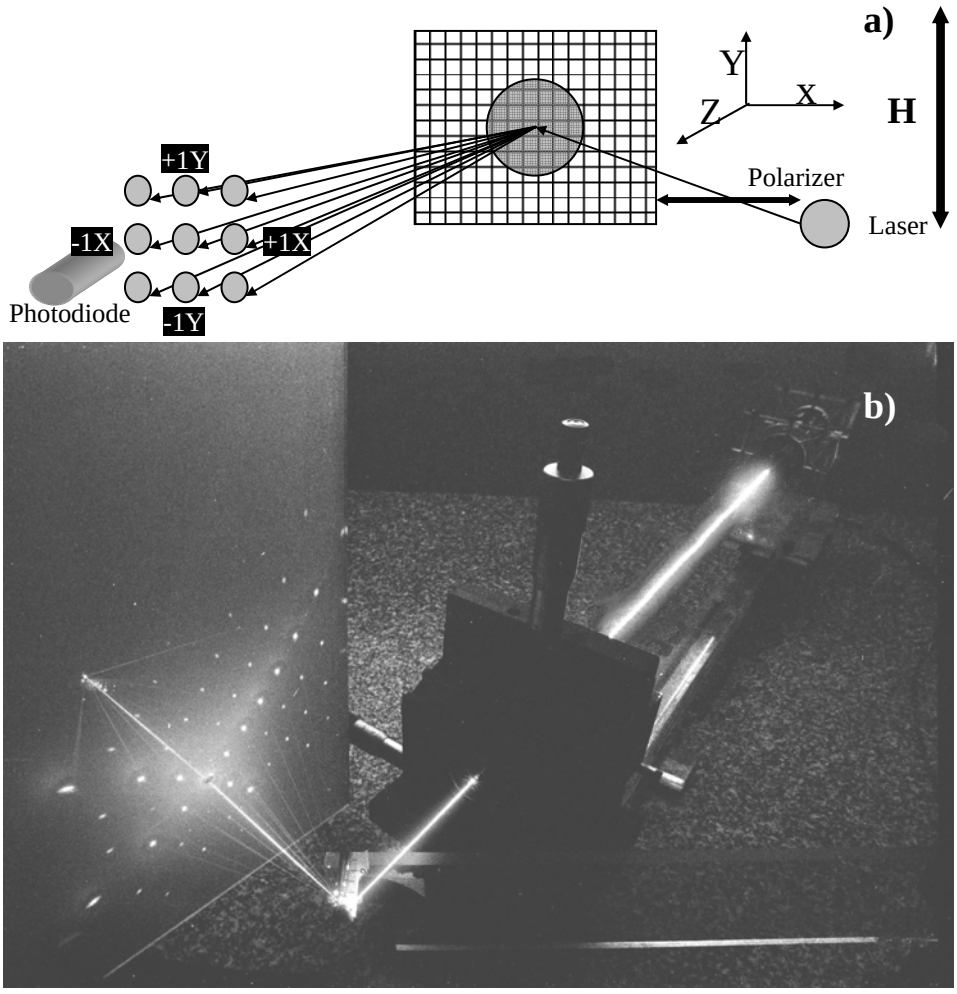

Fig. III-1: a) DMOKE sketch and notation. b) when a patterned sample is illuminated a diffraction pattern appears. The intensity of the diffraction beams is composed by a DC-component and a Kerr component, like the reflection beam. Photo by Jorge M. García.

A rigorous theoretical solution to the D-MOKE problem requires the complete diffraction theory including the magneto-optical contributions. The latter contributions require full knowledge of the magnetic configuration of the system. Such an approach yields the absolute intensities and the magnitudes of the magnetic contributions in each diffracted beam [III.2]. In the vector diffraction approach, not only the boundary conditions for all the diffracted waves must be included but also the magneto-optic contributions in the material itself.

As previously seen, the conventional MOKE is phenomenologically described in terms of the Fresnel (complex) coefficients (**r**) which describe the ratio of the electric fields in the reflected and incident beams. TM polarized (*p*) and TE polarized (*s*) polarizations of the incident and reflected light define the ratios r_{pp}. r_{ss}, r_{ps} and r_{sp}. In order to describe the formalism for DMOKE, the same approach and notation will be employed.

Considering the transverse geometry and following the notation of fig. III-1, the diffraction spots perpendicular to the plane of incidence are termed *m*Y and the ones in the plane of incidence and perpendicular to the laser propagation direction are termed *n*X, where *n* and *m* are integers representing the diffraction order.

Lets denote $E^{(i)}=\begin{pmatrix} E_p^{(i)} \\ E_s^{(i)} \end{pmatrix}$ the incident field and $E^{(r)}=\begin{pmatrix} E_p^{(r)} \\ E_s^{(r)} \end{pmatrix}$ the reflected field whose corresponding intensity is measured by the photodiode.

Assuming a transversal Kerr geometry and according to the corresponding setup (see figs. II-6 and III-1), some Jones matrices related to the optical components of the setup must be considered.

In the transverse configuration, the incoming light is linearly *p*-polarized. This fact will enormously simplify the problem. Thus, $E^{(i)}=\begin{pmatrix} E_p^{(i)} \\ E_s^{(i)} \end{pmatrix}=E_0\begin{pmatrix} 1 \\ 0 \end{pmatrix}$.
This incoming *p*-polarized light illuminate the sample S, whose Jones matrix is $S=\begin{pmatrix} \mathbf{r}_p & \mathbf{r}_{ps} \\ \mathbf{r}_{sp} & \mathbf{r}_s \end{pmatrix}$. As previously seen, these reflectivity coefficients depend on the magnetic material's complex refraction indexes, on the substrate, on the incidence and diffraction angles, and on the complex magneto-optic constants.

Before reaching the photodiode, the light is *p*-polarized again by the polarized P, with Jones matrix $P=\begin{pmatrix} 1 & 0 \\ 0 & 0 \end{pmatrix}$.

Accordingly, the reflected field whose corresponding intensity is measured by the photodiode is given by the expression:

$$E^{(r)}=P\cdot S\cdot E^{(i)} \qquad \text{(III-1)}$$

From this expression it follows:

$$E^{(r)}=\begin{pmatrix} E_p^{(r)} \\ E_s^{(r)} \end{pmatrix} = E_0\cdot \mathbf{r}_p \begin{pmatrix} 1 \\ 0 \end{pmatrix} \qquad \text{(III-2)}$$

Hence, the intensity measured by the photodiode is:

$$I^{(r)}= E_p^{(r)}\cdot E_p^{(r)*} = E_0^2\cdot|\mathbf{r}_p|^2 \qquad \text{(III-3)}$$

The intensity in the different diffraction spots is given by the Fraunhoffer diffraction theory taking into account a distribution of reflectivities of magnetic origin. Thus, the intensity in the n^{th} diffracted is [III.3]

$$I_n=E^n{}_d(E^n{}_d)^* \qquad \text{(III-4)}$$

where $E^n{}_d$ is the electric field value in the n^{th} diffraction order.
In the transversal Kerr configuration case, $E^n{}_d$ might be written in the form:

$$E^n{}_d=E_0(r_{pp}f_n+r^m{}_{pp}\, f_n{}^m) \qquad \text{(III-5)}$$

where E_0 is the incident electric field, r_{pp} and $r^m{}_{pp}$ are –respectively– the non-magnetic and magnetic reflectivity coefficients and f_n and $f_n{}^m$ are –respectively– the non-magnetic and magnetic form factors of the considered lattice.

The form factors are just modulation coefficients. The non-magnetic form factor depends only on the element shape, whereas the magnetic form factor depends also on the spatial distribution of the magnetization in the unit cell.

Assuming a square lattice of period T and denoting **G** a generic reciprocal lattice vector (**G**=n**b**$_1$+ m**b**$_2$, being **b**$_1$=2π/T **i** and **b**$_2$=2π/T **j** the reciprocal lattice base vectors), the non-magnetic form factor in the (n,m) diffracted (n^{th} diffracted in the X direction and m^{th} diffracted in the Y direction) might be expressed:

$$f_{n,m}^{(\mathrm{nm})} = \int_S e^{i\mathbf{G}\cdot\mathbf{r}} dS \qquad \text{(III-6)}$$

where the integral is performed along the unit cell surface S, with position vector represented by **r**=x **i**+y **j**.
Accordingly, (III-6) might be also expressed:

$$f_{n,m}^{(\mathrm{nm})} = \int_S e^{\frac{2\pi i}{\mathrm{T}}(n\mathrm{x}+m\mathrm{y})} d\mathrm{x}d\mathrm{y} \qquad \text{(III-7)}$$

The magnetic form factor should take into account the magnetization distribution within the elements of the array. According to the conventions in fig. III-1, the dependence of the magnetic form factor with the magnetization is:

$$f_{n,m}^{(\mathrm{m})} = \int_S m_{\mathrm{Y}} e^{i\mathbf{G}\cdot\mathbf{r}} dS = \int_S m_{\mathrm{Y}}(\mathrm{x},\mathrm{y}) e^{\frac{2\pi i}{\mathrm{T}}(n\mathrm{x}+m\mathrm{y})} d\mathrm{x}d\mathrm{y} \qquad \text{(III-8)}$$

Since a patterned magnetic sample over a non-magnetic substrate is considered, m_{Y}(x,y) is different from zero only in the (x,y) coordinates corresponding to a magnetic element. Assuming a square magnetic a edged element (this square elements in square lattices will be experimentally studied in the following chapter), the final form of (III-8) is:

$$f_{n,m}^{(\mathrm{m})} = \int_{-a/2}^{a/2}\int_{-a/2}^{a/2} m_{\mathrm{Y}}(\mathrm{x},\mathrm{y}) e^{\frac{2\pi i}{\mathrm{T}}(n\mathrm{x}+m\mathrm{y})} d\mathrm{x}d\mathrm{y} \qquad \text{(III-9)}$$

In the transversal Kerr setup of fig. II-6 and III-1, the signal from the photodiode is partly balanced y a DC-compensator. This way, the DC component is subtracted from the original signal and then amplified before being fed into the oscilloscope. Thus only the magnetic contribution of the total intensity is relevant for our purposes. This magnetic contribution is proportional to:

$$\Delta \mathrm{I}_{n,m}^{(\mathrm{r})} \propto \mathrm{Re}\left(f_{n,m}^{(\mathrm{nm})} \frac{\mathbf{r}_{pp}}{\mathbf{r}_{pp}^{(\mathrm{m})}} f_{n,m}^{(\mathrm{nm})} \right) \qquad \text{(III-10)}$$

If centrosymmetric elements are considered (like all the samples studied in this thesis), equation (III-10) can be simplified, since under this assumption the non-magnetic form factor is real [III.4]:

$$\Delta I_{n,m}^{(r)} \propto f_{n,m}^{(nm)}\,\mathrm{Re}\left(\frac{\mathbf{r}_{pp}}{\mathbf{r}_{pp}^{(m)}}\,f_{n,m}^{(nm)}\right)=$$

$$=\begin{cases}\dfrac{T^2}{\pi^2 nm}Sin\left(\dfrac{an\pi}{T}\right)Sin\left(\dfrac{am\pi}{T}\right)\cdot\mathrm{Re}\left(\dfrac{\mathbf{r}_{pp}}{\mathbf{r}_{pp}^{(m)}}\cdot\int_{-a/2}^{a/2}\int_{-a/2}^{a/2}m_Y(x,y)e^{\frac{2\pi inx}{T}}e^{\frac{2\pi imy}{T}}dxdy\right) & \text{if } m,n\neq 0\\ \dfrac{Ta}{\pi n}Sin\left(\dfrac{an\pi}{T}\right)\cdot\mathrm{Re}\left(\dfrac{\mathbf{r}_{pp}}{\mathbf{r}_{pp}^{(m)}}\cdot\int_{-a/2}^{a/2}\int_{-a/2}^{a/2}m_Y(x,y)e^{\frac{2\pi inx}{T}}e^{\frac{2\pi imy}{T}}dxdy\right) & \text{if } m=0,n\neq 0\\ \dfrac{Ta}{\pi m}Sin\left(\dfrac{am\pi}{T}\right)\cdot\mathrm{Re}\left(\dfrac{\mathbf{r}_{pp}}{\mathbf{r}_{pp}^{(m)}}\cdot\int_{-a/2}^{a/2}\int_{-a/2}^{a/2}m_Y(x,y)e^{\frac{2\pi inx}{T}}e^{\frac{2\pi imy}{T}}dxdy\right) & \text{if } n=0,m\neq 0\end{cases} \qquad \text{(III-11)}$$

Then, equation (III-11) describes the diffracted Kerr signal of a square array of square magnetic elements in a transversal Kerr setup.

Using the notation $K=K'+iK''=\frac{\mathbf{r}_{pp}}{\mathbf{r}_{pp}^{(m)}}$ [III.2], the magnetic component of the intensity in the n^{th} diffracted may be rewritten:

$$\Delta I_{n,n}^{(r)} \propto \{\mathrm{Re}[f_{n,n}^{(m)}]-(K''/K')\mathrm{Im}[f_{n,n}^{(m)}]\} \qquad \text{(III-12)}$$

There is no work in the literature describing the behaviour of K for the diffracted beams, so K"/K' can be tentatively considered to be proportional to the diffraction order and its value might be estimated by an agreement between theory and experiments. For instance, the value of |K"/K'| for permalloy, a soft magnetic material similar to the amorphous $Fe_{80}B_{20}$ used in the following chapter, is in the range 0-0.3 [III.2].

The above description sets the applicability of the presented formula, i.e., the theory is valid for centrosymmetric magnetic elements embedded in an orthogonal array made of materials in which the value of $|K''/K'|\cdot\mathrm{Im}[f_n^m]$ is close to zero. All these conditions except perhaps the latter (that has to be experimentally corroborated) are verified by all the arrays used in this thesis.

Although these equations will be shown to lead to a convenient formalism with which to interpret the DMOKE results, the equations should be treated with some caution since they may not be valid for all situations. In principle, the previous argumentation should provide an expression for the intensity of the diffracted spots only if they are closed to the reflected spot. Otherwise the model does not guarantee accurate results [III.2, III.3]. In order to corroborate whether the DMOKE the theory include all diffraction spots or only the ones presenting the same Kerr geometry than the reflected spot, some experiments will be designed and performed in the next chapter.

3.Polar DMOKE formalism and setup:

The case of DMOKE in a polar Kerr setup is slightly more complicated than the transversal case just explained.

First of all, the conventional polar Kerr setup (fig. II-4) cannot be used, since the sample is placed on the setup in a hollow pole of the electromagnet. Thus, the diffraction pattern is plotted in the electromagnet and therefore the photodiode is no longer capable of measure the corresponding signal.

This major inconvenient was overcame using an alternative polar Kerr setup.

3.1.An alternative polar Kerr setup for DMOKE measurements

This alternative Kerr setup fabricated in the IMM consists of (see fig. III-2) a double conical iron nucleus inserted on a Helmholtz coil. The field in both tips of the iron nucleus is approximately straight. In one of these tips is placed the sample whereas in the other one a Hall probe is placed.

This setup allow the measurement of the diffracted spots but is more sensitive to vibrations and can only measure very small samples, since the field is less homogeneous than in the standard polar Kerr setup. In addition, since no rotation or ellipticity will be measured, but just intensities, the compensators, modulators and lock-in amplifiers can be substituted by a simple set of attenuators, lenses and polarizers.

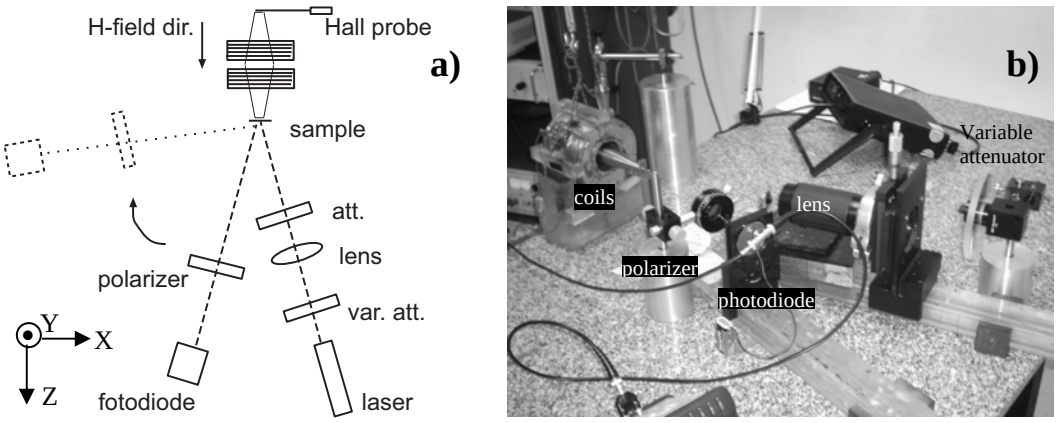

Fig.III-2: Alternative Polar Kerr at the IMM for measuring Polar DMOKE signals. a) sketch b) setup

In this simple setup, a monochromatic He-Ne laser light (λ=633 nm) is used. The polarizer just in front of the photodiode is tuned at 45º of the polarization of the laser beam, to achieve the highest Kerr intensity sensitivity.

The accuracy of the presented setup was corroborated comparing the polar MOKE results of different samples with the corresponding ones measured by a conventional polar Kerr setup like the one described in chapter II.

3.2.Phenomenological formalism

Like in the transversal case, the reflected electric field measured by the photodiode must be determined in order to obtain the Kerr intensity in the diffracted spots. According to fig. III-2, the optical devices that modify the linear polarized light of the laser source are:

1.- The sample, whose Jones matrix is $S=\begin{pmatrix} \mathbf{r}_p & \mathbf{r}_{ps} \\ \mathbf{r}_{sp} & \mathbf{r}_s \end{pmatrix}$

2.- The polarizer in front of the photodiode, whose Jones matrix is $P=\begin{pmatrix} \cos^2\beta & \cos\beta\sin\beta \\ \cos\beta\sin\beta & \sin^2\beta \end{pmatrix}$.

Since the polarizer has been tuned to β=45º to obtain the maximum Kerr intensity variation, P=$\begin{pmatrix} \frac{1}{2} & \frac{1}{2} \\ \frac{1}{2} & \frac{1}{2} \end{pmatrix}$.

The reflected field whose corresponding intensity is measured by the photodiode. Thus, $E^{(r)}=P\cdot S\cdot E^{(i)}$. From this expression it follows:

$$E_p^{(r)} = E_s^{(r)} = \frac{E_p^{(i)}}{2}\left(\mathbf{r}_p - \mathbf{r}_{ps}\right) + \frac{E_s^{(i)}}{2}\left(\mathbf{r}_s + \mathbf{r}_{ps}\right) \qquad \text{(III-13)}$$

Assuming a polar Kerr configuration, the incident angle is θ~0 so $\mathbf{r}_p=\mathbf{r}_s$. Assuming also *p*-polarized incident light (note the laser emits linearly polarized light), $E_s^{(i)} = 0$. Then (III-13) may be rewritten in the form:

$$E_p^{(r)} = E_s^{(r)} = \frac{E_p^{(i)}}{2}\left(\mathbf{r}_p - \mathbf{r}_{ps}\right) \qquad \text{(III-14)}$$

The light intensity measured by the photodiode depends on the polarizer's angle β since the measured intensity is $I^{(r)}= \left|E_p^{(r)}\sin\beta+E_s^{(r)}\cos\beta\right|^2$. As said before, β=45º and $E_p^{(r)} = E_s^{(r)}$. Then $I^{(r)}=2\,E_p^{(r)}\cdot E_p^{(r)*}$.

Applying the Fraunhoffer diffraction theory, the measured field in the n^{th} diffracted is modulated by two form factors: the non-magnetic form factor, $f^{(nm)}$; and the magnetic form factor, $f^{(m)}$.

In this case it will be assumed that the measured samples consists of a square array of circular elements. This is the kind of samples (fabricated with LIL –see chapter I– in the MESA$^+$ Institute of the University of Twente) with perpendicular magnetization that will be measured and studied in detail in forthcoming chapters. Accordingly, the integration surface *S* of the form factors is a circle of radius *a*. Therefore, the non-magnetic form factor might be expressed in polar coordinates:

$$f_{n,m}^{(nm)} = \int_S r e^{iG\,r\cos\alpha}\, dr d\alpha \qquad \text{(III-15)}$$

where **G** is a generic reciprocal lattice vector, **r** the position vector and α represents the angle between the vectors **G** and **r**.

The final expression of the non-magnetic form factor for a square array of cylindrical nanopillars is:

$$f_{n,m}^{(\mathrm{nm})} = \int_S \mathrm{r} e^{i\mathrm{G\,r}\cos\alpha} d\mathrm{r} d\alpha = \int_0^a 2\pi \mathrm{r} \mathrm{J}_0\left(\mathrm{r}G\right) d\mathrm{r}$$
$$= \frac{2\pi a}{G}\mathrm{J}_1\left(aG\right) = \frac{aT}{\sqrt{n^2+m^2}}\mathrm{J}_1\left(\frac{2\pi a}{T}\sqrt{n^2+m^2}\right) \qquad \text{(III-16)}$$

The magnetic form factor should take into account the magnetization distribution within the elements of the array. According to our polar Kerr setup, the dependence of the magnetic form factor with the magnetization is:

$$f_{n,m}^{(\mathrm{m})} = \int_S m_Z e^{i\mathbf{G}\cdot\mathbf{r}} dS = \int_S m_Z e^{i\mathbf{G}\cdot\mathbf{r}} dS \qquad \text{(III-17)}$$

This way, the light intensity in the (*n*,*m*) diffracted is $\mathrm{I}_{n,m}^{(\mathrm{r})} = 2\mathrm{E}_{p,(n,m)}^{(\mathrm{r})} \cdot \mathrm{E}_{p,(n,m)}^{(\mathrm{r})*}$, where $\mathrm{E}_{p,(n,m)}^{(\mathrm{r})} = \frac{\mathrm{E}_p^{(\mathrm{i})}}{2}\left(\mathbf{r}^{(\mathrm{nm})} f_{n,m}^{(\mathrm{nm})} + \mathbf{r}^{(\mathrm{m})} f_{n,m}^{(\mathrm{m})}\right)$, being $\mathbf{r}^{(\mathrm{nm})}$ and $\mathbf{r}^{(\mathrm{m})}$ the non-magnetic and magnetic components –respectively– of the Fresnel coefficients subtraction $\mathbf{r}_p$-$\mathbf{r}_{ps}$, i.e., $\mathbf{r}_p$-$\mathbf{r}_{ps}$ = $\mathbf{r}^{(\mathrm{nm})}$+$\mathbf{r}^{(\mathrm{m})}$.
In our setup, the signal from the photodiode is separated from its DC component and amplified before entering the oscilloscope, so only the magnetic contribution of the total intensity is relevant for our purposes. This magnetic contribution is proportional to:

$$\Delta\mathrm{I}_{n,m}^{(\mathrm{r})} \propto \mathrm{Re}\left(f_{n,m}^{(\mathrm{nm})} \frac{\mathbf{r}^{(\mathrm{nm})}}{\mathbf{r}^{(\mathrm{m})}} f_{n,m}^{(\mathrm{nm})} \right) \qquad \text{(III-18)}$$

The fact that the considered magnetic elements are centrosymmetric simplifies formula (III-18), since under this assumption the non-magnetic form factor is real:

$$\Delta\mathrm{I}_{n,m}^{(\mathrm{r})} \propto f_{n,m}^{(\mathrm{nm})} \mathrm{Re}\left(\frac{\mathbf{r}^{(\mathrm{nm})}}{\mathbf{r}^{(\mathrm{m})}} f_{n,m}^{(\mathrm{nm})} \right) =$$
$$= \frac{aT}{\sqrt{n^2+m^2}}\mathrm{J}_1\left(\frac{2\pi a}{T}\sqrt{n^2+m^2}\right) \cdot \mathrm{Re}\left(\frac{\mathbf{r}^{(\mathrm{nm})}}{\mathbf{r}^{(\mathrm{m})}} \cdot \int_{-a}^{a}\int_{-\sqrt{a^2-y^2}}^{\sqrt{a^2-y^2}} m_Z\left(x,y\right) e^{\frac{2\pi i n x}{T}} e^{\frac{2\pi i m y}{T}} dxdy \right) \qquad \text{(III-19)}$$

Then, equation (III-19) provides the diffracted Kerr signal of a square array of cylindrical nanopillars in a polar Kerr setup.

As it has been theoretically seen, both the transverse and the polar DMOKE signal present a double dependence on the shape of the elements of the considered array. On one hand, the non-magnetic form factor (a completely optical factor), exclusively depending on both the array and the element shapes modulate not only the DC component of the diffraction spot but also the DMOKE component. On the other hand, the magnetic form factor adds a magneto-optical component into the formulae for the DMOKE intensities. In this particular case, not only the shape of both the element and the array must be taken into account but also the relative magnetization distribution within the elements of the array. This fact allows the possibility of studying the magnetization distribution by means of the DMOKE signal. This will be thoroughly studied in chapter IV.

8.Summary:

In addition to the well known MOKE effects explained in chapter II, the recent Diffractive MOKE (DMOKE) effects are phenomenologically detailed for both the transversal and polar configurations. Besides a theoretical explanation of DMOKE, related measurement techniques are presented. DMOKE measurements in transversal geometry are straightforward just using a conventional transverse Kerr setup. On the contrary, an alternative polar Kerr setup must be designed for DMOKE measurements since the conventional configuration is limited by the size of the hole in the hollow pole of the magnet.

The DMOKE signal, available only in patterned samples, has been demonstrated to have a strong dependence not only on the shape of both arrays and its constituent elements but also on the magnetization distribution along the direction in which the external field is applied. Thus, this DMOKE signal has theoretically predicted to provide extra information about the magnetization within the magnetic elements of the sample inaccessible to the conventional MOKE.

In the following chapter, the DMOKE properties of a magnetic ordered array will be analyzed in more detail both experimental and theoretically, proposing a physical interpretation of the DMOKE phenomena as well as some useful applications.

9.References:

[III.1] O.Geoffroy, D.Givord, Y.Otani, B.Pannetier, A.Santos, M.Schlenker, Y.Souche, J.Magn.Magn.Mater., **121**, 513 (1993)

[III.2] M Grimsditch, P. Vavassori. J. Phys.: Condens. Matter **16** R275 (2004)

[III.3] M. Grimsditch. P. Vavassori, V. Novosad, V. Metlushko, H. Shima, Y. Otani, and K. Fukamichi, Phys. Rev. B. **65**, 172419 (2002)

[III.4] P. García-Mochales, J.L. Costa-Krämer, G. Armellas, F. Briones, D. Jaque, J.I. Martín, J.L. Vicent , Appl. Phys. Lett. **81**, 3206 (2002)

[III.5] T. Schmitte, Ph.D. thesis, chapter 3, Rürh-Universitat Bochum (2002)

[III.6] T. Schmitte, A. Westphalen, K. Theis-Bröhl, H. Zabel, Superlattices and Microstructures **34**, 127 (2003)

[III.7] M.C. Hutley, *Diffraction gratings*. Academic Press, London (1982)

[III.8] D. Van Labeke, A. Vial, V.A. Novosad, Y. Souche, M. Schlenker, A.D.D. Santos. Opt. Comm., **124**, 519 (1996)

[III.9] J.L. Costa-Krämer, C. Guerrero, S. Melle, P. Garcia-Mochales, F. Briones Nanotechnology, **14**, 239 (2003)

[III.10] T. Schmitte, O. Schwöbken, S. Goek, K. Westerholt, H. Zabel, J. Magn. Magn. Mat. **240**, 24 (2002)

[III.11] T. Schmitte, T. Schemberg, K Westerholt, H. Zabel, J. Appl. Phys. **87**, 5630 (2000)

[III.12] I. Guedes, N. J. Zaluzec, M. Grimsditch, V. Metlushko, P. Vavassori, B. Ilic, P. Neuzil, R. Kumar, Phys. Rev. B **62**, 11719 (2000)

[III.13] P. Vavassori, V. Metlushko, M. Grimsditch, B. Ilic, P. Neuzil, R. Kumar Phys. Rev. B **61**, 5895 (2000)

[III-14] I. Guedes, M. Grimsditch, V. Metlushko, P. Vavassori, R. Camley, B. Ilic, P. Neuzil, R. Kumar, Phys. Rev. B **66,** 14434 (2002)

[III-15] P. Vavassori, M. Grimsditch, V. Novosad, V. Metlushko and B. Ilic, Phys. Rev. B **67** N (2003)

[III-16] I. Guedes, M. Grimsditch, V. Metlushko, P. Vavassori, R. Camley, B. Ilic, P. Neuzil and R. Kumar, Phys. Rev. B **67**, 24428 (2003)

CHAPTER IV:

MAGNETIZATION REVERSALS AND INTERACTIONS IN 2D ARRAYS BY MEANS OF MOKE AND DMOKE

Index

MAGNETIZATION REVERSALS AND INTERACTIONS IN 2D ARRAYS BY MEANS OF MOKE AND DMOKE

1.Introduction:

Microstructured and, more recently, nanostructured samples have created much interest in recent years because of their potential applications in optical and magnetical storage devices. Particular attention has attracted the magnetical and magneto-optical properties of periodic arrays of micrometer and sub-micrometer elements of very different shapes, specially dots and stripes. The study of these arrays of sub-micron elements is the basis for the development of magnetic memories and nano-patterned recording media, as interelement interaction determine the integration limits of magnetic memories and nano-patterned recording media.

The effect of the interaction between elements in the array has been much less studied than the effect of the size reduction. Magneto-optic techniques and, in particular Diffraction Magneto-Optic Kerr Effect (DMOKE), are most suited to experimentally investigate such effects as showing the high sensitivity needed to monitor the magnetization changes of thin films and very small elements. We have previously shown also that DMOKE supplies valuable information also on the magnetization distribution [IV.1] and anisotropy [IV.2] due to its high sensitivity to magnetic inhomogeneties. This high sensitivity may provide the magnitude of the anisotropy constants analysing the array response on both the reflected an diffracted spots [IV.2]. In the literature not only positive [IV.3], but negative arrays [IV.4] have been studied using Magneto-optic (MO) techniques. The importance of DMOKE is growing up in recent years. This technique has been recently used to study patterned 1D [IV.5], [IV.6],[IV.7] and 2D [IV.7], [IV.8], [IV.9], [IV.10] thin films, and also for negative magnetic arrays [IV.11], [IV.12], [IV.13]. MO loops measured in different diffraction orders reveal marked differences with the loops measured at the reflected (0th order) beam. These differences are more marked as the elements are placed closer in the array, as will be shown below, and the question is to what extent these differences are a signature of magnetic interactions between elements within the array.

When the elements within the array are packed close together, the average magnetic behavior is expected to change with respect to a situation in which the

magnetic elements are magnetically isolated. One of the objectives of this chapter is to explore the possibility of monitoring these magnetic changes by MO means.

As theoretically studied in chapter II, the diffracted beams corresponding to a patterned magnetic sample in a Kerr setup has a magneto-optic component. Thus, the analysis of this magneto-optic component might provide information about the magnetic state of the structure.
But the previous chapter leaves an open question, mandatory to answer in order to properly understand DMOKE. When developing the phenomenological theory of DMOKE it was assumed certain conditions for the diffracted spots that might not be correct. For example, in the transverse configuration, the *m*Y diffracted spots does not strictly hold the transverse geometry, because the "plane of incidence" changes in these particular cases. So, is it correct guessing the *m*Y diffracted are under the conditions of the transverse geometry?
In order to answer this question, the theory must be compared with experiments. Thus, a set of samples are patterned with square lattices of square elements changing the interelement separation.
This set of structures might also help to answer some other important questions:

- When having an ordered array of magnetic elements, is it possible to determine whether the elements are interacting or not?
- Moreover, is it possible to deduce the interelement separation by magneto-optic means?
- Which is the physical meaning of the DMOKE signal?
- and, which is the information the DMOKE signal can provide?

2.Structure design:

In order to answer the proposed questions, a set of patterns consisting of square arrays of square elements is fabricated. In order to study the influence of the interelement separation on the DMOKE signal, the elements of the different arrays are the same size and shape (see chapter III for the influence of the element shape on the DMOKE signal). The size of that elements should be small enough to be considered a 2D pattern and large enough to ensure regular shapes by lithographic means. Thus, the square elements are chosen to be 2μm edged.

On the other hand, the samples should be thick enough to prevent multiple reflections from the substrate (Si in this case) through the samples and thin enough to preserve homogeneity in the growth direction and to be treated as a thin

film and, therefore, treated from a 2D point of view. Thus, the selected material is polycrystalline Co (whose properties are well-known) and the thickness is chosen to be 40 nm.

A previous work [IV.14] has revealed that the interaction threshold for 200 Å thick Fe microelements is around 1 μm. This was deduced from the dependence of the saturation field on the separation between elements, decreasing as the distance is reduced. This is expected, since for an isolated element at magnetic saturation the demagnetization field is created by the surface poles. As another magnetic element is placed nearby some of the flux departs, decreasing the internal field and consequently the field required to saturate it. Since Co and Fe have very similar saturation magnetization values at room temperature (RT), and magnetic interactions are magnetostatic in origin, a similar value for Co micro-patterned arrays is expected. Thus, the selected separations between elements are in the range of the size of the element edge. In particular, the chosen interelement distances are: 0.2, 0.5, 1.0 and 2.0 microns (fig. IV-1). These separations are readily available both for lithographic techniques and micromagnetic simulations.

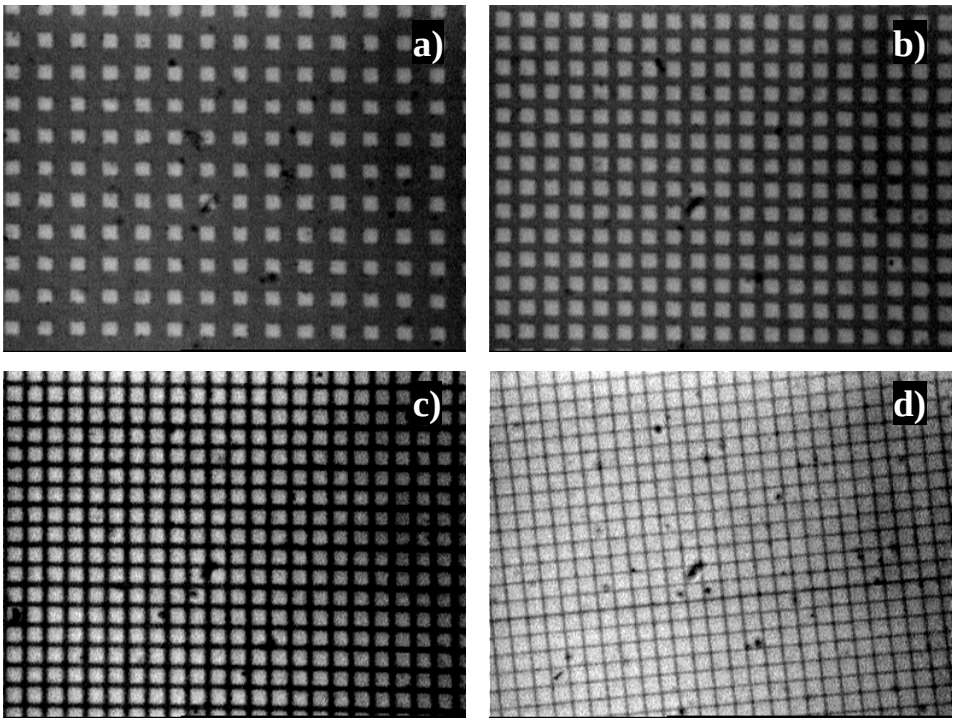

Fig. IV-1: Optical microscope images of the patterns (with in-plane magnetization) used. The square edge in all images is 2μm.

Four complete sets of patterns like the ones in fig. IV-1 are fabricated by either etching and lift-off in e-beam lithographied samples.

Regardless of the patterning method, the polycrystalline Co film is deposited by triode sputtering at room temperature (RT) on a Si substrate. The RT triode sputtered Co film exhibits an uniaxial anisotropy whose easy axis is parallel to the plasma confining field during deposition, with an anisotropy field of 30 Oe. The magnetic properties of the thin film (measured by transverse MOKE) are totally consistent with a Stoner model, i.e., the hysteresis loop depends on the angle of the applied magnetic field with respect to the anisotropy axis, being square with a 30 Oe coercive field when the external field is applied along the easy magnetization axis, and linear and reversible with a saturation field of 30 Oe when the external field is applied along the hard magnetization axis (see fig. IV-2).

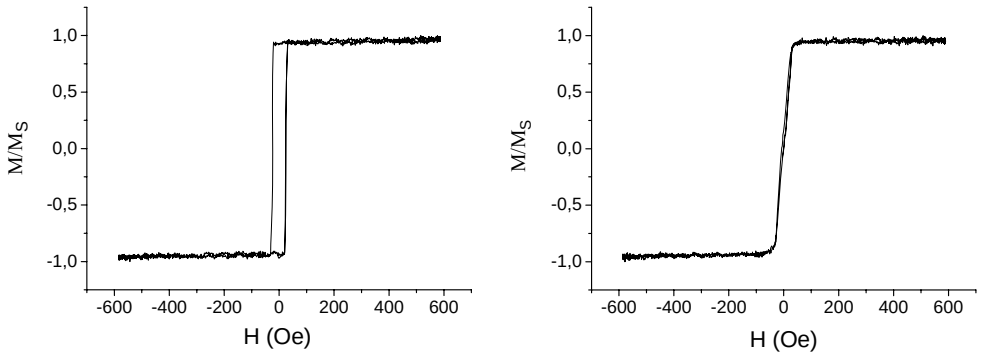

Fig. IV-2: Hysteresis loops for the easy (left) and hard (right) axes of a continuous thin film of polycrystalline Co.

As explained in chapter I, the triode sputtering at the IMM allows the selection of the Co anisotropy axis using the plasma confining field. This fact provide the possibility of studying, in addition, the effect of the magnetic anisotropy in the MO response. The Co anisotropy axis is selected in what follows to lay along the edge of the square magnetic elements.

3.Experimental results. Easy and hard axis:

The structures designed as explained in the previous sections are analyzed by means of transverse MOKE and DMOKE. As explained in chapter III and shown

in the literature ([IV.2], [IV.3], [IV.5], [IV.9]), different diffraction spots provide different DMOKE hysteresis loops. For our purposes, only first order loops are taken into account.

The hysteresis loops obtained for the direct reflected beam and for the first diffraction orders (1X and 1Y, see fig. III-1) when changing the interelement distance are shown in fig. IV-3 (applying the external field parallel to the Co easy axis) and fig. IV-4 (applying the external field parallel to the Co hard axis).

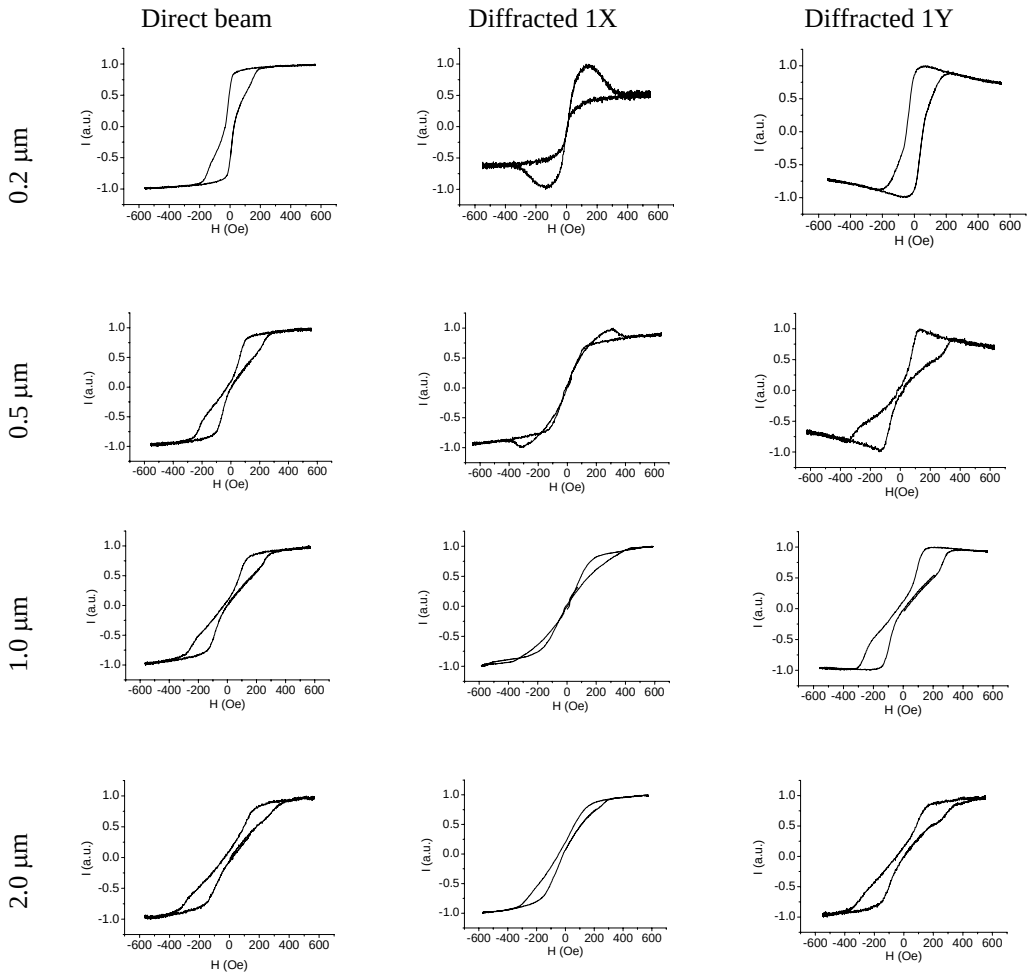

Fig. IV-3: Hysteresis loops, both for the 0^{th} order (reflected) and 1^{st} X and Y diffracted orders, for arrays of 2 µm separated 0.2 µm, 0.5 µm, 1.0 µm and 2.0 µm with external field H parallel to the Co uniaxial anisotropy easy axis.

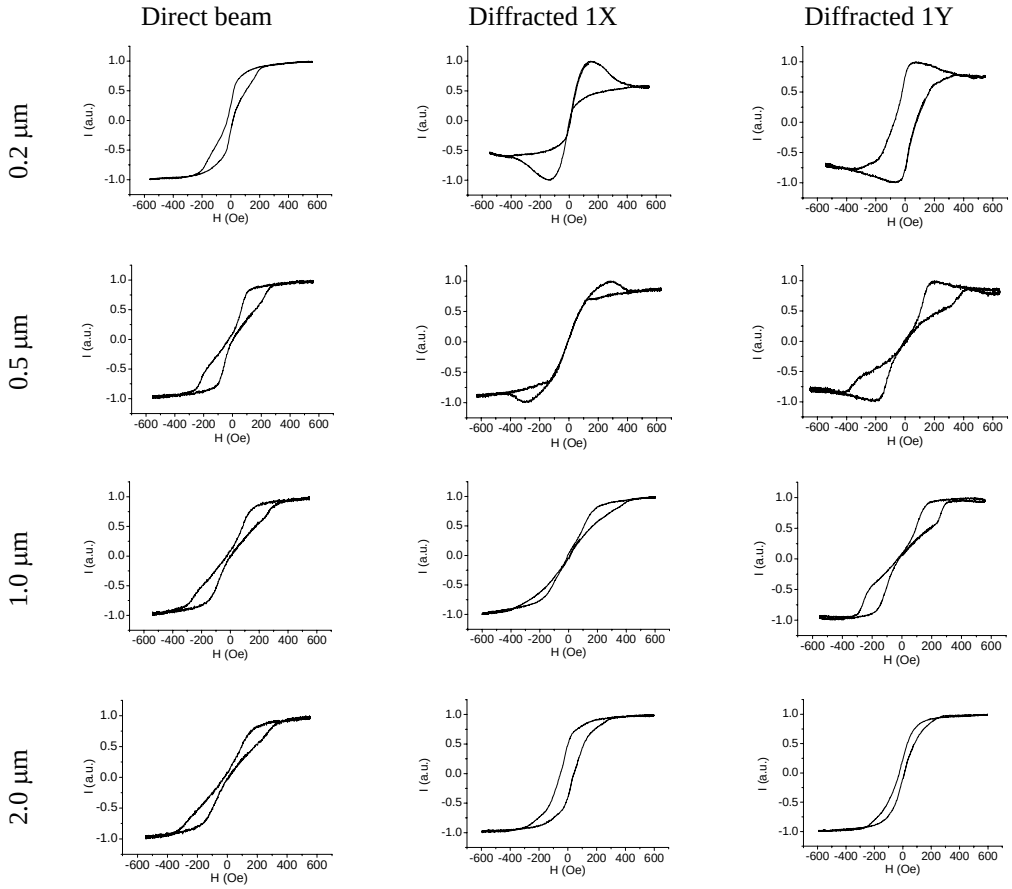

Fig. IV-4: Hysteresis loops, both for the 0^{th} order (reflected) and 1^{st} X and Y diffracted orders, for arrays of 2 µm separated 0.2 µm, 0.5 µm, 1.0 µm and 2.0 µm with external field H parallel to the Co uniaxial anisotropy hard axis.

Comparing the measured hysteresis loops of fig. IV-3 and fig IV-4, it is observed that there is no considerable effect on the MOKE signals of the direction of the Co anisotropy axis with respect to the applied field direction. This points to a magnetization process mainly dictated by the size of the element and perhaps the interaction between them. This is expected, since demagnetising fields (loops saturate at about 400 Oe, figs. IV-3 and IV-4) are at least one order of magnitude larger than the Co anisotropy field, 30 Oe (fig. IV-2). In addition, there is no significative variation of the shape of the reflected beam (0^{th} order) MO response when changing the interelement separation at constant element size. However,

there is a slight tilt of the loop that increases as the elements are separated further, in agreement with the previous consideration of a demagnetizing field of an isolated element that decreases as another element is placed closer and interaction starts. This effect will be analyzed later in section 4.

Contrary to what is observed in the reflected spot magneto-optical component, the diffractive magneto optical components change considerably when changing the interelement separation. The DMOKE signals present some “anomalies” compared to conventional hysteresis loops. First, the reversibility branches of the loop happen, in general, at larger fields than in the reflected loop. The 1X MO loops display a region where the MO signal is larger than at saturation, decreasing as the distance between elements is increased. The 1Y MO loops display a negative slope at the reversibility branch, close to saturation, that again decreases as the distance between elements is increased.

4.The onset of the interaction.

It has been seen that the hysteresis loop corresponding to the direct (reflected) beam exhibits the same shape independently of small changes in the shape of the magnetic elements and no matter the external field is applied along the easy or hard axis of the material (at least for soft materials like polycrystalline Co). Moreover, when changing the interelement separation the hysteresis loops presents a very similar shape. The main difference between them is observed in the saturation field. Indeed, it can be seen (fig. IV-3, left column and fig. IV-4, left column) that an increase in the separation between elements implies an increase in the saturation field, i.e., an increase in the value of the external field needed to reach saturation (see fig. IV-5). Therefore, the hysteresis loop corresponding to larger separations look more tilted.

In fig. IV-5, each point in the plot corresponds to an average of the measurements of four structures from the four sets fabricated. Although these structures present small changes in their shapes, the corresponding hysteresis loops are alike and thus can be averaged.

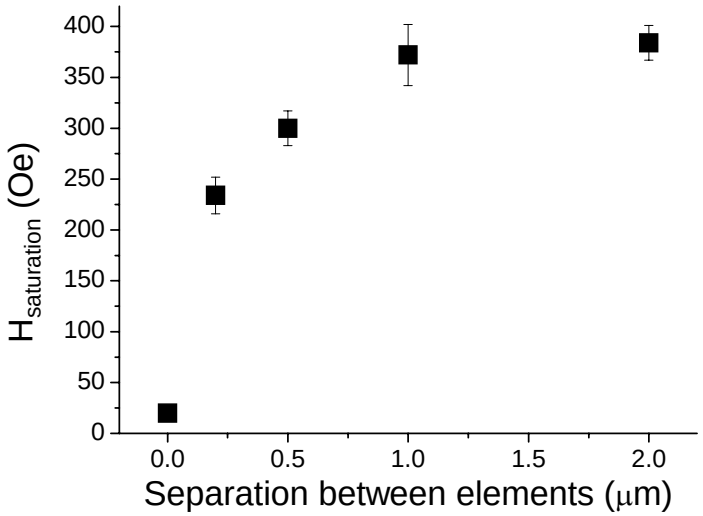

Fig. IV-5: Saturation field vs. interelement distance. Since direct (reflected) hysteresis loops had demonstrated to be unaffected by small changes in the shape of the elements and present the same shape no matter the external field is applied in the easy or hard axis direction of the material, the average for the plot is performed on the 4 sets of structures fabricated. Thus, each point of the plot is an average of 8 measurements. The point at separation 0 μm corresponds to the saturation field of the continuous film.

According to what has been explained, the tilt observed in the loops as a function of the interelement separation might be explained the following way: The applied field is not the effective field acting on the different elements due to a demagnetizing field that opposes the applied field. The effective (or internal) field on an element is the difference between the applied field and the demagnetizing field ($H_{eff}=H_{applied}-H_{demag}$).

The sudden drop of the saturation field when reducing the separation between elements (fig. IV-5) means that the internal field increases as the distance between elements decreases. Therefore, the demagnetizing field H_{demag} decreases when the separation decreases. This suggests that at low separations, indicating the onset of the interaction, part of the magnetic flux closes between different elements, i.e. elements are interacting. Then fig. IV-5 implies interaction between elements when their separation is below 1 μm, similarly to what is observed for Fe epitaxial elements of analogous dimensions [IV.14].

A thorough theoretical explanation will be described in the following chapter, providing also a criterion to determine the distance for the onset of the interaction as a function of the shape and dimensions of the magnetic elements.

5.Theoretical results. Micromagnetic simulations+diffraction theory:

Once the experimental results are obtained, the next step is then to develop a simple model that describes diffractive magneto-optical signals in magnetic arrays. To do so the problem is separated into two: to obtain reasonable magnetization distributions as a function of the external field, and then to use these distributions to calculate the expected diffracted magneto optical signals.

Using the open source code OOMMF © (OOMMF © public code v. 1.1b @ http://math.nist.gov/oommf/) for micromagnetic simulations it can be determined the magnetization dynamics within a single magnetic element. Assuming the elements of the array does not interact and all elements of the array has the same optical and magnetic behavior, considering a single element to perform the simulations is a first approach (not very time consuming) to the magnetization dynamics on an ordered array of magnetic elements. Whether the magnetic elements are interacting or not is not a trivial question and will be one of the goals of the following chapter. In the range of a few microns and lower, the onset of the interaction is mainly dictated by the shape of the elements as it will be explained in detail in chapter V.

According to the transversal Kerr configuration (see fig. II-6) the component of the magnetization that must be taken into account is m_Y (the one perpendicular to the plane of incidence). Substituting the values of $m_Y(x,y)$ provided by the micromagnetic simulation into eq. (III-11), it will be obtained the expected values for the DMOKE intensity at a given external field value. This way, combining micromagnetic simulations and optical diffraction theory, theoretical DMOKE loops are obtained (fig. IV-6). This will allow the interpretation of the experimental data and provides a way to analyze and understand the physical meaning of the magneto-optic diffracted signal.

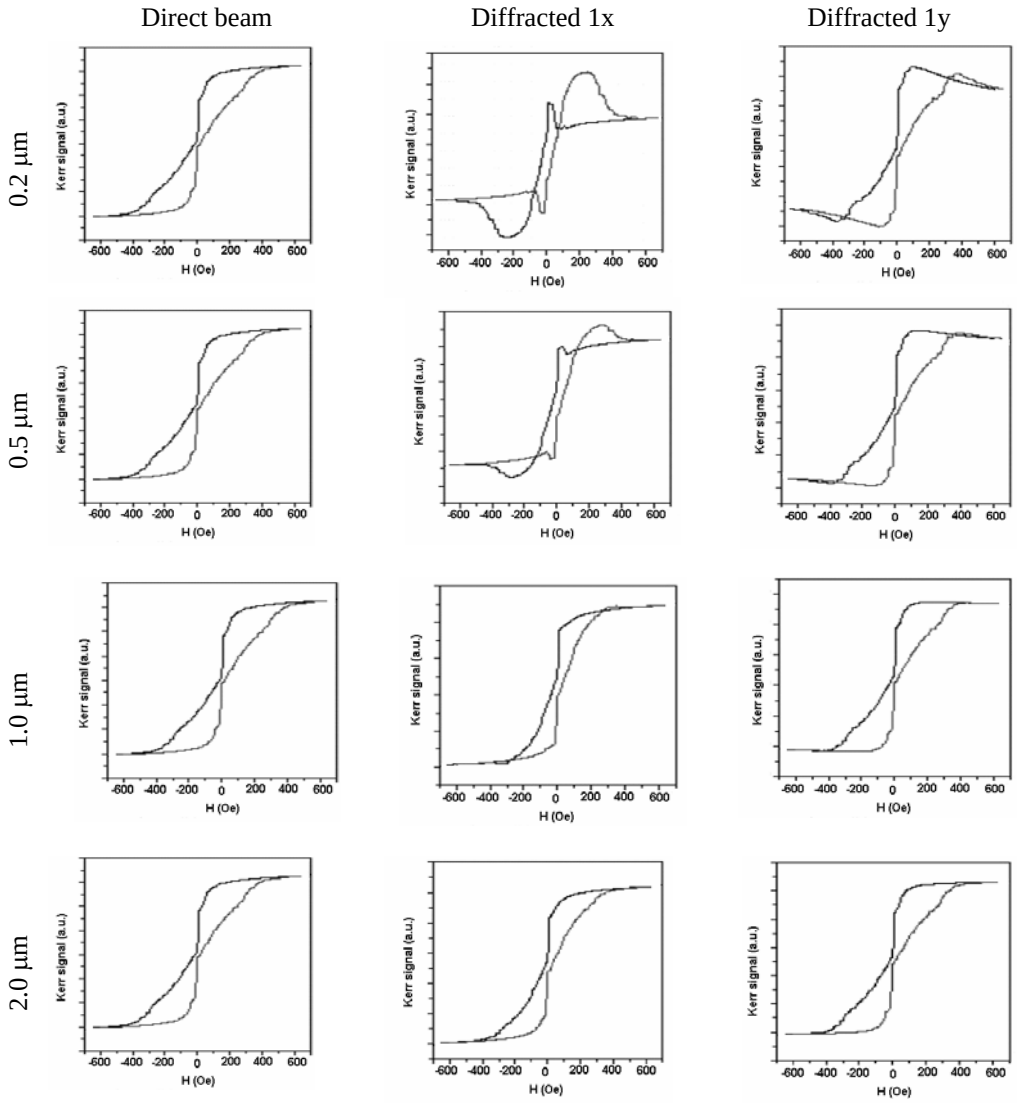

Fig. IV-6: Micromagnetic simulations and the expected MO dependencies in the first diffraction orders calculated using conventional optical diffraction theory for arrays of 2 µm separated 0.2 µm, 0.5 µm, 1.0 µm and 2.0 µm with H parallel to the Co uniaxial anisotropy easy axis.

Since no significative differences are observed between applying the field along the Co easy or hard axis, the comparison between experimental data and the DMOKE model results is presented just for the easy axis case. The simulated hysteresis loops for different interelement distances for both the reflected and first diffraction orders are shown in fig. IV-6.

Since, for simplicity and computational time optimization, the micromagnetic simulations have been performed assuming that the array is composed by non-interacting elements, all direct beam hysteresis loops are equal regardless of their separations. Then, the slight difference between experiments and simulation in the direct beam hysteresis loops has to be attributed to interaction effects. As observed, there are great similarities between experiments (fig. IV-3) and the simulations (fig. IV-6) that can serve to describe the magnetization processes. It has been already mentioned that in the transversal Kerr configuration the measured reflectivity is proportional to the magnetization component parallel to the applied field, without higher order contributions (see chapter III). As such, the measured direct beam MO response represents the array average magnetization and its corresponding hysteresis loops show the evolution of the average magnetization per element when changing the applied external field.

Hysteresis loops for different interelement distances show the same shape: a zero-field area close to reversibility linking two loops. As shown by the micromagnetic simulations (see fig. IV-7) this behaviour is due to a two phase magnetization inversion: first the centre stripe inverts the magnetization. Then the inversion of the magnetization of the edges parallel to the field direction occurs.

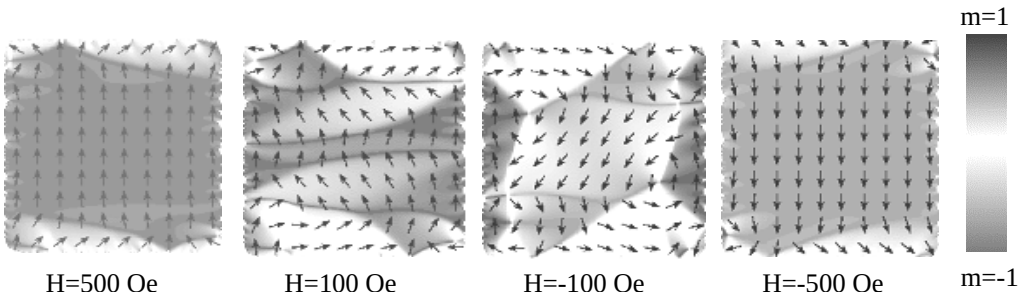

Fig. IV-7: Magnetization distribution in a single square element of the array for different values of the external field H. Only $m_Y(x,y)$, which corresponds to the transversal Kerr effect signal, is displayed in greyscale code.

As explained before in chapter III, the DMOKE signal is strongly affected by the shape of the magnetic elements of the array (accounted in the form factor in eq. III-11). It can be seen fig. IV-8 that a slight change in the squareness (round borders in this case and a shape more trapezoidal-like than square) might deeply alter the shape of the diffracted hysteresis loops. In spite of this fact, the direct

reflected signal is not appreciately modified when introducing this changes in the element's shapes.

On the other hand, not only de DMOKE depends on the shape of the elements, but also the DC component of the diffracted signal. That is because the non-magnetic form factor (eq. III-9) is also modified when changing the element shape. Experimentally, this effect is noticed in a different SNR.

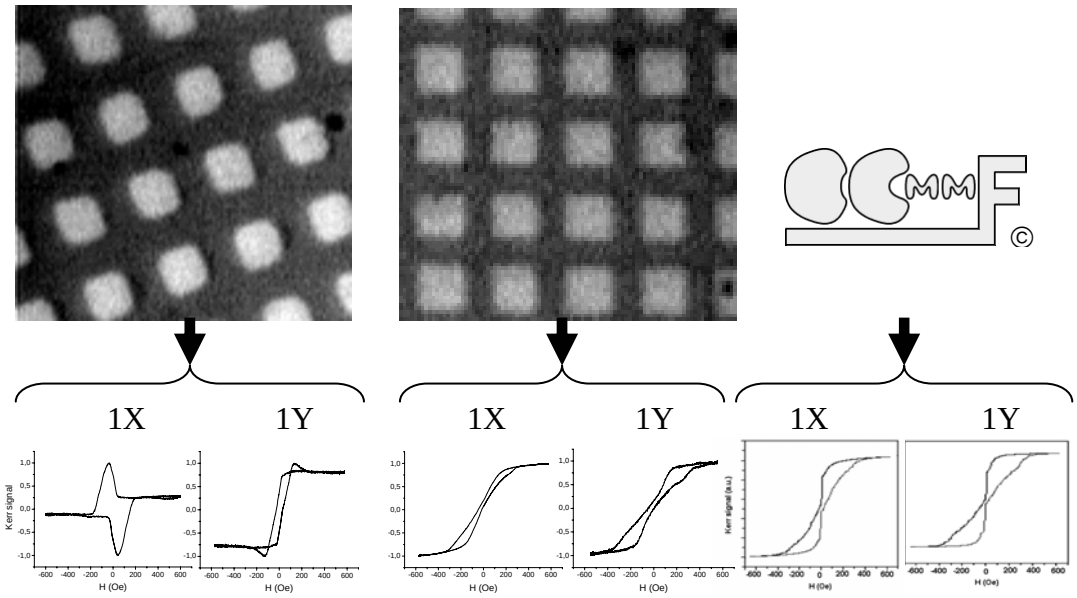

Fig. IV-8: The DMOKE signal strongly depend on the shape of the magnetic elements embedded in the array. The squaremost elements (centre) yields a DMOKE signal very similar to what is obtained in the model based in micromagnetic simulations (right). On the contrary, slightly irregular shapes yield a very different DMOKE signal (left) than the one theoretically predicted.

In spite of the large differences in the DMOKE response shown in fig. IV-8, the corresponding MOKE hysteresis loops are very similar. In higher diffraction orders the DMOKE signal is also altered by irregularities in the element shapes.

This strong dependence on the element shape makes DMOKE a useful technique for quality control purposes on regular arrays of magnetic elements. In addition, depending on the type of defect to be identified, the diffraction order to be used can be suitably chosen.

6.DMOKE and magnetization reversals I: Co

So far, it has been shown that the average magnetization (as seen by the 0^{th} order MO loop) measured in the arrays is described reasonably well by an ensemble of non-interacting elements with the same magnetization distribution, and that the effect of the distance between elements is to decrease the field necessary to saturate the array, symptomatic of an onset of the interactions.

It has been phenomenologically demonstrated in chapter III that the DMOKE signal in diffracted (n,m) (n^{th} diffracted in the X direction and m^{th} diffracted in the Y direction. See fig.III-1 for signs conventions) is proportional to:

$$\text{DMOKE\_signal}(n,m) \propto \text{Re}\left(B\cdot\int_{-a/2}^{a/2}\int_{-a/2}^{a/2} m_y(\text{x},\text{y})\, e^{\frac{2\pi i n x}{\text{T}}} e^{\frac{2\pi i m y}{\text{T}}} d\text{x}d\text{y} \right) \qquad \text{(IV-1)}$$

where $m_Y(x,y)$ is the magnetization projection along the Y direction (which corresponds to the transversal MOKE signal), a is the square length, T the period of the array ($T=a+w$, the square length a plus the interelement distance w) and B is a complex parameter that depends on the material, light wavelength and incidence angle (see [IV.1, IV.8, IV.12] and chapter III).

Whether eq. (IV-1) corresponds to a real –non-complex– expression (or to an expression with negligible imaginary part) or not is unclear. As explained in chapter III, it mostly depends on the quotient of the magnetic and not magnetic part of the Fresnel reflectivity coefficient corresponding to the *p*-polarized component (see eq. III-12 and [IV.15]). As explained in the previous chapter, there is no work in the literature describing the behaviour of K for the diffracted beams, so its value must be estimated by an agreement between theory and experiments. For instance, in [IV.15] the value of |K''/K'| for permalloy is estimated. In this particular case, |K''/K'| is in the range 0-0.3. Permalloy is a soft magnetic material similar to the amorphous $Fe_{80}B_{20}$ that will be used in the following section for comparison purposes.

6.1.Physical interpretation of DMOKE signal

According to the previous discussion, tentatively assuming the expression in (IV-1) is real (or its imaginary part is close to zero), a very simple model for describing the magnetization reversals by means of DMOKE signals might be developed.

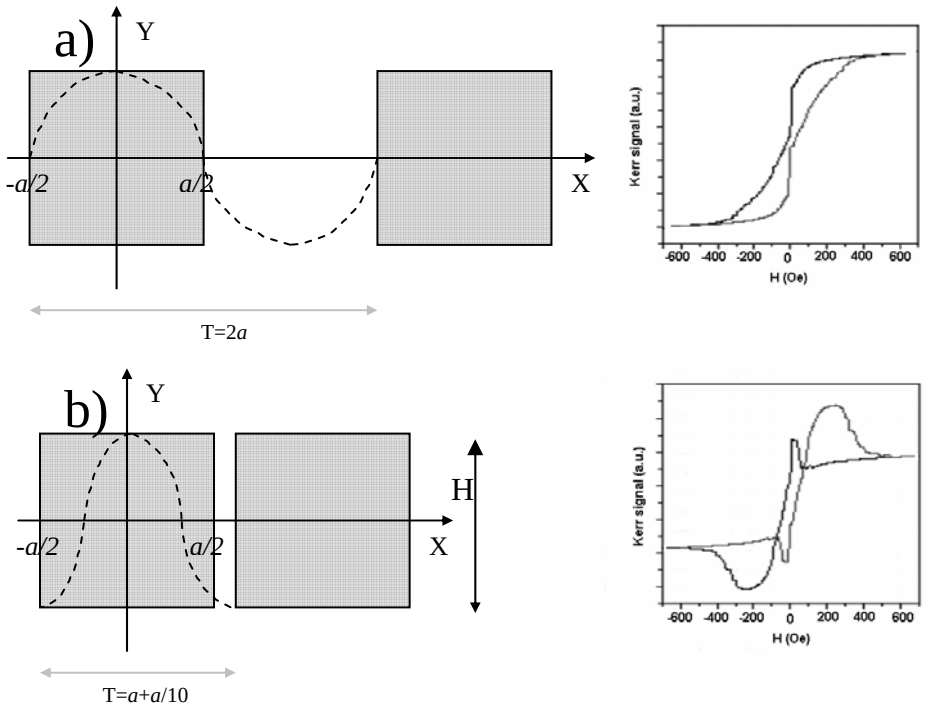

Fig. IV-8: Matching of the weighting factor for the diffracted 1X signal and the corresponding diffracted loops for **a)** *a* and **b)** *a*/10 interelement distances.

Differences in DMOKE signals can be explained as the effect of the matching between the magnetization distribution and the moment associated to the periodicity of the array (Fig. IV-8). The square arrays have been fabricated over a non magnetic substrate. This implies that $m_Y(x,y)=0$ outside the square element, so the integration period is the square length. Thus, for the first diffraction orders (n=1, m=0 for diffracted 1X and n=0, m=1 for diffracted 1Y) the magnetization is weighted by a factor, either $\cos\left(\frac{2\pi x}{T}\right)$ or $\cos\left(\frac{2\pi y}{T}\right)$, that directly depends on the array motif period T. Since T=a+w, different separations implies different weighting of the magnetization distribution, so different diffracted hysteresis loop are expected just because of the geometry of the array.

As shown in fig. IV-8a, when the array period T is twice the length of the element (corresponding to 2 μm interelement distance for 2μm edge elements), the weighting function is positive all over the element, so the corresponding diffracted 1X hysteresis loop should be similar to the direct beam one, as it occurs for this case (fig. IV-3**,** 2μm separation). On the other hand, when the motif period T

approaches the lenght of the element (which corresponds to the continuum), the weighting factor is positive at the center of the element and negative at the edges parallel to the field direction. Then, the magnetization at the edges that run parallel to the field direction weights more, and negatively, for smaller interelement distances (fig. IV-8b).

The Kerr formula for the diffracted intensities (eq. IV-1) tells us that, depending on the interelement separation, there are magnetization distributions (for instance, an $m_Y(x)$ where the central part of the element has switched and the magnetization close to the edges has not switched yet) that have a higher moment than in the saturated state. This explains the anomalous "bump" in the 1X diffracted loop where the signal is larger than at magnetic saturation (fig. IV-3, 0.2µm separation). Similar arguments can be applied to $m_Y(y)$ and the 1Y diffraction order. This matching effect crucial to understand the observed MO dependencies in the diffracted spots, and renders this technique quite useful to discern different reversal mechanisms as shown below.

This way, both the apparent higher saturation field in the 1X and 1Y DMOKE loops and the anomalous bumps and slopes are explained. Although the element has almost reached magnetic saturation, the DMOKE signal is much more sensitive to the magnetization at the edges for closer interelement separations.

Summarizing, the n^{th} DMOKE loop represents the n^{th} Fourier moment of the magnetization distribution. In particular, diffracted 1X (1Y) represents the first Fourier moment of the magnetization distribution projection on the X (Y) axis averaged in the Y (X) axis, $m'_Y(x)$ ($m'_Y(y)$). In spite of the high sensitivity of the DMOKE signal to the interelement separation, there is no obvious signature of the onset of the interaction between elements that can be obtained from the DMOKE signals as their high sensitivity is due to the matching of the array periodicity and the weighting factor. However, this DMOKE signal, being an average information of all the array elements, contains information about the magnetization distributions during reversal, that in the case of interacting elements might be different than those for isolated elements, due to the different local field distributions associated.

6.2.DMOKE for magnetization reversals

According to what previously explained, the DMOKE signal is highly correlated not only with the magnetization distribution but also with the periodicity of the array. If we graph one of the magnetization distribution moments as a function of

the average magnetization (0^{th} moment) it can be found that different reversal mechanisms produce distinct dependencies. Thus, one convenient way to analyse and compare data for different reversal models is to plot each diffracted signal as a function of the reflected signal, which is proportional to the average magnetization. This allows to analyze different magnetization reversal processes irrespectively of the applied field necessary to produce them. This way our experimental data can be correlated with very simple (because the field is not required here either) reversal simulations. Different diffracted signal vs. average magnetization plots can be obtained for different magnetization distributions, some illustrative examples are shown in fig. IV-9.

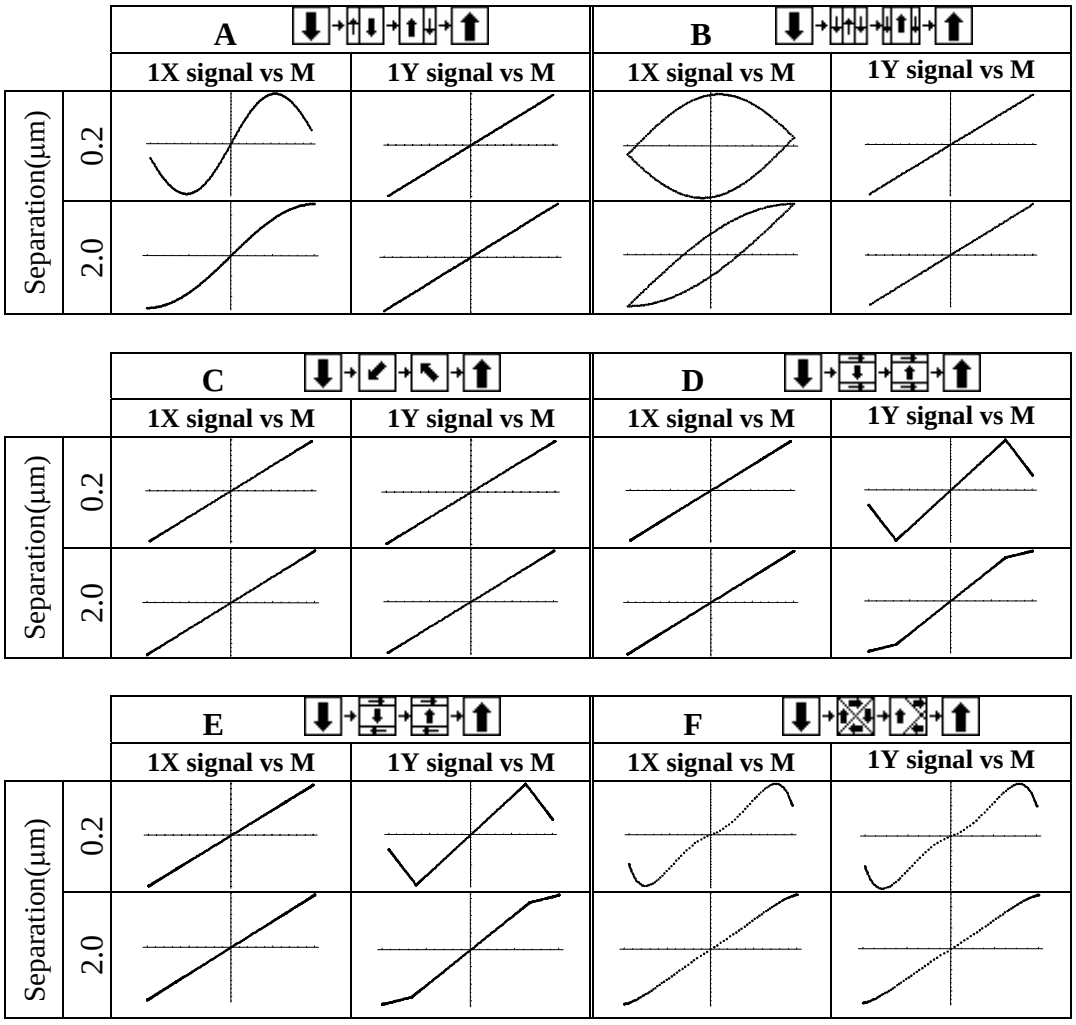

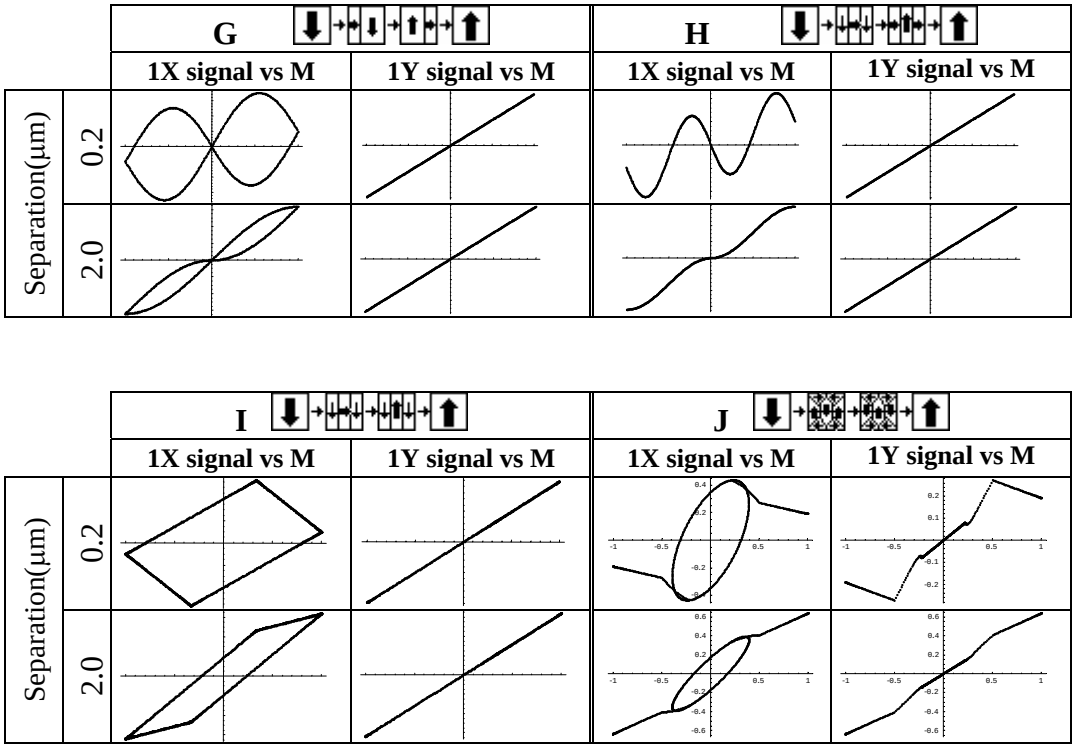

Fig. IV-9: Diffracted signal 1X and 1Y vs. magnetization for different inversion processes: A) Propagation of a single 180º domain wall parallel to the applied field, B) Propagation of two 180º domain wall parallel to the applied field, C) coherent rotation of the magnetization, D) S state with domain walls situated at 1/6 square length of the edge , E) C state with domain walls situated at 1/6 square length of the edge, F) vortex displacement along X axis, G) Two consecutive propagations of a single 90º domain wall, H) Two consecutive propagations of two simultaneous 90º domain walls, I) Rotation of the centre if the element followed by a rotation of the borders, F) Seven domains structure.

Reversals driven by coherent rotations produce linear reversible dependencies of the diffracted signals X and Y on the average magnetization. Domain walls parallel (perpendicular) to the applied field direction that propagate produce sinusoidal dependencies of the X (Y) component and lineal of the Y (X). C and S states show a linear X component and a continuous piecewise-defined Y component. Finally, a vortex-like state presents pseudo-sinusoidal dependencies in both X and Y components. The plots shown in fig. IV-9 can be compared with the experimental data in fig. IV-10 that shows the experimental diffracted signals vs. average magnetization for different separations obtained from the data shown in figs IV-3 & IV-4. As expected, the data shown in fig. IV-10 presents again a

minor relevance of the direction of the field with respect to the Co easy axis, as discussed in Figs 2 & 3, due to demagnetizing fields (loops saturate at about 400 Oe) at least one order of magnitude larger than the Co anisotropy field, i.e., one order of magnitude larger than the material intrinsic properties.

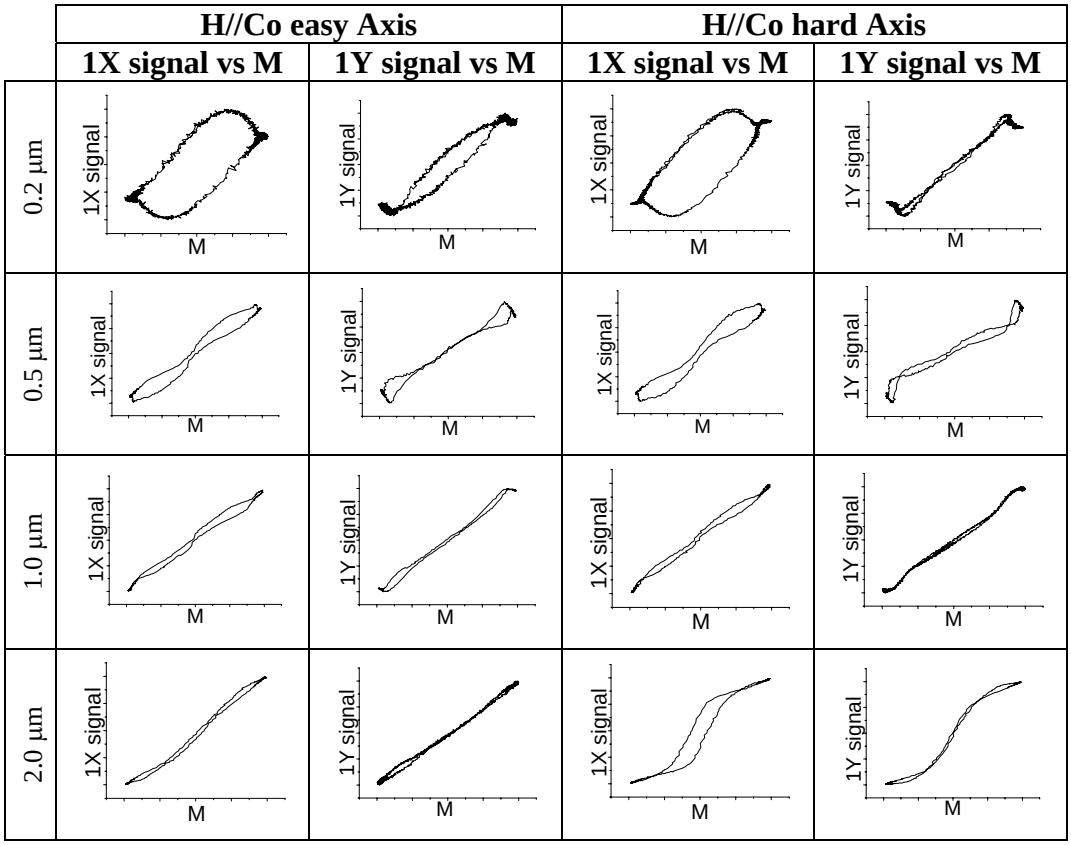

Fig. IV-10: Experimental 1st order diffracted MO signal vs. average magnetization for different interlement (from 0.2 to 2 µm) separations. Data is shown when the field is applied both along the easy and the hard Co axis and parallel to the 2µm Co square element.

The results obtained from the combined micromagnetic simulation and optical diffraction theory (see fig. IV-5) are similar to the experimental ones shown in fig.IV-10 and are not depicted.
Although there is no clear correlation between the experiments shown and the predictions from the simple reversal models shown in fig. IV-9 a few general conclusions can be obtained.

The comparison between the simple reversal models and the obtained experimental data of the 1st order diffractive signals vs. average magnetization

points out to a reversal that for large interelement separations (2μm) is a mixture of vortex (see fig.IV-9 F) and C or S states (fig.IV-9 D & E), while for small interelement distances (0.2 μm) the reversal is driven by the switching first of the central stripe of the square, and then the areas close to the edges. For intermediate separations (1 and 0.5 μm) the experimental data seems to adjust better a combination of one 90º domain wall propagation (see fig. IV-9 G) and C or S states (fig.IV-9 D & E). In this way, there would be a transition from flux closure within elements at large interelement distances, to flux closure between different elements at small interelement distances.

7.DMOKE and magnetization reversals II: $Fe_{80}B_{20}$

The not-so-clear correlation between the previous experimental measurements and the theoretical predictions might be due to a large imaginary part of the quotient of the magnetic and non-magnetic part of the Fresnel coefficient corresponding to the *p*-polarized light (K''/K', see eq. (III-12)). It can be found in the literature [IV.15] that K''/K' is close to zero in permalloy. Thus, if using a soft magnetic material like amorphous $Fe_{80}B_{20}$, it can be expected a better agreement between the experimental measurements and the results for simple model for reversals. In addition, the magnetic softness of $Fe_{80}B_{20}$ enhances the influence of the shape of the pattern elements in the MO response.

The $Fe_{80}B_{20}$ is, as Co, grown in a triode sputtering. Like in the Co case, the plasma confining field in the IMM triode sputtering induces an in-plane uniaxial anisotropy axis in the amorphous material. Thus, the continuous $Fe_{80}B_{20}$ can be characterized by the (transverse MOKE) hysteresis loops with the external field applied parallel and perpendicular to the anisotropy direction. The loops are shown in fig.IV-11.

7.1.MO properties of the continuous film

The magnetic properties of the continuous, 30 nm thick, amorphous $Fe_{80}B_{20}$ thin film are consistent with a Stoner-Wohlfarth model, i.e., the hysteresis loop depends on the angle of the applied magnetic field with respect to the anisotropy axis, being square with ~4 Oe coercive field (fig. IV-11, left plot) when the external field is applied along the easy magnetization axis, and linear with a saturation field of ~13 Oe when the external field is applied along the hard magnetization axis (fig. IV-11, right plot).

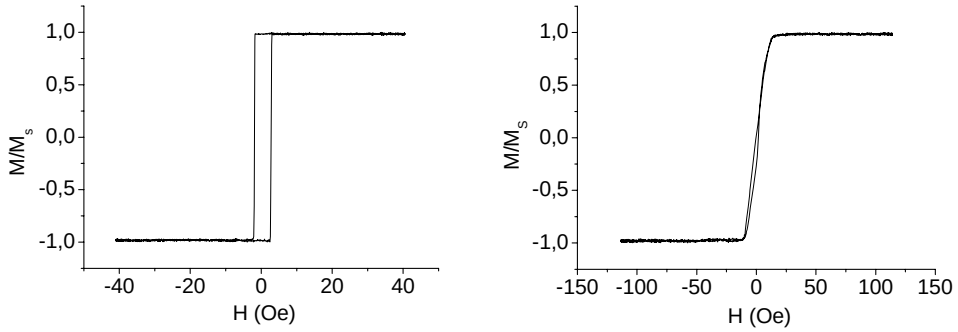

Fig.IV-11: Hysteresis loops of amorphous $Fe_{80}B_{20}$. The material presents an uniaxial anisotropy with a coercive field of 4 Oe (left plot, easy axis) and an saturation field of 13 Oe (right plot, hard axis).

7.2.MOKE and DMOKE signals of the patterned sample

The test pattern studied in this case consists of a square array of 5μm edged 30 nm thick square elements separated 1 μm. Although being a different material, the previous studies on Co provides a clue allowing to assume that under these conditions, the DMOKE hysteresis loops should be markedly different than the conventional (transverse) MOKE loops. According to what expected (fig. IV-12), the 1X diffracted show the "bumps" described before in Co and explained in last section; and the reversibility zone in the 1Y is tilted as in the Co case.

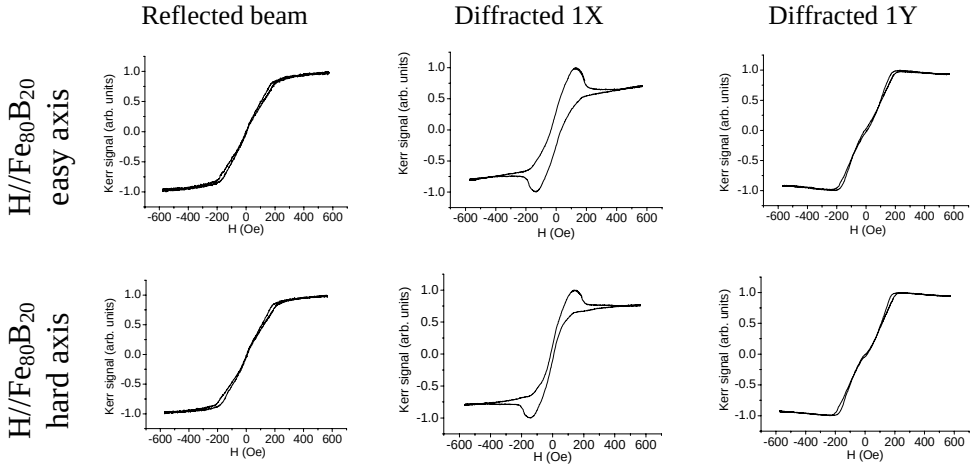

Fig. IV-12: Hysteresis loops, both for the 0^{th} order (reflected) and 1^{st} X and Y diffracted orders, for arrays of 5 μm edged $Fe_{80}B_{20}$ squares separated 1 μm with external field H parallel to the $Fe_{80}B_{20}$ easy and hard axes.

7.3.Reversals by means of DMOKE

Our structures and measurements are within the limits of the theoretical model (see chapter III), so the Kerr formula is applicable. Hence, plotting the Kerr signal vs. the average magnetization, characteristic reversal plots are obtained (fig. IV-13) that can be matched with the theoretical predictions. Comparing our experimental data from fig. IV-13 with the theoretical plots on fig. IV-9, the reversal mechanism that present our patterns might be determined.

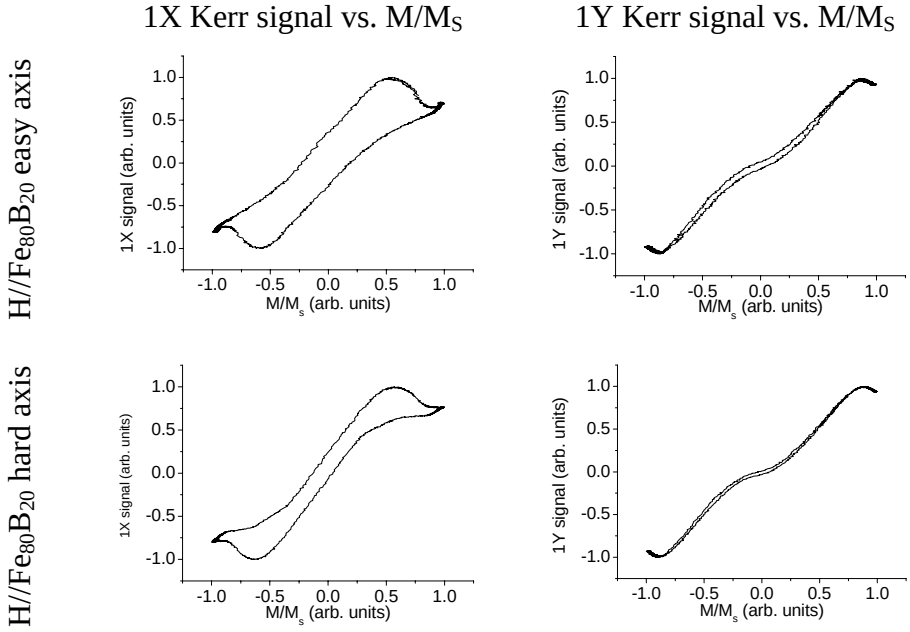

Fig. IV-13: Experimental 1st order diffracted MO signal vs average magnetization for arrays of 5 μm edged $Fe_{80}B_{20}$ squares separated 1 μm. Data is shown when the field is applied both along the easy (top row) and the hard $Fe_{80}B_{20}$ axis (bottom row) and parallel to the square edges.

Comparing the data in fig. IV-13 with the simulation predictions in IV-9, the magnetic elements of our structures should present a reversal mainly driven by a mixture of the Landau domain distribution (fig. IV-9 F) and the seven domain structure (fig. IV-9 J). MFM measurements have been performed to confirm this prediction (fig. IV-14). As no external field is applied during the MFM experiments, the obtained images show the magnetic domain structure of the magnetic elements at remanence. A relatively large distance between tip and

sample (about 70 nm) have been used to minimize tip-induced perturbations [IV.16].

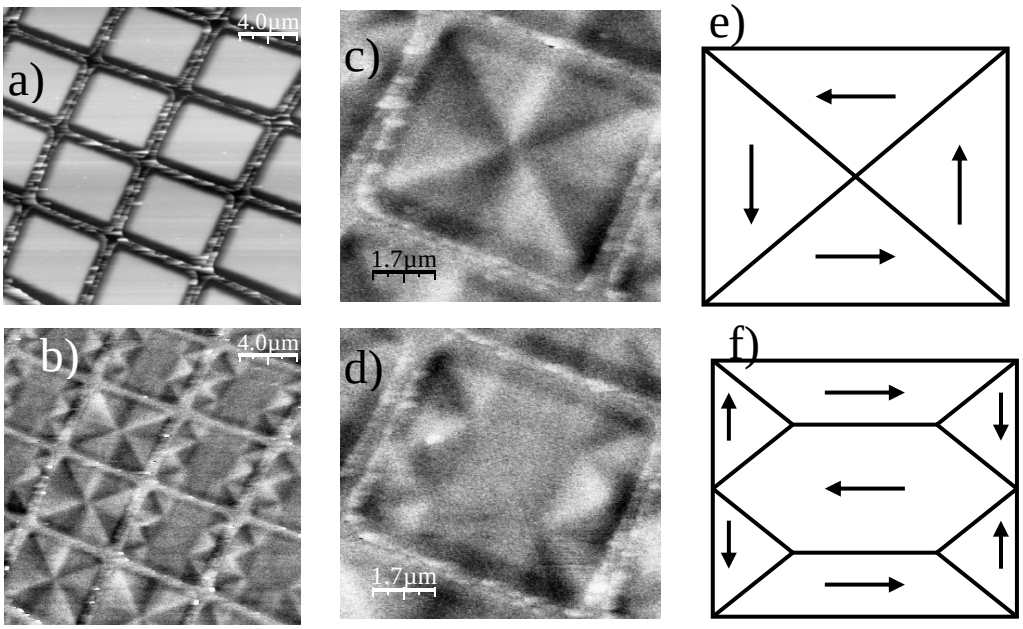

Fig.IV-14: a,b): topographic and magnetic images respectively, obtained by MFM, of an array of square 5µm edged dots. **c,d)**: magnetic images of square dots exhibiting flux-closure magnetic structures with four and seven domains respectively. These are the only two flux-closure magnetic structures present in the pattern at remanence. **e,f)**: schematic domain structures deduced from images **c)** and **d)**, respectively.

As shown in fig. IV-14, with no applied field the square elements of the array exhibit flux-closure remanent states with zero net magnetization in any plane direction. About two thirds of the elements exhibit the seven domain configuration shown in fig.IV-14d) and IV-14f), i.e. having three large domains and four closure domains. As can be seen in fig. IV-14b) for all the elements exhibiting such seven domain state, the large domains are always aligned in the same direction, as a result of the small uniaxial anisotropy induced during the sample growth. If no anisotropy had been induced, probably all the dots would exhibit the flux closure configuration with four domains shown in fig. IV-14c) and IV-14e), the so-called Landau state. In this case, the sense of rotation of magnetization can be clockwise or counter clockwise (fig. IV-14b).

Measurements performed in several areas of the same pattern show that no other domain configurations are present.

Thus, the DMOKE technique has been demonstrated to obtain information about the global magnetic behaviour of magnetic arrays, in contrast with MFM, Lorenz microscopy etc in which local information about the magnetization within single elements is obtained.

Although quite qualitative, and using only the 1^{st} diffraction order, the above discussion illustrates the power of using the DMOKE signal, i.e., the different moments of the magnetization distribution to elucidate reversal mechanisms in magnetic arrays.

8.Polar DMOKE: Co/Pt multilayers

In an analogous manner, using the setup described in chapter III (fig. III-2), the DMOKE signal can be measured in patterned samples with out-of-plane magnetization. The magnetic material used in this case consists of Co/Pt multilayers.

One of the advantages of these Co/Pt multilayers is that its magnetic properties might be tailored suitably choosing the configuration of the structure.

8.1.Tailoring multilayer magnetic properties in continuous films

The magnetic properties of the Co/Pt multilayer strongly depend on the relative thicknesses of the Co and Pt layers and on the number of bilayers. Fig. IV-15 show VSM loops corresponding to some different configurations of Co/Pt bilayers when modifying the number of bilayers (N=10, 26) and its relative thickness (modifying the Co thickness, t_{Co}, while the Pt thickness, t_{Pt}, is kept constant; t_{Co}=0.2, 0.7, 1.0 nm; t_{Pt}=0.7 nm). All the multilayers in fig. IV-15 has been grown in a RF-sputtering at an Ar^+ pressure of 2 μbar (see chapter I for the influence of Ar^+ on the smoothness of the layers)

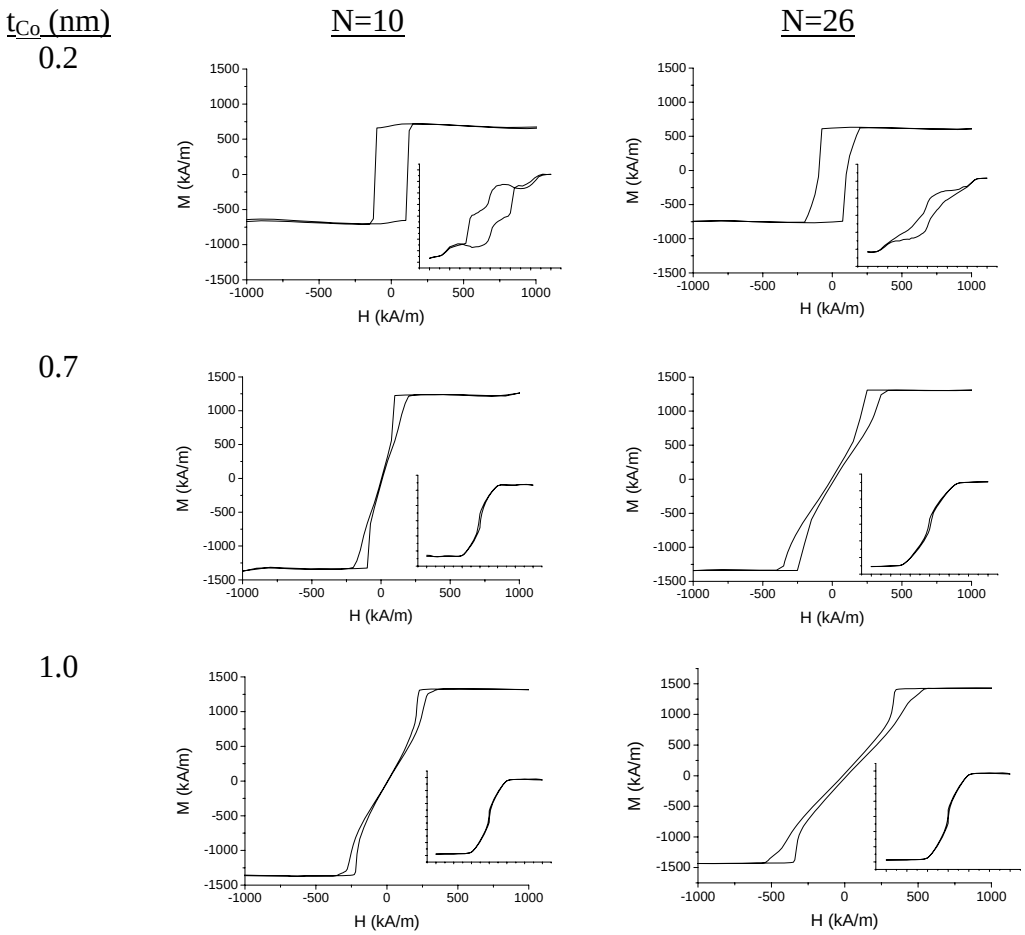

Fig. IV-15: VSM out-of-plane hysteresis loops of Co/Pt multilayers in different configurations, varying the number of bilayers and the thicknesses of Co layers. The insets in each loop are the corresponding in-plane hysteresis loop.

According to the hysteresis loops in fig. IV-15, the squaremost shapes correspond to samples with thinner Co layers. Furthermore, as the number of bilayers increases, the out-of-plane hysteresis loop loses its resemblance with conventional easy axis loops. This trend is also corroborated by VSM measurements on samples with less number of bilayers, yielding these samples a weaker and noisier signal.

The squareness of the out-of-plane hysteresis loop is a very important feature since, once patterned the samples, it will determine the switching field distribution

(SFD) and, therefore, quality of the final patterned sample as a magnetic storage media.

Despite the close-to-zero (or even zero) remanence shown in some of the out-of-plane hysteresis loops of fig. IV-15, the samples still exhibit perpendicular magnetization as it can be seen in the MFM images of fig. IV-16. In all the presented cases except in the configuration (1.0 nm Co/0.7 nm Pt)x26, the black and white domains are clearly defined. In the particular case of the multilayer (1.0 nm Co/0.7 nm Pt)x26, grey zones between the domains appear, thus indicating the presence of a in-plane magnetization component comparable to the out-of-plane one.

The previously mentioned change in the magnetic properties, shown in fig. IV-15, is somewhat visible in the domain size (characterized calculating the average domain period P) of each sample according to MFM images of fig. IV-16.

From the MFM images of fig. IV-16 it can be concluded that the larger the relative thickness of the Co layer, the smaller the domain size. On the other hand, the relationship between the number of bilayers and the domain period is given by the equation:

$$\lambda_c = \frac{l_c}{D} = \left(\frac{p^2}{\pi^3}\right)\sum_{j=1}^{\infty}\frac{1}{n^3}\left(1-\left(1+\frac{2\pi j}{p}\right)e^{-2\pi j/p}\right)\sin^2\left(\frac{\pi}{2}j(1+m)\right) \qquad \text{(IV-2)}$$

where p=P/D, being D the total thickness; $m=\frac{W_1 - W_2}{W_1 + W_2}$ (W_i represent the domain widths) is the reduced magnetization and $l_c=\frac{\gamma_W}{2K_d}$ (γ_w is the specific wall energy and K_d is the stray field energy density) is the characteristic length.

Deeper analyses on the relationship shown in eq. (IV-2) are beyond the scope of this thesis and will not be performed. More details about eq. (IV-2) and its limits of applicability can be obtained in [IV.16].

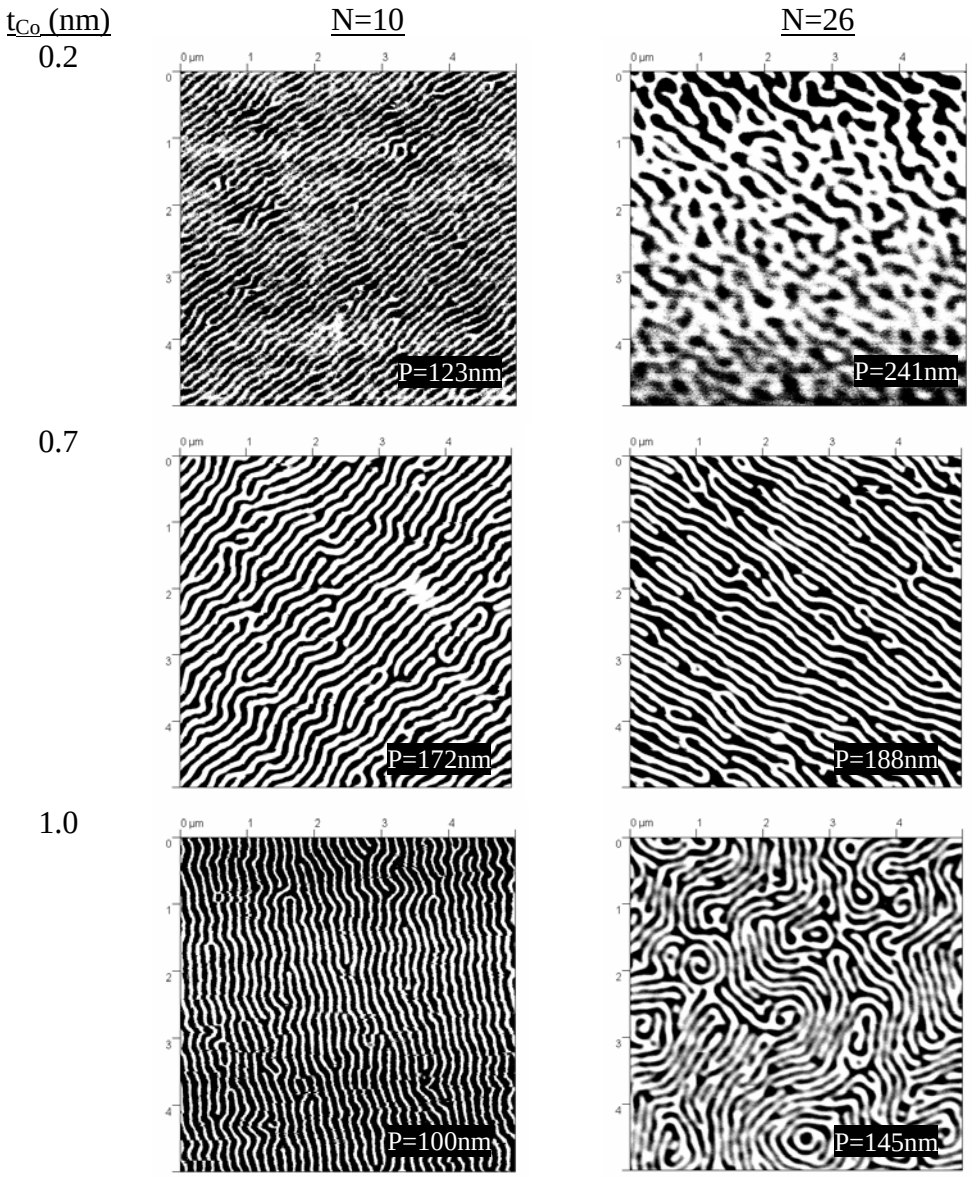

Fig. IV-16: MFM images of Co/Pt multilayers in different configurations, varying the number of bilayers and the thicknesses of Co layers. The parameter P in each image represents the average period of the out-of-plane domains present in the samples.

8.2.MOKE and DMOKE signals of the patterned sample

Amongst the different possible multilayer configurations for the patterned samples, the selected one is (1.0 nm Co/1.0 nm Pt)x26 grown on a Si wafer with a 4 nm Pt underlayer over a SiO_2 coating (used for avoiding the Pt diffusion into the Si). This configuration is chosen in order to provide, once patterned, a lower switching field distribution (SFD) with a large anisotropy making the resulting patterned sample a candidate for a patterning recording media (see reference [IV.19]).

This configuration for the continuous film can be characterized by the hysteresis loops (measured by a commercial VSM, see chapter I) corresponding to its easy and hard axis (fig. IV-17).

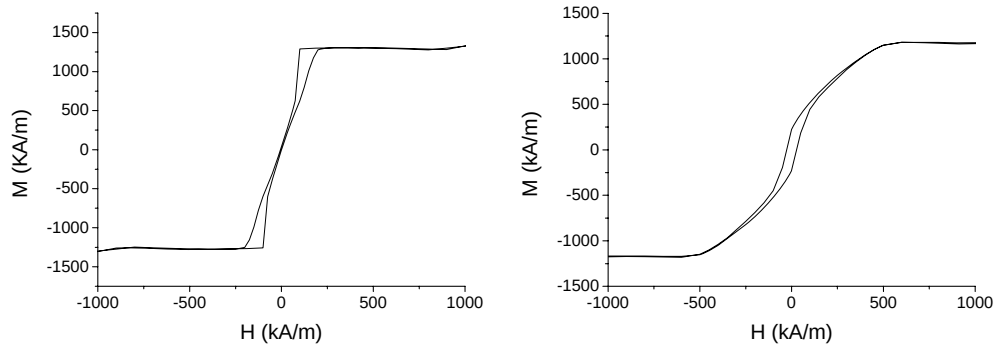

Fig. IV-17: VSM loops of the easy (perpendicular direction, left plot) and hard (in-plane direction, right plot) magnetization directions for a 26 bilayer 1.0 nmCo/1.0 nm Pt continuous film.

The patterning of the Co/Pt multilayer is performed in the LIL setup of the MESA$^+$ Institute, described before in chapter I, followed by an ion beam etching. The final patterned samples consists of 300 nm diameter circular dots embedded in a 600 nm period array (fig. IV-18, top left corner).

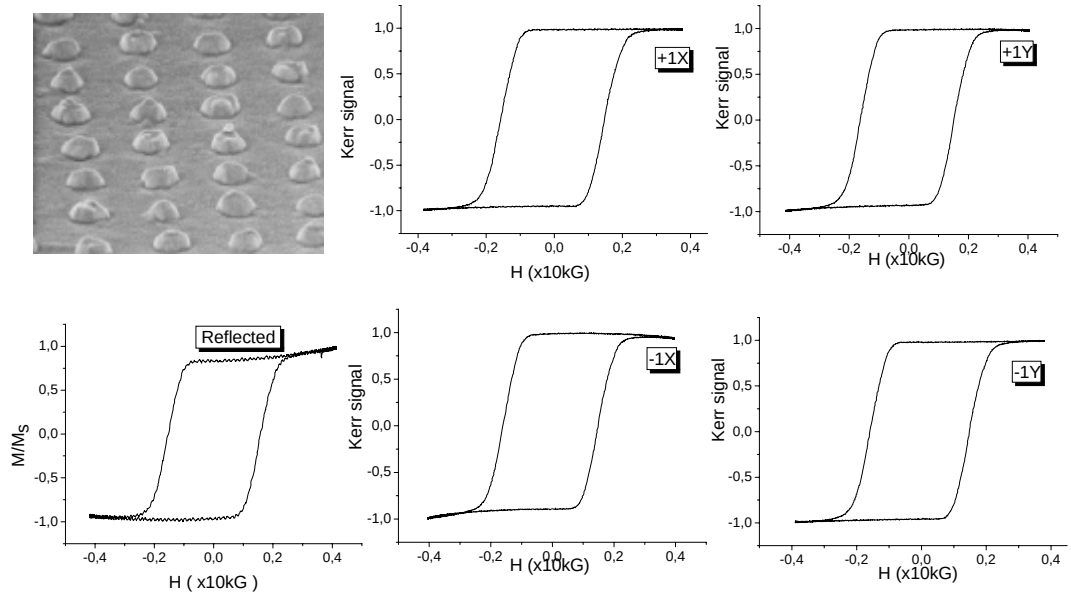

Fig. IV-18: First row, left: A SEM picture of the patterns fabricated by LIL in the MESA$^+$ Institute. Second row, left: Polar MOKE hysteresis loop corresponding to the direct reflected beam. Central column: Diffracted loops +1X and -1X in polar DMOKE. Right column: Diffracted loops +1Y and -1Y in polar DMOKE. See fig. II-8 for details about the setup and geometry.

The hysteresis loops of this patterned sample are characterized using the alternative polar Kerr setup at IMM described in chapter III, fig.III-2. For each first diffracted two loops are measured (fig. IV-18).

8.3.DMOKE and reversal mechanisms

In the polar case, like in the transverse case seen in sections 6 and 7, analogous simple models for the magnetization reversal can be designed accounting for the most probable reversals that might take place and according to the shape of the magnetic elements (fig. IV-19). Again, in order to compare with experimental data, the different reversals are graphically characterized as a function of the DMOKE signal vs. the magnetization.

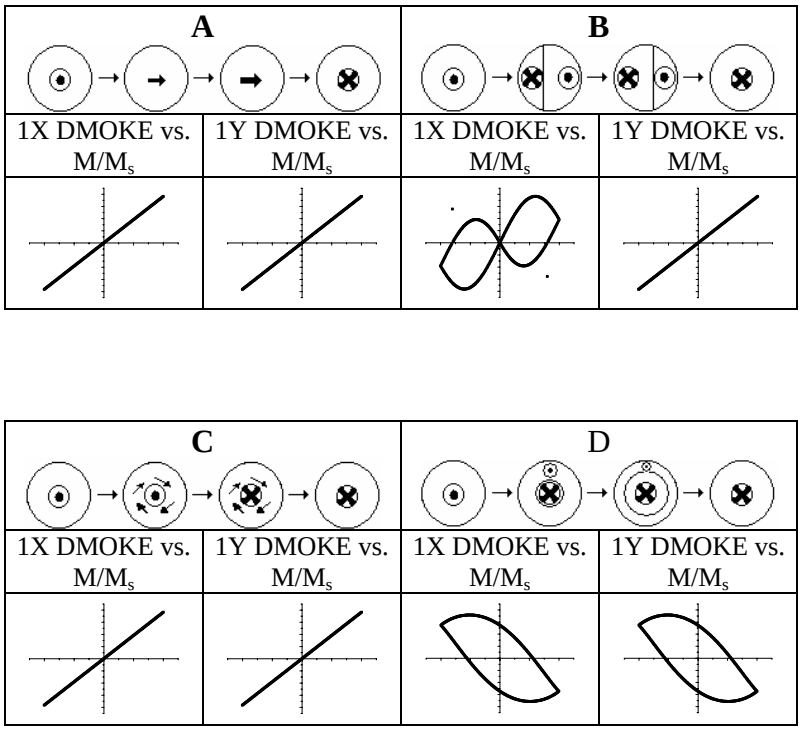

Fig.IV-19: Examples of diffracted signal 1X and 1Y vs. magnetization for different inversion processes: A) Coherent rotation of the magnetization. B) Bloch wall displacement along the X axis. C) Curling reversal; accounts also for fanning reversal. D) Nucleation and propagation of a circular domain wall.

The plots in fig. IV-19 can be compared with experimental data. In this case, the DMOKE loops are very similar to signal in the direct (reflected) beam, pointing at first sight to one of the rotation methods, either coherent rotation, curling or fanning.

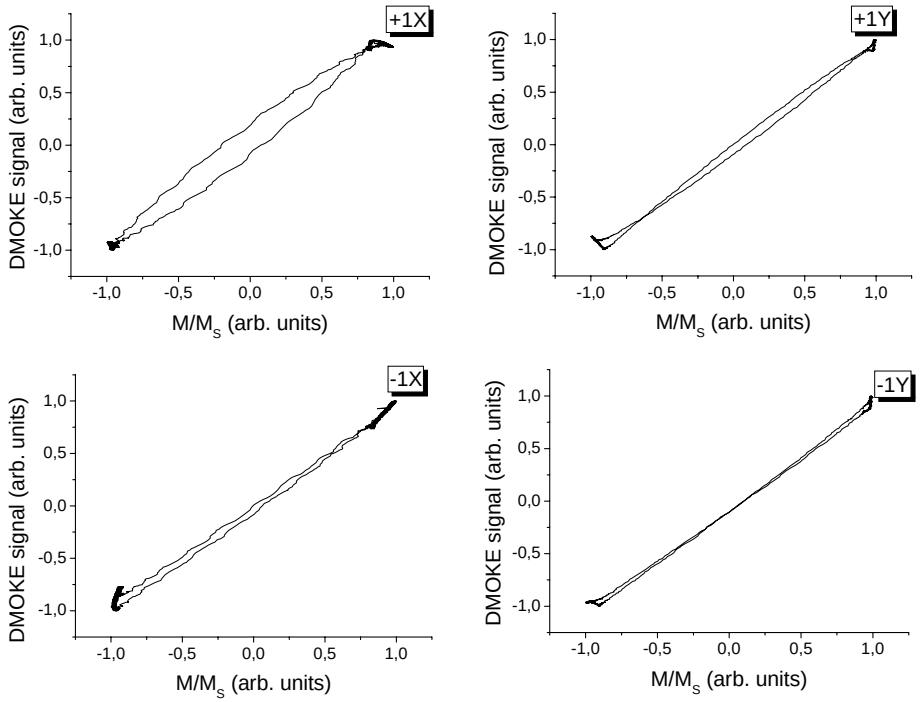

Fig.IV-20: From left to right and from top to bottom, diffracted signal +1X, +1Y, -1X and -1Y vs magnetization corresponding to the hysteresis loops shown in fig. IV-17.

Comparing both the experimental data (fig. IV-20) and reversal simulations (fig. IV-19), a rotation reversal is the most suited reversal mechanism present in the structures. Unfortunately, under the conditions of the polar geometry no difference can be extracted in this simple model between coherent rotation, curling and fanning.

In fig. IV-21, the hysteresis loop for the patterned sample is shown together with some experimental points corresponding to the estimation of the magnetization in the patterned sample. This estimation is obtained subtracting the ratio of dots with downwards magnetization from the ratio of dots with upwards magnetization, once assumed saturation magnetization in each dot.

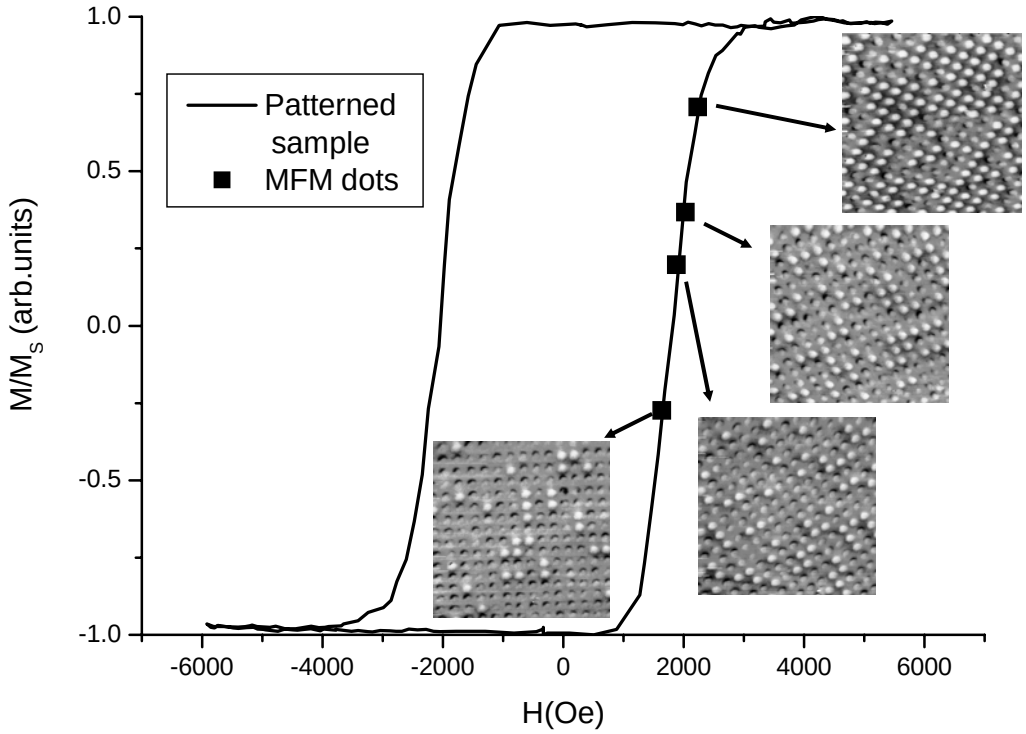

Fig.IV-21: Hysteresis loop of the patterned sample and estimated magnetization assuming a saturation magnetization for the dots (either up or down).

According to fig. IV-21, the statistic performed under the assumption of saturation magnetization in each dot is in agreement with the information about the average magnetization given by the hysteresis loop. Thus, it can be concluded that the slope in the hysteresis loop is mainly due to the SFD of the dots instead of a domain propagation, i.e., rotation of the magnetization is the most suited reversal mechanism present in the patterned sample.

9.Summary and conclusions:

Chapter III left an open question, mandatory to answer in order to properly understand DMOKE. When developing the phenomenological theory of DMOKE it was assumed certain conditions for the diffracted spots that might not be correct. For example, in the transverse configuration, the *m*Y diffracted spots does not strictly hold the transverse geometry, because the "plane of incidence" changes in these particular cases. In addition, we are interested on the relationship between magneto-optics and interactions between the elements of an array.

In order to answer these questions, a set of patterned samples composed of Co microsquare -2 μm edge, 40 nm thickness- embedded in arrays has been investigated. The structures are identical but the separation between elements, set in the range of the element size, according to previous results. In particular, the selected interelement distances have been 0.2, 0.5, 1.0 and 2.0 microns, all of them close to the magnetic interaction threshold.

Once magneto-optical characterized the patterns, it is concluded that there is no significant effect on the MOKE signals of the direction of the Co anisotropy axis with respect to the applied field direction, i.e., the magnetization processes are mainly dictated by the shape of the element and perhaps by the interaction between them, i.e., the magnetostatics.

Then the magneto optical response is measured both at reflected and diffracted beams, and compared with the results of a model that uses micromagnetic simulations and optical diffraction theory to calculate the magneto optical response for different diffracted spots. A satisfactory agreement between the experiments and the predictions from the combined micro-magnetic/optical diffraction model allows the interpretation of the experimental data and provides a way to analyze and understand the physical meaning of the magneto-optic diffracted signal. Thus, the DMOKE provide information about the magnetization dynamics, where the different orders of diffraction represent the moments of the magnetization. In this case, only the 1^{st} order diffraction spots are considered as an illustration.

The anomalous loops observed in the DMOKE are not related in a clear manner to the onset of the interactions, but to the different matching of the moment of the magnetization distributions to the periodicity of the array. The comparison of this diffracted magneto optical experimental data with predictions from simple reversal models allows (under certain conditions detailed in chapter II) the

characterization of different element magnetization reversal mechanisms as the separation between elements in the array varies. This experiment has been performed for both in-plane magnetization (in transverse Kerr configuration) and for out-of-plane magnetization (in polar Kerr geometry). In the out-of-plane magnetization case, the magnetic properties of the sample has been also analyzed as a function of the configuration of the used multilayer.

Finally, using the fact that the direct (reflected) hysteresis loops are more tilted as the interelement distance increases, it has been deduced that the interaction distance between the magnetic -2μm edged- elements is around 1μm. This experimental result can be theoretically corroborated studying the magnetostatic interactions within the array. A thorough investigation in the subject is performed in chapter IV.

Thus, it can be concluded that the theory developed in chapter III is in agreement with experiments, that MOKE signal may serve to experimentally found the onset of the interaction between elements in an array and that DMOKE can be used to both monitor the interelement distance and as a quality control method for patterned samples.

10.References:

[IV.1] P. García-Mochales, J.L. Costa-Krämer, G. Armelles, F. Briones, D. Jaque, J.I. Martín and J.L. Vicent . *Appl. Phys. Lett.*, **81**, 3206 (2002)

[IV.2] D. Jaque, J.I. Martín, G. Armelles, J.L. Costa-Krämer., F. Briones and J.L. Vicent. *J. Appl. Phys*. **91**, 382 (2002)

[IV.3] P. Vavassori, M Grimsditch, V. Novosad, V. Metlushko amd B. Ilic. *Phys. Rev. B* **67** N(2003)

[IV.4] I. Guedes, M. Grimsditch, V. Metlushko, P. Vavassori, R. Camley, B. Ilic, P. Neuzil and R. Kumar. *Phys. Rev. B* **67**, 024428 (2003)

[IV.5] T. Schmitte, T. Schemberg, K. Westerholt, H. Zabel. *J. Appl. Phys*. **87**, 5630 (2000)

[IV.6] Y. Souche, O.Goeffroy, V. Novosad, V. Pishko, B. Pannetier. *J. of the Magn. Society of Japan* **20-Sup S1**, 393 (1996)

[IV.7]T. Schmitte, K. Westerholt, H. Zabel. *J. Appl. Phys*. **92**, 4524 (2002).

[IV.8] M. Grimsditch. P. Vavassori, V. Novosad, V. Metlushko, H. Shima, Y. Otani, and K. Fukamichi. *Phys. Rev. B* **65**, 172419 (2002)

[IV.9] O. Geoffroy, D. Givord, Y. Otani, B. Pannetier, A.D. Santos, M. Schlenker, Y. Souche. *J. Magn Magn Mater.* **121**, 516 (1993).

[IV.10] P. Vavassori, V. Metlushko, M. Grimsditch, B. Ilic, P. Neuzil, R. Kumar. *Phys. Rev. B* **61**, 5895 (2000).

[IV.11] I. Guedes, N.J. Zaluzec, M. Grimsditch, V. Metlushko, P. Vavassori, B. Ilic, P. Neuzil, R. Kumar. *Phys. Rev. B* **62**, 11719 (2000).

[IV.12] I. Guedes, M. Grimsditch, V. Metlushko, P. Vavassori, R. Camley, B. Ilic, P. Neuzil and R. Kumar. *Phys. Rev. B* **66**, 014434 (2002)

[IV.13] P. Vavassori, V. Metlushko, R. M. Osgood III, M. Grimsditch, U. Welp, G. Crabtree. *Phys. Rev. B* **59,** 6337 (1999)

[IV.14] J.L.Costa-Krämer, J.I.Martín, J.L. Menéndez, A.Cebollada, J.V.Anguita, F. Briones and J.L.Vicent. *Appl. Phys. Lett*. **76**, 3091 (2000)

[IV.15] M Grimsditch and P. Vavassori, J. Phys.: Condens. Matter 16 (2004) R275-R294.

[IV.16] J. M. García, A. Thiaville, J. Miltat, K.J. Kirk, J.N. Chapman, F. Alouges, Appl. Phys. Lett. **79**, 656 (2001)

[IV.17] Z. Q. Qiu, S.D. Bader, Rev. Sci. Instrum. **71**, 1243 (2000)

[IV.18] A. Hubert, R. Schäfer. Magnetic Domains, chapter 2. Springer-Verlag Berlin Heidelberg (1998)

[IV.19] R. Murillo, Ph.D. thesis, Universiteit Twente, Enschede (2006)

CHAPTER V:

MAGNETOSTATICS AND INTERACTIONS BETWEEN ELEMENTS IN ORDERED ARRAYS

Index

MAGNETOSTATICS AND INTERACTIONS BETWEEN ELEMENTS IN ORDERED ARRAYS

1.Introduction:

Magnetic storage and memory devices demand an improved understanding of the combined effect of reducing magnetic element sizes and stacking them into arrays. In fact, magnetic elements in arrays that serve for memory or storage should be placed at a distance that avoids cross talking due to interactions between them. In addition, a properly tailored shape anisotropy can be used for magnetic logical devices, propagating binary information through networks of interacting submicrometer magnetic dots [V.1]. Therefore, understanding and designing magnetic interactions between elements at the nanoscopic scale is then a relevant technological challenge. It is well known that when reducing the size of array elements and inter element separations to the nanoscale, magnetostatic interactions become important. On the other hand, the study of ordered arrays of magnetic elements by micromagnetic simulations has an important drawback, the evaluation of the magnetostatic energy. This problem arises from the fact that magnetostatic interactions are long range interactions. This implies that all elements in the pattern will magnetostatically interact to each other. Thus, these interaction is very costly to model by micromagnetic simulations in ordered arrays, that are also very vulnerable to artifacts due to cell or boundary conditions selection. Then, to preserve the accuracy of a micromagnetic simulation of a magnetic element embedded in an array it is necessary to extend the study of conventional single element magnetostatics, adding the effect of stacking nanoelements into close proximity in arrays and the consequent interaction effects. Therefore it is convenient to determine the number of magnetic elements to be considered in the simulation. It also might be useful to know the distance corresponding to the onset of the magnetostatic interaction between magnetic elements.
An approach is presented here capable of efficiently and accurately solve these problems, that analyzes the shape anisotropy due to both element and array shapes. The proposed method considers an analytical expression valid for short inter-element separations and not very costly to evaluate by computational means.

The study of magnetostatics has evolved from the calculation of shape anisotropies and demagnetizing fields for isolated elements of different shapes

[V.2] to the recent studies of the magnetostatic energy behavior for arrays of rectangular elements with magnetization pointing to a given in-plane direction along one of the element's edges [V.3, V.4].
Advances in micro and nanotechnology have allowed the possibility of experimentally investigate the magnetostatic behavior of arrays of nanoelements. Recent works analyze the magnetostatic energy and demagnetizing fields in arrays of micro [V.5] and nano [V.6, V.7] magnetic elements, also taking into account different element shapes [V.8]. Our aim is to study in detail and quantitatively shape anisotropy in thin film nanostructured arrays of magnetic elements, taking into account not only the shape of the elements but also that of the array.

2.Assumptions:

An exact analytical model for arrays of orthorhombic magnetic elements in the nanoscale is presented. Instead of iteratively solving the Landau-Lifshitz-Gilbert equation, the problem might be solved analytically using the following three assumptions:

i. The magnetization is homogeneous within the element.
ii. The magnetization is in plane.
iii. The magnetization points in the same direction in all the elements.

The smaller the element dimensions, the better the first assumption. The second assumption holds generally for thin films, i.e., if the thickness is smaller than the element size and if the material does not have a large perpendicular anisotropy. Anyway, it will be seen that similar formulas to the in-plane magnetization case can be obtained for the case of out-of-plane magnetization. Finally, the third assumption might be reasonable depending on the magnitude of the interaction and on the shape of the array.

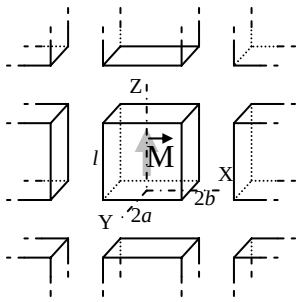

Fig.V-1: Array of orthorhombic (l×2a×2b) magnetic elements. Magnetization lies in the XZ plane. All elements have homogeneous magnetization and it points to the same direction in all the elements of the array.

3.An expression for the magnetostatic energy

In order to study quantitatively shape anisotropy in arrays of orthorhombic magnetic elements, an expression for the magnetostatic energy is needed for free magnetic poles surfaces. The expression used is based on Craik's formula [V.9], since under the first two assumptions of the model summing magnetic dipoles over a volume is equivalent to sum magnetic free poles on the edges of the corresponding volume, i.e., the magnetic potential corresponding to an orthorhombic magnetic element can be expressed as a sum of magnetic surface potentials. According to [V.9] and the notation in Fig. V-1, the magnetic potential for a free poles surface can be expressed as,

$$\phi(x,y,z)=\frac{\sigma}{4\pi\mu_0}\iint_{S'}\frac{1}{\sqrt{(x-x')^2+(y-y')^2+(z-z')^2}}dx'dy' \qquad \text{(V-1)}$$

Assuming without loss of generality that $z'=0$ and integrating on y'.

$$\phi(x,y,z)=\frac{\sigma}{4\pi\mu_0}\int_{-a}^{a}\left(ArcSinh\left(\frac{y+b}{\sqrt{(x-x')^2+z^2}}\right)-ArcSinh\left(\frac{y-b}{\sqrt{(x-x')^2+z^2}}\right)\right)dx' \qquad \text{(V-2)}$$

$$\phi(x,y,z)=\frac{\sigma}{4\pi\mu_0}\left(Q(y+b,x+a,z)-Q(y-b,x+a,z)-Q(y+b,x-a,z)+Q(y-b,x-a,z)\right) \qquad \text{(V-3)}$$

where $\mu_0=4\pi\cdot10^{-7}$ H/m is the vacuum magnetic permeability, $\sigma=\mathbf{M}\cdot\mathbf{n}$ the magnetic free pole density, being **M** the magnetization and **n** an unitary normal vector to the surface and

$$Q(p,t,z)=p\cdot ArcSinh\left(\frac{t}{\sqrt{p^2+z^2}}\right)+t\cdot ArcSinh\left(\frac{p}{\sqrt{t^2+z^2}}\right)-z\cdot ArcTan\left(\frac{pt}{z\sqrt{p^2+t^2+z^2}}\right) \qquad \text{(V-4)}$$

As both arcsinh(x) and arctan(x) are odd functions, some symmetry properties hold:

S1. $\phi(-x,y,z)=\phi(x,y,z)$
S2. $\phi(x,-y,z)=\phi(x,y,z)$
S3. $\phi(x,y,-z)=\phi(x,y,z)$
S4. $\phi(y,x,z)=\phi(x,y,z)$

Applying these symmetry properties in an array like the one shown in Fig. 1 under the assumptions i., ii. and iii., an expression for the magnetostatic energy per unit volume can be obtained:

$$U=\frac{\sigma}{4abl}\sum_{n=1}^{k}\sum_{m=n-1}^{n+1}(-1)^{n+m}\left(2-|n-m|\right)\cdot\sum_{i=-k}^{k}\int_{-b}^{b}\int_{id+(2i-1)a}^{id+(2i+1)a}\phi\left(x,y,z=nd+ml\right)dxdy+$$
$$+\frac{\sigma}{4abl}\sum_{i=-k}^{k}\int_{-b}^{b}\int_{id+(2i-1)a}^{id+(2i+1)a}\phi\left(x,y,z=0\right)dxdy-\frac{\sigma}{4abl}\sum_{i=-k}^{k}\int_{-b}^{b}\int_{id+(2i-1)a}^{id+(2i+1)a}\phi\left(x,y,z=l\right)dxdy \quad \text{(V-5)}$$

Where the summations are performed adding the contributions to the magnetostatic energy due to the *k* nearest neighbors of the considered magnetic element. Note that for $k=\infty$, the calculations corresponds to an infinite array, see for instance [V.9].

Before deeply analyzing the consequences of eq. (V-5), it should be corroborated that it agrees completely with well known basic results regarding magnetostatics and shape anisotropy. In particular, eq. (V-5) must be in agreement with qualitative studies about the magnetostatic energy in isolated magnetic elements [V.3] and arrays [V.10], [V.11].

4.Some simple verifications:

In what follows it will be shown that applying formula (V-5) agrees with some simple cases, well known results are obtained.

4.1.-Under assumption i. is the same sum dipoles in V than sum free poles in S.

The magnetization is related to the pole density by $\nabla\cdot\mathbf{M}=-\rho$ and the magnetic potential is related to the magnetic field by $\nabla\Phi=-\mathbf{H}$. Taking this two equalities into account, it follows:

$$\frac{1}{2}\int_V \nabla\cdot(\mathbf{M}\Phi)dV = \frac{1}{2}\int_V \nabla\cdot\mathbf{M}\Phi dV + \frac{1}{2}\int_V \mathbf{M}\cdot\nabla\Phi dV = -\frac{1}{2}\int_V \rho\Phi dV - \frac{1}{2}\int_V \mathbf{M}\cdot\mathbf{H}dV \tag{V-6}$$

Moreover, applying the Gauss theorem it follows:

$$\frac{1}{2}\int_V \nabla\cdot(\mathbf{M}\Phi)dV = \frac{1}{2}\int_S \mathbf{M}\Phi d\mathbf{S} = \frac{1}{2}\int_S \mathbf{M}\cdot\mathbf{n}\Phi dS = \frac{1}{2}\int_S \sigma\Phi dS \tag{V-7}$$

Combining equations (V-6) and (V-7), the magnetostatic energy might be expressed as:

$$\mathrm{U} = -\frac{1}{2}\int_V \mathbf{M}\cdot\mathbf{H}dV = \frac{1}{2}\int_S \sigma\Phi dS + \frac{1}{2}\int_V \rho\Phi dV \tag{V-8}$$

This way, the magnetostatic energy is originated by field sources due to volume and surface pole densities. Applying assumption i. of the model i.e. homogeneous magnetization, ρ=0. Therefore our analytical model is equivalent to the one described in [V.3].

4.2.-The magnetostatic energy at *d*=0 (continuum) is zero

For square arrays of square elements, if *d*=0, eq. (V-5) can be rewritten as follows:

$$\begin{aligned}\mathrm{U} &= \frac{\sigma}{4abl}\sum_{n=1}^{\infty}\sum_{m=n-1}^{n+1}(-1)^{n+m}\left(2-|n-m|\right)\cdot\int_{-b}^{b}\int_{-\infty}^{\infty}\phi\left(\mathrm{x,y,z}=ml\right)\mathrm{dxdy} + \\ &+ \frac{\sigma}{4abl}\int_{-b}^{b}\int_{-\infty}^{\infty}\phi\left(\mathrm{x,y,z}=0\right)\mathrm{dxdy} - \frac{\sigma}{4abl}\int_{-b}^{b}\int_{-\infty}^{\infty}\phi\left(\mathrm{x,y,z}=l\right)\mathrm{dxdy} = \\ &= \frac{\sigma}{4abl}\int_{-b}^{b}\int_{-\infty}^{\infty}\left(\sum_{\mathrm{n}=1}^{\infty}(-1)^{n+m}\left(2-|n-m|\right)\phi\left(\mathrm{x,y},ml\right)+\phi\left(\mathrm{x,y},0\right)-\phi\left(\mathrm{x,y},l\right)\right)\mathrm{dxdy}\end{aligned} \tag{V-9}$$

.

If we re-write the integrand of eq. (V-9)

$$-\sum_{n=1}^{\infty}\phi\left(x,y,(n-1)l\right)+2\sum_{n=1}^{\infty}\phi\left(x,y,nl\right)-\sum_{n=1}^{\infty}\phi\left(x,y,(n+1)l\right)+\phi\left(x,y,0\right)-\phi\left(x,y,l\right)=$$

$$=-\sum_{n=0}^{\infty}\phi\left(x,y,nl\right)+2\sum_{n=1}^{\infty}\phi\left(x,y,nl\right)-\sum_{n=2}^{\infty}\phi\left(x,y,nl\right)+\phi\left(x,y,0\right)-\phi\left(x,y,l\right)=0 \qquad \text{(V-10)}$$

Thus, if the interelement separation of the square array is zero, the corresponding magnetostatic energy is zero.

4.3.-Square shapes do not produce shape anisotropy

From the symmetry properties of $\phi(x,y,z)$ (**S1, S2** & **S3**) it follows that for an isolated single-domain element there is no magnetostatic contribution due to the magnetic potential generated by one pole surface when evaluated at its two neighbor perpendicular surfaces. This implies, for an isolated element (k=0 in eq. V-3), that the magnetic potential generated by a pole surface should be only evaluated at its opposite surface. Therefore, if magnetization points to an arbitrary direction within the XZ plane at an angle θ with the X axis, the obtained formula for the magnetostatic energy for a single element is (using the notation in fig. V-1):

$$U_\theta=\frac{M\cos^2\theta}{4abl}\int_{-a}^{a}\int_{-b}^{b}\left[\phi(x,y,z=0)-\phi(x,y,z=l)\right]dydx +$$

$$+\frac{M\sin^2\theta}{4abl}\int_{-l/2}^{l/2}\int_{-b}^{b}\left[\phi(x,y,z=0)-\phi(x,y,z=2a)\right]dydx \qquad \text{(V-11)}$$

where the first summand is the contribution to the magnetostatic energy due to surfaces parallel to plane XY and the second one is the contribution to the magnetostatic energy due to surfaces parallel to plane YZ. As the considered element shape is a square, l=2a, according to the previous formula, the magnetostatic energy provided by a magnetic square element under the previously mentioned conditions, does not depend on the angle between the magnetization and the edge of the square, i.e., there are no preferential directions for the magnetization within an isolated square element. The shape anisotropy in this case ($K_S=U_{\theta=0}-U_{\theta=90}$) is then zero.

Using the same argument it can easily be proved that if the magnetization points to an arbitrary direction within the space, the corresponding shape anisotropy is zero.

Independently of the number of nearest-neighbors considered, due to the symmetry properties of the $\phi(x,y,z)$ function and assumption iii of the model, it is trivial to prove that the magnetostatic energy contribution of two pole surfaces perpendicular and equidistant to a pole surface providing the magnetic potential is zero, i.e., if $U_{\theta=90}$ is the magnetostatic energy when the magnetization points along the Z axis, $U_{\theta=0}$ is the magnetostatic energy when the magnetization points along the X axis, and θ is the angle between the magnetization and the Z axis, the magnetostatic energy for a magnetization pointing to an arbitrary direction θ is $U_\theta=U_{\theta=90}\cos^2\theta+U_{\theta=0}\sin^2\theta$.
When considering a square array of square elements, where $l=2a$ and the interelement distances in X and Y directions, d_X and d_Y, hold $d_X=d_Y=d$, the value of the magnetostatic energy, when having an arbitrary angle θ between the magnetization and the X axis, is independent of θ because $U_{\theta=90}=U_{\theta=0}$. This demonstrates that there is no shape anisotropy in square arrays of square elements.

4.4.-Rectangular elements produce shape anisotropy

From eq. (V-5) and the symmetry properties of the magnetic potential can easily be seen that the magnetostatic energy per unit volume at $\theta=0$ ($U_{\theta=0}$) is different from $U_{\theta=90}$. This way a shape anisotropy exists.

5.Magnetostatic energy vs. nearest neighbors:

In order to quantitatively study the magnetostatic energy and shape anisotropy in rectangular shapes (in arrays or in elements) some calculations using formula (V-5) must be performed. As previously seen equation (V-5) may be extended to an infinite array, so an approximation to *k* neighbors is needed to perform the calculations. The chosen number *k* of neighbors should provide good accuracy and not very large computing time. It can be demonstrated (see Appendix B) that the error due to consider *k*-nearest neighbors strongly depends on the interelement separation, being specially large for small interelement distances and small number of neighbors *k*. For instance, for an interelement separation d=1nm, the minimum number of neighbors *k* needed to obtain an error below 1% is k=20.

With a slight modification eq. (V-5) provides the magnetostatic energy for a magnetic element situated in a corner of a finite array. The calculations performed for a square array (d=1nm) of square elements (l=100nm) show that the difference

between the magnetostatic energy per unit volume for a square magnetic element in the corner of a finite square array, and that for a magnetic element in the center of the same array is below 4% for k=20. This difference rapidly decreases as the distance between elements in the array increases, as expected. Accordingly, all arrays up to 41×41 (d=1nm & l=100nm) elements might be considered as infinite arrays from the magnetostatic energy point of view. For d=5 nm & l=100 nm elements, 15×15 is enough.

In what follows, a value of k=20 is used (see Appendix B) since it provides the value of the magnetostatic energy per unit volume for an infinite array within an error margin of a few percent. In addition, the calculations are performed considering element sizes and ranges technologically relevant: around 100 nm lateral size and 5 nm thickness. Obviously the shape anisotropy is calculated as the difference in magnetostatic energy per unit volume when the magnetization points along the two relevant directions (X and Z axes).

6.Element and array shape anisotropy:

It is well known that there is no magnetostatic or shape anisotropy for square shaped elements or arrays (see [V.10, V.11]). Let us now consider square elements in a rectangular array, i.e. the interelement distance in the X direction (d_X) differs from the interelement separation in the Z direction (d_Z). In these cases, a uniaxial shape anisotropy appears in the direction of the short interelement distance, i.e., rectangular shaped arrays provide a preferential magnetization direction due to magnetostatic interactions.

The shape anisotropy due to the array shape will be termed *array shape anisotropy* and the shape anisotropy due to the individual element shape termed *element shape anisotropy*.

For the particular case of a rectangular array d_X= 1nm, d_Z=100 nm of square 100 nm edged & 5 nm thick elements (l=100 nm, b=0.025·l=5 nm, 2a=l), the difference between the magnetostatic energies in the two perpendicular directions is of the order of $K_s=0.35\ M^2/(4\pi\mu_0)$ (see fig. V-2a), which is about $0.73\cdot10^5$ J/m^3 using the saturation magnetization valued of Co at Room Temperature. This value is, for comparison purposes, of the same order of magnitude than the value of the Fe magneto crystalline K_1 anisotropy constant ($K_1 = 0.48\ 10^5$ J/m^3 , [V.12]). Therefore, suitably choosing the interelement distances large shape anisotropies might appear.

Array shape anisotropy magnitudes depend not only in the ratio d_Z/d_X between the interelement separation in the Z axis (d_Z) and the interelement distance in the X axis (d_X) (**fig. V-2a**) but also on the interelement distance values (**fig. V-2b**): increasing the interelement distances ratio (d_Z/d_X) increase the shape anisotropy value at constant d_X=1 nm (**fig. V-2a**). On the other hand, at fixed interelement separation ratio (d_Z/d_X), increasing the values of the interelement distances (d_Z and d_X) decreases the shape anisotropy (**fig. V-2b**).

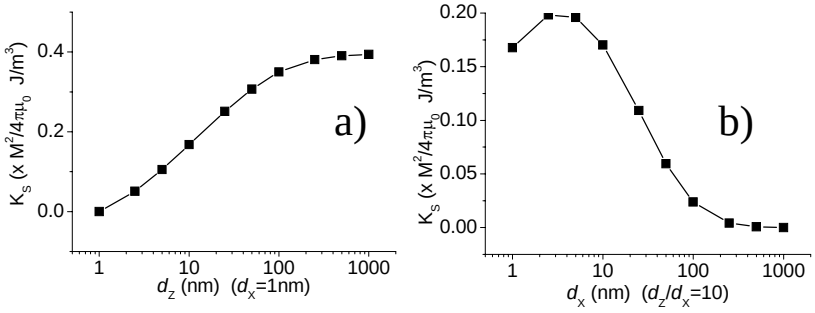

Fig. V-2: a) Shape anisotropy values vs. d_Z at constant interelement distance in X axis (d_x=1 nm). **b)** Shape anisotropy values vs. d_X at constant. interelement distance ratio (d_z/d_x=10)

This double dependency of the array shape anisotropy provides the largest values for large interelement separation ratios, with lower separation values, as intuitively expected from an interaction. Summarizing, the closest the shortest distance between elements, and the largest aspect ratio of the lattice, produces the largest array shape anisotropy.

7.Interaction distance:

In Fig. V-3 the magnetostatic energy per unit volume in rectangular arrays (d_X=1 nm) of square 100 nm edged elements when the magnetization points along the X and Z directions is compared with the values of magnetostatic energy per unit volume in square arrays with the same interelement separation.

The change in array shape anisotropy is due to the change of magnetostatic energy per unit volume in the direction on largest interelement distance (fig. V-3).

7.1.Magnetostatic energy vs. array shape

Note that in the particular case of the rectangular array of square elements with the magnetization pointing to the direction of the shortest interelement distance, the rectangular lattice of squares behaves almost as the corresponding limiting case (lines with magnetization along the long direction -zero magnetostatic energy-) regardless of the element separation in the perpendicular direction.

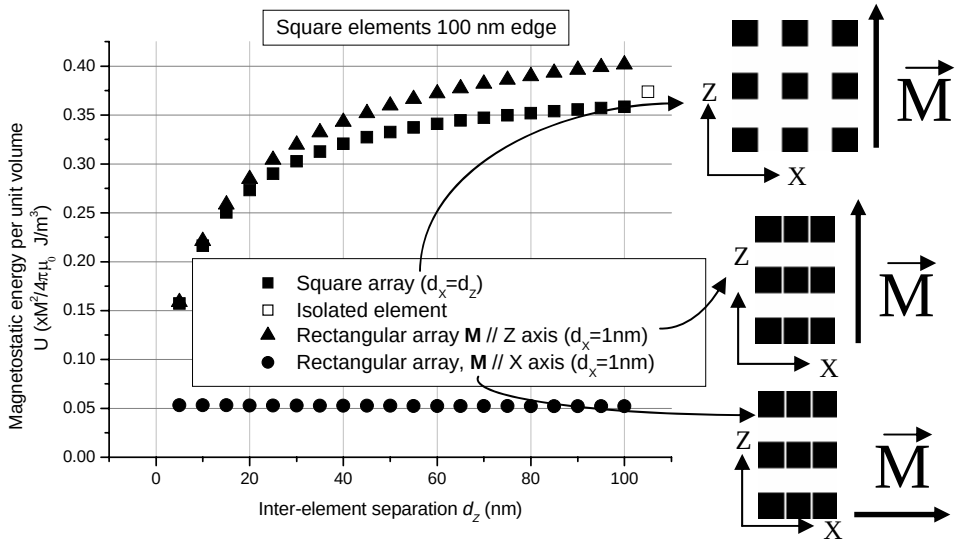

Fig. V-3: Magnetostatic energy per unit volume vs. interelement separation for i) square arrays of square elements (100 nm edge), ii) rectangular arrays of square 100 nm edged elements with horizontal interelement separation fixed to 1 nm and magnetization in the Z direction, and iii) rectangular arrays of square 100 nm edge elements with horizontal interelement separation fixed to 1 nm and magnetization in the X axis. The hollow square represents the value of the magnetostatic energy for an isolated square element (100 nm edge).

Fig. V-3 also shows that when increasing the interelement separation in square arrays, the magnetostatic energy per unit volume tends to the value of an isolated element, as expected. In addition, when the elements are placed closer, the magnetostatic energy per unit volume approaches zero (the value corresponding to the continuum). Moreover, when considering square arrays of rectangular elements the same limiting cases are obtained (fig. V-4 and [V.3]). Accordingly, it can be established a criterion in which the elements of an array are interacting when the magnetostatic energy per unit volume of the array is 90% of the magnetostatic energy per unit volume of the corresponding isolated element [V.3].

For example, for a square array of square *l*-edged elements, the interacting threshold corresponds to an interelement separation of $d=0.6 \cdot l$. This value agrees with the one experimentally found for 2μm edge Co square arrays where the saturation field deviates from the isolated square (~1 μm), a signature of the onset of the interaction (see [V.13] and chapter IV).

Accordingly, the micromagnetic simulations performed in chapter IV for isolated magnetic elements are accurate only in the cases of separations 1.0 and 2.0 μm.

The magnetostatic energy values obtained with the proposed model can be compared to experimental data considering the structures set studied in chapter IV (square arrays of 2μm edged square elements with interelement separations 0.2, 0.5, 1.0 and 2.0 μm, see fig. V-4). The experimental values to be compared with the magnetostatic energy are the saturation field values for each interelement separation, since the saturation field is intimately related with magnetostatics as explained in chapter IV.

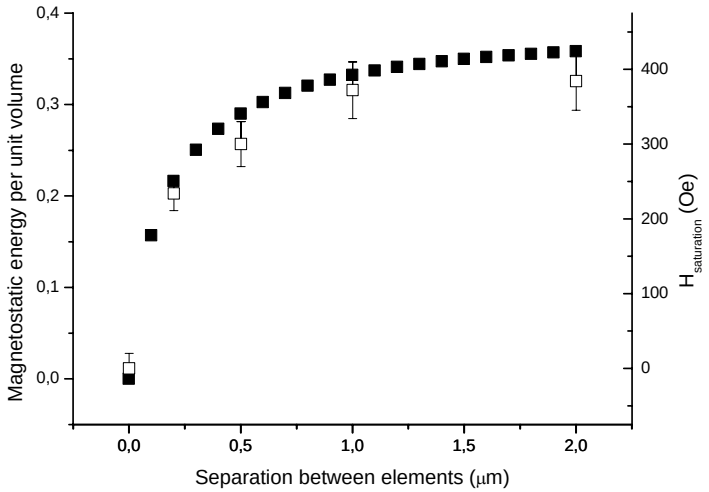

Fig. V-4: Theoretical magnetostatic energy per unit volume and experimental saturation field for square arrays of 2μm edged square elements as a function of the interelement separation. The experimental data are also plotted in fig. IV-5 (see chapter IV for details).

According to fig. V-4, both theoretical and experimental data follow the same trend, what strengthen the validity of the criterion for determining the onset of the interaction.

The interelement distance value for the interaction threshold depends on the thickness (although weakly for this thickness range). Thus, a distance for the interaction threshold $d=0.6 \cdot l$ is also valid for the data presented in chapter IV.

The separation value where the array can be considered as an interacting array is somehow arbitrary, but should not be mistaken with the one in which the elements in the array switch simultaneously (like in a domino effect), like the one reported in [V.14].

7.2.Magnetostatic energy vs. element shape

The behavior of the magnetostatic energy per unit volume in a square array as a function of the separation between magnetic elements depends on the shape of the elements, as it can be seen in fig.V-5.

In particular, the largest aspect ratios (large $h=l/2a$, corresponding to the least square elements) yield the lower values for the magnetostatic energy per unit volume. Notice this behavior is completely logical since in the limiting case of $h \rightarrow \infty$ (i.e., no magnetic material), the corresponding magnetostatic energy per unit volume must be zero.

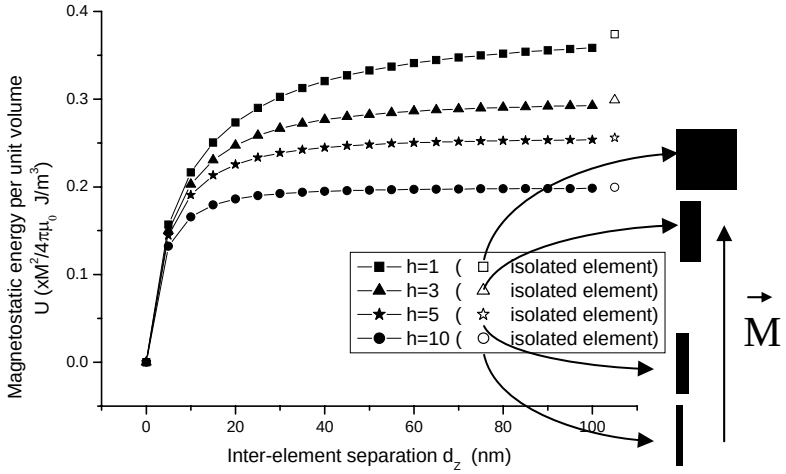

Fig. V-5: Magnetostatic energy values for square arrays of rectangular elements of different aspect ratios ($h=l/2a$, l=100 nm) as a function of the interelement distance. Hollow symbols represent the values for isolated elements.

7.3.Onset of the interaction vs. element shape

According to the established criterion to decide whether an array is interacting or not and to the dependence of the magnetostatic energy per unit volume on the shape of the elements embedded in the array, the minimum distance for the onset of the interaction might change as the shape of the array varies.

Fig. V-6 represents the interelement separation corresponding to the onset of the interaction in an square array of rectangular magnetic elements as a function of the aspect ratio of the magnetic elements. The magnetic elements are assumed to be saturated in the direction of the large element direction.

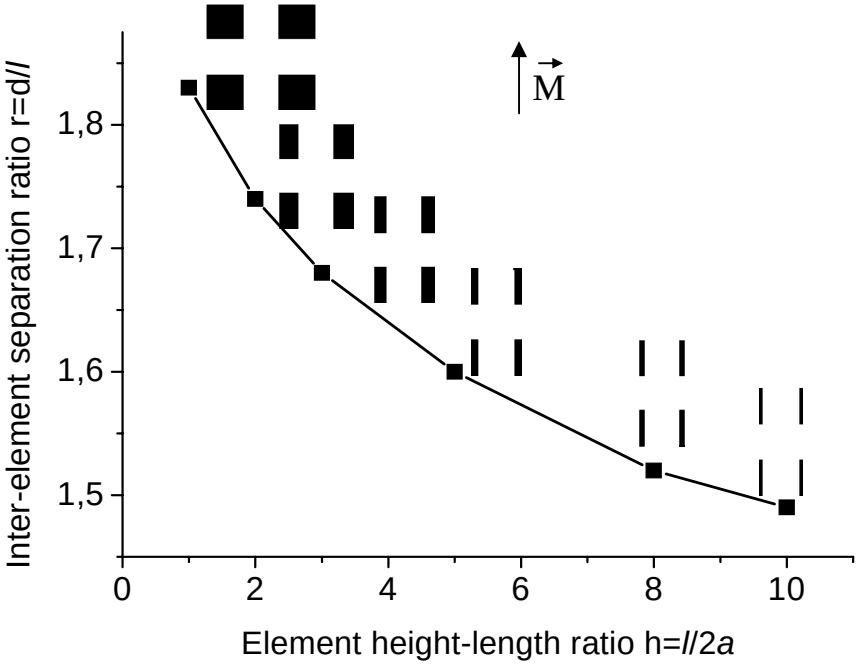

Fig. V-6: Interelement separation ratios in which magnetostatic energy of a square array of different rectangular elements reaches 90% of the value corresponding to an isolated element, i.e., minimum interelement separation in which magnetostatic coupling may be neglected.

According to fig. V-6, the larger aspect ratio of the magnetic elements of an square array, the lower interelement separation for the onset of the interaction.

8.Perpendicular magnetization in cylindrical magnetic elements

Equation (V-5) only holds for prisms (rectangular elements) in a rectangular lattice. Other common shapes like circles (cylinders) might be studied using the same method, but the corresponding formula for the magnetostatic energy per unit volume will increase its complexity. In this particular case, perpendicular magnetization will be considered, accounting for some patterns fabricated with LIL in the MESA$^+$ Institute for Nanotechnology. The notation and problem conditions in this case is shown in fig. V-7.

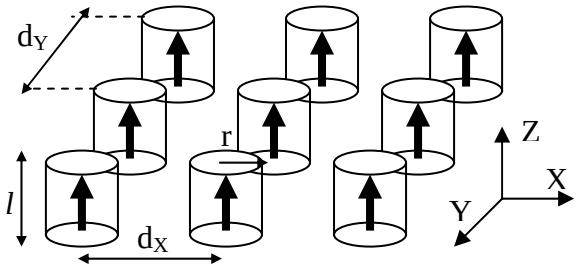

Fig. V-7: Problem conditions. Rectangular array of cylindrical magnetic elements with out-of-plane magnetization

Starting again from eq. (V-1) and using the notation in fig. V-7, the magnetic potential might be expressed

$$\phi(x,y,z)=\frac{M}{4\pi\mu_0}\int_{-r}^{r}\left(ArcSinh\left(\frac{y+\sqrt{r^2-x'^2}}{\sqrt{(x-x')^2+z^2}}\right)-ArcSinh\left(\frac{y-\sqrt{r^2-x'^2}}{\sqrt{(x-x')^2+z^2}}\right)\right)dx' \tag{V-12}$$

Since both the coordinates *x*' and *y*', and *x* and *y* are related by the boundary conditions, the obtention of the magnetostatic potential in this case, contrary to the case of rectangular elements, is not straightforward. In order to by-pass this problem, an expression for the magnetostatic energy can be obtained by

integrating in both *y*' and *x* (independent variables) leading to formula very similar to the one for rectangular elements.

The magnetostatic energy in terms of the magnetic potential is:

$$U = M\iint_S \phi dxdy = M\int_{-r+b}^{r+b}\int_{a-\sqrt{r^2-(y-b)^2}}^{a+\sqrt{r^2-(y-b)^2}} \phi(x,y,z)dxdy \qquad \text{(V-13)}$$

Since we are integrating in *y*' and *x* instead of *y*' and *x*', the corresponding formula for the magnetostatic energy is given by equation (V-14).

$$U = \int_{-r+b}^{r+b}\int_{-r}^{r} \xi(x',y,z)dx'dy \qquad \text{(V-14)}$$

where

$$\begin{aligned}\xi(x',y,z) = {} & Q\left(y+\sqrt{r^2-x'^2}, x'+a+\sqrt{r^2-(y-b)^2}, z\right) - \\ & Q\left(y-\sqrt{r^2-x'^2}, x'+a+\sqrt{r^2-(y-b)^2}, z\right) - \\ & Q\left(y+\sqrt{r^2-x'^2}, x'+a-\sqrt{r^2-(y-b)^2}, z\right) + \\ & Q\left(y-\sqrt{r^2-x'^2}, x'+a-\sqrt{r^2-(y-b)^2}, z\right)\end{aligned} \qquad \text{(V-15)}$$

and

$$Q(p,t,z)=p\cdot\text{ArcSinh}\left(\frac{t}{\sqrt{p^2+z^2}}\right)+t\cdot\text{ArcSinh}\left(\frac{p}{\sqrt{t^2+z^2}}\right)-z\cdot\text{ArcTan}\left(\frac{pt}{z\sqrt{p^2+t^2+z^2}}\right) \qquad \text{(V-16)}$$

The variables *a* and *b* represents the Cartesian coordinates in the XY plane of the circle center in which the magnetostatic potential is evaluated. Note that we are under the assumption (without loss of generalization) that the coordinates of the center of the circular surface that generates the magnetic potential within the XY plane is (0,0).

Performing the change of variable $x=x'+a$ in (V-14) (This step is just a notation simplification. The variable *x* of the change of variable is independent of the *x* of the previous integration), equation (V-17) is obtained.

$$U = \int_{-r+b}^{r+b}\int_{-r+a}^{r+a} \varepsilon(x,y,z)dxdy \qquad \text{(V-17)}$$

where

$$\varepsilon(x,y,z) = Q\left(y+\sqrt{r^2-(x-a)^2}, x+\sqrt{r^2-(y-b)^2}, z\right) -$$
$$Q\left(y-\sqrt{r^2-(x-a)^2}, x+\sqrt{r^2-(y-b)^2}, z\right) -$$
$$Q\left(y+\sqrt{r^2-(x-a)^2}, x-\sqrt{r^2-(y-b)^2}, z\right) +$$
$$Q\left(y-\sqrt{r^2-(x-a)^2}, x-\sqrt{r^2-(y-b)^2}, z\right) \qquad \text{(V-18)}$$

Equation (V-17) provides the magnetostatic energy associated with two free poles surfaces. In order to obtain the magnetostatic energy per circular element, the contributions of all free poles surfaces within the planes Z=0 and Z=*l* must be added.

Unfortunately, the expression from equation (V-17) only one symmetry property holds:

$$\int_{-r+b}^{r+b}\int_{-r+a}^{r+a} \varepsilon(x,y,z)dxdy = \int_{-r+a}^{r+a}\int_{-r+b}^{r+b} \varepsilon(y,x,z)dxdy \qquad \text{(V-19)}$$

In this case of cylindrical elements, the function $\varepsilon(x,y,z)$ has no physical meaning, contrary to the case of rectangular elements, but it is necessary to perform the simplification leading to eq. (V-17) and, therefore, to the obtaining of an expression for the magnetostatic energy.

9.Free poles magnetic field estimation:

The magnetostatic energy is a useful magnitude to study shape anisotropies, but a closely related magnitude, the magnetic field generated by the free poles surfaces, must be also considered in order to analyze reversals within the magnetic elements of the array and is also useful to study interactions between elements, like magnetic information transmission in close-by elements [V.1] or pattern transfer from a lithographed array into a exchange decoupled continuous film (see chapter VII).

Once an expression for the magnetic potential is obtained, it is quite straightforward to derive an expression for the magnetic field generated by the free poles surfaces. This estimation is useful for analyzing the behavior of magnetic nanoparticles on top of the array, like in bitter techniques [V.15]. Such an study set the basis for the development at the IMM of a biomedical magnetic sensor.

Note that the magnetic elements are supposed to be under saturation, according to the model conditions, so the conclusions obtained should not be extended beyond the state of magnetic saturation for each individual magnetic element. The notation and conditions used to determine the expressions for the magnetic potential are in Fig. V-8.

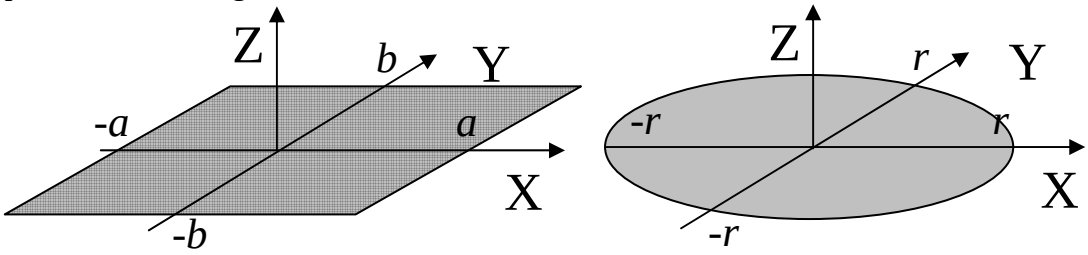

Fig. V-8: Problem conditions. Free poles surfaces: square (prism element) and circle (cylindrical element).

From the magnetic potential the corresponding stray field is be determined using the well known equation:

$$H=-\nabla\phi \qquad \text{(V-20)}$$

9.1.Square shapes

In order to determine the stray field associated to a square free poles surface, equation (V-3) will be used. Thus, the three partial derivatives of function $Q(t,p,z)$ (defined in eq. (V-4)) must be calculated.

$$\frac{\partial Q}{\partial p} = ArcSinh\left(\frac{t}{\sqrt{p^2+z^2}}\right),$$

$$\frac{\partial Q}{\partial t} = ArcSinh\left(\frac{p}{\sqrt{t^2+z^2}}\right),$$

$$\frac{\partial Q}{\partial z} = -ArcTan\left(\frac{pt}{z\sqrt{p^2+t^2+z^2}}\right) \qquad \text{(V-21)}$$

This way, the magnetic field associated to the square free pole surface is $H=(H_x,H_y,H_z)$, where:

$$H_x = \frac{M}{4\pi\mu_0}\left(-ArcSinh\left(\frac{y+b}{\sqrt{(x+a)^2+z^2}} \right) + ArcSinh\left(\frac{y-b}{\sqrt{(x+a)^2+z^2}} \right) + \right.$$
$$\left. + ArcSinh\left(\frac{y+b}{\sqrt{(x-a)^2+z^2}} \right) - ArcSinh\left(\frac{y-b}{\sqrt{(x-a)^2+z^2}} \right) \right)$$

$$H_y = \frac{M}{4\pi\mu_0}\left(-ArcSinh\left(\frac{x+a}{\sqrt{(y+b)^2+z^2}} \right) + ArcSinh\left(\frac{x-a}{\sqrt{(y+b)^2+z^2}} \right) + \right.$$
$$\left. + ArcSinh\left(\frac{x+a}{\sqrt{(y-b)^2+z^2}} \right) - ArcSinh\left(\frac{x-a}{\sqrt{(y-b)^2+z^2}} \right) \right)$$

$$H_z = \frac{M}{4\pi\mu_0}\left(ArcTan\left(\frac{(x+a)(y+b)}{z\sqrt{(x+a)^2+(y+b)^2+z^2}} \right) - ArcTan\left(\frac{(x+a)(y-b)}{z\sqrt{(x+a)^2+(y-b)^2+z^2}} \right) \right.$$
$$\left. - ArcTan\left(\frac{(x-a)(y+b)}{z\sqrt{(x-a)^2+(y+b)^2+z^2}} \right) + ArcTan\left(\frac{(x-a)(y-b)}{z\sqrt{(x-a)^2+(y-b)^2+z^2}} \right) \right) \quad \text{(V-22)}$$

Note that equations (V-22) provides field values of the type $\frac{M}{4\pi\mu_0}\cdot\xi(x,y,z)$, where $\xi(x,y,z)$ is a dimensionless function.

Assuming the material used in this case is Co (like in most of the structures presented in this thesis), M=1.79 Wb/m^2.
Therefore,

$$H = \frac{1.79}{(4\pi)^2\cdot 10^{-7}}\,A/m \cdot \frac{4\pi Oe}{10^3\,A/m}\cdot\xi(x,y,z) = 1424\ Oe\cdot\xi(x,y,z).$$

The results are plotted for X and Z field components in the contour plots of figs. (V-8) & (V-9), assuming 5 μm edged square elements separated 1 μm.

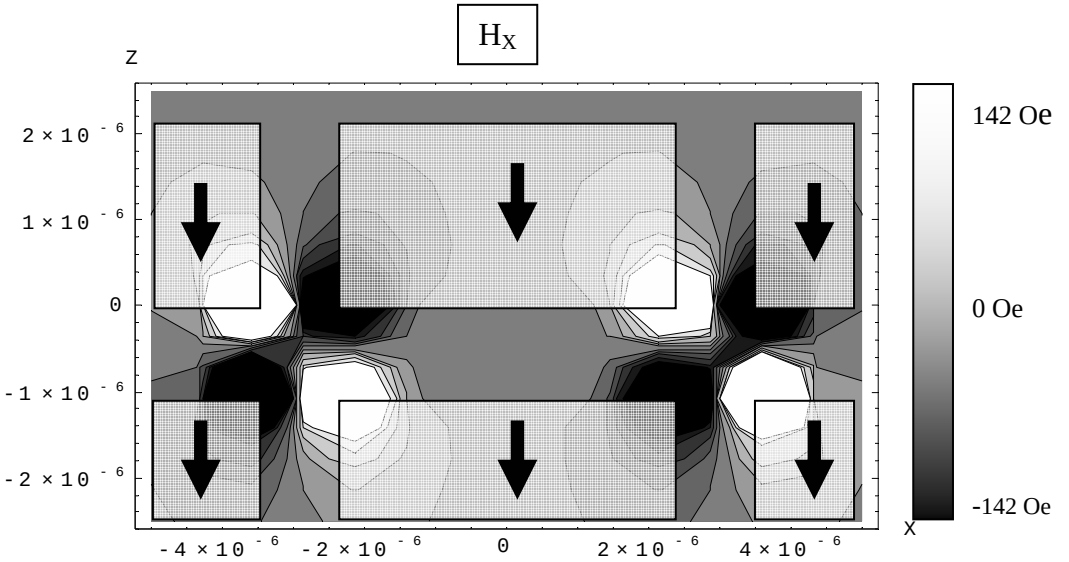

Fig. V-9: Contour plot for the X component of the magnetic field corresponding to an array of square magnetic elements with in-plane magnetization.

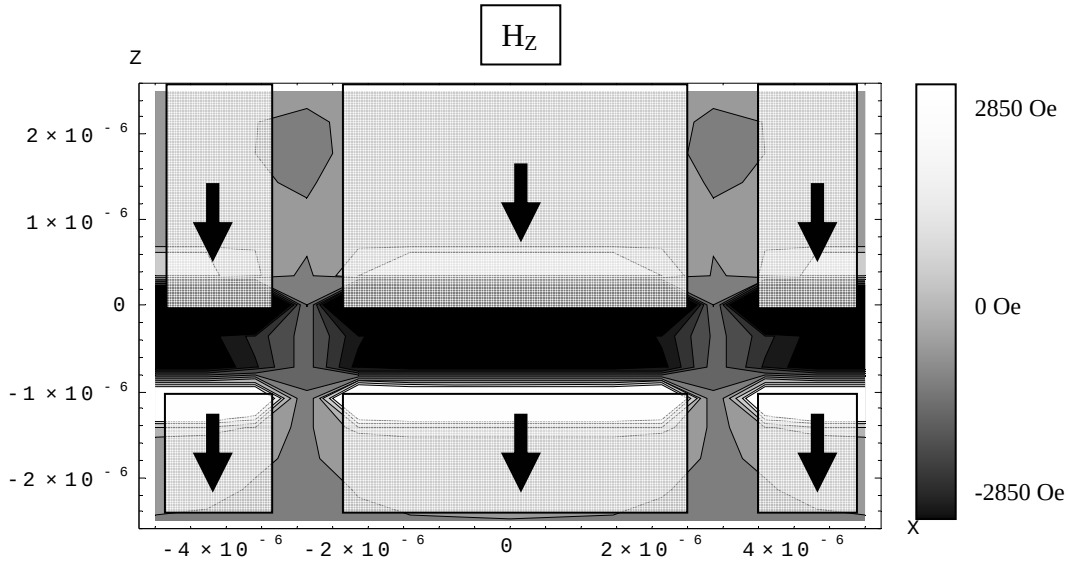

Fig. V-10: Contour plot for the Z component of the magnetic field corresponding to an array of square magnetic elements with in-plane magnetization.

As it can be seen in figs. V-9 and V-10, the field in the nearby of the magnetic elements is very intense (around 3 kOe in the Z component in the vicinity of a free pole surface). This fact will be used in chapter VI to tailor domains in a heterostructure composed by a pattern on top of a continuous thin film.

9.2.Circular shapes

Again, equation (V-20) might be used to determine the magnetic field corresponding to a circular surface of magnetic free poles from the expression of its magnetic potential. Since under our conditions we have no analytical expression for ϕ, a numerical approach must be used.
Applying eq. (V-20) to eq. (V-12) and provided the integrating and derivate variables are independent as it occurs in this case it follows:

$$H_X = \frac{\partial \phi}{\partial x} = \frac{M}{4\pi\mu_0}\int_{-r}^{r}\left[-\frac{(x-x')\left(y+\sqrt{r^2-x'^2}\right)}{(x-x')^2+z^2}h_+(x,x',y,z)+\frac{(x-x')\left(y-\sqrt{r^2-x'^2}\right)}{(x-x')^2+z^2}h_-(x,x',y,z)\right]dx'$$

$$H_Y = \frac{\partial \phi}{\partial y} = \frac{M}{4\pi\mu_0}\int_{-r}^{r}\left[h_+(x,x',y,z)+h_-(x,x',y,z)\right]dx'$$

$$H_Z = \frac{\partial \phi}{\partial z} = \frac{M}{4\pi\mu_0}\int_{-r}^{r}\left[-\frac{z\left(y+\sqrt{r^2-x'^2}\right)}{(x-x')^2+z^2}h_+(x,x',y,z)+\frac{z\left(y-\sqrt{r^2-x'^2}\right)}{(x-x')^2+z^2}h_-(x,x',y,z)\right]dx' \quad \text{(V-23)}$$

where

$$h_{+}(x,x',y,z)=\frac{1}{\sqrt{\left(x-x'\right)^{2}+z^{2}+\left(y+\sqrt{r^{2}-x'^{2}}\right)^{2}}}$$

$$h_{-}(x,x',y,z)=\frac{1}{\sqrt{\left(x-x'\right)^{2}+z^{2}+\left(y-\sqrt{r^{2}-x'^{2}}\right)^{2}}} \qquad \text{(V-24)}$$

According equations (V-23), the X and Z component of the field can be spatially resolved. In this case, 300 nm diameter dots in a 600 nm period array are considered.

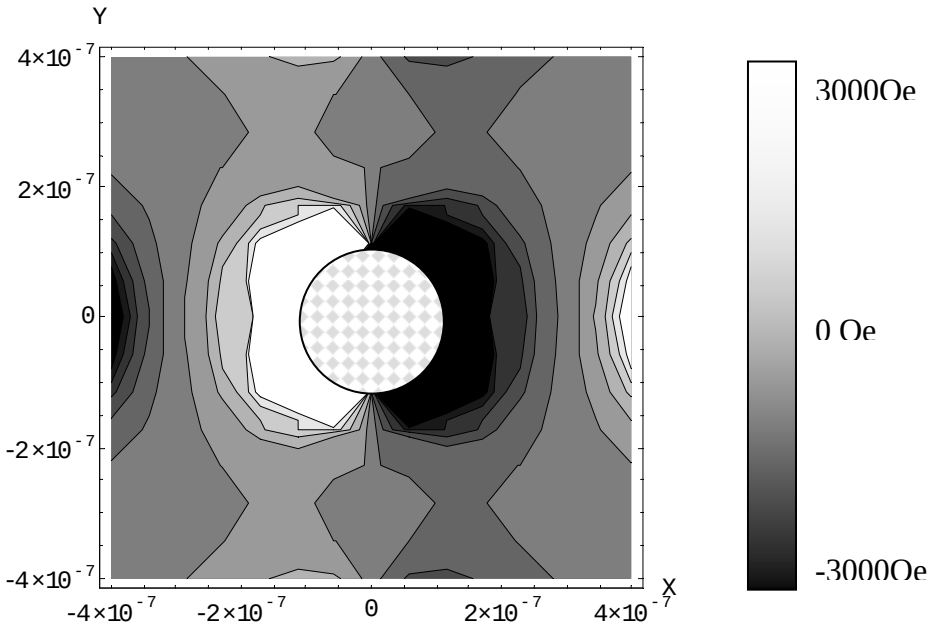

Fig. V-11: Contour plot for the X component of the magnetic field corresponding to an array of circular magnetic elements with out-of-plane magnetization.

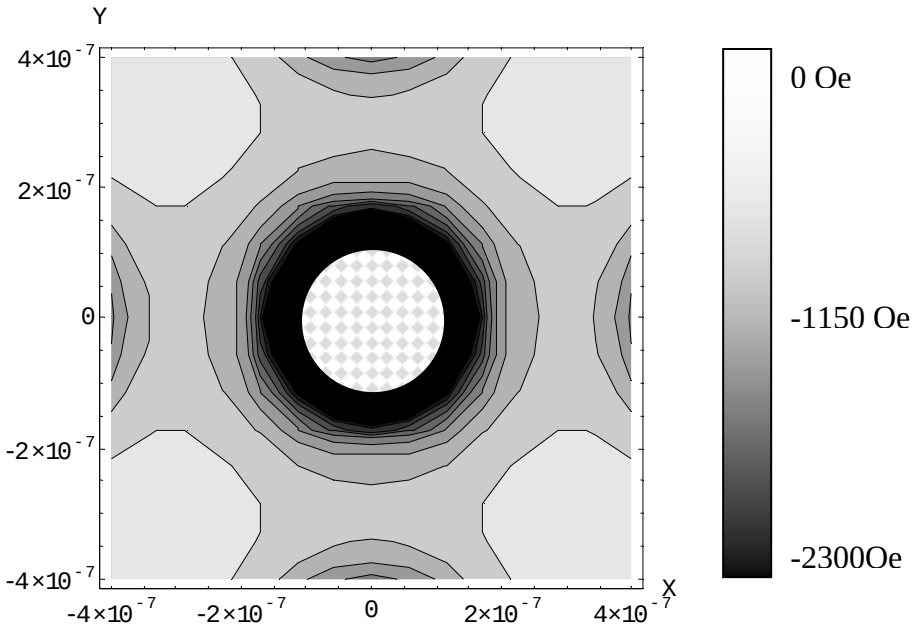

Fig. V-12: Contour plot for the X component of the magnetic field corresponding to an array of circular magnetic elements with out-of-plane magnetization.

According to equations (V-23), the interaction field of one dot from its 8 nearest neighbors in the conditions of figs. V-11 and V-12 is around 35 Oe (2.74 kA/m). Compared to the values of the field in close proximity to the magnetic dots, this interaction field is very low, thus corresponding to a non-interacting-dots situation.

If, for instance, a situation in which 300 nm diameter dots are placed in a 320 nm period lattice is considered, the corresponding interaction field increases its intensity to 400 Oe (31.89 kA/m). The interaction field in this case has a magnitude comparable with the field in the vicinity of a dot, a clear sign of interaction between the dots of the array.

The interaction field is a value to be taken into account in recording media in order to avoid cross-talking.

10.Beyond the basic assumptions of the model:

The basic assumptions to develop the analytic model are not mandatory. For instance, in section 9 it has been seen that an analogous formula can be done for perpendicular magnetization (removing assumption ii) and in the case of non-rectangular shapes. Assumption iii might be also removed just subtracting twice the contribution of the element(s) with the magnetization in the opposite direction. But the most complex assumption to remove is assumption i (homogeneous magnetization within the magnetic element). In this particular case, the domain wall yields a spatial distribution of magnetic free poles that must be take into account for magnetostatic considerations.

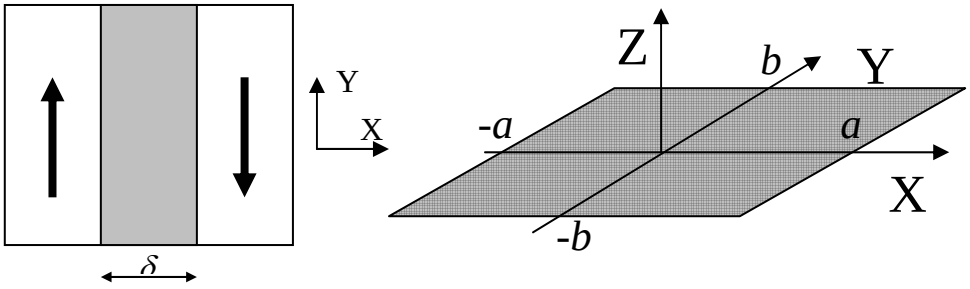

Fig. V-13: Sketch and notation for magnetostatics in a 180º Bloch domain wall in a flat surface.

Lets assume, for simplicity, a 180º Bloch domain wall and let's use the notation in fig. V-13. In these conditions, the coordinate origin is situated in the center of the domain wall.

In this case of a domain wall, the surface free pole distribution, given by σ is not a constant but a function spatially resolved, varying (according to the notation in fig. V-13) along the X axis (once assumed homogeneity in the Y axis).

10.1.Free pole distribution in a 180º Bloch domain wall

According to [V.12] and [V.17], the angle θ between the spins and the normal direction (Z axis)as a function of the position in the Bloch wall (given by the position in the X axis) is specified by the equation:

$$x' = \sqrt{\frac{A}{K}} Log\left(tg\left(\frac{\theta}{2} + \frac{\pi}{4} \right) \right) \tag{V-25}$$

Hence

$$\theta = 2 \cdot arctg\left(e^{x'/\sqrt{A/K}} \right) - \frac{\pi}{2} \tag{V-26}$$

Graphically,

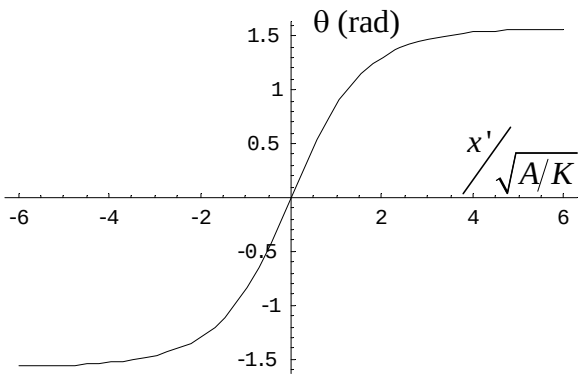

Fig. V-14: Spatially resolved magnetization angle (θ=±π/2 represents the in-plane directions) in a 180º Bloch domain wall.

Therefore, the free pole density in the surface is given by:

$$\sigma = M_S \cos\left(2 \cdot arctg\left(e^{x'/\sqrt{A/K}} \right) - \frac{\pi}{2} \right) \tag{V-27}$$

Graphically,

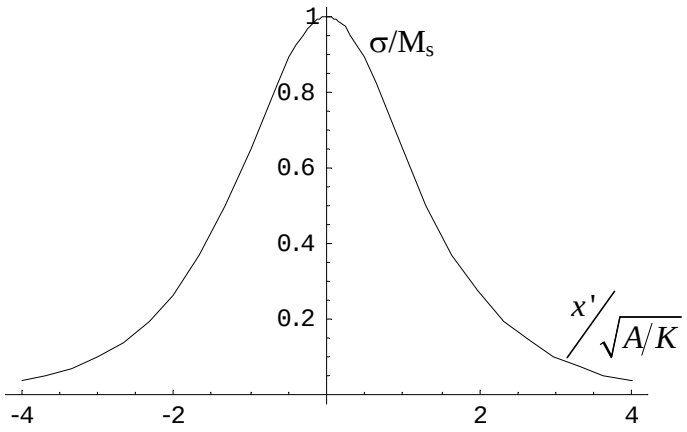

Fig. V-15: Free pole distribution with out-of-plane magnetization.

According to references [V.12] and [V.17], it can be considered $\delta=\pi\sqrt{\frac{A}{K}}$, where $\sqrt{\frac{A}{K}}$=L is called exchange correlation length. In fig. V-14 it can be seen that the chosen domain wall width accounts for around 70% of the area of the plot.

Hence, from the values for magnetic anisotropy and exchange constant, it can be estimated the corresponding domain wall width of a 180º Bloch wall. Table V-1 show some examples of materials used along this thesis.

Material	A (pJ/m)	K (kJ/m^3)	M_S (Wb/m^2)	$\sqrt{\frac{A}{K}}$=L (nm)	$\delta=\pi\sqrt{\frac{A}{K}}$ (nm)
Co	13	410	1.79	5.6	17.7
Fe	20	42	2.00	21.8	68.5
$Fe_{80}B_{20}$	16	2.8	1.60	75.6	237.5

Table V-1: Values for exchange constant, magnetic anisotropy, saturation magnetization, exchange correlation length and estimation for the domain wall width of a 180º Bloch wall for different materials using along the thesis.

10.2. An expression for the magnetostatic energy

Applying eq. (V-27) in eq. (V-2) , an expression for the magnetic potential can be obtained.

$$\phi(x,y,z) = \frac{1}{4\pi\mu_0}\int_{-\delta/2}^{\delta/2}\cos\left(2ArcTan\left(e^{x'/\sqrt{A/K}}\right)-\frac{\pi}{2}\right)\left(ArcSinh\left(\frac{y+b}{\sqrt{(x-x')^2+z^2}}\right)-ArcSinh\left(\frac{y-b}{\sqrt{(x-x')^2+z^2}}\right)\right)dx' \quad \text{(V-28)}$$

Once the magnetic potential is determined, it can be calculated both the magnetostatic energy and the its corresponding field.

In order to calculate the magnetostatic energy, both the contributions associated to the magnetic potential of the different free poles surfaces of the magnetic element and the contributions corresponding to the domain walls present within the magnetic element must be considered. All these calculations enormously increases the complexity of the model and it is not worthy for our initial purposes.

10.3.An expression for the magnetic field associated to a domain wall

An expression for the magnetic field associated to the domain wall can be easily obtained just deriving the magnetic potential by the different coordinates. In order to simplify the calculations, it can be assumed that the domain wall width is very small compared to the size of the magnetic element, like the 2μm edged squares presented in chapter IV vs. its corresponding domain wall width according to table V-1, $\delta \leq 20$nm.

Thus, assuming $b \to \infty$, the different components of the magnetic field associated to a 180º Bloch domain wall are:

$$H_X(x,y,z) = \int_{-4a}^{4a}\sigma(x')\frac{-2(x-x')}{(x-x')^2+z^2}dx'$$

$H_Y(x,y,z)=0$

$$H_Z(x,y,z)=\int_{-4a}^{4a}\sigma(x')\frac{-2z}{(x-x')^2+z^2}dx' \qquad \text{(V-29)}$$

Where $\sigma(x')$ is given by eq. (V-27)

If, for instance, Co is the chosen material, eqs. (V-29) can be evaluated in the vicinity of the domain wall using the fact that, for cobalt, M_S=1.79 Wb/m^2.

Hence,

$$\frac{M}{4\pi\mu_0}\cdot\xi=\frac{1.79 Wb/m^2}{(4\pi)^2\cdot10^{-7}H/m}\cdot\xi=\frac{1.79}{(4\pi)^2\cdot10^{-7}}A/m\cdot\frac{4\pi Oe}{10^3 A/m}\cdot\xi=1424\ \text{Oe}\cdot\xi.$$

Where ξ is a dimensionless value.

Therefore, the values for H_X and H_Z as a function of the distance can be plotted, assuming a 60nm thick thin film:

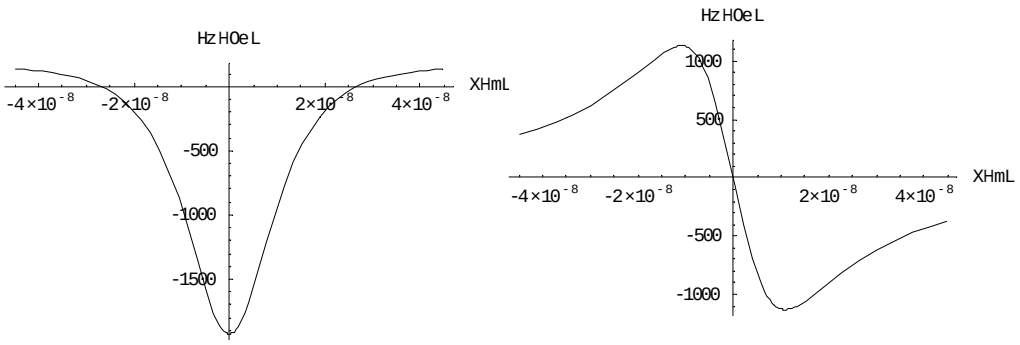

Fig. V-16: H_Z (left) and H_X (right) components of the magnetic field associated to a 180º Bloch domain wall in Co as a function of the position in the X axis.

The plots in fig. V-16 can be summarized in fig. V-17, where the modulus of the demagnetizing field is plotted as a function of the position in the X axis for a 60nm thick Co thin film.

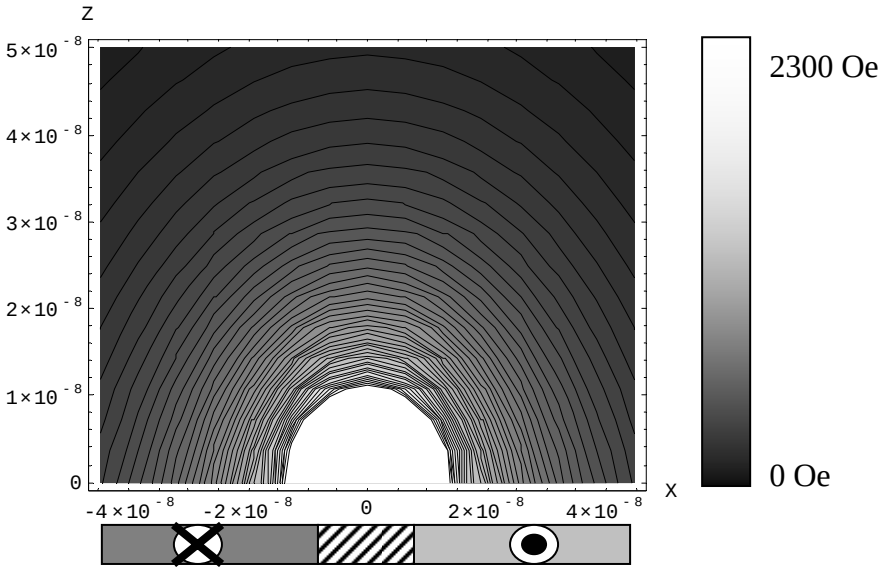

Fig. V-17: Modulus of the magnetic field corresponding to a 180º Bloch domain wall in a 60nm thick Co thin film. At the bottom of the contour plot, a sketch of the cross section is shown, where the Bloch wall in centered in the X origin.

10.4.Magnetic field vs. film thickness

The absolute value of the stray field depends not only on the distance (*d*) from the domain wall, but also on the thickness (*t*) of the magnetic thin film. These dependences can be graphically seen in fig. V-18, where the magnetic field is calculated in the origin of coordinates.

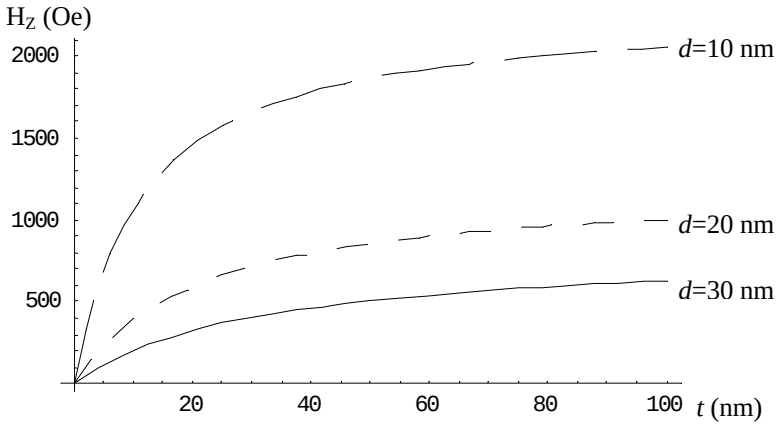

Fig.V-18: Magnetic field component Z (H_Z) from a 180º Bloch domain wall for Co as a function of the distance from the thin film surface and its thickness.

An analogous plot can be performed for the maximum value X component in the same condition. In this particular case, this corresponds to a magnetic field calculated in the position x=10nm (see fig. V-19).

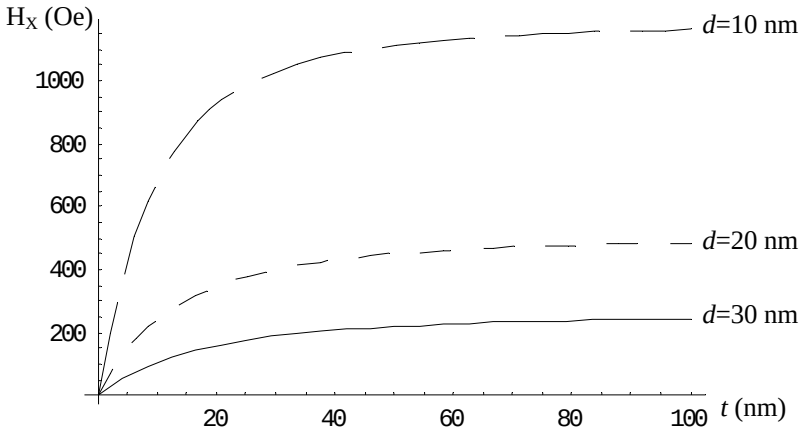

Fig.V-19: Magnetic field component X (H_X) from a 180º Bloch domain wall for Co as a function of the distance from the thin film surface and its thickness.

11.Conclusions:

An exact analytic formula for the magnetic potential in orthorhombic magnets $2a\times2b\times l$ arrays is presented. This formula is used to obtain the magnetostatic energy per unit volume and the shape anisotropy for different arrays of magnetic elements. The presented formalism is very flexible as it can be

a) extended to non homogeneous distribution of the magnetization of the elements of the array, i.e., remove assumption number iii of the model
b) used to make calculations in both finite and infinite arrays
c) used to calculate the magnetostatic energy of any element within a finite array or in arrays with defects.
d) used to establish a criterion for the minimum number of elements to be considered for a micromagnetic simulation of an array to be realistic depending on the element size and separation.

According to this formalism it has been calculated the shape anisotropy for different array and element shapes, the dependence on the interelement separation

in both square and rectangular arrays and the effect of the element shape in the magnetostatic energy. It also has been shown that the obtained results agree with our previous experimental measurements.

Circular shapes are also studied, obtaining similar formulae.

From the expressions for the magnetic potential in each considered case it might be derived an expression for the stray fields, useful for solving problems regarding magnetization reversals. Using a similar expression it is possible to calculate the field applied to a given magnetic element due to its nearest neighbors.

The developed model provides the theoretical framework to the experiments studied in chapter IV and suggest the possibility of tailoring the anisotropy of a magnetic array by means of the shape of both the array and its constituent elements. This is discussed in detail in chapter VI.

12.References:

[V.1] R.P. Cowburn, M.E. Welland, Science **287**, 1466 (2000)

[V.2] R.L. Joseph, E. Schlömann, J. Appl. Phys. **36**, 1579 (1964)

[V.3] E. Tsymbal. Appl. Phys. Lett.. **77**, 2740 (2000)

[V.4] E. Tsymbal. J. Magn. Magn. Mater. **130**, L6 (1994)

[V.5] E. Gu, E. Ahmad, S.J. Gray, C. Daboo, J.A.C. Bland, L.M. Brown, Phys Rev. Lett. **78**, 1158 (1997)

[V.6] A. Encinas-Oropesa, M. Demand, L. Piraux., I. Huynen, U. Ebels. Phys Rev. B. **63,** 104415 (2001)

[V.7] A. Encinas-Oropesa, M. Demand, L. Piraux., U. Ebels, I. Huynen. J. Appl. Phys. **89**, 6704 (2001)

[V.8] R.P. Cowburn. J. Phys D: Appl. Phys. **33**, R1 (2000)

[V.9] D. Craik. *Magnetism. Principles and applications.* Wiley 1995

[V.10] P. Belobrov , R. S. Gekht and V. A. Ignatchenko., Sov. Phys. JETP **57**, 636 (1983)

[V.12] P. Politi and M.G. Pini, Phys. Rev. B **66**, 214414 (2002)

[V.13] S. Chikazumi. *Physics of magnetism.* Robert E. Krieger Pub. Co. (1986)

[V.14] J. L. Costa-Krämer, R. Alvarez-Sánchez, A. Bengoechea, F. Torres, P. García-Mochales, and F. Briones, Phys. Rev. B **71**, 104420 (2005)

[V.15] J.L. Costa-Krämer, J.I. Martín, J.L. Menéndez, A. Cebollada, J.V. Anguita, F. Briones, y J.L. Vicent, Appl. Phys. Lett. **76** 3091 (2000)

[V.16] W. Szmaja, J. Magn. Magn. Mat. **234**, 13 (2001)

[V.17] A. Aharoni, IEEE Trans. Magn. **27**, 3539 (1991)

[V.18] C. Kittel. Rev. Mod. Phys. **21** 541 (1949)

CHAPTER VI:

TAILORING ANISOTROPY IN A MAGNETIC ARRAY

Index

TAILORING ANISOTROPY IN A MAGNETIC ARRAY

1.Introduction

In chapter V, a theoretical model describing the magnetostatic energy and shape anisotropy in an array of magnetic elements was presented. According to this model (in agreement with results in the literature, [VI.1-VI.5]), both the array and element shape are anisotropy sources. This suggests the possibility of tailoring the shape anisotropy in a magnetic array. To investigate this possibility, the effect of both element and array shape must be quantitatively studied in detail using the analytical model of chapter V in order to establish a comparison. In particular, from this comparison the possibility of looking for a square array of rectangular elements whose shape anisotropy is the same than the corresponding to a given rectangular array of square elements is studied. Provided the theoretical dimensions of both arrays are available for lithographic techniques, they can be fabricated together with a third array combining the rectangular shape of one of the arrays with the rectangular elements of the other. If this so-designed array has no shape anisotropy, the theoretical model of chapter V, in spite of its simplicity, will appear to be a powerful tool to tailor the shape anisotropy of a given array of magnetic elements.

2.Compensating the anisotropy:

The analytical model developed in chapter V allows us to show in what follows that it is possible to balance the anisotropy due to a given single element of rectangular shape with the shape anisotropy of an adequate rectangular array.

The idea is that the magnetization due to the element shape tends to align parallel to the element long axis. On the other hand, the interaction between neighbors tends to align the magnetization parallel to the direction of the shortest interelement separation. In addition, calculations of chapter V and previous works [VI.1,VI.2] demonstrate that square shapes do not produce anisotropy, either due to the array or to the element shape. Thus, for a rectangular array of rectangular

elements where the array shape anisotropy axis is perpendicular to the element shape anisotropy and both anisotropies have the same magnitude, the overall shape anisotropy should be zero.

Fig. VI-1 establishes a comparison between array shape anisotropy (fig. VI-1a) and element shape anisotropy (fig. VI-1b) in the same conditions used in chapter V, i.e., the element edge in the Z direction is 100 nm large, the thickness of the thin film is 5nm (see fig. V-1 for details). Note that negative values represents an easy axis along Z axis direction, while positive values represents an easy axis along the X axis direction. The shape anisotropy values for a given array are calculated subtracting the magnetostatic energy of the array saturated in the Z direction to the magnetostatic energy of the same array saturated in the X direction.

In fig. VI-1a) the array shape anisotropy of a rectangular array of square elements is plotted as a function of the interelement separation in the X axis (d_X) for different values of the interelement distance in the Z axis (d_Z). On the other hand, fig. VI-1b) is a plot of the element shape anisotropy of a square array of rectangular elements vs. the aspect ratio of the element ($h=l/2a$, being l and $2a$ the size of the magnetic element in the Z and X direction respectively) for different interelement separations (d_X or d_Z, provided the period in both X and Z directions must be the same, i.e., $d_X+2a=d_Z+l$).

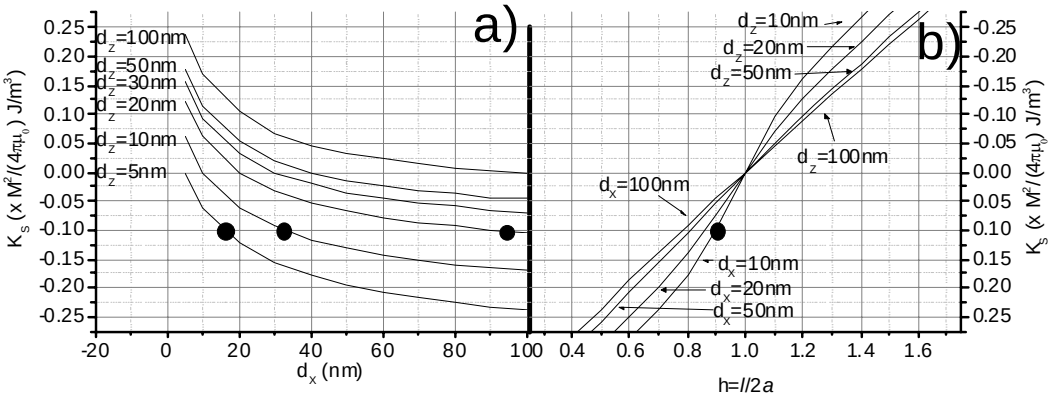

Fig. VI-1: a) Shape anisotropy for rectangular arrays of square elements (100 nm edge, 5 nm thick). **b)** Shape anisotropy for square arrays of rectangular elements (l=100 nm, 5 nm thick). Negative values represents an easy axis along Z axis direction, while positive values represents an easy axis along the X axis direction. Filled circles denote particular lattice (fig.VI-1a) and individual (fig. VI-1b) shape anisotropies that cancel each other (notice the vertical axes of Fig. VI-1b is inverted with respect to VI-1a).

According to fig. VI-1a) the array shape anisotropy decreases as the interelement separations increases. Moreover, this decrement is steeper for the lower values of interelement separation in both X and Z axes. According to the way the shape anisotropy is calculated, there is a symmetry between X and Z axes.

Fig. VI-1b) shows that the element shape anisotropy rapidly decreases when the element aspect ratio increases. The effect of the interelement separation in this case is much lower, slightly modulating the effect of the aspect ratio. Thus, lower interelement separation enhances the shape anisotropy and the effect of the interelement separation once reached the non-interacting threshold (fig. VI-1b, d_Z=50nm and d_Z=100nm. See chapter V, section 7) is barely noticeable. There is another limit imposed by the interelement distance. It has been shown (see fig.V-4) that no matter the element shape, the magnetostatic energy of an array of magnetic elements in close contact is zero. This effect is particularly intense in arrays of lower aspect ratio elements, as it can be seen in the plot for d_X=10nm and d_Z=10nm of fig. VI-1b) in which an steeper part of the graph appears for values of *h* in the vicinity of 1 (square elements).

Comparing Figs. VI-1 a) and VI-1 b), it can be observed that large lattice aspect ratios are needed to obtain the same shape anisotropy as the ones due to small element aspect ratios. For example, the shape anisotropy due to an element aspect ratio of *h*=0.9 in a square array in which d_X=10nm (fig. VI-1b) can be achieved using a rectangular array of square elements with interelement separations d_X=92nm and d_Z=20nm (representing an aspect ratio of $d_Z/d_X \approx 0.22$, around 4 times larger than the element aspect ratio).

In both the array and the element shape anisotropy cases, once given a value for the shape anisotropy, there is not an unique array providing this given value but a group with different parameters but with a similar aspect ratio (see in fig. VI-1 a&b the filled circles within the plots). For example, given $|K_S|=0.1\ \frac{M^2}{4\pi\mu_0}$ J/m^3, the following arrays can provide such a shape anisotropy (amongst many others):

- A square array of rectangular elements with interelement separation d_X=10nm and an aspect ratio of *h*=0.9.
- A square array of rectangular elements with interelement separation d_X=50nm and an aspect ratio of *h*=0.8
- A rectangular array of square elements with interelement separations d_X=16nm and d_Z=5nm.
- A rectangular array of square elements with interelement separations d_X=92nm and d_Z=20nm.

3.Samples design:

In order to experimentally corroborate the theoretical statements of the previous section, some patterns are fabricated. Since we are interested on measuring the shape anisotropy of the structure, a soft magnetic material should be used. This way, the magnetocrystalline anisotropy will be lower than the designed shape anisotropy. In spite of that, a low uniaxial anisotropy is interesting since it allows the study of the effect of the easy and hard anisotropy axes in the measurements.

Consequently, the selected material used for fabricating the arrays is the amorphous alloy $Fe_{80}B_{20}$, magnetically characterized in chapter IV, section 7 (see fig. IV-11).

The second step is the selection of the arrays to be patterned. The arrays will be grouped in triplets consisting of:

1. a square array of rectangular elements with a given uniaxial anisotropy, denoted by SR (S accounting for Square array and R for Rectangular elements)
2. a rectangular array of square elements presenting the same anisotropy than the previous one, denoted by RS (R accounting for Rectangular array and S for Square elements)
3. a rectangular array of rectangular elements combining the element parameters of the SR array with the array parameters of the RS array. Using the same notation, this array will be called RR.

Each array of the array triplet should present such a shape that:

1. provides an uniaxial anisotropy larger than the magnetic anisotropy of the $Fe_{80}B_{20}$.
2. has dimensions available for lithographic techniques, guaranteeing regular shapes of both the array and its constituent elements.

As stated in the previous section, in order to obtain the same shape anisotropy, larger aspect ratios must be used in array shape anisotropy. Therefore, from the lithographic point of view, the RS pattern is more troublesome than the SR. Thus, the dimensions of the RS structure are to be used to determine the shape anisotropy to be considered, conditioning this way the dimensions of the SR and the RR patterns.

Two triplets of structures are fabricated. In the first one, the shape anisotropy is chosen to be perpendicular to the uniaxial anisotropy of the $Fe_{80}B_{20}$ while in the second one, the shape anisotropy is parallel to the material anisotropy.

In fig. VI-2, the selected dimensions for the samples are schematically shown.

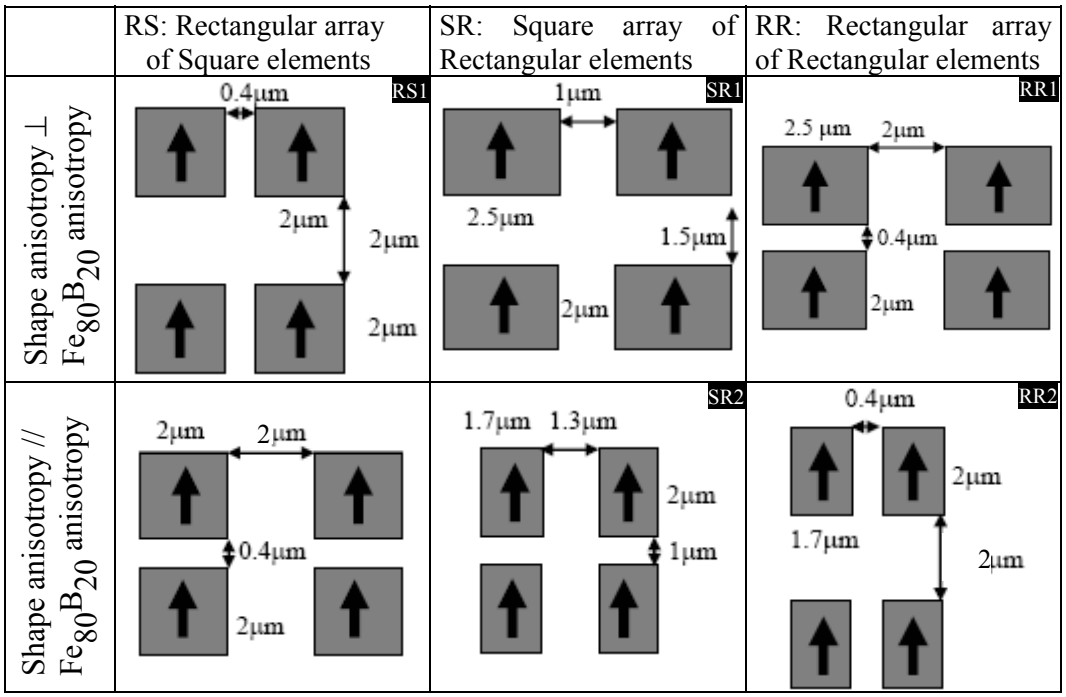

Fig. VI-2: Schematic presentation of the structures to be used and their dimensions. The RS and SR are chosen to have the same shape anisotropy. RR samples combine the dimensions of RS and SR. It has to be demonstrated that this RR samples are isotropic. The black arrows inside the magnetic elements points to the direction of the magnetocrystalline material.

The fabricated arrays shown in fig. VI-2 are in the micrometer range in order to ensure regular shapes. Since the analytical model is scalable, the experimental data from this samples can be anyway correlated with theoretical predictions. Thus, in order to correlate experiments with theoretical predictions, the arrays in fig.VI-2 are chosen to be 100 nm thick.

It is noteworthy to remember that the three basic assumptions of the models listed in chapter V section 2 easily hold on reduced dimensions samples. Nevertheless, amorphous $Fe_{80}B_{20}$ is a soft material with in-plane magnetization so it can be easily saturated in a given direction and, thus, the three assumptions of the theoretical model should in principle hold.

The dimensions of the samples are chosen to theoretically provide an anisotropy one order of magnitude larger than the $Fe_{80}B_{20}$ uniaxial anisotropy. Larger anisotropies might be chosen still within the lithographic limits but this so-designed patterns would not easily be magnetically saturated in the available MO measuring devices at the IMM.

4.MO measurements:

The samples from fig. VI-2 are analyzed performing the measurements with a transversal MOKE. From each simple two kinds of measurements should be done. On one hand, all SR and RS samples ought to be proven to present uniaxial anisotropy whereas RR samples ought to be proven to be isotropic. On the other hand, this shape anisotropy must be calculated in order to compare with the expected values from the theoretical model.

As seen in previous chapters, the Stoner-Wohlfahrt behavior of a continuous film of magnetic material no longer hold when the sample is patterned. Therefore the chosen parameter for checking the uniaxial behavior of the samples is the saturation field H_k, which is also the parameter used to calculate the shape anisotropy. Thus, the uniaxial behavior is shown using polar plots of the saturation field H_k vs. the angle between the sample and the plane of incidence. Though this angle dependency is somewhat arbitrary, all samples are measured in the same conditions, choosing as 0º the direction of the $Fe_{80}B_{20}$ hard axis (coincident with one of the elements edges). The polar plots shown in figs. VI-3, VI-4, VI-5, VI-6, VI-7 and VI-8 present the same scaling for better comparison.

The shape anisotropy of the arrays might be obtained from the MO measurement just using the difference of the saturation fields of each sample at 0º and 90º.

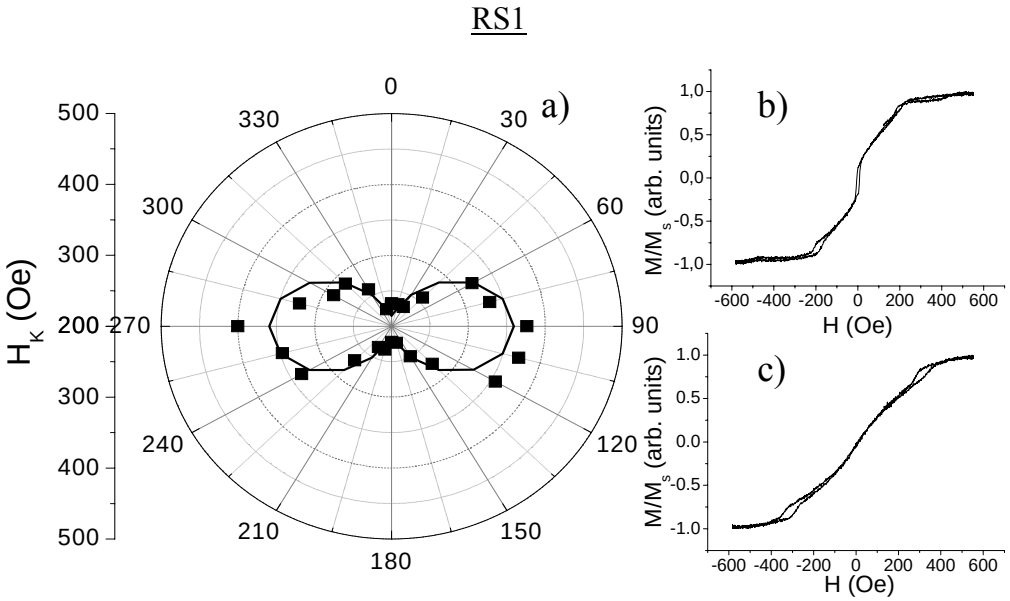

Fig. VI-3: a) Polar plot of saturation field (H_k) vs. angle between sample RS1 and the plane of incidence. The continuous line is a fitting of the experimental points to an uniaxial anisotropy. **b)** MO hysteresis loop of sample RS1 at 0º. **c)** MO hysteresis loop of sample RS1 at 90º.

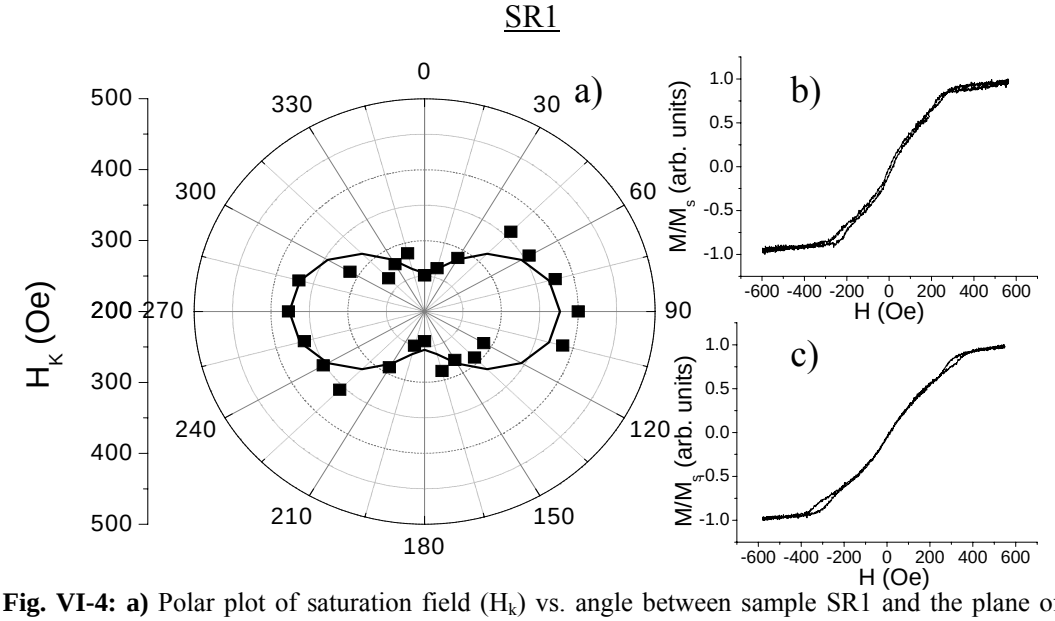

Fig. VI-4: a) Polar plot of saturation field (H_k) vs. angle between sample SR1 and the plane of incidence. The continuous line is a fitting of the experimental points to an uniaxial anisotropy. **b)** MO hysteresis loop of sample SR1 at 0º. **c)** MO hysteresis loop of sample SR1 at 90º.

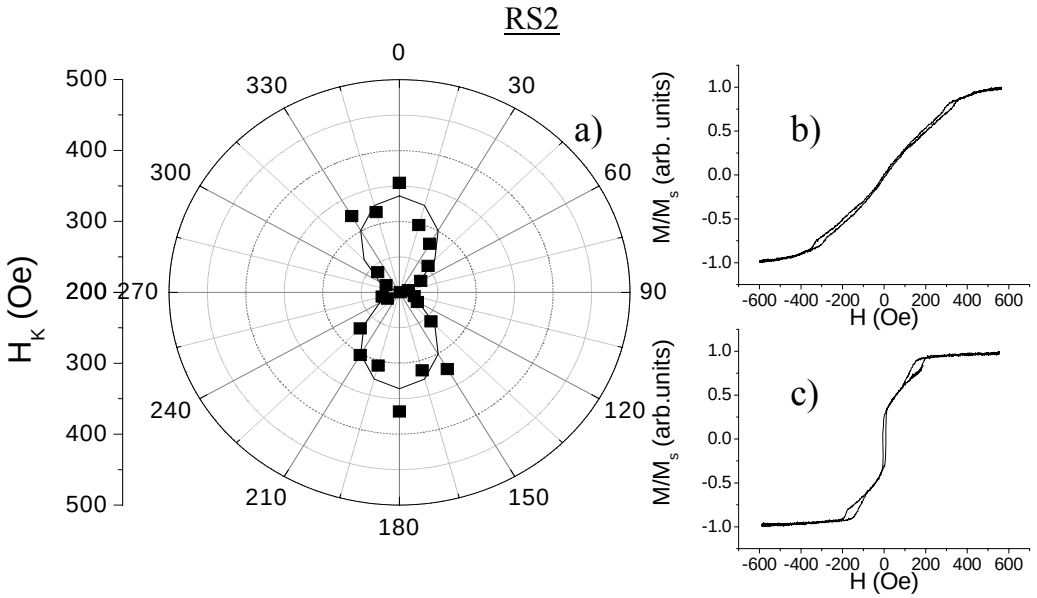

Fig. VI-5: a) Polar plot of saturation field (H_k) vs. angle between sample RS2 and the plane of incidence. The continuous line is a fitting of the experimental points to an uniaxial anisotropy. **b)** MO hysteresis loop of sample RS2 at 0º. **c)** MO hysteresis loop of sample RS2 at 90º.

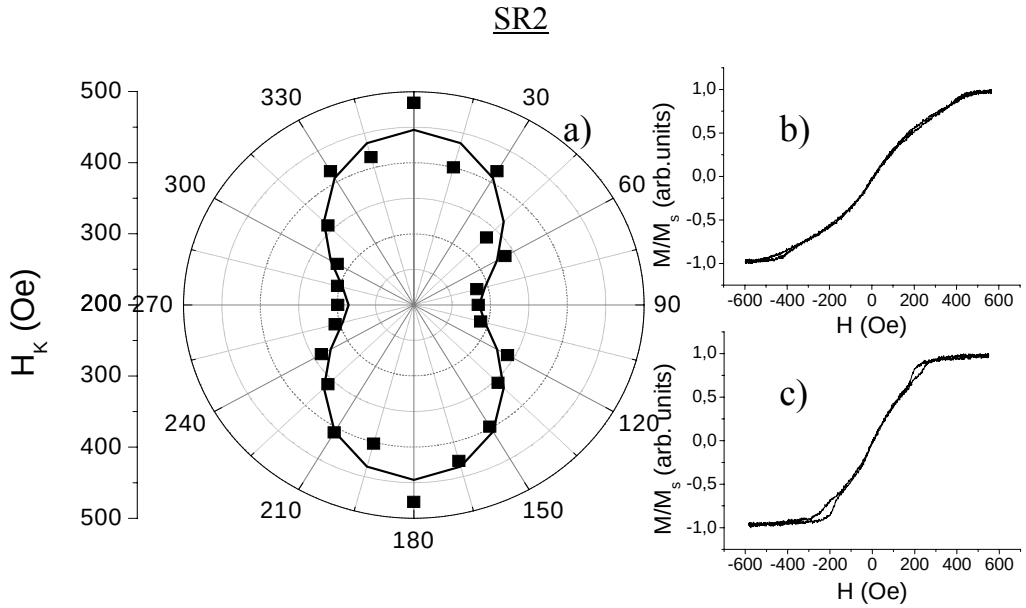

Fig. VI-6: a) Polar plot of saturation field (H_k) vs. angle between sample SR2 and the plane of incidence. The continuous line is a fitting of the experimental points to an uniaxial anisotropy. **b)** MO hysteresis loop of sample SR2 at 0º. **c)** MO hysteresis loop of sample SR2 at 90º.

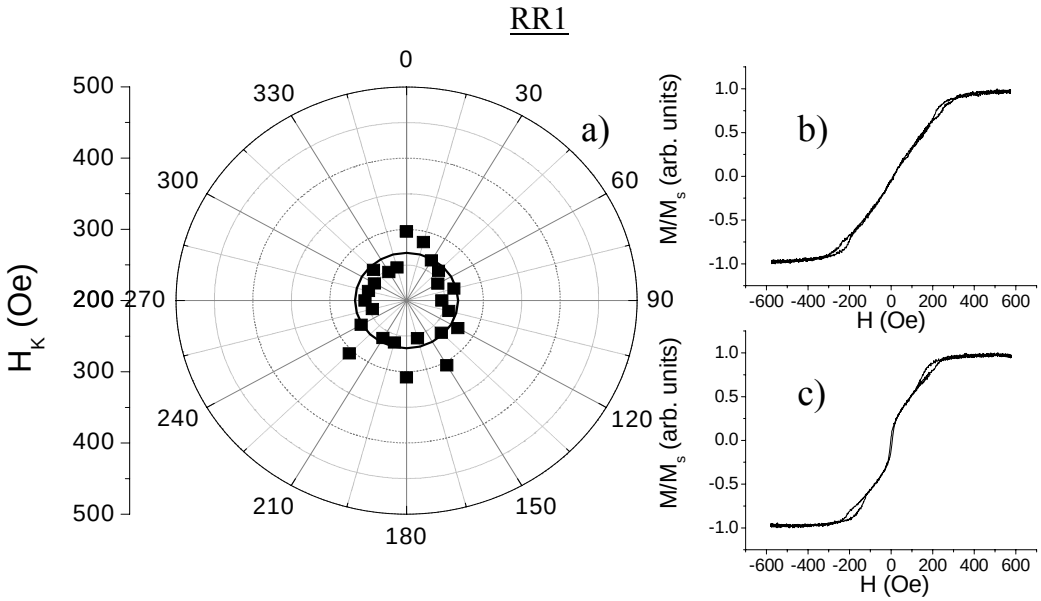

Fig. VI-7: a) Polar plot of saturation field (H_k) vs. angle between sample RR1 and the plane of incidence. The continuous line is a fitting of the experimental points to an uniaxial anisotropy. **b)** MO hysteresis loop of sample RR1 at 0º. **c)** MO hysteresis loop of sample RR1 at 90º.

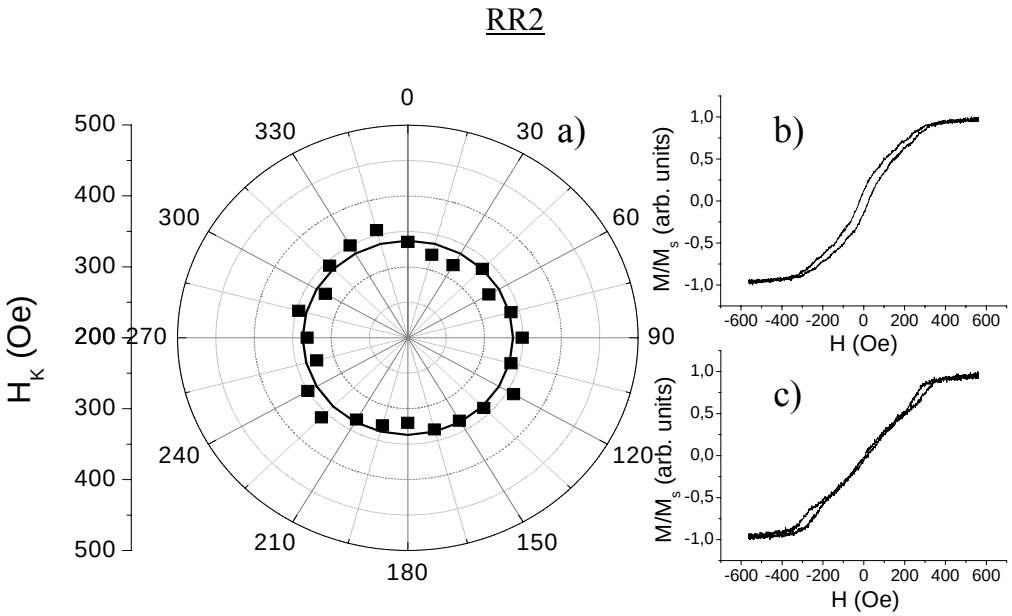

Fig. VI-8: a) Polar plot of saturation field (H_k) vs. angle between sample RR2 and the plane of incidence. The continuous line is a fitting of the experimental points to an uniaxial anisotropy. **b)** MO hysteresis loop of sample RR2 at 0º. **c)** MO hysteresis loop of sample RR2 at 90º.

The continuous line in figs. VI-3, VI-4, VI-5, VI-6, VI-7 and VI-8 corresponds to a fitting of the data to the function representing an uniaxial anisotropy:

$$H=A\cdot\cos^2\theta+B\cdot\sin^2\theta \qquad \text{(VI-1)}$$

Since the data approximately adjust to such a function, it can be stated that both RS and SR present an uniaxial anisotropy. The direction of this anisotropy is the predicted by theory regardless of the orientation of the easy axis of the amorphous $Fe_{80}B_{20}$: RS1 and SR1 are designed to exhibit an easy magnetization axis in the direction labelled 0º whereas RS2 and SR2 geometries are designed to present an easy axis in the direction marked as 90º.

As it occurs in previous chapters, the MO signal of the arrays does not resemble that of its corresponding continuous film. This occurs because patterned thin films favours flux closure within the magnetic elements. Two important consequences follows:

- the saturation field in the patterned samples is, as theoretically expected, one order of magnitude larger than the thin film one (see table VI-1), being somewhat closer to the maximum field available in the IMM transverse MOKE setup.
- Remanent magnetization does no longer provide information about the shape anisotropy and the saturation field must be used.

The expected theoretical shape anisotropy of the four arrays RS1, SR1, RS2 and SR2 is $K_S=0.1\frac{M^2}{4\pi\mu_0}=16.2$ kJ/m^3.

The experimental values for shape anisotropy in the samples RS1, SR1, RS2 and SR2 are calculated using the constants A and B of the fitting in eq. (VI-1) to the experimental data. In this fitting, A represents the maximum H_k and B the minimum saturation field, corresponding to the saturation fields in the directions 0º and 90º. The subtraction $A-B=|\Delta H_k|$ provides an estimation for the shape anisotropy in the pattern just using the equation:

$$K_S=\frac{1}{2}\left|\Delta H_k\right| M_S \qquad \text{(VI-2)}$$

The experimental values for shape anisotropy of the different patterns are shown in table VI-1.

Sample	Experimental $\|\Delta H_k\|$ (Oe)	Experimental K_S (kJ/m^3)
Continuous film	30	1.91
RS1	144	9.16
SR1	122	7.77
RS2	142	9.04
SR2	161	10.25

Table VI-1: Saturation field and shape anisotropy values for the continuous $Fe_{80}B_{20}$ and the $Fe_{80}B_{20}$ arrays RS1, SR1, RS2, SR2.

More information can be obtained from figs. VI-3, VI-4, VI-5 and VI-6. The geometries of RS1 and RS2 are identical. The only difference between this two samples is the orientation of the uniaxial anisotropy of the $Fe_{80}B_{20}$ with respect to the shape anisotropy. In RS1 both anisotropies are perpendicular whereas in RS2 they are parallel. Since both the shape anisotropy and the hysteresis loops in the different orientations of the external field are alike, it can be concluded that the influence of the anisotropy of the material is negligible. Such a result is expected since it has also been seen in Co square arrays of square elements in chapter IV (see figs. IV-3 and IV-4).

In spite of the quantitative disagreement between the expected shape anisotropy and the measured one (around half the theoretical value), the magnetostatic behavior of the samples is the predicted by the analytical model.

According to figs. VI-7 and VI-8 the rectangular arrays of rectangular elements designed with the compensation conditions (the shape of the array is given by the RS sample and the shape of the element by the SR sample, see fig. VI-2) present a saturation field independent of the magnetization direction. Therefore, RR1 and RR2 samples show no shape anisotropy. Their corresponding shape anisotropies are:

$K_{S,RR1}=0\pm1.3$ kJ/m^3
$K_{S,RR2}=0\pm0.8$ kJ/m^3

5.Summary and conclusions:

In this chapter, it has been demonstrated –both theoretically and experimentally- that, by changing suitably the array shape within the interaction range, magnetic anisotropies can be induced in arrays. This lattice shape anisotropy has been calculated, correlated with values measured in lithographically fabricated arrays, and demonstrated that such anisotropy, when array dimensions are adequately chosen, can compensate the anisotropy due to the individual element shape, making the array magnetically soft. Moreover, despite the mismatch between the theoretical predictions and the experimental data, the anisotropy value measured in the fabricated arrays is in the range predicted by the analytical model and the patterns show the expected overall magnetic behavior.

6.References:

[VI.1] P. Belobrov , R. S. Gekht and V. A. Ignatchenko., Sov. Phys. JETP **57**, 636 (1983)

[VI.2] P. Politi and M.G. Pini, Phys. Rev. B **66**, 214414 (2002)

[VI.3] W.F. Brown Jr., Phys. Rev., **105**, 1479 (1957)

[VI.4] Y. Ishii, M. Sato, J. Appl. Phys, **65**, 3146 (1989)

[VI.5] M. Sato, Y. Ishii, J. Appl. Phys., **66**, 983 (1989)

CHAPTER VII:

PATTERN TRANSFER FROM 1D AND 2D ARRAYS ONTO A CONTINUOUS FILM

Index

PATTERN TRANSFER FROM 1D AND 2D ARRAYS ONTO A CONTINUOUS FILM

1.Introduction:

According to the results of the analytical model for the magnetostatic energy presented in chapter V, the stray field and gradients of the elements embedded on an ordered array of magnetic elements is very intense in the close proximity of the surfaces of free poles. Thus, if an ordered magnetic array is fabricated on top of a magnetic thin film, this thin film might be affected by the demagnetizing field from the elements of the array. The main objective of this chapter is, therefore, to experimentally study the effect of the array on the continuous layer, paying special attention to the domain reversal in that continuous layer and its relationship with the reversal in the array on top of it. This analysis is technologically relevant for the development of magnetic random memories. Previous experiments [VII.1] using Fe/MgO/Fe magnetic tunnel junctions (MTJs) explored the possibility of performing an overetching in order to couple the magnetization of the Fe layers. In what follows it is demonstrated that no overetching is necessary to obtain antiferromagnetic coupling between two exchange decoupled ferromagnetic layers.

If the elements embedded in the pattern of the previously mentioned heterostructures are large enough, a Kerr microscope like the one described in chapter II is the most suited tool to monitor the spatially resolved magnetization reversals. Moreover, the information from the Kerr microscope can be compared with MOKE measurements.

The previously mentioned experiments before will serve to answer the main questions proposed in this chapter:

- Are the domains in the patterned side correlated to the domains in the continuous side of a sample consisting on an ordered array on top of continuous thin film?
- Are the magnetostatic interactions from the array strong enough to transfer the domains from the patterned side to the continuous film?
- In case the previous question is affirmatively answered, is there any diffraction effect in the continuous film due to the domain transfer?

2.Samples design and fabrication:

In order to answer the proposed questions some structures consisting on a pattern over a continuous thin film are fabricated.

A transparent substrate is used in order to measure the magneto-optic response of the heterostructures in both the pattern and the continuous film. The thickness of the continuous thin film should be large enough to achieve opacity when using laser light. Fabricating an opaque continuous film ensures that the pattern does not optically and magneto-optically influences the flat surface, thus guaranteeing that the observed effects are due exclusively to the continuous film. Accordingly, a 80 nm thick Co continuous layer is grown by triode dc sputtering. This thickness guarantees optical opacity for a 633 nm wavelength 1.5 mW laser light. Indeed, the transmittance of this film was measured to be less than 10^{-5}.

Between the pattern and the continuous film a non-magnetic layer of chromium is grown in order to exchange decouple the two magnetic layers. Since exchange coupling is a short range interaction, the interlayer non-magnetic film can be thin enough to enhance the magnetostatic interactions between pattern and thin film while preserving the two layers exchange decoupled. Accordingly, a 6 nm thick Cr film is grown after the continuous layer and before the pattern is fabricated.

In chapter V, section 11, the demagnetizing field due to a 180º Bloch domain wall was studied. In particular the demagnetizing field values as a function of the thickness of the thin film and the distance from this film were presented (see figs. V-16, V-18 and V-19). According with this theoretical prediction, any 180º Bloch wall in the flat surface creates a stray field actuating on the elements of the pattern (separated, as previously said, from the flat surface by a non-magnetic 6 nm thick Cr thin film) of more than 2 kOe.

In this case, the preferred situation consists of a magnetostatic interaction of the domains within the magnetic elements of the patterning in the continuous film. Since the stray field at any distance from the free poles increase with the thickness of the material (figs. V-18 and V-19), the thickness of the elements embedded in the pattern should be larger than the thickness of the flat surface, i.e., more than 80 nm.

Unfortunately, according to fig. V-17, the magnitude of the stray fields corresponding to thicknesses above 80 nm are very similar when the separation of the layers is around 10 nm. In particular, if the thickness of the pattern is chosen

to be twice the thickness of the continuous film, its corresponding stray field is only 6% larger than the stray field of the continuous film. Anyway, reversals are directly related with energetic balances (in which magnetostatics are present) and just indirectly associated to stray fields.

Later on, it will be studied by means of Kerr microscopy whether this difference is large enough for our interests.

Henceforward, the two sides of the sample will be termed the patterned and the flat sides (see fig. VII-1).

Two types of structure will be discussed in detail: arrays of Co microstripes on top of a continuous Co layer (1D heterostructures) and arrays of Co (Fe) microsquares on top of continuous Co (Fe) (2D heterostructures). Typical array element sizes and array periodicities are chosen in the micrometer range. This size allows magnetic domain visualization with a conventional Kerr microscopy setup, and the array periodicity generates diffracted beams at conveniently spaced angles.

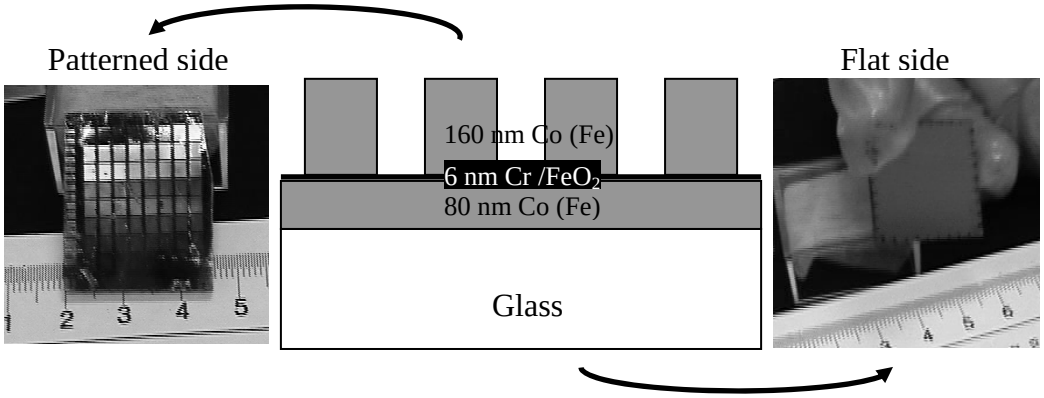

Fig. VII-1: Center: Sketch of the structures fabricated. On a glass substrate, a 80 nm thick Co (Fe) thin film is sputtered. Then a chromium/Fe_oxide 6 nm thick interlayer is grown. On top of it the 1D/2D structure is fabricated by optical/e-beam lithography. Left: Photo of the patterned side of one of the 1D heterostructures fabricated. Right: Flat side of the same sample. The marks in the corner are drawn to locate the position of the lithographies when performing the measurements.

2.1 Fabrication of 1D heterostructures

The 1D heterostructures are microfabricated by optical lithography on a continuous 80 nm thick film of polycrystalline Co sputtered on glass. Both the patterned and the flat surfaces are grown with Co by triode sputtering. As said before in previous chapters, the plasma confining field in the triode sputtering yields an uniaxial anisotropy in the direction of that field. The easy magnetization axis of the Co of the patterned side is always along the direction of the stripes short axis in order to yield surfaces of free poles. The easy axis of the Co of the flat side can be parallel or perpendicular to the stripe long axis in order to study if there is any effect of this antiparallel configuration in the MO response. Hence, the samples named PePe, whenever both easy axis of the magnetization are perpendicular to the stripes long axis; or PaPe if the easy magnetization axis of the continuous film is oriented parallel to the stripes long axis.

The mask used consists of stripe patterns with widths in the range 2-100 μm and inter stripe spacing from 4 to 8 μm. Specifically the patterns used are 100_8, 50_8, 25_8, 12_3, 6_3, 4_4, 2.5_4, where the first number denotes the stripe width and the second the stripe to stripe separation, both in μm.

Thus, the 1D heterostructures labeling is defined as follows: first the array width, then the array interspacing and finally the direction of the Co anisotropy axes with respect to the stripe long axis for both the continuous layer and the stripe pattern –using Pe for perpendicular and Pa for Parallel–. This way, the structure named "50_8 PePe" is a sample in which i) the stripes are 50 μm width separated 8 μm and ii) the anisotropy of the continuous Co is perpendicular to the stripe long axis in both the continuous layer and the stripe pattern. However "50_8 PaPe" represents a structure with the same dimensions but with the anisotropy of the continuous Co layer parallel to the stripe long axis.

2.2. Fabrication of 2D heterostructures

The second type of samples are 2D arrays of Fe (Co) squares on top of a continuous Fe (Co) layer. The Fe continuous layer, also grown by DC triode sputtering, is consistent with the Stoner-Wohlfarht model with an anisotropy field of 10 Oe (see fig. VII-2). The arrays consist of squares of edge size in the range 80 - 15mm, and inter-squares width from 20 mm to 3 mm. Assuming the same 1D heterostructures labeling, the following 2D structures are fabricated: 80_20, 60_10, 30_5 and 15_3. The micro-structured arrays are fabricated by e-beam lithography over a 1.2 mm PMMA thick layer, in a 400x400mm^2 working area.

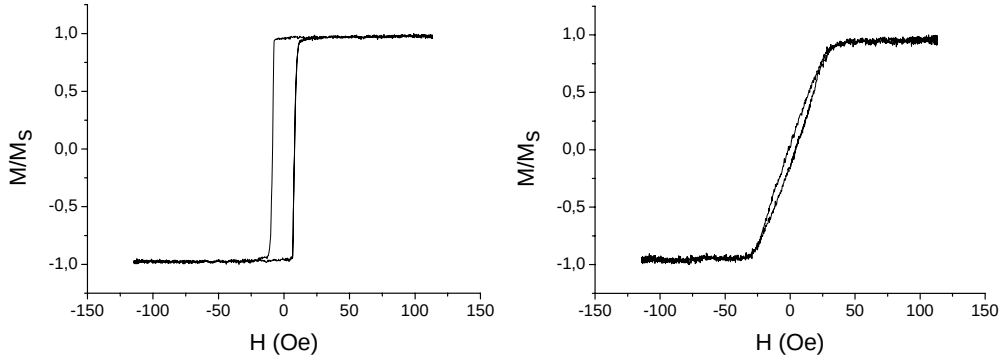

Fig.VII-2: Hysteresis loops of polycrystalline Fe. The material presents an uniaxial anisotropy with a coercive field of 8 Oe (left plot, easy axis) and an saturation field of 30 Oe (right plot, hard axis).

In the case of the structures created by e-beam lithography (2D heterostructures) the square array is exchange decoupled from the continuous film by an intermediate 6 nm thick sputtered Cr layer (when using Co) or by a Fe oxide layer (when using Fe) created by oxygen plasma (at 50 W during 5 minutes).

The structures fabricated as explained during this section allows magneto-optic measurements both when illuminating from the patterned side or from the flat side (fig. VII-1). At magnetic saturation the patterned side reflects and diffracts while the flat side just reflects.

3.MOKE measurements:

Transverse magneto optic Kerr effect (TMOKE) measurements are performed by illuminating with a 633 nm He-Ne laser both sides of our heterostructures. The incidence angle is 60º, and the spot diameter is focused in such a way that illuminates most of the chosen pattern. This way, the measurement will provide information of the average magnetic behavior of the motif.
The magnetic field is applied perpendicular to the stripes long axis in 1D structures and parallel to both square edges directions in 2D structures. In the latter case, it will be distinguished between 0º and 90º orientations. The first one accounts for an external field applied in the direction of the easy axis of the

material, whereas in 90º orientation the field is applied perpendicular to the easy axis of the material.

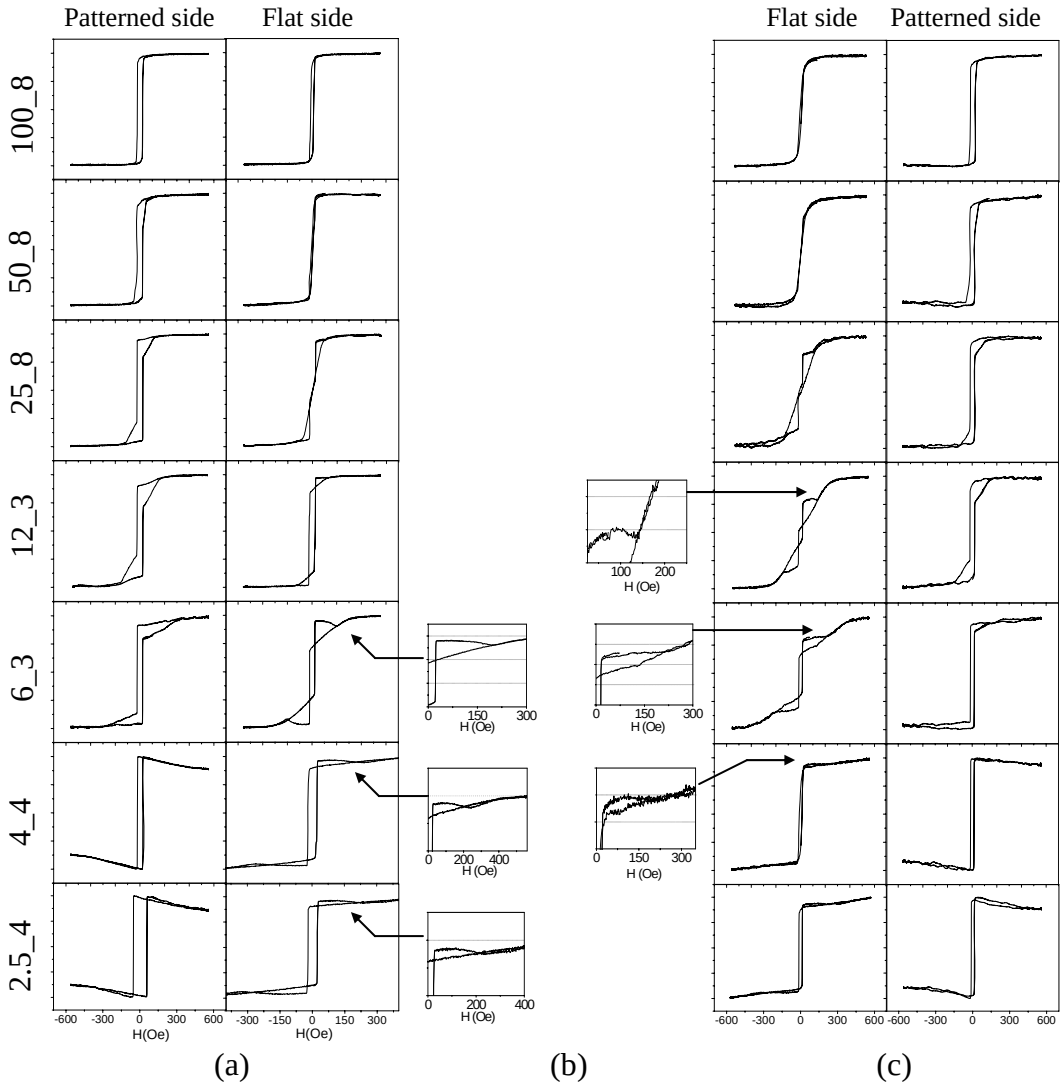

Fig. VII-3. Conventional transverse MOKE measurements (relative magnetization M/M_S vs. external field H) for Co/1D Co heterostructures, illuminating at both sides of the sample. (a) Patterned side and flat side hysteresis loops corresponding to "PePe" structures. The Co anisotropy for both the stripes and continuous layer, are perpendicular to the stripes long axis. (c) Flat side and patterned side hysteresis loops corresponding to "PaPe" structures. The easy axis for the Co stripes is parallel to the stripes, but the continuous layer anisotropy remains perpendicular to the stripes. (b) Central insets: details of the flat side of "6_3 PePe", "4_4 PePe", "2.5_4 PePe", "12_3 PaPe", "6_3 PaPe" and "4_4 PaPe", the hysteresis loops that exhibit a negative differential susceptibility when illuminating at flat side.

Fig. VII-3 reviews conventional MOKE measurements for "Co/1D Co" heterostructures. The left side shows the hysteresis loops –when illuminating at both the flat and the patterned sides– obtained for the heterostructures whose easy axis is perpendicular to the stripe long axis (PePe structures). The right side shows the result for the structures with the stripes Co easy axis parallel to the stripe long axis (PaPe structures). The applied magnetic field is enough to achieve magnetic saturation except perhaps for the narrowest stripes (4_4 mm and 2.5_4 mm structures). In these particular cases, where the stripes width and separations are close to the patterning threshold of the optical lithography, most of the motifs are rather irregular or even badly damaged.

From Fig. VII-3 it is clear that the hysteresis loops illuminating each side of the structure are different. This is consistent with the fact that the micro-element arrays are exchange decoupled from the continuous layer. The continuous layer is opaque at this wavelength and, consequently, when illuminating the patterned side we obtain information about the stripes magnetization plus the interstripe contribution. But when illuminating the flat side only the continuous film magnetization is measured. The saturation field increases as the stripe width decreases as expected from magnetostatic considerations. On the other hand, the stripes easy axis orientation with respect to the anisotropy axis of the continuous layer seems not to play an important role as the corresponding measured PePe and PaPe loops are qualitatively similar. For bigger stripe lateral dimensions and interstripe spacing, the coercive field varies in a narrow range of approximately 17 Oe, but the saturation field is quite sensitive to these changes.

The above arguments are general, but there are interesting features that deserve to be examined in detail. Some of these structures, when illuminating the flat side, display hysteresis loops with a negative differential susceptibility (see fig. VII-3.b). This points to the growth of domains with the magnetization oriented opposite to the applied magnetic field direction. The most plausible explanation of this behavior is the formation of an inversion domain underneath the stripes, due to the magnetostatic energy reduction. In fact, it can be seen that the negative differential susceptibility appears more clearly in the structures in which the interstripe represents a larger percentage of the total area.

This interesting finding is studied in what follows monitoring the reversals by means of Kerr microscopy.

4.Kerr microscopy analysis of 1D structures:

Both the patterned and the flat side are monitored during reversals using the homemade Kerr microscope at the IMM described in chapter II.

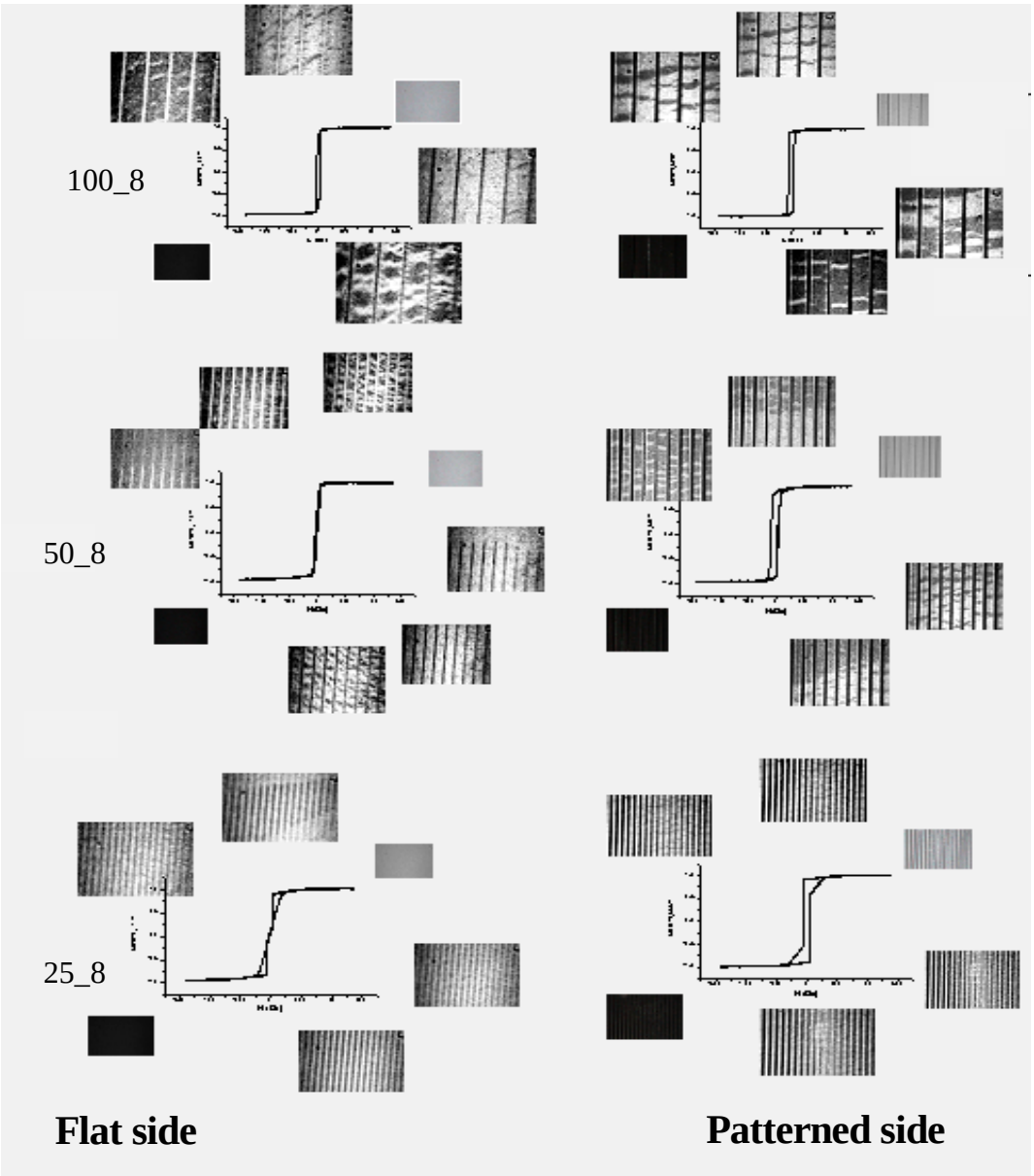

Figure VII-4: Magnetic domain images and its corresponding hysteresis loops for some structures Co/1D Co. Observing through the glass substrate, it can be seen that a periodic domain structure is generated in the flat ferromagnetic thin film at certain field values.

After recording a whole loop using a sinusoidal field at 10 mHz, the 100 seconds video has been edited and certain frames have been selected for further image processing. The processing consists of a contrast enhancement by subtracting the image corresponding to saturation magnetization from a domain image at a certain field value.

The results, shown in fig. VII-4, are compared with its corresponding hysteresis loops from fig.VII-3. Due to the limited optical power of the Kerr microscope, the domain reversal can only be properly monitored in the largest structures, where the domains are clearly visible and no diffraction effects of the incident light distorted the images.

As previously seen when analyzing the hysteresis loops from fig. VII-3, the anisotropy orientation for the Co layers in the structure "Co/1D Co", i.e., the PePe and PaPe structure, plays a minor role so the discussion can be henceforward restricted to heterostructures with both easy axis perpendicular to the stripes long axis (“PePe”).
According to the measurements in fig. VII-4, the suspicion of an inversion domain beneath the stripes is corroborated. It can be seen in the different images that no matter the dimensions of the stripe, an exact replica of the patterned side is yielded in the flat side.

According to what is shown in fig. VII-5 (b) the reversal mechanism in the patterned side basically consists on a nucleation of domains along the stripes, separated by 180º Bloch domain walls. As the external field increases, these domains propagates all along the stripes till saturation.

The reversal in the flat side can be divided in four different steps:

- The first one is a small coherent rotation of the flat side as a whole
- In a second step, the rotation continues excepting the area corresponding to the interstripe surface, that became visible with an orientation opposite to the field direction.
- The third step consists in nucleation and propagation of 180º domains. But the nucleation of domains is produced only in the area underneath the stripes, as it can be clearly seen in fig. VII-5 (a) in both orientations of the magnetization.

Once the domains in the flat side exhibits a complete replica of the stripes, the area of the continuous film under the interstripe begin a rapid reversal also by domain propagation.

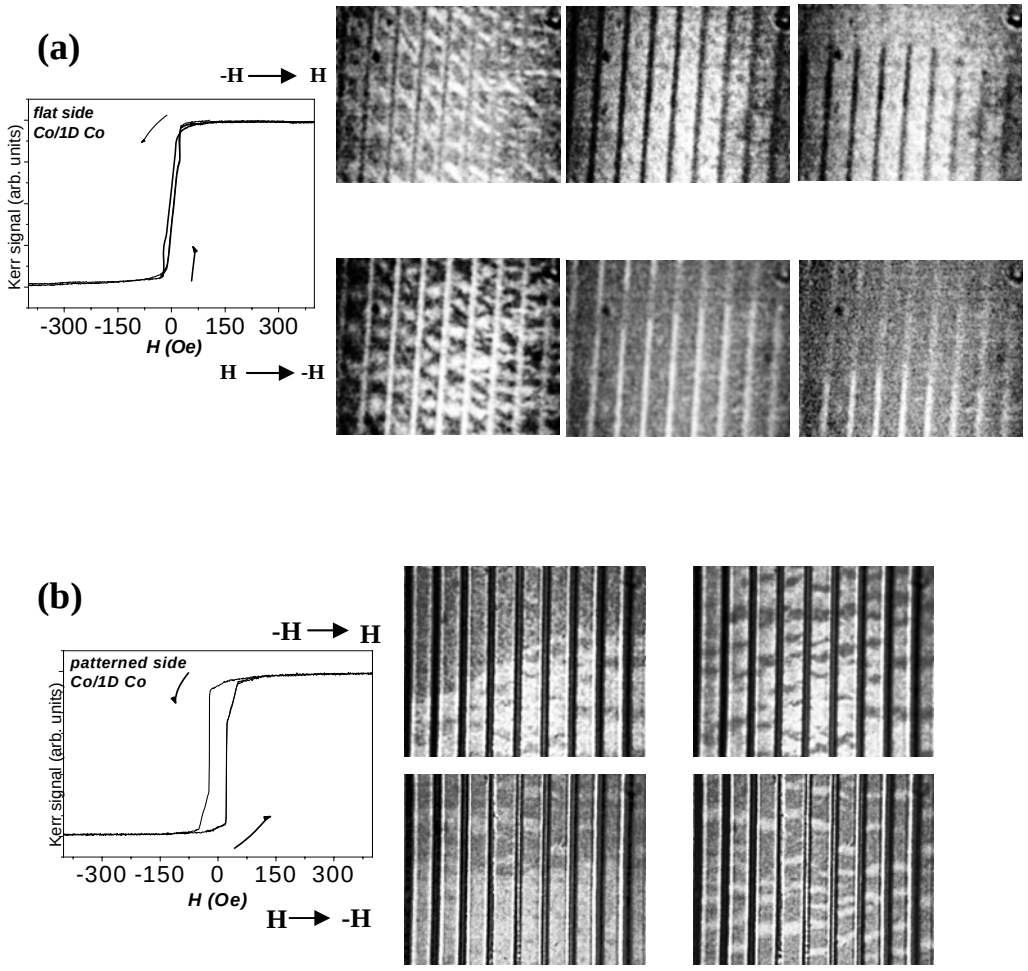

Fig. VII-5: Magnetic domain images related to conventional hysteresis loops for the heterostructure "50_8 PePe Co/1D Co", illuminating either at flat (a) and patterned (b) sides. Images show some domain distributions when the applied field drives the magnetization from positive saturation to negative saturation and back. Observing through the glass substrate, we can see that a periodic domain structure is generated in the flat ferromagnetic film at certain field values (a). According to the longitudinal Kerr geometry used, the external field in all the images is applied perpendicular to the stripes long axis.

Thus, the behavior of the interstripe area is markedly different from the under-stripe area. Indeed, all the interstripe areas seem to behave coherently and unconnected to the under-stripe zones. Once again is worthy to stress that at selected field values a domain replica of the periodic topographic structure is observed, i.e., all the magnetization under the stripe is aligned antiparallel to the interstripe area. This is a pure magneto-optic grating. Taking into account that when the sample is saturated the continuous layer only reflects, illuminating one of these periodic domain structures, diffraction spots at regular positions due to the pattern periodicity are expected to appear at the same diffraction angles than the diffraction spots yielded by the patterned side.

The reversal in both sides of the sample are closely related. In fig. VII-6, the average magnetization of the flat side (proportional to its MO signal) is plotted as a function of the average magnetization in the patterned side. The plot is made in such a way that each (x,y) coordinate of the figure correspond to a given external field value.

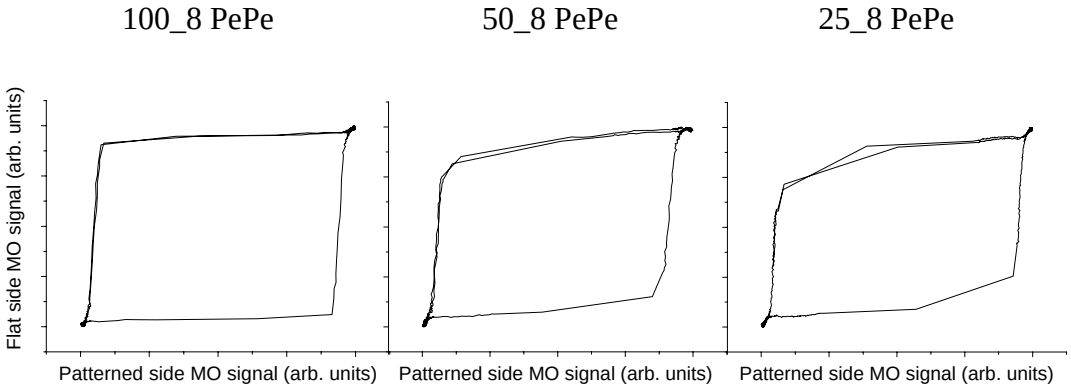

Fig. VII-6: Patterned side MO signal vs. Flat side MO signal for the three cases analyzed in fig. VII-4, i.e. 100_8, 50_8 and 25_8 PePe heterostructures. The points in all the three plots corresponds to values of average magnetization for a given external field value.

According to fig. VII-6, the first part of the reversal consist of a more or less extended zone in which the magnetization in both sides of the sample smoothly

increases, corresponding to the rotation previously described. As the external field increases, the average magnetization in the patterned side increases. This increment is due to domain propagation and corresponds to the steepest zone of the hysteresis loop. While the reversal is occurring in the patterned side, the flat side remains with a constant magnetization. The onset of the reversal in the flat side is produced when the patterned side is almost saturated. This reversal is also steep according to the hysteresis loops (see fig. VII-3) and is due to domain propagation (see figs. VII-4 and VII-5). Once the propagation has concluded, which corresponds to a situation in which only the interstripe area has an opposite-to-field magnetization, both sides of the sample saturates simultaneously in the direction of the external field.

As it can be seen in the loops of fig. VII-3 and fig. VII-6 and in the images of fig. VII-4 and fig. VII-5, although not reversible, the reversal is symmetric in the other direction.

5.Kerr microscopy analysis of 2D structures:

An analogous study might be performed in the case of 2D structures for two different materials, Fe and Co.

5.1.Co/2D Co heterostructures

Fig. VII-7 show the hysteresis loops of the 2D Co structures and Kerr microscopy images of the domain distribution for different field values. As in the case of the 1D heterostructures, the switching external field is set to a frequency of 10 mHz. The external field is applied along the squares edges, distinguishing two different orientations. In the 0º orientation both the external field and the anisotropy direction of the material are parallel whereas in the 90º orientation this orientations are perpendicular.

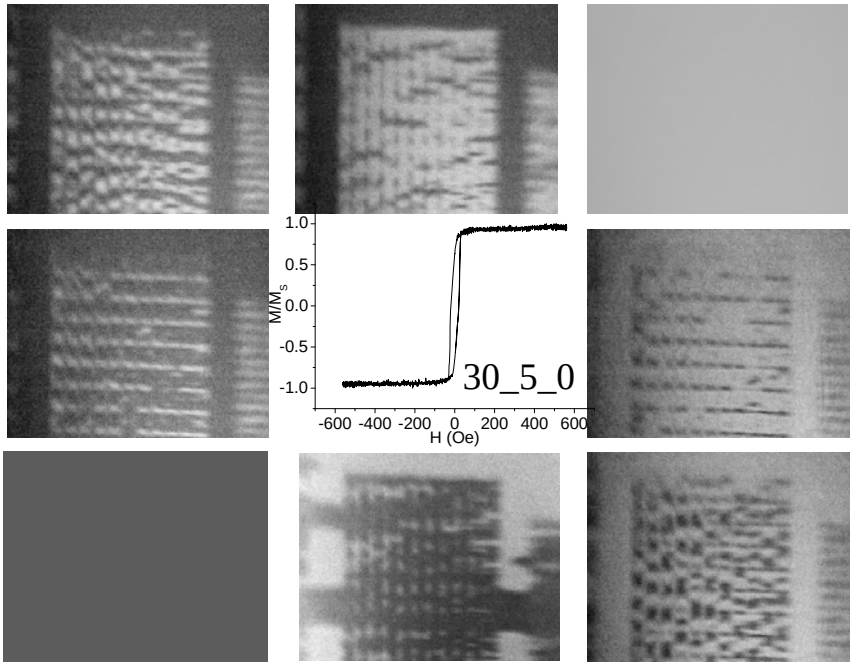
1.0
0.5
0.0
-0.5
-1.0
M/M_S
-600 -400 -200 0 200 400 600
H (Oe)
30_5_0

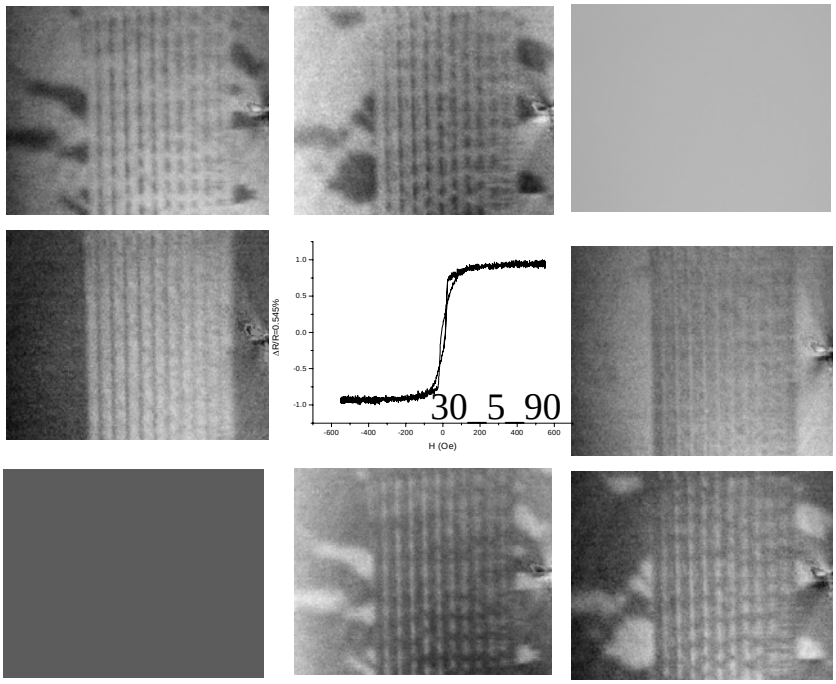
30_5_90
H (Oe)

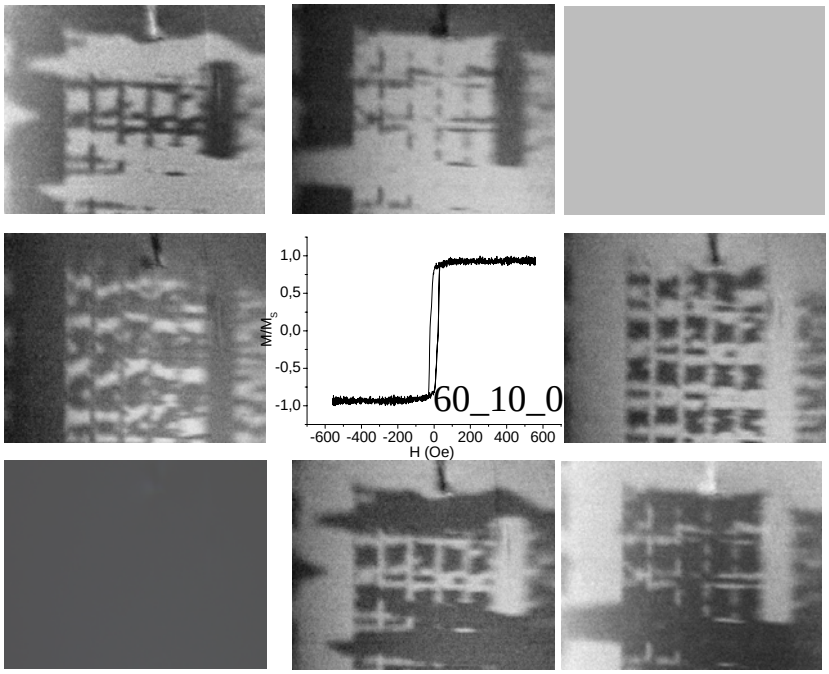
1,0
0,5
0,0
-0,5
-1,0
M/M$_S$
-600 -400 -200 0 200 400 600
H (Oe)
60_10_0

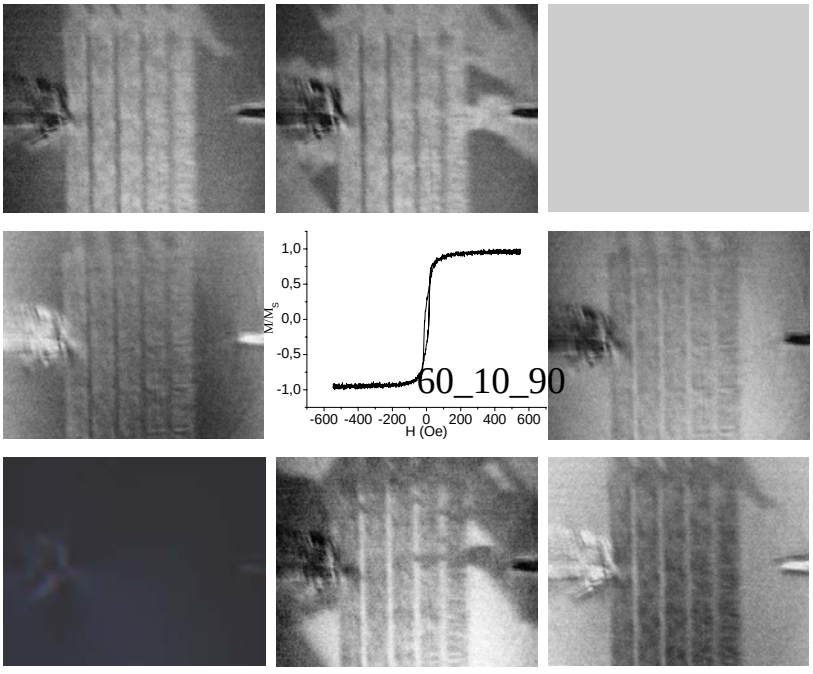
1,0
0,5
0,0
-0,5
-1,0
M/M$_S$
-600 -400 -200 0 200 400 600
H (Oe)
60_10_90

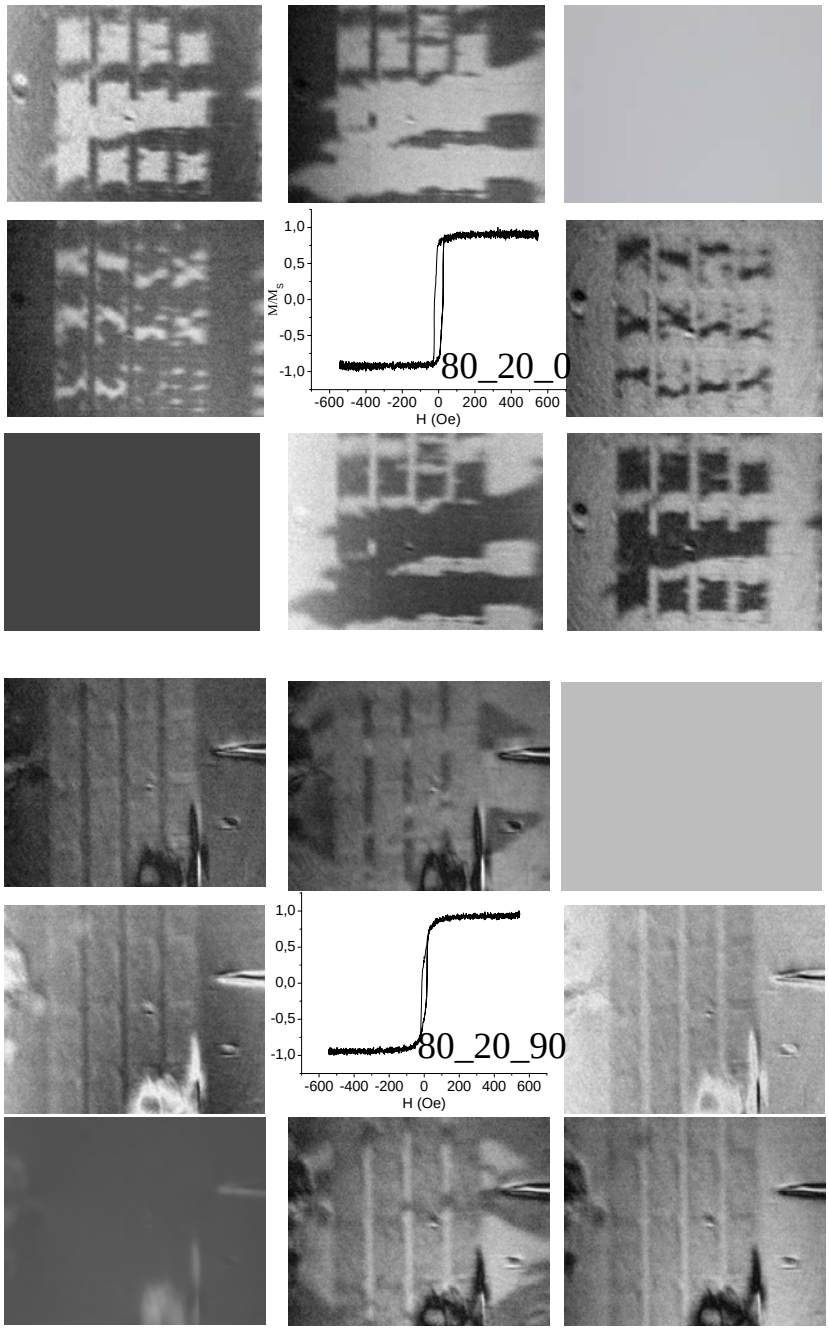

Fig. VII-7: Some images for the samples Co/2D Co, illuminating through the glass substrate. a) Applying the external field parallel to de Co easy axis. The images are related with the conventional hysteresis loops (average information); however we can obtain local information about magnetization inhomogeneties; b) applying the external field perpendicular to the Co easy axis, twice per loop a periodic domain structure appears. Notice that it is clearly different applying the field perpendicular or parallel to the Co anisotropy axis.

5.2.Fe/2D Fe heterostructures

In fig. VII-8, the same study is presented for identical 2D structures but changing the sputtered material to Fe.

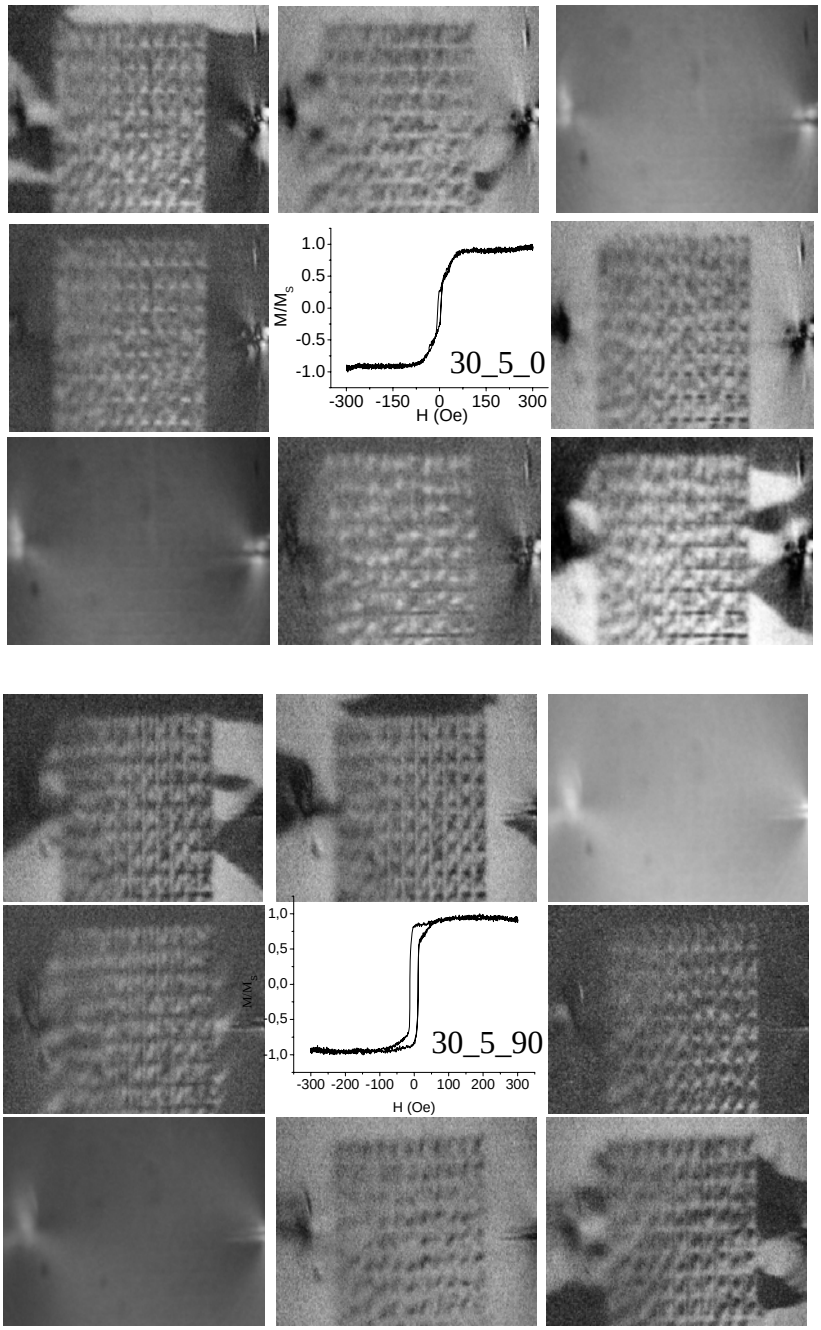

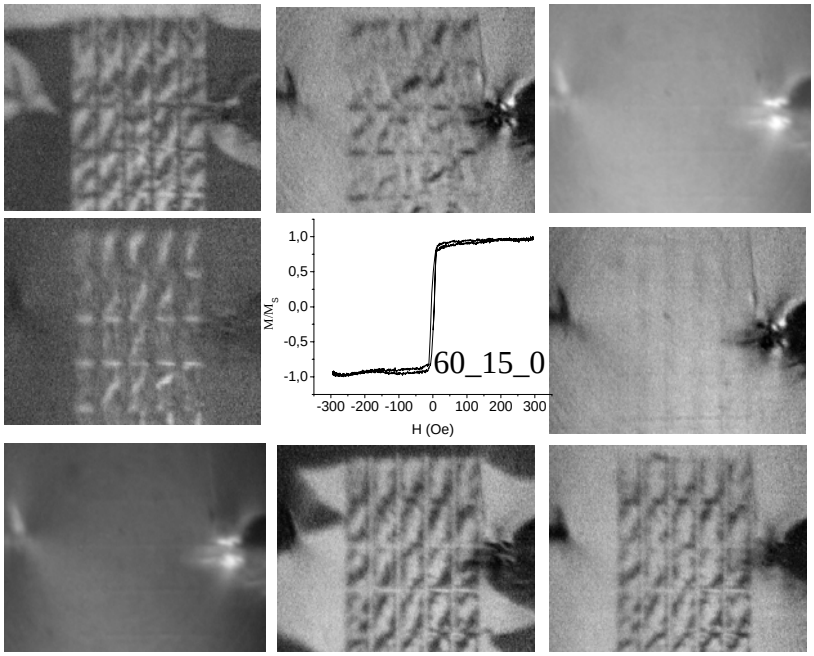
1,0
0,5
0,0
-0,5
-1,0
M/M$_S$
-300 -200 -100 0 100 200 300
H (Oe)
60_15_0

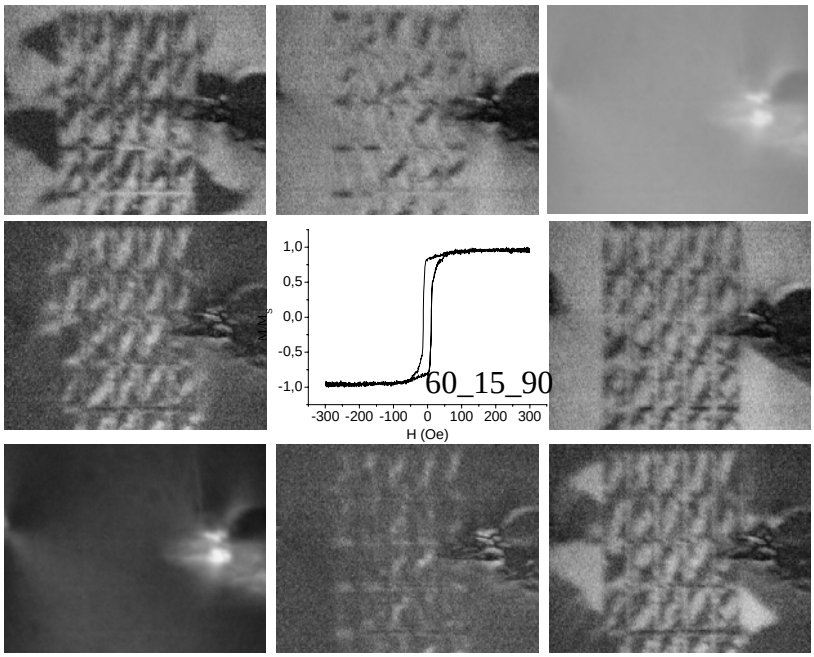
1,0
0,5
0,0
-0,5
-1,0
M/M$_S$
-300 -200 -100 0 100 200 300
H (Oe)
60_15_90

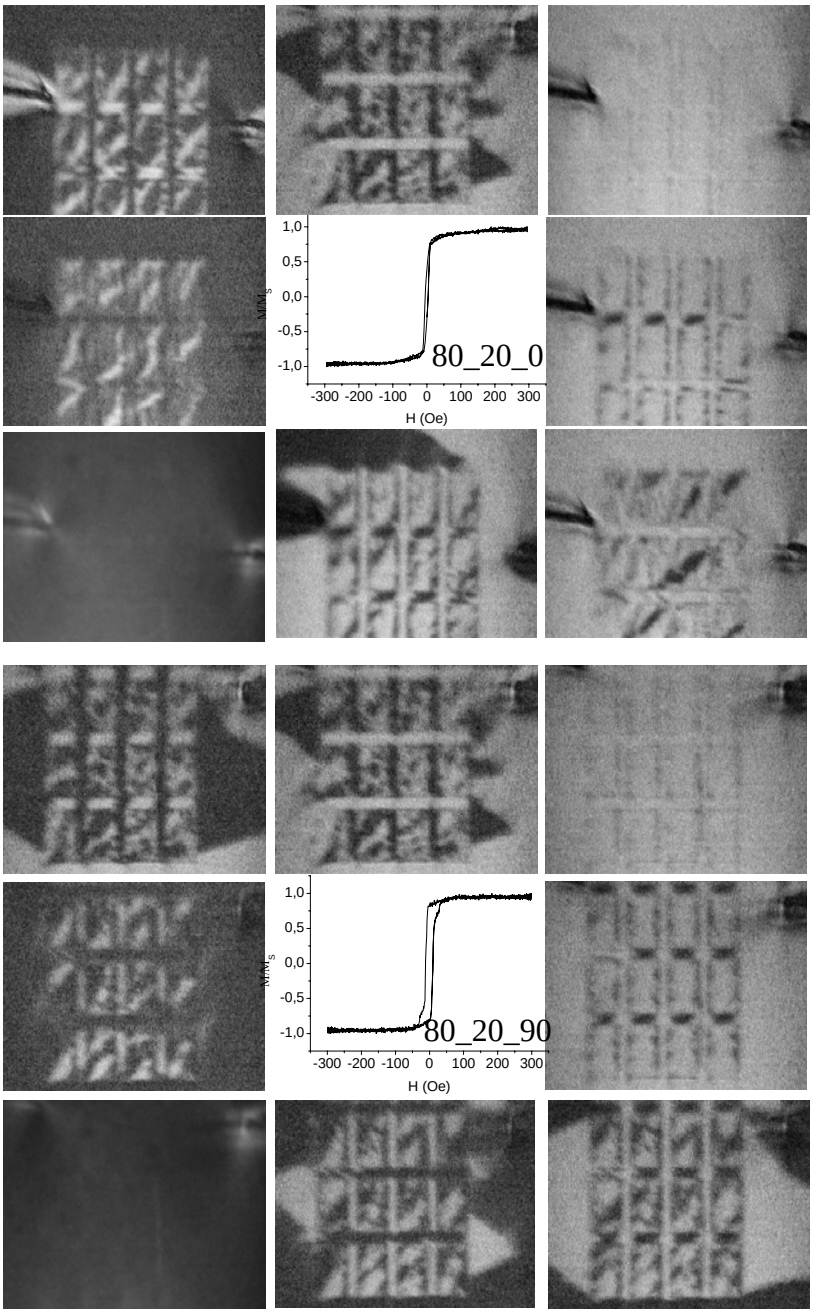

Fig. VII-8: Some Kerr microscopy images of the flat side of the heterostructures Fe/2D Fe and its corresponding hysteresis loops. In these cases the structure is broken in smaller domains and no periodic structure is reported. The observations applying the field perpendicular and parallel are basically the same (magnetization leads to a diagonal domains orientation). However, the domain structure illuminating at patterned side is markedly different (exchange coupling is not operative).

Figs. VII-7 and VII-8 show Kerr microscopy images with its corresponding hysteresis loops for similar measurements in "Co/ 2D Co" and "Fe/ 2D Fe" heterostructures. As explained before, the fabrication process for these heterostructures guarantee that exchange coupling is not operative between the pattern and the continuous layer.

5.3. Magnetization reversals in the 2D heterostructures flat side

The external magnetic field produces magnetic free poles at saturation at the surfaces perpendicularly oriented to the applied field. In fig. VII-8 ("Fe/2D Fe" heterostructure) both the 0º and 90º orientations shows similar domain structures during a complete field cycle, whereas in the case of "Co/2D Co" the domain structures are not similar (see fig. VII-7). This might be due to small differences in the interelement distances along different directions or, most probably, to the effect of the Co uniaxial anisotropy.

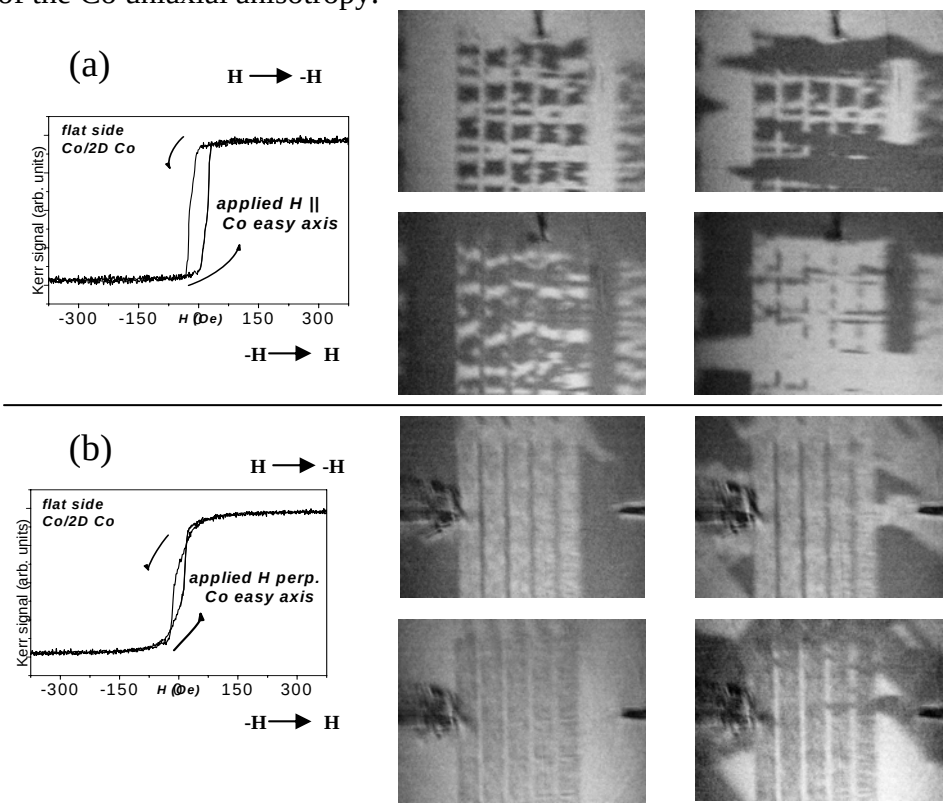

Fig. VII-9: Hysteresis loops and domain images at selected field values for heterostructures 60_10 (Co/2D Co) illuminated through the glass substrate. (a) Images at 0º orientation, i.e., when the external field is applied parallel to Co easy axis; (b) Images at 90º orientation, i.e., when the external field is applied perpendicular to Co easy axis. Notice the different patterns when applying the field perpendicular or parallel to the Co anisotropy axis.

In fig. VII-9, it can be seen that the most clear periodic domain replica of the Co/2D Co heterostructures are observed in the 90º orientation, i.e., when applying the external field perpendicular to the Co easy axis. However, the Fe/2D Fe heterostructures presents a very different behavior (fig. VII-10). In these structures, no matter the chosen orientation, a group of diagonal domains appear under the square magnetic elements of the patterned side.

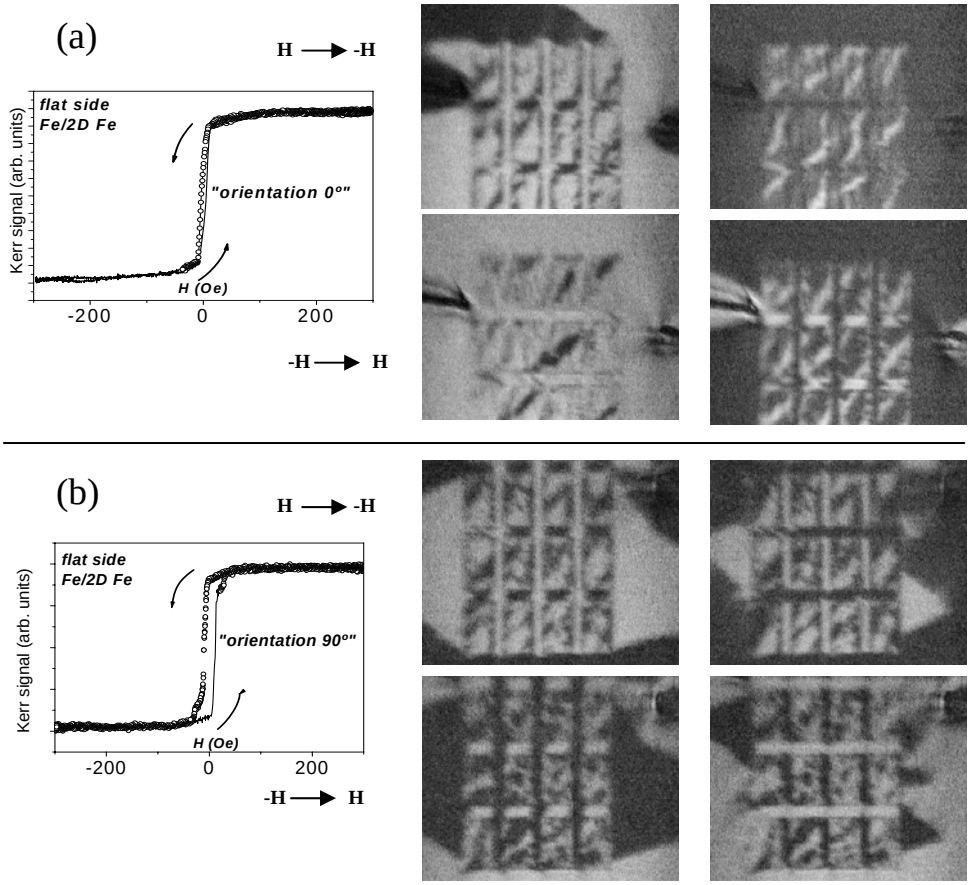

Fig. VII-10: : Hysteresis loops and domain images at selected field values for heterostructures 80_20 (Fe/2D Fe) illuminated through the glass substrate. (a) Images at 0º orientation, i.e., when the external field is applied parallel to Fe easy axis; (b) Images at 90º orientation, i.e., when the external field is applied perpendicular to Fe easy axis. Notice the similarities of the different domain patterns when applying the field perpendicular or parallel to the Fe anisotropy axis.

In all cases the inversion process is as follows: First, an inversion underneath the topographic pattern followed by a domain nucleation and propagation. This domain propagation is responsible for the big jumps observed in the hysteresis loops. All the images in figs. VII-9 and VII-10 are taken in the nearby of the 0 Oe field, just before and after these big jumps in the hysteresis loops occurs.

The domain structure in the flat side of the Co/2D Co heterostructure in the 0º orientation shows a feature not present in the rest of structures and orientation. It consist in a combination of the domain propagation corresponding to the under-square area with the domain propagation of the continuous film. In the rest of the cases, even at near-to-saturation the replica of the patterned side is still visible.

6. Pure Magneto-optic diffraction. The lighthouse effect:

It has been studied that the flat side of the presented heterostructures show at certain field values domains replica of the structure in the patterned side. This behavior leads to the suspect that diffraction spots might appear when illuminating the flat side. These diffraction spots, if any, should not be intense because they are consequence of domain contrast. Since the relative MO reflectivity ($\Delta R/R$, the ratio between the MO signal and the total reflectivity) in both Fe and Co is around 0.5%, the intensity of the diffraction spot is, at most, 1% of the intensity of the reflected spot. Therefore, all those lattices producing diffraction spots close to the reflected one should be avoided for this experiment. Also the diffraction spots at large distances from the reflected spot are somewhat troublesome since the diffraction beams might illuminate the coils and, thus, cannot be measured.

6.1. Diffraction spots from the flat side

Due to the difference in intensity between the reflection and the diffraction beams, the effect cannot be directly see. In order to properly appreciate the effect, a diffusive screen is used (see fig. VII-11). The intensity of the direct (reflected) spot must be attenuated. Thus, an opaque adhesive tape is placed in the diffusive screen where the reflected beam illuminates (fig. VII-11, left image). Setting the sweeping frequency of the external field to an intermediate value (between 0.1 and 2 Hz), a diffraction spot can be clearly seen blinking twice per loop (fig. VII-11, right image).

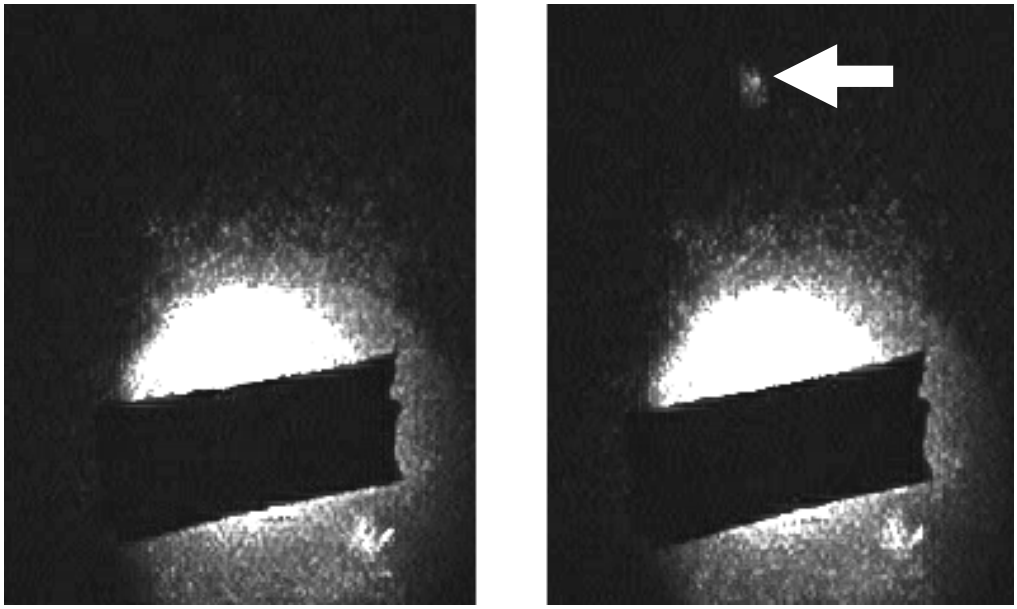

Fig. VII-11: When the heterostructures are illuminated on the flat side, a diffraction spot (corresponding to the domains replica of the pattern) appears. This diffraction spot appears only twice per loop at selected field values. Thus, this diffraction spot (right image, signaled with a white arrow) blinks much like a lighthouse. This effect can only be seen through a diffusive screen attenuating the reflection spot (left image).

According to what has been explained, these diffraction spots appearing when illuminating the flat side at selected field values can be tentatively attributed to the periodic domain structure in the flat continuous magnetic film (reported in the previous sections). This assumption is supported by the different magnetic behaviors observed when the magnetic 2D array is exchange coupled or decoupled to the continuous magnetic film, and by micromagnetic simulations. All this will be thoroughly analyzed in the following section of this chapter.
Anyway, the assumption is supported by the fact that the angular position of the diffraction spot corresponds to the periodicity of the array. Note also that this lighthouse diffraction spot appears in the corresponding position (according to the dimensions of the array) regardless of the material used, and in spite of the reversal mechanism present (as previously said, Fe/1D Fe and Co/1D Co heterostructures show different reversals).

Once localized these diffraction spots that blink much like a lighthouse when the magnetic field switches, the photodiode can be placed at the corresponding

angular position. Thus, the diffracted light dependence on the applied magnetic field can be measured by means of transversal DMOKE (fig. VII-12).

6.2.DMOKE in "lighthouse" beams

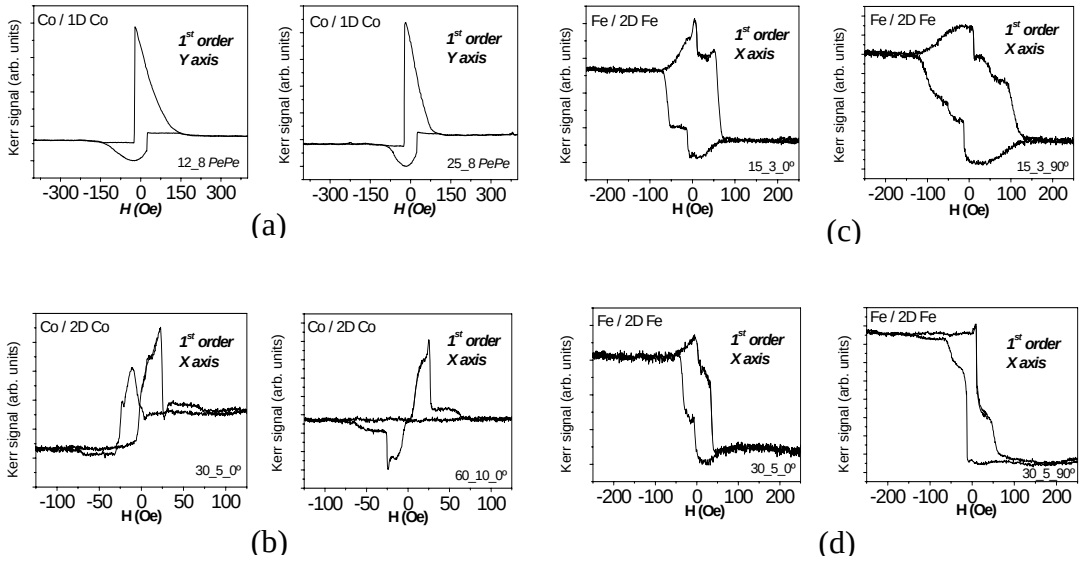

Fig. VII-12. Transverse DMOKE dependencies for different heterostructures. (a) 1Y diffraction spots of 12_3 PePe and 25_8 PePe Co/1D Co heterostructure. (b) 1X diffracted spots of 30_5 and 60_10 Co/2D Co heterostructures, both at 0º orientation. (c) 1X diffraction spot of 15_3 Fe/2D Fe heterostructure at 0º and 90º orientation. (d) 1X diffraction spot of 30_5 Fe/2D Fe heterostructure at 0º and 90º orientations.

The dependence of the first order diffracted light on the applied magnetic field is shown in fig. VII-12 (see figs. VII-3, VII-4, VII-5, VII-7, VII-8, VII-9 and VII-10 for reflected beam -zero-order- loops) for different structures: fig. VII-12 (a) "Co/1D Co", fig. VI-12(b) "Co/2D Co" and fig. VII-12(c)&(d) "Fe/2D Fe". In the latter case we also show the first order diffraction spot intensities dependencies in the 90º orientation.

Turning back to the domain images ("Co/1D Co" and "Co/2D Co" structures in Fig. 3 and 4), the induced periodic domain structure at the flat ferromagnetic film ought to lead to a diffraction spot that appears twice per field cycle and, due to the symmetry, it should be an even function of the applied magnetic field. This is expected since the reflectivity, in the transversal Kerr configuration, depends only

on the magnetization component along the applied field direction. The experimental findings shown in fig. VII-12 do not agree with this fact. The reason for this behavior is not clear yet, and it might be due to a variety of reasons that are currently under investigation. Notice however that the first loop shown in figure VII-12(b) resembles very much an even function of the field with a small odd function superimposed. This could be due to the presence of diffuse light, besides the diffracted light, that also carries magneto-optic component. Supporting this statement, notice that in none of the cases the diffracted light vanishes at magnetic saturation as seen in the hysteresis loops in the reflected spots. This would point out to that either the sample is not "technically" saturated, having small closure domains, or that although our continuous film is opaque, there are small variations in the reflectivity (in principle less than 10^{-5}) between the area under the magnetic elements and the interelement area that diffract light even at magnetic saturation.

7. Micromagnetic simulations of the heterostructures:

The experimental findings described so far are correlated with micro-magnetic simulations performed with the OOMMF 1.1b code [VII.20] with 3D spins in a 2D mesh. In particular, the simulations are performed for the case of the 1D heterostructures. The 2D mask used represents the cross section of the stripes array period. Thus, according to the chosen axis notation (see fig. VII-13) and to the way OOMMF performs calculations in a 2D mesh using the FastPipe Demag specification, the direction along the stripe (X axis direction) is supposed to be infinite. Even with this simple model the experimental results might be reproduced.

As an example, results for a heterostructure consisting of 4 mm wide stripes and 4 mm wide inter-stripe with infinite long stripe axis are presented in Fig. VII-13, where the magnetization at different H values are shown for the cross section of one period of the 1D array. The stripes in this case are exchange decoupled by removing one layer of magnetic elements between the stripes and continuous film. Fig. VII-13 shows the magnetization component along the applied field direction (where the external field is applied in the horizontal page direction) in a complete field loop (both H to -H and –H to H sweeps) at 150 Oe field steps.

Notice that twice per loop an inversion domain forms at the continuous layer area under the stripes (fig. VII-13). This occurs when the understripe orients

antiparallel to the stripe magnetization -that remains parallel to the field- in order to reduce the magnetostatic energy.

As the Co anisotropy axis lies along the stripe long direction, the combined effect of crystalline anisotropy and shape anisotropy makes the stripe magnetization remain parallel to the field longer.

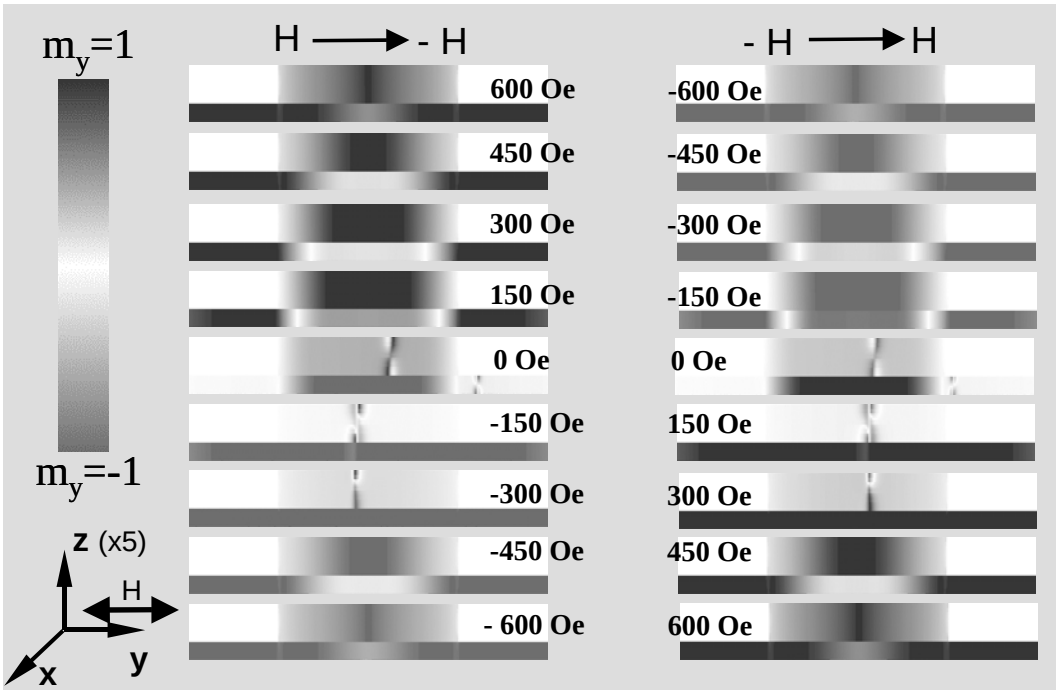

Fig.VII-13: Micromagnetic simulations of a 4_4 PePe Co/1D Co heterostructure. The magnetization spatially resolved is shown in a cross section of one period of the array (stripe over continuous film) for different values of the external magnetic field. The left column shows the reversal when the external field switches from 600 Oe to -600 Oe. The right column shows the reversal when the external applied field switches from -600 Oe to 600 Oe.

Due to the double thickness of the stripe its weight in the potential energy is larger, as discussed in a previous section of this chapter. This is supported by experiments in which the continuous layer and the stripe were fabricated with the same thickness. In these experiments, neither this inversion domain in the continuous layer nor the pure magneto-optic diffraction (the lighthouse effect) are observed.

The hysteresis loops obtained when illuminating from both sides deduced from the micromagnetic simulation data are also shown in fig. VII-14 (a)&(b). Note that the experimentally observed negative differential susceptibility when illuminating the flat side is reproduced in the simulations, supporting once more the original suspicion of inversion domains underneath the stripes.

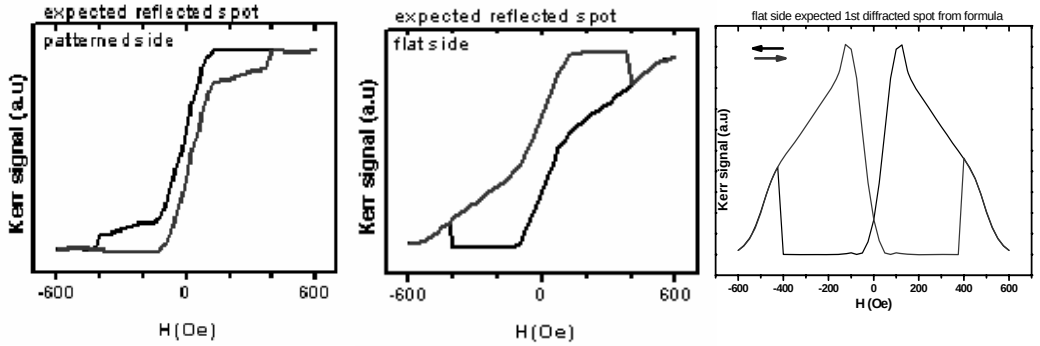

Fig. VII-14: Hysteresis loops from micromagnetic simulations of a 4_4 Co/1D Co heterostructure. (a) hysteresis loop of the expected reflected spot from the patterned side. (b) hysteresis loop of the expected reflected spot from the flat side. (c) Loop corresponding to the expected lighthouse effect 1Y signal.

Fig. VII-14(c) shows the result of calculating the diffracted light intensity (1st order, X direction) using the micromagnetic simulation domain structure and the expression (eq. VII-1) that provides the diffracted intensity from a given magnetization distribution $m_X(x)$ in a periodic structure of period T:

$$I_n \propto \left| \int_{-T/2}^{T/2} \left(1 + A m_x(x)\right) e^{i\frac{n2\pi x}{T}} dx \right|^2 \qquad \text{(VII-1)}$$

The expression in eq. VII-1, very similar to the deduced in chapter III, is obtained in the same manner. The main difference is that, in this case, also the interelement area is magnetic.

The resulting loop in fig. VII-14(c), accounting for the diffracted MO response is an even function of the field. Thus, according to the model, the diffraction spot appears twice per loop as it occurs.

8. Exchange coupled vs. exchange decoupled heterostructures:

The lighthouse effect was previously presented as a special feature characteristic of the exchange decoupled samples. This statement can be experimentally corroborated fabricating a similar structure exchange coupled [VII.18]. This exchange coupled sample is fabricated growing a 240 nm Co thin film (160+80 nm) and then performing an ion beam etching (IBE) using a mask of photoresist.

8.1.Experimental measurements

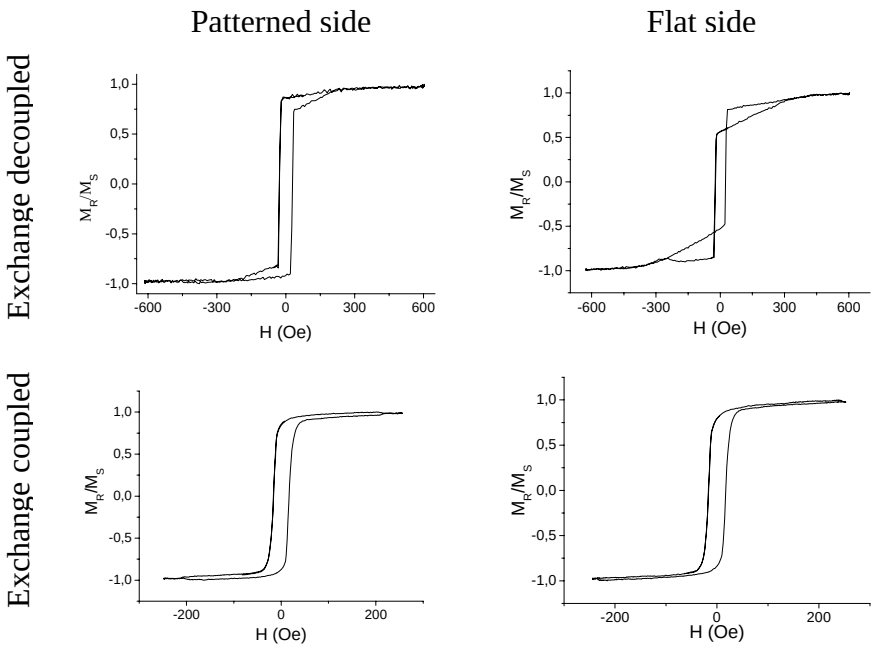

Fig. VII-15: Hysteresis loops of the patterned (left column) and flat (right column) side of a 6_3 Co/1D Co heterostructure when the pattern is exchange decoupled (top row) and coupled (bottom row).

It can be seen in the plots from fig. VII-15 that the behavior of the average magnetization in the exchange coupled sample is very different from the case of exchange decouple. This difference is even more marked in the MO signal from the flat side of the sample. Indeed, according to the shape of the hysteresis loops in the exchange coupled case, the reversal seems to occur simultaneously in the two sides of the sample. On the contrary, it was previously shown (figs. VII-6 and VII-13) that in the exchange decoupled samples the reversals in the flat side start when the array in the patterned side is almost magnetically saturated.

This different behavior is the responsible of the absence of the domains replica of the pattern and, consequently, of the lighthouse effect.

8.2.Micromagnetic simulations

These statements might be corroborated by micromagnetic simulations.

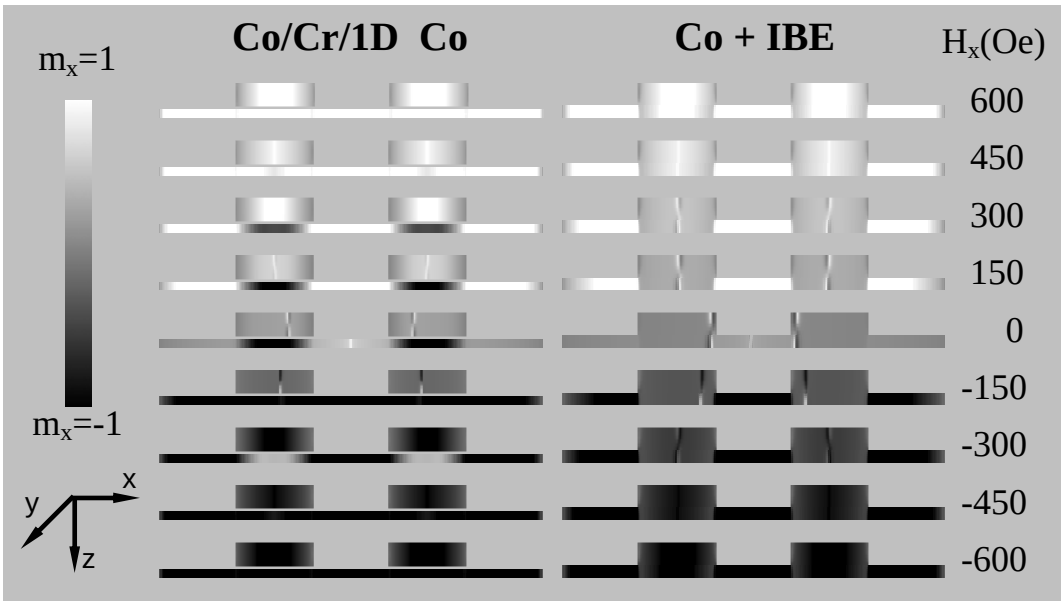

Fig.VII-16: Micromagnetic simulations of a 6_3 PePe Co/1D Co heterostructure. The magnetization spatially resolved is shown in a cross section of two periods of the array (stripe over continuous film) for different values of the external magnetic field (applied in the X axis direction). The left column shows the reversal when the external field switches from 600 Oe to -600 Oe in a exchange decoupled sample. The right column shows the reversal when the external applied field switches from 600 Oe to -600 Oe in a exchange coupled sample.

In fig. VII-16 a 6_3 Co/1D Co heterostructure is simulated when both the array is exchange coupled and exchange decoupled to the continuous film. The simulations are performed in the same conditions of the one in fig. VII-13. Thus, a 2D mask simulating the cross section of the heterostructure is used, assuming therefore that the stripes in the Y direction are infinitely long. In the case of the exchange decoupled sample (fig. VII-16, left column), the decoupling is simulated by removing one layer of magnetic elements between the stripes and continuous film.

Using the spatially resolved magnetization distribution provided by the micromagnetic simulations, the corresponding hysteresis loops of the patterned and flat side might be obtained (fig. VII-17).

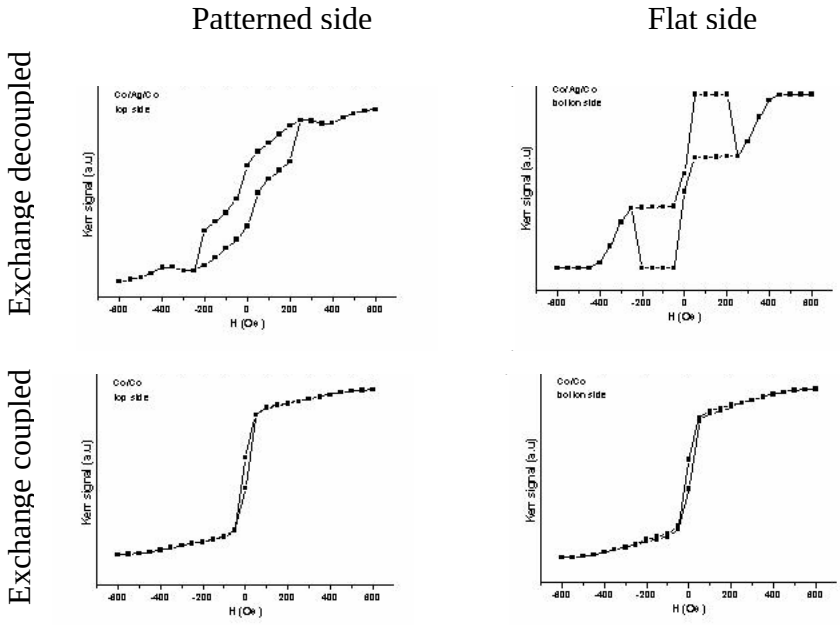

Fig. VII-17: Simulated hysteresis loops of the patterned (left column) and flat (right column) side of a 6_3 Co/1D Co heterostructure when the pattern is exchange decoupled (top row) and coupled (bottom row).

Despite the loops in fig. VII-17 does not exactly correspond to the experimental ones shown in fig. VII-15, there is a qualitative agreement between theory and

experiments. The hysteresis loops of the patterned and flat side of the exchange coupled case are very similar. However, in the exchange decoupled case, these loops are markedly different and the flat side loop clearly presents a zone with negative differential susceptibility, as it occurs in the corresponding experimental loop (see figs. VII-3(b) and VII-15).

9.An alternative method for domains replica of a lithography

The tailored domains introduced in this chapter might be useful for developing magnetic sensors by means of the Bitter technique. The main problem of the heterostructures studied is that the flat side (the side interesting for developing the sensor) is stuck to the glass substrate. Thus, according to the field values calculated in chapter V for domain walls and taking into account that the substrate is around 1 mm thick, there is no possibility of using the Bitter technique.

An alternative method is presented in this section. It consists on implanting the magnetically soft amorphous alloy $Fe_{80}B_{20}$ (see fig. IV-11) with ^{14}N ions. This method tries to take advantage of the fact (see [VII.21]) that the BN bonding is exothermic and that the Fe_XN_Y bonding is not very endothermic. The BN molecule is not magnetic whereas the Fe_xN_y is uniaxial, biaxial or non-magnetic depending on the values of x and y. Therefore, the method consists on performing the implantation through a mask of resist in order to locally change the magnetic behavior of the thin film.

9.1.Kerr microscopy images

Using the same mask as the case of the 1D heterostructures in a 30 nm thick $Fe_{80}B_{20}$ continuous film and removing the resist after an impantation with 10^{15} ^{14}N ions/cm^2, the reversal of the samples are monitored in the Kerr microscope (fig. VII-18).

Reversals in this so made structures consist of a nucleation and a subsequent propagation of domains in the implanted zone, followed by a propagation+nucleation of domains in the un-implanted zone (vice-versa if the external field is applied parallel to the magnetization hard axis of the $Fe_{80}B_{20}$).

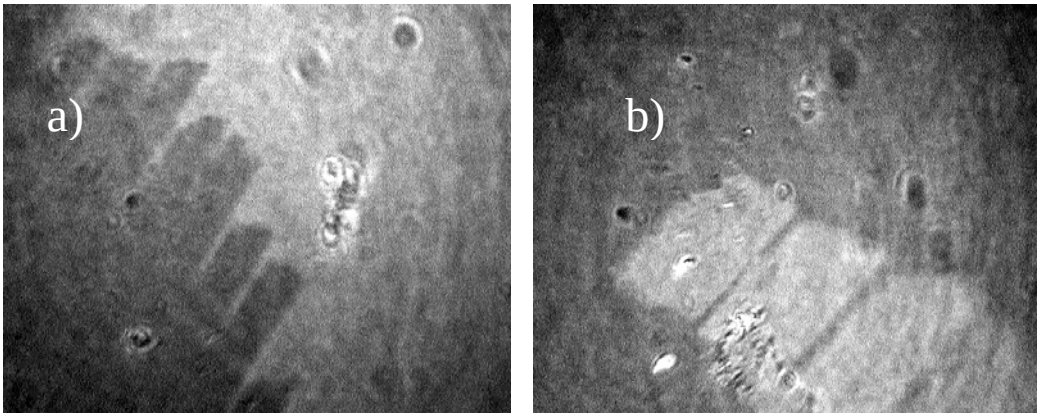

Fig. VII-18: Kerr microscope images of a regular structure of magnetic domains induced by ^{14}N implantation in a $Fe_{80}B_{20}$ thin film. a) corresponds to the structure 25_8 and b) to 100_8

9.2.MO measurements

In order to properly understand the macroscopic effect of the implantation, both the easy and hard axis hysteresis loops of implanted $Fe_{80}B_{20}$ continuous film are measured in a transverse Kerr setup (fig. VII-19).

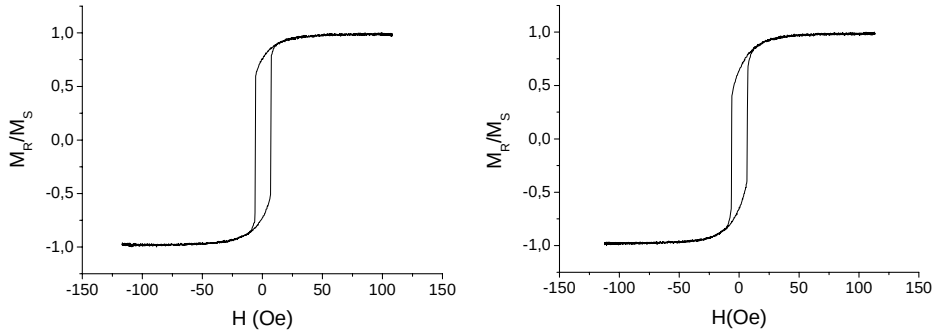

Fig. VII-19: Hysteresis loops for implanted $Fe_{80}B_{20}$. Left plot: the external field is applied along the un-implanted $Fe_{80}B_{20}$ easy axis. Right plot: the external field is applied along the un-implanted $Fe_{80}B_{20}$ hard axis.

According to fig. VII-19, the un-implanted easy and hard axis directions does no longer correspond to easy and hard magnetization directions in the implanted $Fe_{80}B_{20}$. In spite of this fact, X-ray diffraction measurements shows that the resulting material is still amorphous.

The plots in fig. VII-19 seems Stoner-Wohlfahrt-like hysteresis loops. Since the amorphous $Fe_{80}B_{20}$ is consistent with the Stoner-Wohlfahrt model (see chapter IV), polar plots of the relative remanence applying the external field at different orientations can be performed (fig. VII-20).

According to fig. VII-20, the macroscopic effect of the implantation in the amorphous $Fe_{80}B_{20}$ is the 45º rotation of the magnetic anisotropy axis. Consequently there are a certain range of field values in which the reversal of the implanted zone will occur while the magnetization in the un-implanted zone remains in the same direction.

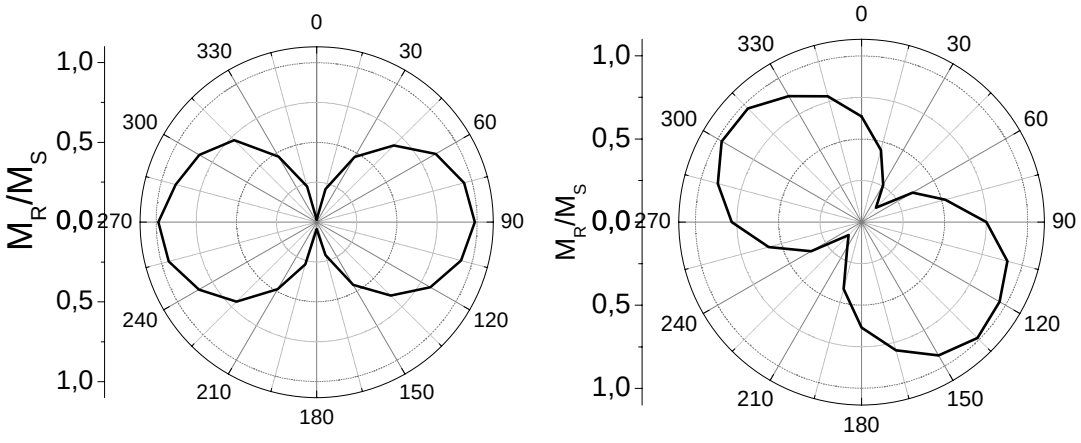

Fig. VII-20: Polar plot of M_R/M_S vs. the angle between the magnetization and the sample's edge for 30nm thick $Fe_{80}B_{20}$ continuous film (left polar plot) and for the same thin film after implantation with 10^{15} ^{14}N ions/cm^2 (right polar plot).

There are two major inconveniences of the presented method. The first one is that the amorphous $Fe_{80}B_{20}$ is a soft magnetic material, therefore the lithography replica appears in a narrow range of values of the external field.

The second major inconvenience is related to the resist. When performing the implantation not only the metal is chemically modified, but also the resist. Thus, the resist became harder to remove with acetone and even with commercial resist removers like Microposit Remover.

10.Summary and conclusions

In this chapter it has been analyzed in detail the magnetization processes and the magneto optical behavior of heterostructures consisting of a periodic array of micro-sized ferromagnetic elements deposited on top of a continuous ferromagnetic film. The 1D and 2D patterns are fabricated using two different materials (Fe and Co) with sizes in the micrometer range in order to be able to correlate magnetization processes and magneto optical behavior with domain observations using Kerr microscopy, and to obtain diffraction spots well resolved angularly.

Choosing the appropriate thick and lateral dimensions and using a transparent substrate allows the magneto optical characterization from both sides of the heterostructures. By comparing loops from either side it is possible to discern if the magnetization behaves coherently along the heterostructures.

By means of MO techniques it has been demonstrated that the fabricated 1D and 2D structures on top of a continuous film, only when the two layers are exchange decoupled, are responsible of the presence of an array of regular domains in the flat side of the sample, replica of the array in the patterned side. This array of regular domains is responsible of a pure magneto optical diffraction in the flat side of the sample that can be modulated with an applied magnetic field.

Comparing the experiments with micromagnetic simulations it has been demonstrated that the exchange decoupling produces an inversion domain under the patterned magnetic elements due to the magnetostatic energy reduction. These inversion domains create on the flat side of the sample a domain replica of a lithographically defined pattern. This way, the reported experiments demonstrate the feasibility of transferring a pattern from a mask into a domain structure.

An alternative method of transferring a pattern into a continuous film is reported. It consists of performing an implantation with ^{14}N ions on an amorphous $Fe_{80}B_{20}$ thin film using a resist mask. This second method has the advantage of leaving the

flat side uncovered (whereas in the case of the 1D and 2D heterostructures the flat side is covered by the pattern on one side and by the glass substrate in the other).

The implantation alters the $Fe_{80}B_{20}$ alloy changing therefore its magnetic properties. The macroscopic effect consist of a 45º rotation of the easy axis of the resulting amorphous compound which allow the appearance of ordered domains replica of the mask used.

11.References:

[VII.1] C. Martinez-Boubeta, J.L. Costa-Krämer, A. Cebollada, J. Phys.: Cond. Mat., **15**, 1123 (2003)

[VII.2] D. Jaque, J.I. Martin, G. Armelles, J.L. Costa-Krämer, F. Briones and J.L. Vicent, J. Appl. Phys., **91**, 382 (2002).

[VII.3] P. Garcia-Mochales, J.L. Costa-Krämer, G. Armelles, F. Briones, D. Jaque, J.I. Martin and J.L.Vicent, Appl. Phys. Lett. **81**, 3206 (2002)

[VII.4] O. Geoffroy, D. Givord, Y. Otani, B. Pannetier, A.D. Santos, M. Schlenker and Y. Souche, J. Magn. Magn. Mat., **121**, 516R (1993)

[VII.5] T. Schmitte, O. Schwöbken, S. Goek, K. Westerholt and H. Zabel, J. Magn. Magn. Mat., **240**, 24 (2002)

[VII.6] T. Schmitte, T. Schemberg, K Westerholt and H. Zabel, J. Appl. Phys. **87**, 5630 (2000)

[VII.7] T. Schmitte, K. Westerholt and H. Zabel, J. Appl. Phys., **92,** 4524 (2002)

[VII.8] I. Guedes, N. J. Zaluzec, M. Grimsditch, V. Metlushko, P. Vavassori, B. Ilic, P. Neuzil and R. Kumar, Phys. Rev. B, **62,** 11719 (2000)

[VII.9] M. Grimsditch and P. Vavassori, J. Phys.: Cond. Mat., **16**, R275 (2004)

[VII.10] D. van Labeke, A. Vial, V. A. Novosad, Y. Souche, M. Schelenker and A. D. Dos Santos, Opt. Comm., **124**, 516 (1996)

[VII.11] M. Grimsditch, , P. Vavassori, D. Novosad, V. Metlushko, H. Shima, Y. Otani, and K. Fukamichi, Phys. Rev, B, **65**, 172419 (2002)

[VII.12] I. Guedes, M. Grimsditch, V. Metlushko, P. Vavassori, R. Camley, B. Ilic, and P. Neuzil, R. Kumar, Phys. Rev. B, **66,** 14434 (2002)

[VII.13] P. Vavassori, M. Grimsditch, V. Novosad, V. Metlushko and B. Ilic, Phys. Rev. B., **67**, 134429 (2003)

[VII.14] I. Guedes, M. Grimsditch, V. Metlushko, P. Vavassori, R. Camley, B. Ilic, P. Neuzil and R. Kumar, Phys. Rev. B., **67**, 24428 (2003)

[VII.15] P. Vavassori, V. Metlushko, R. M. Osgood III, M. Grimsditch, U. Welp and G. Crabtree, Phys. Rev. B., **59**, 6337 (1991)

[VII.16] P. Vavassori, V. Metlushko and M. Grimsditch, Phys. Rev. B., **61**, 5895 (2000)

[VII.17] Y. Souche, M. Schelenker and A. D. Santos, J. Magn. Magn. Mat., **140**, 2179 (1995)

[VII.18] J. L. Costa-Krämer, C. Guerrero, S. Melle, P. García-Mochales and F. Briones, Nanotech., **14**, 239 (2003)

[VII.19] A. Hubert and R. Schäfer, *Magnetic Domains*, Springer (2000)

[VII.20] M.J. Donahue and D.G. Porter, OOMMF User's Guide version 1.0 (Gaithersburg, MD; National Institute of Standards and Technology) [Online] Avalaible: http://math.nist.gov/oommf/: (1999)

[VII.21] Handbook of chemistry and physics, 69th edition, CRC Press (1989)

APPENDIXES:

Index

APPENDIX I.A: SOME MAGNETIC UNITS

Term	Symbol	SI unit	cgs unit	Conversion factor
Magnetic induction	B	Tesla (T)	Gauss (G)	1 T = 10^4 G
Magnetic flux	Φ	Weber (Wb)	G·cm^2	1 Wb= 10^8 G·cm^2
Magnetic field	H	A/m	Oersted (Oe)	1 A/m = $4\pi/10^3$ Oe
Magnetization	M	A/m	emu/cm^3	1 A/m = 10^{-3} emu /cm^3
Mass magnetization	σ	A·m^2/kg	emu/g	1 A·m^2/kg = 1 emu/g
Magnetic moment	m	A·m^2	emu	1 A·m^2 = 10^3 emu
Volume susceptibility	κ	adimensional	adimensional	4π (SI) = 1 (cgs)
Mass susceptibility	χ	m^3/kg	emu/Oe· g	1 m^3/kg = $10^3/4\pi$ emu /Oe· g
Magnetic anisotropy	K	J/m^3	erg/cm^3	1 J/m^3 = 10 erg/cm^3
Demagnetizing energy in thin films	K_d	$\frac{1}{2}\mu_0 M_S^2$ (J/m^3)	$2\pi M_S^2$ (erg/cm^3)	1 J/m^3 = 10 erg/cm^3
Permeability of free space	μ_0	H/m	adimensional	$4\pi\cdot10^{-7}$ H/m = 1 (cgs)

APPENDIX II.A: THEORETICAL BACKGROUND OF THE POLAR KERR EFFECT

According to the description of the polar Kerr setup given in chapter II (see figure II-4), the theoretical description which leads to the measurement of the rotation and ellipticity is detailed.

Light transmission through the optical arrangement sketched in fig. II-4 is described by the following vector equation:

$$\mathbf{E}^{(r)}=\mathbf{P}_2\cdot\mathbf{R}\cdot\mathbf{C}\cdot\mathbf{M}\cdot\mathbf{P}_1\cdot\mathbf{E}^{(i)} \tag{A-1}$$

where

$$\mathbf{E}^{(x)}=\begin{pmatrix}E_p^{(x)}\\ E_s^{(x)}\end{pmatrix},\ x=\text{i, r} \qquad \mathbf{R}=\begin{pmatrix}r_{pp} & r_{ps}\\ r_{sp} & r_{ss}\end{pmatrix}$$

$$\mathbf{P}_1=\begin{pmatrix}\frac{1}{2} & \frac{1}{2}\\ \frac{1}{2} & \frac{1}{2}\end{pmatrix} \qquad \mathbf{P}_2=\begin{pmatrix}\cos^2\beta & \sin\beta\cos\beta\\ \sin\beta\cos\beta & \sin^2\beta\end{pmatrix}$$

$$\mathbf{C}=\begin{pmatrix}e^{i\gamma/2} & 0\\ 0 & e^{-i\gamma/2}\end{pmatrix} \qquad \mathbf{M}=\begin{pmatrix}e^{i\varphi/2} & 0\\ 0 & e^{-i\varphi/2}\end{pmatrix} \tag{A-2}$$

represents the Jones matrices of the different optic elements of the setup.

The modulator M has temporally periodic birefringent phase shift, $\varphi=\varphi_0\sin(\omega_M t)$, with frequency $\omega_M=2\pi\cdot 50\text{kHz}$ and amplitude $\varphi_0=2.41$. This value is a compromise for detecting the Fourier components I_1 and I_2 of the light intensity at ω_M and $2\omega_M$ by use of the lock-in amplifiers A_1 and A_2 (fig. II-4).

Henceforward, it will be useful to express the complex Fresnel reflection coefficients of matrix R in its polar representation:

$$r_{pp}=r_{pp}\cdot e^{i\delta_{pp}} \qquad r_{ss}=r_{ss}\cdot e^{i\delta_{ss}} \qquad r_{sp}=r_{sp}\cdot e^{i\delta_{sp}} \tag{A-3}$$

By distinguishing r_{pp} from r_{ss}, the description holds at arbitrary angles of incidence θ.

Evaluation of equation (A-1) is straightforward. By relating the linearly polarized light wave behind P_1 to the initial intensity, $I^{(i)}$, it follows:

$$E_p^{(i)} = E_s^{(i)} = \sqrt{I^{(i)}/2} \tag{A-4}$$

According to eqs. (A-1) and (A-2), the reflected intensity measured by the detector is:

$$I^{(r)} = \left(E^{(r)}\right)^2 = \hat{I}\frac{I^{(r)}}{2} \tag{A-5}$$

In this equation, the intensity amplitude Î might be expressed as

$$\hat{I} = A + B\cdot\cos(\varphi+\gamma) + C\cdot\sin(\varphi+\gamma) \tag{A-6}$$

where

$$A = r_{pp}^2\cos^2\beta + r_{ss}^2\sin^2\beta + r_{sp}^2 + r_{sp}\cdot\sin 2\beta\,[\,r_{pp}\cos(\delta_{pp}-\delta_{sp}) - r_{ss}\cos(\delta_{ss}-\delta_{sp})]]$$

$$B = \sin 2\beta\,[\,r_{pp}\,r_{ss}\cos(\delta_{ss}-\delta_{pp}) - r_{sp}^2\,] + 2\,r_{sp}\cdot[\,r_{ss}\sin^2\beta\cdot\cos(\delta_{ss}-\delta_{sp}) + r_{pp}\cos^2\beta\cdot\cos(\delta_{pp}-\delta_{sp})]$$

$$C = r_{pp}\,r_{ss}\sin 2\beta\cdot\cos(\delta_{ss}-\delta_{pp}) + 2\,r_{sp}\cdot[\,r_{ss}\sin^2\beta\cdot\cos(\delta_{ss}-\delta_{sp}) + r_{pp}\cos^2\beta\cdot\cos(\delta_{pp}-\delta_{sp})] \tag{A-7}$$

According to the setup in fig.II-4, the lock-in will only provide information about the DC-component and the first two Fourier components of Î. Consequently, these Fourier components should be deduced from eqs. (A-6) and (A-7) using the relations:

$$\sin\varphi = \sin(\varphi_0\sin(\omega_M t)) = 2J_1(\varphi_0)\sin(\omega_M t) + 2J_3(\varphi_0)\sin(3\omega_M t) + \ldots$$

$$\cos\varphi = \cos(\varphi_0\sin(\omega_M t)) = 2J_0(\varphi_0) + 2J_1(\varphi_0)\sin(2\omega_M t) + \ldots \tag{A-8}$$

being J_i, i=0,1,2, … the Bessel function of order i. Thus, (A-6) might be expressed in the form:

$$\hat{I}=\hat{I}_0+\hat{I}_1 \sin(\omega_M t) +\hat{I}_2 \sin(2\omega_M t) +\hat{I}_3 \sin(3\omega_M t)+ \ldots \quad \text{(A-9)}$$

here, the expansion coefficients are

$$\hat{I}_0=A+ J_0(\varphi_0) (B\cdot\cos\gamma+C\cdot\sin\gamma)$$

$$\hat{I}_1=2\, J_1(\varphi_0) (C\cdot\cos\gamma-B\cdot\sin\gamma)$$

$$\hat{I}_2=2\, J_2(\varphi_0) (B\cdot\cos\gamma+C\cdot\sin\gamma) \quad \text{(A-10)}$$

Equations (A-7) and (A-10) can be considerably simplified appropriately choosing specific values for β and γ. There are two important cases:

(a) β=0 and γ=0 (p polarization)

$$\hat{I}_0= r_{pp}^2 + r_{sp}^2 -2\, J_0(\varphi_0)\; r_{pp}\; r_{sp} \cos(\delta_{pp}-\delta_{sp})$$

$$\hat{I}_1=4\, J_1(\varphi_0)\; r_{pp}\; r_{sp} \sin(\delta_{pp}-\delta_{sp})$$

$$\hat{I}_2=-4\, J_2(\varphi_0)\; r_{pp}\; r_{sp} \cos(\delta_{pp}-\delta_{sp}) \quad \text{(A-11)}$$

(b) $\beta=\frac{\pi}{2}$ and γ=0 (s polarization)

$$\hat{I}_0= r_{ss}^2 + r_{sp}^2 +2\, J_0(\varphi_0)\; r_{ss}\; r_{sp} \cos(\delta_{ss}-\delta_{sp})$$

$$\hat{I}_1=4\, J_1(\varphi_0)\; r_{ss}\; r_{sp} \sin(\delta_{ss}-\delta_{sp})$$

$$\hat{I}_2=4\, J_2(\varphi_0)\; r_{ss}\; r_{sp} \cos(\delta_{ss}-\delta_{sp}) \quad \text{(A-12)}$$

Since $r_{sp}^2 << r_{ss}^2$, $r_{sp}^2 << r_{pp}^2$ and $J_0(\varphi_0)\sim 0$ when $\varphi_0\sim 2.41$ and using equations (II-5) and (A-3), the following ratios are obtained:

$$\left(\frac{\hat{I}_1}{\hat{I}_0}\right)_{\beta=0,\gamma=0} = 4\, J_1(\varphi_0)\, \frac{r_{sp}}{r_{pp}} \sin(\delta_{sp}-\delta_{pp}) = 4\, J_1(\varphi_0)\, \tan(\varepsilon_p)$$

$$\left(\frac{\hat{I}_2}{\hat{I}_0}\right)_{\beta=0,\gamma=0} = -4\, J_2(\varphi_0)\, \frac{r_{sp}}{r_{pp}} \cos(\delta_{sp}-\delta_{pp}) = -4\, J_2(\varphi_0)\, \theta_p$$

$$\left(\frac{\hat{I}_1}{\hat{I}_0}\right)_{\beta=\frac{\pi}{2},\gamma=0} = -4\, J_1(\varphi_0)\, \frac{r_{sp}}{r_{ss}} \sin(\delta_{sp}-\delta_{ss}) = -4\, J_1(\varphi_0)\, \tan(\varepsilon_s)$$

$$\left(\frac{\hat{I}_1}{\hat{I}_0}\right)_{\beta=\frac{\pi}{2},\gamma=0} = 4\, J_2(\varphi_0)\, \frac{r_{sp}}{r_{ss}} \cos(\delta_{sp}-\delta_{ss}) = 4\, J_2(\varphi_0)\, \theta_s \qquad \text{(A-13)}$$

Hence, apart from numerical factors, the normalized lock-in signals at ω_M and $2\omega_M$ directly yield the Kerr ellipticities and rotations respectively. In addition, by taking ratios of two light signals, fluctuations due to instabilities of the light source (intensity $I^{(i)}$, eq. (A-5)) and of the optical setup are very efficiently eliminated. In practice, recording of the signals (A-12) requires two different amplifiers with unknown additional proportionality constants. They have to be accounted for by specific calibration procedures [II.12].

It is important to note that the whole treatment holds also for the longitudinal Kerr geometry.

APPENDIX V.A: SYMMETRY PROPERTIES OF THE MAGNETIC POTENTIAL

Previous to the demonstration of the symmetry properties some trivial symmetry properties of function Q are shown.

Properties of Q function:

1. Q(t,p,z)=Q(p,t,z)
2. Q(-p,t,z)=-Q(p,t,z)
  2.1.- Q(0,t,z)=0
3. Q(p,-t,z)=-Q(p,t,z)
  3.1.- Q(p,0,z)=0
4. Q(p,p,0)=2p·ArcSinh(1)
5. Q(p,t,-z)=Q(p,t,z)

From these properties, some trivial properties for ϕ follows:

Properties of ϕ function:

1. ϕ(-x,y,z)= ϕ(x,y,z)
2. ϕ(x,-y,z)= ϕ(x,y,z)
3. ϕ(x,y,-z)= ϕ(x,y,z)
4. ϕ(y,x,z)= ϕ(x,y,z)

Proofs:

1. ϕ(-x,y,z)=

$$= \frac{\sigma}{4\pi\mu_0} (Q(y+b,-x+a,z)- Q(y-b,-x+a,z)- Q(y+b,-x-a,z)+ Q(y-b,-x-a,z))=$$

$$= \frac{\sigma}{4\pi\mu_0} (-Q(y+b,x-a,z)+ Q(y-b,x-a,z)+ Q(y+b,x+a,z)- Q(y+b,x+a,z))=$$

$$= \phi(x,y,z)$$

2. ϕ(x,-y,z)=

$$=\frac{\sigma}{4\pi\mu_0}\,(Q(-y+b,x+a,z)-Q(-y-b,x+a,z)-Q(-y+b,x-a,z)+Q(-y-b,x-a,z))=$$

$$=\frac{\sigma}{4\pi\mu_0}\,(-Q(y-b,x+a,z)+Q(y+b,x+a,z)+Q(y-b,x-a,z)-Q(y+b,x-a,z))=$$

$=\phi$(x,y,z)

3. ϕ(x,y,-z)=

$$=\frac{\sigma}{4\pi\mu_0}\,(Q(y+b,x+a,-z)-Q(y-b,x+a,-z)-Q(y+b,x-a,-z)+Q(y-b,x-a,-z))=$$

$$=\frac{\sigma}{4\pi\mu_0}\,(Q(y+b,x+a,z)-Q(y-b,x+a,z)-Q(y+b,x-a,z)+Q(y+b,x+a,z))=$$

$=\phi$(x,y,z)

4. ϕ(y,x,z)=

$$=\frac{\sigma}{4\pi\mu_0}\,(Q(x+a,y+b,z)-Q(x+a,y-b,z)-Q(x-a,y+b,z)+Q(x-a,y-b,z))=$$

$$=\frac{\sigma}{4\pi\mu_0}\,(Q(y+b,x+a,z)-Q(y-b,x+a,z)-Q(y+b,x-a,z)+Q(y-b,x-a,z))=$$

$=\phi$(x,y,z)

APPENDIX V.B: ACCURACY OF THE *k*-NEAREST NEIGHBORS APPROXIMATION

The magnetostatic energy contribution requires the evaluation of the formula (IV-5), which evaluates the magnetostatic contributions due to an element considering k neighboring layers. If k=0 it would be an evaluation considering isolated elements, k=1 considering 1st neighbors and so on. It is interesting to quantify the contribution to the magnetostatic energy as additional neighbors are considered in the evaluation of the total energy.

Let U(k) be the value of the magnetostatic energy considering k neighbors. One way to quantify the necessity of introducing more terms is to measure the relative weight of the contribution of the new terms with respect to the value of the first neighbors approximation, i.e., [U(k-1)-U(k)]/U(1). Fig. A-1 plots the relative increase in magnetostatic energy contribution as k increases and the 8·k k-neighbors are considered.

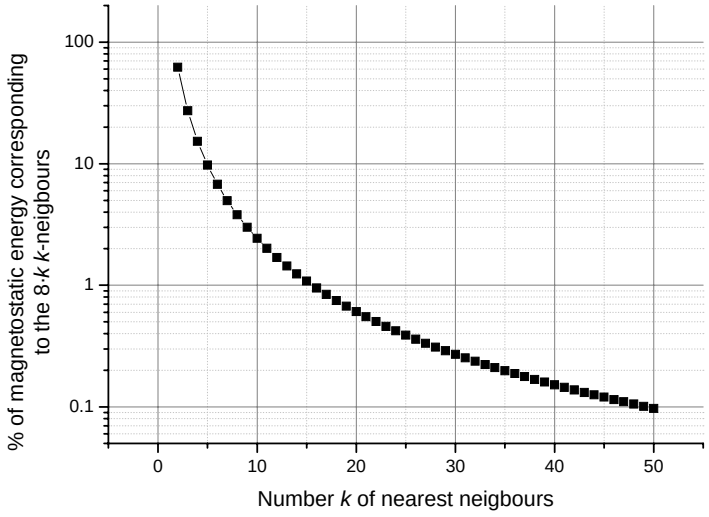

Fig. A-1: Percentage of magnetostatic energy value in the k-nearest neighbors approximation that represents the contribution due to the 8·k k-neighbors. Percentages are presented in logarithmic scale.

Data from fig. A-1 can be fitted by a function proportional to $y=1/x^2$. Assuming β is the proportionality constant, this implies that the sum of all percentages,

$$\sum_{n=2}^{\infty}\frac{U(k-1)-U(k)}{U(1)}=1-\frac{U(\infty)}{U(1)}\text{, is }\beta\cdot\sum_{n=2}^{\infty}1/n^2=\beta(\pi^2/6-1). \qquad \text{(A-14)}$$

Thus, $U(\infty)=U(1)\cdot(1-\beta(\pi^2/6-1))$

Therefore, if the number of neighbors is set to k, a $100\frac{U(k)-U(\infty)}{U(\infty)}\%$ is neglected, where $\frac{U(k)-U(\infty)}{U(\infty)}=\frac{1-\beta\left(\sum_{n=1}^{k}1/n^2-1\right)}{1-\beta\left(\pi^2/6-1\right)}-1$ and β depends on the interelement distance. For example, for d=100 nm, $\beta=2.527\cdot10^{-2}\pm3\cdot10^{-5}$. Thus for k=2 around 1% is neglected; for k=20, less than 0.2%; and for k=100, less than 0.03%. For comparison purposes if d=5 nm, 14% is neglected for k=2.

SUMMARY

SUMMARY

This thesis is dedicated to understand the magnetic properties of 1D and 2D magnetic arrays both theoretically and experimentally, focusing on studying interactions between the different elements of the array themselves and the array with a continuous ferromagnetic thin film by magneto-optical means.

The interaction in 2D arrays, relevant for both magnetic storage media and magnetic logical devices, is thoroughly studied by MOKE and DMOKE means in a set of patterns with fixed element size and different interelement separation. Both types of measurements reveal to be essential for our purposes. MOKE measurements provide an estimation for the onset of the interaction. On the other hand, due to the strong dependence of the DMOKE response on both the element shape and the array periodicity, the separation between magnetic elements can be monitored by means of the DMOKE signal. This is useful for the development of an ophthalmic implantable orbital pressure transducer, part of an ongoing research project in the IMM.
In addition, when combining the information from MOKE and DMOKE signals the reversal mechanisms present in the array can be determined, thus being valuable alternative to study switching mechanisms in patterning media.

The previously explained experimental findings are correlated with a theoretical model for magnetostatics in arrays. Although based on somewhat restrictive assumptions, this analytical model reveals to be a flexible and powerful tool to study shape anisotropy and interactions between elements in magnetic arrays, being an important complement to micromagnetic simulations. Using the same formalism, it can be also calculated stray fields and gradients corresponding to arrays and elements of different shapes and materials. Moreover, the model can be extended to stray fields due to Bloch domain walls. The obtained results are useful for studying reversal mechanisms as well as nanoparticle manipulation for biomedical applications.

The theoretical model indicates that both the array and its embedded elements are sources of shape anisotropy. Both effects are studied and quantified, leading to the conclusion that it is possible to compensate the element shape anisotropy by

suitably choosing the shape of the array. This theoretical statement is experimentally corroborated by magneto-optical measurements in a set of patterns whose dimensions are given by the analytical model. With such an experiment it is demonstrated the possibility of tailoring the shape anisotropy in a magnetic array.

If a magnetic pattern is fabricated on top of a magnetic thin film and both layers are exchange decoupled, the interactions between the structure and the continuous film can be studied. This interaction is the responsible of a pattern transfer, that can be observed by Kerr microscopy in the flat side of the fabricated heterostructure if a transparent substrate is used. The magnetic domains in the pattern are shown to be directly correlated to the magnetic domains in the continuous film. This is relevant for both biomedical applications and arrays of magnetic random memories (extends a previous work related to magnetic tunnel junctions).

The pattern transferred to the continuous film entails the apparition of a novel pure magneto-optic effect, called the lighthouse effect. It consists on the intermittent apparition of a diffraction spot in the continuous side of the heterostructures during reversals. This effect, experimentally studied in both 1D and 2D arrays with in-plane magnetization and corroborated with micromagnetic simulations can be seen by direct observation in a conventional Kerr setup.

All the knowledge and tools generated by this thesis set the basis for future development of some of the ongoing projects at the IMM related to patterning media, nanoparticle manipulation and biomedical sensors.

RESUMEN

Esta tesis está dedicada al análisis de las propiedades magnéticas de redes 1D y 2D de elementos magnéticos tanto teórica como experimentalmente, centrándose en el estudio por medios magneto-ópticos de las interacciones entre distintos elementos de la red y en las interacciones de dichos elementos con una lámina delgada ferromagnética.

Las interacciones en redes 2D, relevantes tanto para medios de grabación magnética como para dispositivos lógicos magnéticos, se estudian en profundidad por medio del MOKE y DMOKE en un conjunto de redes con tamaño de elemento fijo y separación entre elementos variable. Ambos tipos de medidas demuestran ser esenciales para nuestros propósitos. Las medidas MOKE proporcionan una estimación para el comienzo de la interacción entre elementos. Por otra parte, debido a la gran dependencia de la respuesta DMOKE a la forma de los elementos y al periodo de la red, la separación entre elementos magnéticos puede ser monitorizada por medio de la señal DMOKE. Esto es útil para el desarrollo de un transductor implantable de presión ocular, parte de un proyecto de investigación del IMM.
Además, combinando la información proporcionada por las señales MOKE y DMOKE, se pueden determinar los mecanismos de inversión de la imanación presentes en la red, convirtiéndose así en una alternativa valiosa de cara a estudiar los mecanismos de conmutación en medios litografiados.

Las conclusiones anteriormente presentadas se relacionan con un modelo teórico para la energía magnetostática en redes. Aunque basado en hipótesis un tanto restrictivas, este modelo teórico demuestra ser una herramienta flexible y eficaz para estudiar la anisotropía de forma y las interacciones entre elementos de redes magnéticas, siendo así un importante complemento para las simulaciones micromagnéticas en redes. Utilizando este mismo formalismo, se pueden calcular además stray fields y gradientes correspondientes a redes de elementos de diferentes formas y materiales. Además, el modelo puede ampliarse a campos generados por paredes de Bloch. Los resultados obtenidos son útiles para el estudio de los mecanismos de inversión así como para la manipulación de nanopartículas de cara a aplicaciones biomédicas.

El modelo teórico indica que tanto la red como sus elementos constituyentes son fuentes de anisotropía de forma. Estudiando y cuantificando ambos efectos, se llega a la conclusión de que es posible compensar la anisotropía de forma debida a los elementos eligiendo adecuadamente la forma de la red. Esta afirmación basada en teoría se corrobora experimentalmente por medio de medidas magneto-ópticas en un conjunto de redes cuyas dimensiones están dadas por el modelo teórico. Mediante un experimento de este tipo, se demuestra la posibilidad de diseñar la anisotropía de forma en una red de elementos magnéticos.

Si la red magnética está fabricada sobre una lámina delgada magnética y ambas capas están desacopladas por canje, se pueden estudiar las interacciones entre la estructura y la capa continua. Esta interacción es la responsable de una transferencia de patrones, que puede ser observada mediante microscopía Kerr en la cara plana de la heteroestructura siempre que se use un sustrato transparente. Los dominios magnéticos en el patrón están directamente relacionados con los dominios magnéticos en la película continua. Esto es relevante tanto para aplicaciones biomédicas como para memorias de acceso aleatorio –MRAM- (ampliando un trabajo previo relativo a uniones túnel magnéticas).

El patrón transferido a la película continua conlleva la aparición de un novedoso efecto puramente magnético, el llamado “efecto farito”. Este efecto consiste en la aparición intermitente de un máximo de difracción en la cara continua de la heteroestructura durante el proceso de inversión de la imanación. Este efecto, experimentalmente estudiado en redes 1D y 2D con imanación en el plano y contrastado con simulaciones micromagnéticas puede ser observado directamente en un dispositivo experimental Kerr convencional.

Todo el conocimiento y herramientas generadas por esta tesis sienta las bases para el futuro desarrollo de algunos de los proyectos actuales del IMM relativos a medios litografiados, manipulación de nanopartículas e implantes sensores biomédicos.

ABOUT THE AUTHOR

Rubén Álvarez Sánchez was born in Gijón (Spain) in July 1976. He studied a BSc in Mathematics at the Faculty of Sciences at the University of Oviedo (1994-1998) subsequently followed by a BSc in Physics in the same Faculty (1998-2002). While studying physics, he was contracted as assistant teacher in the Faculty of Engineering on Computer Sciences at the University of Oviedo (1999). Afterwards, he actively participates in an European research project regarding genomics (1999-2001), contributing with a software capable of calculating genetic diversity coefficients. The result of that work was some papers in genetic publications and some contributions to international congresses.

During his BSc in Physics he became interested in magnetism. This interest eventually lead his way to the Instituto de Microelectrónica de Madrid (IMM-CSIC). From December 2002 he was appointed for a PhD position at IMM. The outcome of his PhD research project is the subject of this thesis.

ras000@gmail.com

LIST OF PUBLICATIONS

Papers related to this thesis

- J. L. Costa-Krämer, A. Bengoechea, **R. Álvarez-Sánchez**, F. Briones, Pure Magneto-optic diffraction and Kerr microscopy of periodic domain structures, IEEE Trans. Mag. **41**, 4229 (2005)

- J. L. Costa-Krämer, **R. Álvarez-Sánchez**, A. Bengoechea, F. Torres, P. García-Mochales, and F. Briones, *Diffractive magneto-optics, magnetic interactions, and reversal mechanisms in Co microsquare arrays,* Phys. Rev. B **71**, 104420 (2005)

- J. L. Costa-Krämer, **R. Álvarez-Sánchez**, A. Bengoechea, and F. Briones, *Magnetism and Magneto Optics in Nanostructure Arrays*, AIP Conf. Proc. **757**, 125 (2005)

- **R. Álvarez-Sánchez**, J. L. Costa-Krämer, F. Briones, *Analytical model for shape anisotropy in thin film nanostructured arrays: Interaction effects,* J. Magn. Magn. Mat. **307**, 171 (2006)

- **R. Álvarez-Sánchez**, J. L. Costa-Krämer, J.M. García-Martín, J. Anguita and F. Briones, *Domain structure and reversal mechanisms through difracted magneto-optics in $Fe_{80}B_{20}$ microsquare arrays*, submitted to J. Appl. Phys. (2006)

- **R. Álvarez-Sánchez**, J. L. Costa-Krämer, *Tailoring shape anisotropy in a 2D magnetic array*, submitted to Appl. Phys. Lett. (2006)

- **R. Álvarez-Sánchez**, V. Sombroek, R. Murillo-Vallejo, M. Siekman, T. Bolhuis, L. Abelmann and J. L. Costa-Krämer, *Tailoring domain size in Co/Pt multilayers*, in preparation. (2006)

Other papers

- I. Fernández, M.S. Martín-González, R. González-Arrabal, **R. Álvarez-Sánchez**, F. Briones and J.L. Costa-Krämer, *Nitrided FeB amorphous thin films for magneto mechanical systems*, submitted to Phys. Rev. B (2006)

Contributions to international conferences

A) Oral presentations

- J.L. Costa-Krämer, **R. Alvarez-Sánchez**, J.V.Anguita, G. Armelles A. Bengoechea, C.M. Boubeta, F.Briones, A. Cebollada, C. Clavero, I. Fernández, J. M. García, E. López-Ponce, M. Martín-Gónzalez, B. Te Dorsthorst, A. Wennberg, *Magnetism and magneto optics in nanostructures*, US –Spain workshop on nanomaterials, Segovia, September 2005

- J.L. Costa-Krämer, **R. Alvarez-Sánchez**, J.V.Anguita, G. Armelles, C.M. Boubeta, A. Bengoechea, F.Briones, A. Cebollada, C. Clavero, P. García-Mochales, Y. Huttel, *Epitaxial nanostructures ferromagnetic tunnel junctions*, MRS Spring Meeting, San Francisco, March 2003

B) Posters

- R. González-Arrabal, I.Fernández, M. Martín-Gónzalez, **R. Alvarez-Sánchez**, J.L. Costa-Krämer, F. Briones, *Nitrided Fe80B20 amorphous thin films for NEMS*, Trends in Nanotechnology 2006 (TNT 2006), Grenoble, September 2006

- **R. Alvarez-Sánchez**, J.L. Costa-Krämer, F. Briones, *Tailoring anisotropy in a magnetic array*, Trends in Nanotechnology 2005 (TNT2005), Oviedo, September 2005

- B. te Dorsthorst, J. L. Costa-Krämer, R. Murillo, C. Clavero, G. Armelles, J. M. García-Martín, M. S. Martín-González, **R. Alvarez-Sánchez**, F. Briones and L. Abelmann, *Magneto optical properties and reversal mechanisms in large area arrays of perpendicularly magnetized nanodots*, Trends in Nanotechnology 2005 (TNT2005), Oviedo, September 2005

- **R. Alvarez-Sánchez**, J.L. Costa-Krämer, F. Briones, *Magnetostatics in nanostructured arrays: Beyond the dipolar approximation*, Trends in Nanotechnology 2004 (TNT2004), Segovia, September 2004

- **R. Alvarez-Sánchez**, J.L. Costa-Krämer, P. García-Mochales, A. Bengoechea, F. Torres, F. Briones, *Magneto optics and magnetic interactions in Co micro-square arrays*, Trends in Nanotechnology 2003 (TNT2003), Salamanca, September 2003

- A.Bengoechea ,J.L. Costa-Krämer, P. García-Mochales, **R. Alvarez-Sánchez**, F. Briones, *Pure magneto optic diffraction and domain observations in periodic domain structures fabricated on flat surfaces*, Trends in Nanotechnology 2003 (TNT2003), Salamanca, September 2003

- **R. Alvarez-Sánchez**, J.L. Costa-Krämer, P. García-Mochales, A. Bengoechea, F. Torres, F. Briones, *Magneto optics and magnetic interactions in Co micro-square arrays*, XVIII International Colloquium on Magnetic Films and Surfaces (ICMFS 2003), Madrid, July 2003

- A.Bengoechea ,J.L. Costa-Krämer, P. García-Mochales, **R. Alvarez-Sánchez**, F. Briones, *Pure magneto optic diffraction and domain observations in periodic domain structures fabricated on flat surfaces*, XVIII International Colloquium on Magnetic Films and Surfaces (ICMFS 2003), Madrid, July 2003

LIST OF ABBREVIATIONS

AFC	AntiFerromagnetically Coupled media
DMOKE	Diffractive Magneto-Optic Kerr Effect
IMM	Instituto de Microelectrónica de Madrid
LIL	Laser Interference Lithography
MBE	Molecular Beam Epitaxy
MFM	Magnetic Force Microscope
MO	Magneto-Optic
MOKE	Magneto-Optic Kerr Effect
MTJ	Magnetic Tunnel Junction
OOMMF ©	Object Oriented MicroMagnetic Framework
PMMA	PolyMethylMethacrilate
RT	Room Temperature
SEM	Scanning Electron Microscope
SFD	Switching Field Distribution
SNR	Signal to Noise Ratio
SPM	Scanning Probe Microscopy
UV	UltraViolet
VSM	Vibrating Sample Magnetometer

ACKNOWLEDGMENTS

A four years thesis work is a road no one walks alone. During these years I have met a lot of people from all over the world from whom I have learnt loads of worthwhile things (not all the kind that appears in a CV).

I feel thankful and indebted to these people -they know who they are-, but I would need a thesis-length document to express my gratitude.

For this reason I just mention a few of them, the ones who deserve a special acknowledgement since they all have decisively contributed to the development of this thesis.


Prof. Fernando Briones


Dr. José Luis Costa Krämer


Ana Bengoechea


Dr. Pedro García-Mochales


Dr. Francesc Torres


Dr. Rogelio Murillo


Vincent Sombroek


Dr. José Anguita

¡Muchas gracias!

Dank u wel!


Dra. Marisol Martín González


Dr. José Miguel García Martín


Ir. Martin Siekman


Barry te Dorsthorst


Ir. Thijs Bolhuis


Dr.Ir. Leon Abelmann


Prof. Juan José Sáenz


Dra. Sonia Melle


Dr. José Ignacio Martín